Radiative π^0 photoproduction in the region of the $\Delta(1232)$ resonance

by

Evangeline Joy Downie

Presented as a Thesis for the Degree of Doctor of Philosophy

Nuclear Physics Experimental Research Group
Department of Physics and Astronomy
University of Glasgow

December 2006

© E. J. Downie, 21st December 2006

Abstract

The $\Delta^+(1232)$ is the first excited state of the proton. The Δ-isobar states (the Δ^-, Δ^0, Δ^+ and Δ^{++}) are the lowest lying of the baryon resonances, and very well isolated. As such they form an excellent testing ground for the variety of Quantum Chromodynamics inspired models of hadronic structure. The resonance electromagnetic multipoles would be of particular theoretical interest. Due to the strongly decaying nature of the Δ-isobar, physicists have only been able to ascertain the masses and widths of these resonances and some of their transition multipoles, but not their static properties.

However, due to its short lifetime, the Δ^+ has a comparatively large width of ~120 MeV. This allows us to access the dipole magnetic moment of the Δ^+ (μ_{Δ^+}) through radiative self-decay whereby a Δ^+ is formed at the upper end of its mass range and radiatively decays to a Δ^+ of lower mass. This process has an amplitude that depends on μ_{Δ^+}. The secondary Δ^+ decays to a nucleon and a pion. This work is concerned with the $\Delta^+ \rightarrow \pi^0 p$ decay channel and the π^0 subsequently decays to a photon pair. We observed this three-photon, single proton, final state to reconstruct the $\gamma p \rightarrow \gamma' \pi^0 p$ reaction.

We studied this reaction in the A2 collaboration's Tagged Photon Experimental Hall at the Institut für Kernphysik in Mainz, Germany. The Glasgow Photon Tagging Spectrometer converted part of the MAMI B 883 MeV electron beam to an energy-tagged linearly polarised photon beam. Reaction products were detected in the new CB@MAMI 4π spectrometer setup composed of the Crystal Ball and TAPS detectors. The Crystal Ball was augmented with a pair of Multi-Wire Proportional Chambers for charged particle tracking. A plastic scintillator barrel, the Particle Identification Detector, was also specifically designed for the CB@MAMI experimental series to provide charged particle identification by ΔE/E methods. The experiment took place throughout several beam periods between July 2004 and January 2005.

We have analysed the new CB@MAMI data and have found ~20,000 radiative π^0 photoproduction events. From this event set we have produced preliminary total cross sections which agree well with the previous result and have a much improved statistical error.

The series of photon asymmetry measurements for $\gamma p \rightarrow \gamma' \pi^0 p$ we present herein represent the first measurement of this observable and indicate a downward trend in photon asymmetry both with increasing photon beam energy and with increasing production photon energy. The photon asymmetry results are well established.

Although not yet at the stage of μ_{Δ^+} extraction, due to the factor of ~ 40 higher statistics of this measurement, the additional physical

observables that have been measured and the recent intensive development of the theoretical models, we believe that the μ_{Δ^+} result extracted from this data will be far more accurate than that obtained from the only previous experiment carried out in 2000/01 [1].

Declaration

The data presented in this thesis were obtained as part of the CB@MAMI experimental series of the A2 Collaboration at the Institut für Kernphysik at Johannes Gutenberg University in Mainz, Germany. I participated fully in the preparation and execution of the experiment and the analysis of these data is entirely my own work. This thesis was composed by myself.

Evangeline Joy Downie

To my father, Alexander S. Downie, and Minnie Nelson.

Acknowledgements

Thanks are due Prof. Günther Rosner for offering me the opportunity to work with the NPE group from 2001 when I first became an NPE Summer project student, right through to my current position as an NPE Post-Doc. Thanks are also due to the A2 Collaboration for allowing me to participate in the experimental setup, running and data analysis of the CB@MAMI experimental series, and to all the staff of the Institut für Kernphysik in Mainz for providing such a high quality, stable beam for the experiment. Thank you to EPSRC for funding my PhD.

I'll be eternally grateful to J. R. M. Annand for his supervision and friendship over the last six years (and for introducing me to ddd). I have appreciated the friendship and advice of Cameron McGeorge and, most recently, his patience and care as a proof-reader of this work! I am grateful for the trust that Dan Watts put in me, allowing me to work so extensively on the PID, and for his supervision, advice and friendship during my skip visits. Ken Livingston has been an invaluable adviser on both polarisation issues and the wider work, and a fantastically patient sysadmin (I promise never to use "rm -rf *" in anger again). I really appreciate the great patience, friendship and technical expertise afforded me by Scott Lumsden and Tony Clarkson. In recent months, Douglas MacGregor has been a frequent adviser, Bob Owens has been a font of wisdom and experience and Derek Glazier has been an excellent analysis adviser, colleague and friend.

Over the last six years, I have enjoyed working with all of the NPE group members and thank them all for their assistance, encouragement, advice and friendship. Special mention has to be made of three of those from the early years: David Hamilton, Duncan Middleton and Andreas Reiter, for welcoming me to the group and providing advice on everything from ROOT operation to Collaboration politics. I have shared an office with many of the NPE students, but extra appreciation has to go to longest suffering: Morgan Murray, Kris Monstad, Craig Shearer, Gordon Hill and Eilidh McNicoll.

As for all the Mainzers, what can I say? Thanks are due to the entire A2 collaboration who have been an immensely friendly, interesting and fun group of people to work with. Thanks especially to Martin Kotulla for his analysis advice and staunch encouragement. Richard Codling and Claire Tarbet – I couldn't have picked a better pair with whom to share my night shift psychosis (we'll write the graphic novel yet)! Dirk Krambrich was amazingly tolerant of my poor soldering and bad programming. I also enjoyed our many ice creams. As for all of the Zeitungs Ente crowd (you know who you are - I won't name names), thanks, it was a lot of fun!

Nearer home, I have to thank my parents, Barbara and Alex Downie, and the rest of my family and friends, for their patient years of encouragement and support. I am especially grateful to my Mum for all she has done since we lost Dad. Thanks are more than due to the congregation of Victoria Tollcross Church of Scotland - I don't think that I could have found a larger and more diverse group of angels / comedians / cheerleaders / friends. And finally John: chauffeur, career adviser, proof-reader, physics consultant, agony uncle and nurse, there's no end to your talents and I couldn't have done this without you - at least half of the award is yours.

Contents

1 Introduction 1
- 1.1 The Early Years 1
- 1.2 The Trouble with Rutherford's Model 3
- 1.3 The Particle Zoo 4
- 1.4 The Glue 6
- 1.5 The Building Blocks 7
- 1.6 The Model 8
- 1.7 Excited States 8
- 1.8 The $\Delta(1232)$ Testing Ground 10
- 1.9 Our Experiment 10

2 Relationship of the $\gamma p \rightarrow p\pi^0\gamma'$ Reaction to the Magnetic Dipole Moment of the Δ^+ 13
- 2.1 Quantum Field Theory and the Effective Lagrangian 13
- 2.2 The Unitary Effective Lagrangian Model 14
- 2.3 The Chiral Effective Field Theory Model 19
- 2.4 Model Predictions and Dependence of the μ_{Δ^+} Result 22

3 Previous Work 27
- 3.1 Measurement of the Magnetic Dipole Moment of the Δ^{++} 28
  - 3.1.1 External Emission Dominance, the Soft Photon Approximation and the Extraction of $\mu_{\Delta^{++}}$ 28
  - 3.1.2 The UCLA Measurement 30
  - 3.1.3 SIN / PSI Measurement 38
  - 3.1.4 Discussion of $\mu_{\Delta^{++}}$ Experiments 43
- 3.2 Measurement of the Magnetic Dipole Moment of the Δ^+ by $p(\gamma, p\pi^0\gamma')$ 43

4 Experimental Equipment 49
- 4.1 Overview 49
- 4.2 Photon Beam 49
  - 4.2.1 MAMI 50
  - 4.2.2 Glasgow Tagger 53
  - 4.2.3 Beam Monitoring & Tagging Efficiency Measurement . . . 55
  - 4.2.4 Polarised Photon Production 56
- 4.3 Liquid Hydrogen Target 58
- 4.4 Crystal Ball System 59
  - 4.4.1 The Crystal Ball 59

4.4.2 Particle Identification Detector 61
4.4.3 Multi-Wire Proportional Chambers 62
4.5 The TAPS Forward Angle Spectrometer 65
4.5.1 BaF_2 65
4.5.2 Veto 67
4.6 Experiment Electronics 67
4.6.1 Crystal Ball and Trigger Electronics 67
4.6.1.1 ADC Branch 68
4.6.1.2 TDC Branch & Triggers 69
4.6.1.3 PID & MWPC Electronics 70
4.6.2 TAPS Electronics 70
4.6.3 Overall Control 70

5 Event Reconstruction 73
5.1 Analysis Software 73
5.2 Photon Tagger Calibrations 76
5.2.1 Random Subtraction 77
5.2.2 Timing Calibration & Alignment 78
5.2.3 Energy Calibration 78
5.2.4 Tagging Efficiency 79
5.3 CB System Calibrations 80
5.3.1 NaI Crystals 80
5.3.2 Particle Identification Detector Calibrations 81
5.3.2.1 Position Calibration 82
5.3.2.2 Energy Calibration 83
5.3.2.3 Time Calibration 84
5.3.3 Particle Identification 85
5.3.4 Multi-Wire Proportional Chambers 85
5.4 TAPS Calibrations 86
5.4.1 Barium Fluoride Energy Calibration 86
5.4.2 Barium Fluoride Time Calibration 87
5.4.3 TAPS Veto Calibrations 87
5.4.4 TAPS Particle Identification 88
5.5 Calorimeter Clustering Algorithm 89
5.6 Proton Energy Correction 90
5.7 Determination of the Degree of Linear Photon Polarisation 92
5.8 Photon Asymmetry of $\gamma p \rightarrow p\pi^0$ 95

6 Event Selection and Analysis 101
6.1 Simulation 101
6.1.1 Event Generation 101
6.1.2 Analysis of Simulated Data Sets 102
6.2 Conventions 104
6.3 Background Channels 105
6.3.1 Background Due to $\gamma p \rightarrow p\pi^0$ 105
6.3.2 Background Due to $\gamma p \rightarrow p\pi^0\pi^0$ 105
6.4 Data Cuts 106

6.4.1 Initial Selection . . . 106
6.4.2 Clustering Algorithm and Photon Angles . . . 106
6.4.3 Removal of TAPS Background . . . 106
6.4.4 Identification of π^0 . . . 108
6.4.5 Proton Energy Correction . . . 109
6.4.6 Beam Energy . . . 110
6.4.7 Real Split-Off Removal . . . 110
6.4.8 Momentum Conservation . . . 111
6.4.9 Removal of $\gamma p \rightarrow p\pi^0$ by Pion Energy . . . 111
6.4.10 Invariant Mass Difference . . . 111
6.4.11 Missing Mass of the γ' . . . 114
6.4.12 Invariant Mass of the π^0 . . . 115
6.5 $2\pi^0$ Background Subtraction . . . 115
6.5.1 π^0 Invariant Mass-Based Subtraction . . . 116
6.5.2 $p(\gamma, \pi^0\pi^0 p)$ Cross Section-Based Subtraction . . . 117
6.6 $p(\gamma, \pi^0 p)$ Background Subtraction . . . 117
6.7 Cross Section . . . 120
6.8 Photon Asymmetry . . . 123
6.9 Analysis of $p(\gamma, \pi^0 p)$ . . . 125

7 Discussion of Results and Conclusions 127
7.1 Total Cross Section Results . . . 127
7.1.1 Total Cross Section of $\gamma p \rightarrow \gamma'\pi^0 p$ . . . 127
7.1.2 Normalised Yield for $\gamma p \rightarrow \pi^0 p$ . . . 129
7.1.3 Systematic Error in Cross Section Measurements . . . 130
7.1.4 Discussion of Total Cross Sections . . . 135
7.2 Photon Asymmetry of $\gamma p \rightarrow p\pi^0\gamma'$ . . . 140
7.3 Discussion of $\gamma p \rightarrow p\pi^0\gamma'$ Photon Asymmetry . . . 147
7.4 Conclusions . . . 147

A Design & Construction of The Particle Identification Detector 151
A.1 Detector Design . . . 151
A.2 Construction . . . 154
A.3 Detector Designs . . . 158
A.4 Simulation Results . . . 161

B Polarised Photon Production 163

C Measuring a Photon Asymmetry 167
C.1 Experimental Definition of Photon Asymmetry . . . 167
C.2 Calculation of Statistical Errors in a Photon Asymmetry Measurement . . . 171

D Tables of Results 173
D.1 Cross Section of $p(\gamma, \gamma'\pi^0 p)$ . . . 173
D.2 Photon Asymmetry of $p(\gamma, \gamma'\pi^0 p)$ . . . 173

List of Figures

1.1 The atom. (a) depicts the Thompson model with the negative electrons dispersed throughout a positively charged medium. (b) depicts Rutherford's model, with the dense central positively charged nucleus, surrounded by empty space and the orbiting electrons. . . 2

1.2 The results of the quark model. The quark content is shown in the upper line of text in each circle, and the conventional name in the lower line. Charge (q) and strangeness (s) quantum numbers are shown by the dashed and dotted lines, respectively. Where multiple particles share the same q/s combination, they appear superimposed, however they differ in other quantum numbers that are not illustrated here. In the case of (b), the π^0, η and η' particles are formed by different linear combinations of $u\bar{u}$, $d\bar{d}$ and $s\bar{s}$. . . . 9

1.3 A simple view of the excitation of a proton to form a Δ^+. 9

1.4 Diagrammatic representation of $\gamma + p \rightarrow \Delta^+ \rightarrow \Delta^+\gamma'$, showing the shaded Breit-Wigner mass distribution of the Δ^+, the proton being excited to form a high-mass Δ^+, which subsequently decays, with the emission of a photon, to form a lower mass Δ^+, which decays to form a π^0 meson and a proton. Extracted from [1]. . . . 11

2.1 Feynman Diagram representation of each of the processes included in [2]. Process (a2) is sensitive to μ_{Δ^+}. Extracted from [2]. 15

2.2 Diagrams for the $\gamma p \rightarrow \pi N$ reaction in the $\Delta(1232)$ region: Δ resonance excitation (a), vector meson exchange (b), nucleon pole terms (c1-c2), pion pole term (d) and Kroll-Ruderman term (e). Extracted from [2]. 16

2.3 Total cross sections for $\gamma p \rightarrow p\pi^0$ (left panel) and $\gamma p \rightarrow n\pi^+$ (right panel). The solid curve is the result of the full unitary model, the dashed curve indicates the result of the tree-level calculation, and the dotted curve shows the unitarised $\Delta(1232)$ contribution. The data for $\gamma p \rightarrow p\pi^0$ are from MacCormick [3] and Ahrens [4]. The data for $\gamma p \rightarrow \pi^+ n$ are from McPherson [5], Fissum [6], MacCormick [3] and Ahrens [4]. Extracted from [2]. 17

2.4 Differential cross section for the $\gamma p \rightarrow \pi^0 p$ reaction (left panel) and $\gamma p \rightarrow \pi^+ n$ reaction (right panel) at different photon lab energies E_γ as a function of the c.m. angle θ. The data are from MAMI [7] and Bonn [8]. See Figure 2.3 for further notation. Extracted from [2]. 18

2.5 Diagrams for the $\gamma p \rightarrow \gamma' \pi^0 p$ interaction in the next-to-leading order of the χEFT calculation presented. Doubled lines represent Δ propagators. Extracted from [9]. 22
2.6 Predictions of the Unitary Model [2], described in Section 2.2. Upper panel: outgoing photon energy dependence of the cross section $d\sigma/dE_{\gamma'}^{c.m.}$ multiplied by $E_{\gamma'}^{c.m.}$ for κ_{Δ^+}=3 and at three different beam energies. The dashed curve represents the results of the tree-level approximation and the solid curve the result of the unitary model. Data are from [1]. Lower panel: Prediction of the variation of the photon asymmetry with $E_{\gamma'}^{c.m.}$ at a laboratory frame beam energy of 400 MeV. Dotted curve shows the result for $\kappa_{\Delta^+} = 0$, solid line for $\kappa_{\Delta^+} = 3$. Extracted from [2]. 24
2.7 The predictions of the χEFT theory [9], described in Section 2.3. Upper panel: the ratio of $\gamma p \rightarrow \gamma' \pi^0 p$ to $\gamma p \rightarrow p \pi^0$ cross sections. Data are from [1]. Middle panel: the linear-polarisation photon asymmetry of the $\gamma p \rightarrow \gamma' \pi^0 p$ cross sections differential w.r.t. $E_{\gamma'}^{c.m.}$ and the pion c.m. angle. The data point at $E_{\gamma'}^{c.m.} = 0$ corresponds to the $\gamma p \rightarrow p \pi^0$ photon asymmetry reported in [7, 10]. Lower panel: the circularly polarised photon asymmetry as a function of $E_{\gamma'}^{c.m.}$. Extracted from [2]. 25

3.1 Experimental setup for $\mu_{\Delta^{++}}$ study by UCLA. Reproduced from [11] 31
3.2 Comparison of measured and calculated cross sections as a function of: (a) α_γ at $E_\gamma = 40$ MeV and $T_{\pi^+} = 269$ MeV, and (b) E_γ, averaged over photon counters $G_1 - G_{10}$ for 263 MeV π^- (upper panel) and 269 MeV π^+ (lower panel). Reproduced from [11]. . . . 33
3.3 Comparison of measured and calculated ratio P_1 as a function of: (a) α_γ at $E_\gamma = 15-30$ MeV and (b) E_γ for several different angles, averaged over neighbouring photon counters. Reproduced from [11]. 34
3.4 Comparison of measured and calculated ratios: (a) P_2 and (b) P_3 as a function of E_γ for several different angles, averaged over neighbouring photon counters. Reproduced from [11]. 35
3.5 Comparison of measured and calculated ratios (a) R_+ and (b) R_- as a function of E_γ for several different angles, averaged over neighbouring photon counters. Reproduced from [11]. 36
3.6 Comparison of $\pi^+ p \rightarrow \pi^+ p \gamma$ cross section in the lab frame as a function of E_γ for $T_{\pi^+} = 324$ MeV for photon counters G_1 (upper panel) and G_{13} (lower panel) with SPA theory by Liou and Nutt [12] and data points from [11]. Reproduced from [11]. 37
3.7 $\pi^+ p \rightarrow \pi^+ p \gamma$ differential cross section in the lab frame as a function of $\mu_{\Delta^{++}}$, as calculated by [13]. The horizontal lines show the measured laboratory cross section as reported in [11] for: (a) photon counters G_4 and G_{11} at T_π =298 MeV for E_γ =60 MeV and 58 MeV, respectively. (b) photon counter G_1 at T_π = 269 MeV, 298 MeV and 324 MeV with E_γ =43 MeV, 58 MeV and 69 MeV, respectively. Reproduced from [11]. 38

3.8 Experimental setup for $\mu_{\Delta^{++}}$ study at SIN / PSI. Reproduced from [14]. 39
3.9 Comparison between UCLA data (circles) with the SIN low angle data set (triangles). Reproduced from [15]. 41
3.10 Comparison of all-angle SIN differential cross section with different models: SPA (dash/dot), EED (dashes), MIT (dots). Reproduced from [15]. 42
3.11 Bremsstrahlung polarised-target asymmetry versus photon energy. The curves are predictions from MIT theory for several values of $\mu_{\Delta^{++}}$, with data points from [14]. Reproduced from [14]. 43
3.12 The TAPS experimental setup at MAMI, showing the six smaller TAPS blocks and the larger forward wall. 44
3.13 The missing mass of the $(\pi^0 p)$ system in the final state for two different photon beam energies. The peak near 0.02 (GeV/c^2)^2 is from $2\pi^0$ production and is cut away, that at 0.00 (GeV/c^2)^2 shows the true $\gamma'\pi^0 p$ production. The dotted and dashed lines are the respective lineshapes from a GEANT 3 simulation. Extracted from [1]. 45
3.14 The reaction cross section for $\gamma p \rightarrow \gamma' p \pi^0$, as measured by the TAPS & A2 Collaborations [1,16]. The three lines are predictions of the cross section based on different values of μ_{Δ^+} from [17]. . . 46

4.1 The experimental setup, showing the MWPCs and PID inside the Crystal Ball, and TAPS covering the downstream region. 50
4.2 The MAMI facility, showing RTMs 1, 2 and 3 (MAMI-B) which were in use for this experiment, the Harmonic Double Sided Microton (HDSM – MAMI-C), planned to raise the electron beam energy to 1.5 GeV, and the A2 experimental hall where the experiment took place. 51
4.3 A racetrack microtron showing the increased path radius with increasing energy and the relationship between ΔE for the electron and the phase of the cavity oscillation. 52
4.4 The Glasgow Tagger. Adapted from [18]. 54
4.5 The A2 Goniometer 57
4.6 Goniometer Alignment Scan Results: the photon energy is plotted radially from the centre of the ring and the azimuthal angle indicates the angular position at which the energy spectrum was sampled. Left panel: An initial goniometer scan showing asymmetry, which indicates crystal misalignment. The superimposed lines show the fit results which locate the proper alignment position. Right panel: A goniometer scan after the diamond crystal has been aligned using the scan results shown on the left. Four-fold symmetry indicates successful alignment. 58
4.7 The liquid Hydrogen target. Figures reproduced from [19]. 60
4.8 The Crystal Ball 61
4.9 The Particle Identification Detector 63

4.10 ΔE / E plot from experimental data showing particle separation. The red band shows a typical selection region for protons, the blue band for charged pions. An electron peak can be seen near the origin. 64

4.11 Wire chamber diagram, showing anode wires and cathode winding. 64

4.12 The TAPS forward wall configuration. 66

4.13 A TAPS element. 66

4.14 The layout of the Crystal Ball trigger electronics. 68

5.1 The AcquRoot data storage and analysis system. Extracted from [20]. 74

5.2 The analysis architecture applied in this work. Adapted from [20]. 75

5.3 Spectrum indicating the blue dotted “prompt” and the red lined “random” region of the Tagger time OR spectrum. 77

5.4 Spectrum showing Tagger time alignment for all of the July data. 78

5.5 The tagging efficiency as a function of Tagger channel, illustrating the variation with time and polarisation orientation. The sudden change in tagging efficiency near channel 200 is due to the Diamond radiator. As coherent bremsstrahlung is more strongly forward-peaked than normal bremsstrahlung, a large increase in tagging efficiency is observed at the coherent edge (see Appendix B). Left panel: Tagging efficiency variation throughout the run period, red crosses show tagging efficiency for $\|$ run 2852 (early in the experimental run period), blue crosses for $\|$ run 3398 (late in the run period) and black crosses show the average tagging efficiency values used in this work. Right panel: red crosses show tagging efficiency for $\|$ run 2852, blue crosses for $\perp$ run 2853 and black crosses show the average tagging efficiency values used in this work. 80

5.6 Crystal Ball element time alignment results for the entire July data set. 81

5.7 Azimuthal position calibration of Particle Identification Detector. Left panel: Azimuthal angle of CB clusters in coincidence with PID elements for events with one hit in each detector. Right panel: Projection of left panel for PID element 0. The strong peak results from charged particles (such as electrons) passing from the target, through the PID and into the CB creating a signal in both detectors. We use this to identify the ϕ position of each PID element. The weaker peak $\sim 180°$ from the stronger one results from reactions emitting particles 180° apart in ϕ, such as $p(\gamma, \pi^+ n)$, where the neutral particle makes a detectable signal in the CB, but the charged particle stops in the PID. 82

5.8 Energy calibration of Particle Identification Detector. 83

5.9 ΔE/E Plot for all PID elements showing the pion cut (Blue Line) and the proton cut (Red Line) for all PID scintillators and all CB cluster energy deposits >5 MeV, using the 883.25 MeV beam and liquid Hydrogen target. 85

5.10 The TAPS BaF_2 energy calibration. Left panel: TAPS energy spectrum showing pedestal peak and cosmic muon energy deposit. Right panel: TAPS energy spectrum showing exponential + Gaussian distribution fit used to obtain the cosmic muon peak position in channel space. Extracted from [21]. 87

5.11 Pulse shape analysis of BaF_2 crystal output. Left panel: the energy deposit in the short gate ADC is plotted against that in the long gate. Right panel: the information is converted to polar coordinates then projected in the slices indicated by the red lines on the y-axis to allow selection. Extracted from [22]. 88

5.12 Explanation of the fitting procedure applied to the BaF_2 pulses to separate the proton and photon peaks. The large peak results from photon energy deposits, the smaller peak on the left results from protons. Extracted from [22]. 89

5.13 The result of the energy calibration for photons and protons. Left panel: π^0 energy calculated from θ_p and incoming beam energy plotted against measured π^0 energy from NaI pulse height (all π^0 variables are obtained from reconstruction of the π^0 from its two decay photons). Right panel: proton energy calculated from θ_p and incoming beam energy plotted against measured proton energy. . 90

5.14 Proton energy correction for $30° < \theta_p < 32°$. Upper left panel: Plot showing measured proton energy vs that calculated from θ_p and E_γ. Upper right panel: Graph showing fit results for measured proton energy projections of the 2D plot vs proton energy calculated from θ_p and E_γ. Lower panels: As above panels, but after proton energy correction has been applied. It can be seen that the proton energy correction improves the proton energy determination significantly. 91

5.15 The first eight $E_p(E_\gamma\theta_p)$ slice projections for $30° < \theta_p < 32°$. The $E_p(E_\gamma\theta_p)$ range is shown in the upper right hand corner of each plot. Fitting Gaussian distributions to each plot produced a representative measured energy value for each bin, only failing at higher $E_p(E_\gamma\theta_p)$ due to low statistics. 93

5.16 First eight $E_p(E_\gamma\theta_p)$ slice projections for $20° < \theta_p < 22°$. The $E_p(E_\gamma\theta_p)$ range is shown in the upper right hand corner of each plot. It was impossible to produce a representative measured energy value for each plot. 94

5.17 Illustration of the *anb* calculation. Upper panel: enhanced Tagger spectrum showing agreement between data (black line) and calculation (blue line). Lower panel: polarisation output from *anb*. Right panel: input parameters for part of July data. 96

5.18 Measured photon asymmetry of $\gamma p \rightarrow p\pi^0$ for $\theta_p^{c.m.} = 90^\circ \pm 5^\circ$ and photon beam energies of 400 ± 10 MeV (left) and 420 ± 10 MeV (right). 97

5.19 Random subtracted para (black crosses) and perp (blue circles) data showing why only counts outside of the shaded area were included in the normalisation of the $\gamma p \rightarrow p\pi^0$ data. The CB acceptance is very low at $\phi = \pm 180^\circ$ and $\phi = 0^\circ$, as can be seen by the dip in the data at these points. We artificially force the acceptance to zero (for the purposes of the normalisation) in the dotted regions to give the acceptance a 90°-symmetry in order that the acceptance changes affect both samples equally. 98

6.1 $E_{\gamma'}$ distributions from the two $p(\gamma, \gamma'\pi^0 p)$ simulation event generators. The red line shows the distribution from gppi0a, and the blue line shows the $1/\mathrm{E}_{\gamma'}$ dependent gppi0b distribution. 102

6.2 Simulated TAPS cluster time vs. cluster energy plot showing the identification of photons and protons in the AcquRoot analysis of simulated $\gamma p \rightarrow \gamma'\pi^0 p$ events. 103

6.3 The angle difference between photon pairs showing the effect of the clustering algorithm on photon cluster distributions. The crosses show the difference in angle between all possible pairs of photons reconstructed using the basic clustering algorithm, while the circles show the result for the iterative cluster algorithm. 107

6.4 The angle difference between photon pairs showing the effect of requiring that the angle difference between all photons must be greater than 30° to ensure no pseudo-split-off contamination. The black points show July data with all cuts save the one under study, the red crosses show analysed gppi0a simulated data and the blue crosses show analysed gppi0b simulated data. 107

6.5 The time difference between photon pairs showing the effect of requiring that the magnitude of the time difference between all photons must be less than 7 ns. This removes events having four clusters due to random coincident electromagnetic background in TAPS early in the analysis, but has little effect on the final event sample. The green points show the time difference between all possible photon pairs after only the initial particle identification and number cut has been made. There is a large peak around zero corresponding to coincident photons in the CB and TAPS. The low level EM background in TAPS throughout the TDC time window can be seen. The black points correspond to the final event sample without the application of the timing cut, showing that the constant background is effectively removed by the other cuts. . . . 108

6.6 The polar angle of γ' in the lab frame showing the effect of the cut requiring all photon angles be greater than 8° (in the lab frame) on the polar angle of the γ'. Without this cut, $\theta_{\gamma'}$ displays an unphysical peak below 8° where the small angle random electromagnetic background in TAPS dominates the real event sample. The black points show July data with all cuts save the one under study, the red crosses show analysed gppi0a simulated data and the blue crosses show analysed gppi0b simulated data. 109

6.7 The energy of γ' in the centre of mass system, showing the effect of a cut requiring $E_{\gamma'}^{c.m.} > 30$ MeV. Black points show July data with all cuts save the one under study. The black points show July data with all cuts save the one under study, the red crosses show analysed gppi0a simulated data and the blue crosses show analysed gppi0b simulated data. 110

6.8 The momentum balance in x-, y- and z-directions in the laboratory system showing the effect of the missing momentum cuts (Section 6.4.8). The black points show July data with all cuts save the one under study, the red crosses show analysed gppi0a simulated data and the blue crosses show analysed gppi0b simulated data. The simulation results agree well with the measured distributions. The discrepancy in the centre of the z-distribution should be remedied by incorporating the slight target misalignment (~10mm) into the simulation. 112

6.9 The difference between the measured energy of the π^0 and that calculated using $p(\gamma, \pi^0 p)$ kinematics in the centre of mass system, showing the cut requiring the difference be less than -25 MeV. Green points show data before all cuts are made to illustrate clearly the width of the zero-centred $\gamma p \rightarrow p\pi^0$ events. The black points show July data with all cuts save the one under study, the red crosses show analysed gppi0a simulated data and the blue crosses show analysed gppi0b simulated data. A small enhancement can be seen around zero in the final data, this is removed by our cut, without sacrificing too large a proportion of our final event sample. The gppi0b simulation results agree well with the final distribution and therefore is used for the final cross section normalisation. . . 113

6.10 The missing mass evaluated as the difference between the invariant mass of the π^0 and γ' and the missing mass calculated using the beam, target and proton (Equation 6.6). The black points show July data with all cuts save the one under study, the red crosses show analysed gppi0a simulated data and the blue crosses show analysed gppi0b simulated data. 114

6.11 The missing mass of the γ', as defined in Equation 6.7. The green circles show the results of the simulated $\gamma p \rightarrow p\pi^0\pi^0$ data. The black points show July data with all cuts save the one under study, the red crosses show analysed gppi0a simulated data and the blue crosses show analysed gppi0b simulated data. 115

6.12 The invariant mass of the π^0 after all other cuts have been made, showing the final invariant mass limits. The $p(\gamma,\pi^0\pi^0p)$ background can be clearly seen either side of the true event peak. The black points show July data with all cuts save the one under study, the red crosses show analysed gppi0a simulated data and the blue crosses show analysed gppi0b simulated data. The correction for this background is discussed in Section 6.5. 116

6.13 The invariant mass of the π^0 after all other cuts have been made, showing the applied cuts. The blue points correspond to the results from the $p(\gamma,\pi^0\pi^0p)$ simulation, the red from gppi0b simulation results and the green points show the sum of the two simulated contributions. The green trace matches the black experimental data points at and above the true π^0 invariant mass. 117

6.14 The subtraction of $p(\gamma,\pi^0\pi^0p)$ background based on the invariant mass of the π^0 after all other cuts. The four panels show the variation in background with increasing E_γ in 50 MeV-wide E_γ bins. The black points show the original unsubtracted data, the red shows the $p(\gamma,\pi^0\pi^0p)$ contribution to be subtracted and the blue shows the final subtraction result. It can be seen that only minimal subtraction is required at $E_\gamma < 450$ MeV where the photon asymmetries and μ_{Δ^+} are evaluated. 118

6.15 The cross section of $p(\gamma,\pi^0\pi^0p)$ from [23]. 118

6.16 The acceptance of $p(\gamma,\pi^0\pi^0p)$ calculated from the simulation. . . 119

6.17 The effective cross section due to $p(\gamma,\pi^0\pi^0p)$ contamination. . . . 119

6.18 The cross section of $p(\gamma,\pi^0p)$ from [23]. 120

6.19 The acceptance of $p(\gamma,\pi^0p)$ calculated from the simulation. . . . 121

6.20 The effective cross section due to $p(\gamma,\pi^0p)$ contamination. 121

6.21 Tagger scalers (upper left), multiplied by the tagging efficiency (upper right) give the number of photons impinging on the target from each Tagger channel (lower histogram). 122

6.22 The total number of tagged photons in each E_γ bin for all beam times. 123

6.23 The total number of detected $p(\gamma,\gamma'\pi^0p)$ events in each E_γ bin for all beam times. 124

6.24 The efficiency of the CBTAPS system for $p(\gamma,\gamma'\pi^0p)$ events as a function of E_γ. 124

6.25 The total number of $p(\gamma,\gamma'\pi^0p)$ events in each E_γ bin for all beam times. 125

7.1 The $p(\gamma, \gamma'\pi^0 p)$ cross section, before $p(\gamma, \pi^0 p)$ subtraction, for the entire data set, illustrating the methods of $p(\gamma, \pi^0\pi^0 p)$ subtraction. The square markers represent the raw $p(\gamma, \gamma'\pi^0 p)$ cross section before $p(\gamma, \pi^0\pi^0 p)$ subtraction, the open circles indicate the cross section after subtraction using the $p(\gamma, \pi^0\pi^0 p)$ cross section measured in [23], and the triangles represent the cross section after subtraction by fitting to the π^0 invariant mass distribution. The subtraction methods agree well in the region $E_\gamma < 450$ MeV where both photon asymmetries and μ_{Δ^+} are evaluated. 128

7.2 The $p(\gamma, \pi^0 p)$ background subtraction from our $p(\gamma, \gamma'\pi^0 p)$ cross section determination. Filled circles and triangles show the $p(\gamma, \gamma'\pi^0 p)$ cross section for the full data set before and after $p(\gamma, \pi^0 p)$ subtraction, respectively, and open circles show the $p(\gamma, \pi^0 p)$ contamination calculated as described in Section 6.6. 129

7.3 The $p(\gamma, \gamma'\pi^0 p)$ cross section for each of the beam times. Open circles show the $p(\gamma, \gamma'\pi^0 p)$ cross section for the July beam time, filled squares show that from September, filled circles show that from January, and triangles show the cross section calculated from the entire data set from all three beam times combined. 130

7.4 The final $p(\gamma, \gamma'\pi^0 p)$ cross section. Triangles show the cross section from this work and circles show that determined in [23]. The solid line shows the prediction of the χEFT model [9]. The χEFT model is currently undergoing further development, which should bring the model prediction closer to the measured cross section. The final results from this work represent a vast improvement in statistical error over the previous measurement. 131

7.5 The normalised yield for $p(\gamma, \pi^0 p)$ from this work compared to the cross section measured in [24] (squares) and [23] (filled circles). Triangles show the yield from the July data set, open circles show that from the September data set. After the simulation is extended to include trigger effects we expect the low E_γ discrepancy to vanish (see Section 7.1.3). 132

7.6 Systematic tagging efficiency error evaluation. Crosses show the maximum and minimum recorded tagging efficiencies for each channel and the circles show the mean tagging efficiency for each channel used in the final cross section calculations. The enhancement in tagging efficiency around channel 200 is due to the forward-peaking of the coherent bremsstrahlung which results in a sharp increase in tagging efficiency at the coherent edge. 133

7.7 Kinematic distributions of final state γ' in the centre-of-mass frame for the July data set: polar angle (upper panel), azimuthal angle (middle panel) and energy (lower panel). Black crosses correspond to the final July data set, red to the gppi0a simulated data set and blue to the simulated gppi0b data set. The gppi0b simulation results agree well with the real data, with only slight disagreement in the $E_{\gamma'}$ spectrum, which should be remedied by the adjustments to the simulation listed in 7.1.3. 136

7.8 Kinematic distributions of final state π^0 in the centre-of-mass frame for the July data set: polar angle (upper panel), azimuthal angle (middle panel) and energy (lower panel). For further notation see Figure 7.7. The gppi0b simulation results agree with the experimental data better than gppi0a. The slight disagreement in the θ_{π^0} and E_{π^0} spectra should be remedied by the adjustments to the simulation listed in 7.1.3. 137

7.9 Kinematic distributions of final state proton in the centre-of-mass frame for the July data set: polar angle (upper panel), azimuthal angle (middle panel) and energy (lower panel). For further notation see Figure 7.7. Again the gppi0b simulation results agree with the experimental data better than gppi0a. The disparity between the simulation results and experimental data at low θ_p should be remedied by the adjustments to the simulation listed in 7.1.3. . . 138

7.10 Ratio of cross sections derived using event generator models gppi0a and gppi0b. The gppi0a-derived cross section is divided by that from gppi0b. The difference between the gppi0a and gppi0b simulation models is far larger than the difference between the gppi0b simulated data and the experimental results (as can be seen in Figures 7.7, 7.8 and 7.9), thus we expect the uncertainty due to the input generated event set to be smaller than the deviations observed here. 139

7.11 Cos(2ϕ) fit to the $p(\gamma, \gamma'\pi^0 p)$ azimuthal distribution for all θ_{π^0} and $E_{\gamma'}$ using: July data set with 340 MeV $< E_\gamma <$ 440 MeV (upper panel) and September data set with 300 MeV $< E_\gamma <$ 400 MeV (lower panel). Plots show statistical error only. 141

7.12 Variation of asymmetry with $E_{\gamma'}$ for $p(\gamma, \gamma'\pi^0 p)$ for all θ_{π^0} and $E_{\gamma'}$ using: July data set with 340 MeV $< E_\gamma <$ 440 MeV (upper panel) and September data set with 300 MeV $< E_\gamma <$ 400 MeV (lower panel). The points at $E_{\gamma'} = 0$ MeV are derived from the analysis of $p(\gamma, \pi^0 p)$ with the same cuts as $p(\gamma, \gamma'\pi^0 p)$. Points show statistical error bars, grey-shaded bars show the magnitude of the absolute systematic error in each bin. The smaller systematic uncertainty for 300 MeV $< E_\gamma <$ 400 MeV is due to the factor of $\sim$10 lower $p(\gamma, \pi^0\pi^0 p)$ contamination. The model predictions are shown in Figure 7.13 for comparison. 142

7.13 Variation of asymmetry with $E_{\gamma'}$ for $p(\gamma,\gamma'\pi^0p)$ as predicted by the Unitary model (upper panel) and the χEFT model (lower panel). The Unitary model result appears to agree better with the data shown in Figure 7.12 than the χEFT model. 143
7.14 Evaluation of systematic error due to $p(\gamma,\pi^0\pi^0p)$ contamination for 340 MeV $< E_\gamma <$ 440 MeV (July data), black points show real event sample, blue points show simulated $p(\gamma,\pi^0\pi^0p)$ results. Upper panel shows π^0 invariant mass fit which gives the scaling factor for $p(\gamma,\pi^0\pi^0p)$ contamination. Lower panel shows resulting contribution of simulated $p(\gamma,\pi^0\pi^0p)$ to the $E_{\gamma'}$ distribution. The expected contamination in the September data set is a factor of ten smaller. 145
7.15 Evaluation of systematic error due to shifting coherent edge position. Upper panels show July results, lower show September. Left panels show the polarisation tables for three coherent edges: blue for a coherent edge position ∼5 MeV lower and red for one ∼5 MeV higher than the black mean edge position used in the final analysis. The right hand side shows the resulting asymmetries, colour coded according to their corresponding edge position. 146
7.16 Evaluation of magnitude of total systematic error (solid line) showing error contribution due to shifting coherent edge position (dotted line) and error contribution due to $p(\gamma,\pi^0\pi^0p)$ contamination (dashed line). The upper panel shows error composition for 340 MeV$< E_\gamma <$ 440 MeV (July data) and the lower panel shows error composition for 300 MeV $< E_\gamma <$ 400 MeV (September data). . . 148

A.1 The Particle Identification Detector. The upper diagram shows the positioning of the PID between the target enclosure and wire chambers. The lower photograph shows the assembled PID connected to an oscilloscope for testing prior to installation. 152
A.2 Tests of Five Prototype Elements 154
A.3 PID positioning in the Crystal Ball. The left panel shows the positioning of the prototype elements in a plastic tube inside the CB for testing. The right panel shows the final assembled detector positioned in the plastic tube inside the CB before the MWPCs were ready. 155
A.4 Construction of the PID. The left panel shows the barrel of PMTs assembled on the brass support tube ready for gluing. The middle panel shows the assembly of the self-supporting scintillator barrel. The right panel shows the final gluing when the PMT and scintillator barrels were connected. 156
A.5 PID electronics. 157
A.6 Scintillator element design. 158
A.7 Light guide design. 158
A.8 Aluminium upstream support ring. 159
A.9 Brass tube for upstream support ring location. 160

A.10 PMT support ring. 160
A.11 Sample results for simulation showing exit position and angular spread for 20 MeV protons passing through 2 mm of scintillator. . 161
A.12 Sample results for simulation showing the energy loss, exit position and angular spread for 25.31 MeV protons passing through a 2 mm scintillator at a 20° angle. 162

B.1 Representation of the reciprocal lattice and the allowed momentum pancake in momentum space. By orientation of the crystalline radiator, it is possible to position only the reciprocal lattice vector of choice within the allowed momentum pancake. 164
B.2 The effect of radiator type on Tagger hit pattern (Tagger channels are shown in reverse order to highlight $1/E_\gamma$ dependence). The spectrum for a crystalline diamond radiator (upper panel) is divided by that due to an amorphous Ni radiator (middle panel) to produce the enhanced plot (lower panel) which clearly shows the position of the coherent edge. 165

C.1 Raw histograms of ϕ_{π^0} in the reaction $p(\gamma,\pi^0p)$, with no limits on θ_p and 340 MeV $< E_\gamma <$ 440 MeV for perpendicular polarisation orientation (left) and parallel polarisation orientation (right). The effect of the metal plate between the CB hemispheres can be seen at 0° and ±180°. 170
C.2 Illustration of photon asymmetry for $p(\gamma,\pi^0p)$ with no limits on θ_p and 340 MeV $< E_\gamma <$ 440 MeV. Applying Equation C.16 to the distributions illustrated in Figure C.1 gives a properly normalised $\cos(2\phi - \phi_0)$ distribution (left). To this distribution, we apply a fitting function to determine the amplitude A of the photon asymmetry and ϕ_0 and to check for any vertical offset (right). 170

List of Tables

1.1 The three generations of matter, reproduced from [25]. 6

1.2 The four forces of nature and their mediating particles. The graviton has not yet been observed - the listed properties are based on theoretical prediction. **Although technically infinite in range, effects due to the strong force are more typically seen at scales* $\sim 10^{-15}m$ *due to the colour-neutral formation of matter.* 6

1.3 Different quark model predictions for μ_{Δ^+} 11

5.1 The results of the initial beam polarisation check. 99

5.2 The results of the extended beam polarisation check. 100

6.1 Conventional symbols. All values are as measured in the centre of mass frame, save for E_γ which is always reported as measured in the lab frame. 104

D.1 Total cross section of $p(\gamma,\gamma'\pi^0p)$ for $E_{\gamma'}^{c.m.} > 30$ MeV, based on the entire data set, systematic error is estimated to be ±14.5%. 173

D.2 The photon asymmetry of $p(\gamma,\gamma'\pi^0p)$ for $E_{\gamma}^{c.m.} > 30$ MeV. 173

D.3 The photon asymmetry of $p(\gamma,\gamma'\pi^0p)$ for 340 MeV $< E_\gamma <$ 440 MeV, based on the July data set. The result for $E_{\gamma'} = 0$ MeV is derived from the analysis of $p(\gamma,\pi^0p)$ with the same E_γ range as $p(\gamma,\gamma'\pi^0p)$. 174

D.4 The photon asymmetry of $p(\gamma,\gamma'\pi^0p)$ for 300 MeV $< E_\gamma <$ 400 MeV, based on the September data set. The result for $E_{\gamma'} = 0$ MeV is derived from the analysis of $p(\gamma,\pi^0p)$ with the same E_γ range as $p(\gamma,\gamma'\pi^0p)$. 174

Chapter 1

Introduction

1.1 The Early Years

In the early 20th Century, Physicists were aware that atoms could break down and spit out fragments that they termed radiation. This radiation had been classified as α, β and γ, according to how heavy and penetrating it was. In 1869, Mendeleev had arranged the elements according to their relative atomic masses, obtained through painstaking chemical detective work, and grouped them, according to their chemical properties, to form the periodic table. However, it was generally believed that the structure of an atom was much like that of a plum pudding: a spherical, permeable, positively charged medium (the "pudding"), with the electrons, like plums, dotted throughout (Figure 1.1(a)). The plum-pudding model of the atom was proposed by J.J. Thomson, who had studied and identified electrons, but had been unable to find any similar positively charged particles.

In 1909, Ernest Marsden, an undergraduate working at the direction of Ernest Rutherford (1908 Nobel Prize winner), performed a seemingly routine experiment to eliminate an unlikely hypothesis. Marsden aimed a source of α particles (^4_2He nuclei) at a thin gold foil and observed the results using a small zinc-sulphide-coated glass screen and a microscope. When an α particle strikes zinc sulphide, it causes the zinc sulphide to flash, an effect known as "scintillation". As his observation equipment was on the same side of the gold foil as his α-source, Marsden expected to see no scintillation at all. Electrons were so much lighter than the α-particles (an electron has $\sim$1/8000th of the mass of an α-particle) that it was physically impossible for an isolated electron to scatter an α-particle backwards towards his scintillation detector. In the "plum-pudding" model, electrons were widely dispersed and the positively charged medium too dilute to allow the concentration of mass or charge required to substantially alter the course of an α particle. To his great surprise, he found that some α-particles were scattered into his detector, and he saw approximately one scintillation every second. After a week of rigorous checking, he reported his results to Rutherford. Ernest Rutherford concluded from Marsden's observations that, instead of a plum pudding, the atom resembled the solar system [26]. His model of the atom was almost entirely empty space. There was a dense, positively charged core, the "nucleus", which was surrounded by a cloud of fast-moving electrons. He proposed that the elec-

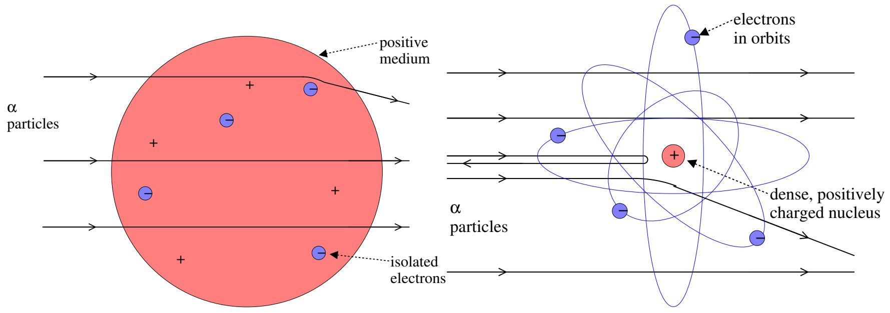

(a) (b)

Figure 1.1: The atom. (a) depicts the Thompson model with the negative electrons dispersed throughout a positively charged medium. (b) depicts Rutherford's model, with the dense central positively charged nucleus, surrounded by empty space and the orbiting electrons.

trons moved around the nucleus in circular paths, or "orbits", as the Earth does the sun. These electron orbits extended to, and defined, the boundaries of the atom (Figure 1.1(b)). This ground-breaking hypothesis was swiftly confirmed by other experiments, and the challenge became to capture and dissect this tiny "fly in the cathedral", the nucleus [27].

Nine years later (in 1918) Rutherford himself bombarded a Nitrogen target with α particles, using similar equipment to that which Marsden had used. He observed that some of the outgoing particles did not appear to be either α particles or Nitrogen nuclei. Upon further examination, he discovered that he was detecting Hydrogen nuclei. He deduced from this that he was transforming Nitrogen into Oxygen with the emission of a Hydrogen nucleus and concluded that Nitrogen must contain Hydrogen nuclei. He decided that the Hydrogen nucleus must be a fundamental[1] particle and named it the proton [28]. Since that time the proton and its uncharged relative, the neutron, which was later discovered by Chadwick under Rutherford's guidance [29], have been subjected to extensive experimental study and theoretical pondering.

In 1931 the proton was accelerated by Cockcroft and Walton (at Cambridge) to penetrate and smash Lithium atoms in their famous experiment using extremely high voltages, vacuums and Plasticine to tremendous effect [27, 30]. In the same year Lawrence and Livingston (at the University of California, Berkeley) produced the first proton cyclotron, only 4.5 inches in diameter, to accelerate protons up to energies of 80 keV [31]. Thus the proton became an experimental probe and tool for accessing the secrets of the atomic nucleus. By 1948, the technology of the cyclotron had advanced so far that the 184 inch proton cyclotron [32] - mentioned in Chapter 3 - was operational at Berkeley and being used both in nuclear experiments and in experimental treatments for cancer.

---

[1] A fundamental particle is one which cannot be further broken down and has no internal structure, i.e. is homogeneous and indivisible.

1.2 The Trouble with Rutherford's Model

Rutherford's model of the atom contained a major flaw. From classical electrodynamics, we know that a charged particle moving in a curved path will continually emit radiation. The electrons in the Rutherford atom would radiate, continually losing energy. The lower the energy an electron has, the smaller the radius of its orbit becomes, thus Rutherford's atom is unstable, and the electrons would ultimately spiral into the nucleus. Conversely, Rutherford's atom has no clearly defined radius - the more energetic an electron is, the further out it will orbit, and the larger the radius of the atom will become. Both things are contrary to what had been observed: physicists knew that atoms of a specific element all had the same radius, and the stability of the atom was generally accepted.

Throughout the late nineteenth and early twentieth century, physicists were investigating another group of problems, initially unrelated to the structure of the atom. There were several basic, easily observed and commonly agreed upon phenomena, for which physicists were unable to produce an underlying theory. For example: physicists could not produce an equation to adequately explain and predict the colour and intensity of light that an object would produce when it was heated (known as black-body radiation); and they could not explain why passing an electric current through different gases caused them to emit light of different colours, which, when separated using a prism, showed not the continuous rainbow that one sees with white light, but a set of discrete lines (atomic emission spectra).

In 1900, Max Planck found an equation that reproduced the black body radiation spectrum [33,34]. When he tried to derive the equation from first principles, he found that the only way to make it work was to assume that, instead of a continuous spectrum of energies, only specific values or "quanta" of energy were allowed in nature [35].

Bohr applied Planck's new quantisation to Rutherford's atomic model in 1913 [36], and placed the electrons into what he termed "stable orbits" in which the electrons had a definite energy and would not radiate. The specific lines in the atomic emission spectra could then be interpreted as the definite energies emitted from transitions between the allowed energies of these "stationary" orbits. This theory allowed the exact description and prediction of the emission lines seen for the Hydrogen atom. After the neutron was discovered, and the structure of heavier nuclei became understandable, the quantised energy levels for many of the heavier atoms were predicted and found to agree with the observed emission spectra.

This quantisation theory was extended by such famous physicists as Einstein [37], Heisenberg [38], de Broglie [39–41], and Schrödinger [42], with the assistance of many others, to become the theory known today as "Quantum Mechanics". Classical mechanics is sufficient to describe the macroscopic world as it was experienced both then and now. However, as we go to smaller and smaller scales, classical mechanics begins to fail, and we see "quantum" effects.

The most startling difference between quantum and classical mechanics is that quantum mechanics is probabilistic, where classical mechanics is deterministic.

Classical mechanics, given every available piece of data about a system at a specific point in time, will tell you exactly what should happen next, but quantum mechanics, given the same set of data, will give you the probability of certain states occurring next, but will not tell you absolutely what will happen.

Heisenberg defined a further uncertainty - “Heisenberg’s Uncertainty Principle” (HUP) [43]. In the case of a particle, such as an electron in an atomic orbit, there are specific pairs of variables (“conjugate” variables) such as energy and lifetime, or position and momentum, that cannot simultaneously be known with infinite precision. He quantified this in the equations labelled 1.1 and 1.2, where h is Planck’s constant.

$$\Delta E \Delta \tau \geq \frac{h}{4\pi} \tag{1.1}$$

$$\Delta p \Delta x \geq \frac{h}{4\pi} \tag{1.2}$$

It is the magnitude of Planck’s constant that gives the scale of the quantum universe. As $h = 6.626 \times 10^{-34}$ joule seconds, the effects of the quantisation and the uncertainty principle are only seen on atomic scales or smaller.

The major result of quantum mechanics, is that small scale systems, such as nuclei, can exist in a series of different, discrete, states, and that each one of these possible states has a set of characteristics, codified as quantum numbers, that completely describe it. One of the most important of these quantum numbers is spin which, as the name suggests, characterises the internal angular momentum of the particle. Every particle, such as the proton or neutron, has its own intrinsic spin. When these particles are combined in a more complicated system, the spin of the system results from the intrinsic spins of its components and their orbital angular momentum and depends strongly on the mutual interactions of the components.

Particles can be divided into two major classifications according to their spin: bosons, which have integer spin (0, 1, 2, ...); and fermions, which have half-integer spin ($\frac{1}{2}$, $\frac{3}{2}$, $\frac{5}{2}$, ...). Fermions, such as the protons and neutrons in the nucleus, obey a rule known as the “Pauli Exclusion Principle” PEP, which states that no two fermions in the same system can occupy the same state (i.e. have an identical set of quantum numbers) [44].

1.3 The Particle Zoo

Some seventy-five years on, we have learned much about the proton and now have a relatively broad empirical knowledge of many of its properties. For instance, we now know the mass of the proton, with extremely high precision, to be $(1.67262171 \pm 0.00000029) \times 10^{-27}$ kg [45]. The equipment and methodology used to study the nucleus and its components still follow the same basic principles: a particle beam impinges on a target and the interaction products are observed with detectors of some form or another, but the targets, detector systems and data analysis have become vastly more complex. In the course of this increasingly complicated study, physicists have encountered more than simply the familiar proton, neutron and electron, and their various combinations. A vast range of different particles has been identified, to the extent that physicists came to be the keepers of a "particle zoo".

In 1964 Murray Gellman and George Zweig (with additional independent contributions from the Israeli Yuval Ne'eman and the Japanese team of Kazuhiko Nishijima and T. Nakano), independently suggested that the reason so many particles species had been found was that the proton, the neutron and their rapidly expanding array of counterparts were not fundamental particles in themselves, but were composed of other, simpler, building blocks. These building blocks Gellman named "quarks". He proposed that there were three types, or "flavours", of quark (which he named up, down and strange) and that their different combinations resulted in the many different particle types [46]. He even produced diagrams of the sets of particles that could be formed using combinations of two quarks (particles now known as mesons) and particles, like the proton and neutron, that could be formed with combinations of three quarks (now called baryons) (Figure 1.2). In Gellman's model, the proton was composed of a combination of two up quarks and a down quark (represented **uud**) and the neutron contained two down and one up quark (**udd**). All particles composed of quarks became known as hadrons.

In 1969, Gellman's suggestion that the proton was not fundamental was demonstrated experimentally when a high energy electron beam was fired at a proton target at the Stanford Linear Accelerator (SLAC) [47]. The resulting distribution of the scattered electrons showed, as the α-particles did for the atom in 1911, that the proton had underlying structure. The experimentalists termed the components of this proton structure "partons" at first. Today, we accept this as the first experimental observation of the quark.

As experiments have increased in energy, we have discovered that there are not three, but six types of quark: up, down, strange, charm, bottom and top (listed in order of increasing mass). Although we still believe that the electron is a fundamental particle, we no longer believe it to be the only light charged particle (lepton). We have discovered two other similar particles: the mu and the tau. Each of these three particles has a corresponding neutrino, an electrically neutral particle of far lower mass than its corresponding lepton. All of these particles, the six quarks and the six leptons, have a corresponding anti-particle, which has the same mass, and an equal but opposite charge. In everyday life, everything around us is mostly composed of the lighter types of matter: the up and down quarks and the electron. Observation of the other "generations of matter" (Table 1.1) is limited to nuclear interactions at high energy physics laboratories like CERN. We have also discovered that, within the hadron family, mesons can be created and destroyed easily, provided one has sufficient energy, but the number of baryons in the world appears to be constant.

In the course of scientific investigation of the nucleus, massively diverse studies have been undertaken. At one extreme, are the heavy ion studies, whereby scientists have sought to create and study more exotic, heavier and diverse nuclei and probe the properties of these complex entities. At the other extreme are the exceedingly high energy particle physics studies at places like CERN, where scientists strive for ever-greater centre-of-mass collision energies to produce the

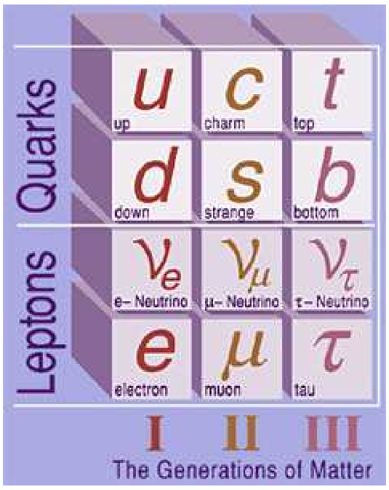

Table 1.1: The three generations of matter, reproduced from [25].

Force	Source	Mediating Particle	Mediating Particle Mass / GeV	Range	Relative Strength
Gravity	mass	graviton	0.0	infinte	10^{-39}
Weak	weak charge	$W^{\pm}(Z^0)$	80.4 (91.2)	$\sim 10^{-18}m$	10^{-5}
Electro-magnetic	electric charge	photon (γ)	0.0	infinite	10^{-2}
Strong	colour charge	gluon	0.0	infinite*	1

Table 1.2: The four forces of nature and their mediating particles. The graviton has not yet been observed - the listed properties are based on theoretical prediction. **Although technically infinite in range, effects due to the strong force are more typically seen at scales* $\sim 10^{-15}m$ *due to the colour-neutral formation of matter.*

heavier generations of quark and study the extremes of hadronic behaviour, extending to ever smaller distance scales. In the middle of these, lies medium-energy or hadronic physics and our experiment.

1.4 The Glue

Inside hadrons, quarks are tightly bound by a force known as the “strong force”. There are four fundamental forces in nature, summarised in Table 1.2. Each has a source and a mediating particle. We are all aware of gravity, however this plays a negligible role on the atomic scale. The next most familiar of these is the electromagnetic force, the source of which is electrical charge. The electromagnetic force is mediated by virtual photons - tiny packets of light that exist only by borrowing energy from the particles upon which they act. Without these virtual photons communicating the existence of the positively charged nucleus, the approaching α particle would not be repelled until it actually touched the surface of the nucleus, and we know this is not the case. Electromagnetic charge exists only in two forms: positive and negative. To make an electrically neutral object, one simply requires equal numbers of positive and negative charge. It is also possible to observe an isolated positive or negative charge.

The source of the strong force is colour charge. The strong force is 60 times stronger than the electromagnetic repulsion between two up quarks at a distance of 3×10^{-17}m (the up quark has an electromagnetic charge of $+\frac{2}{3}$). The effects of colour charge are communicated by mediating particles known as gluons. Only quarks and gluons posses colour charge and so only they are affected by the strong force. Colour charge exists as 3 colours and 3 anti-colours, and the only way to form colour-neutral objects is to combine the three colours, the three anti-colours, or any colour with its anti-colour. The strong force is so strong that quarks are confined to these colour-neutral arrangements, for example: quark-antiquark pairs (mesons) and three-quark combinations (baryons). Other colour-neutral combinations are not ruled out by the theory, such as the four-quark, one-antiquark combination known as the pentaquark, but, as yet, there has not been conclusive experimental proof of their existence [48].

1.5 The Building Blocks

Hadronic structure is now believed to be far more complex than the three quarks and quark / anti-quark combinations described by the Gellman model. Gellman's proposed quark components are now referred to as the "valence quarks", and it is believed that these valence quarks are surrounded by a sea of quark-antiquark pairs popping in and out of the vacuum, all held together by the colour-charge carrying, electrically neutral, gluons.

In general, the best way to discover how a complex entity is constructed, is to dismantle it. Clinicians have gained volumes of knowledge from the process of autopsy. Observing the nature of the constituents - their mass, their shape, the way they connect - gives information about the available combinations, the limits of the final construction and its likely behaviour. By looking at a set of Lego bricks, it is possible to plan and predict many of the possible final structures and their bulk properties.

This option is denied the hadronic physicist. If one tries to pull a quark-antiquark pair (a meson) apart, it requires tremendous energy, and before the point where the quarks could be considered separate, another quark-antiquark pair emerges from the vacuum to form two new mesons. A quark has never been observed in isolation (and there are strong reasons to believe that we never shall) and so we have never had the opportunity to directly observe exactly how the individual components of the proton are formed and most importantly, how they combine with each other. Instead, we find ourselves looking at a catalogue of Lego constructions and trying to work out what the Lego brick looks like.

1.6 The Model

In Sections 1.4 & 1.5, we have introduced what is now known as the theory of Quantum Chromodynamics (QCD). As we can not directly observe the individual quarks and gluons, we have to find some other experimental method to test QCD. To do this, we use the theory of QCD to calculate key properties of the various hadrons, and compare the calculated results to the experimentally measured values.

To perform these calculations, it is necessary to make some simplifying approximations due to the complexity and intractability of the mathematics at hadronic scales. Different sets of approximations are possible, and each of these sets is known as a model. Using a model, it is possible to predict a set of hadronic properties that can be experimentally tested. Some properties are insensitive to the QCD model used to predict them, i.e. no matter which model one uses, the results always agree. Others, such as magnetic dipole moment, are very model dependent. Experimental measurements of model independent properties are useful for testing QCD itself. Measurements of strongly model dependent properties provide a valuable test of the various models. Such tests indicate the regions in which each model is most applicable and highlight regions where the simplified calculation fails.

1.7 Excited States

In Figure 1.2, we show the results of the quark model. Comparing Figure 1.2(a) the baryon octet and Figure 1.2(c) the baryon decuplet, one can see that many of the particles have the same valence quark content. This means that it is possible to produce many of the particles in the baryon decuplet by simply supplying baryon octet members (such as the proton and neutron) with enough energy to change the arrangement of their quarks in order to have total spin of $\frac{3}{2}$ instead of the octet total spin of $\frac{1}{2}$. This can be naively viewed as exciting a quark spin-flip to increase the particle mass, and change it from a ground state baryon to one in an excited state. For example, in the experiment described herein, a proton in the liquid Hydrogen target is excited to form a Δ^+ (Figure 1.3).

These excited states are known as resonances as they are very short-lived. The mean lifetime of the Δ^+ is $\sim 10^{-24}$ seconds. With the exception of the Ω^- which decays by the weak force, all of these excited states, or baryon resonances, decay by the strong force to their ground-state configuration - the baryon octet states - commonly with the emission of a meson and always with a lifetime similar to that of the Δ.

Using Einstein's famous equation [49], more fully expressed as:

$$E^2 = p^2c^2 + m^2c^4, \tag{1.3}$$

we see that mass forms part of the total energy of a particle or resonance. If we apply the HUP (Equation 1.1) we find that, because the proton has an exceptionally long mean lifetime (large Δt), we can determine its mass (ΔE) with

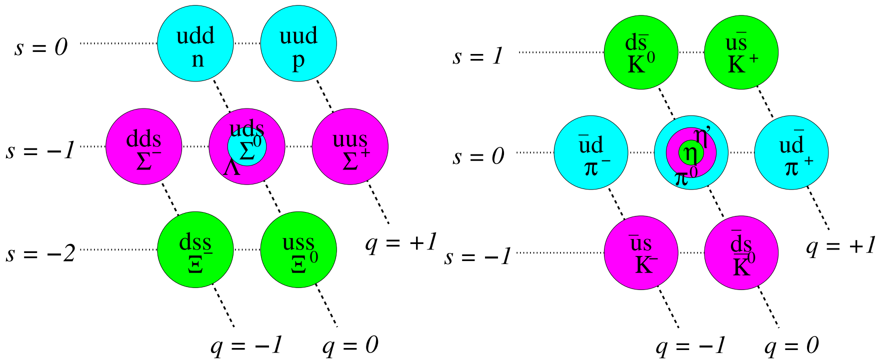
s = 0
udd n
uud p
s = −1
dds Σ−
uds Σ0 Λ
uus Σ+
s = −2
dss Ξ−
uss Ξ0
q = +1
q = −1
q = 0
s = 1
ds̄ K0
us̄ K+
s = 0
ūd π−
ud̄ π+
η'
η
π0
s = −1
ūs K−
d̄s K̄0
q = +1
q = −1
q = 0

(a) The ground state baryon octet with total spin 1/2

(b) The pseudoscalar meson nonet

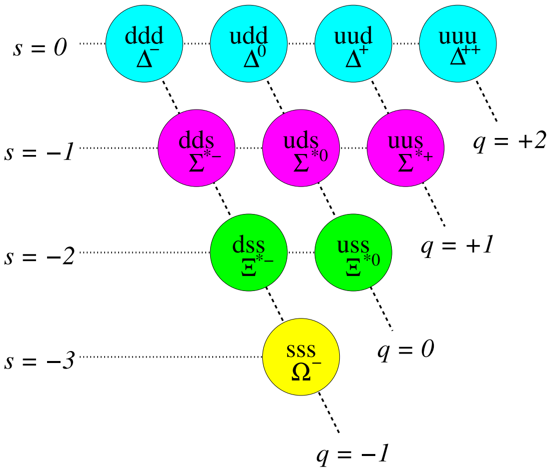
s = 0
ddd Δ−
udd Δ0
uud Δ+
uuu Δ++
s = −1
dds Σ*−
uds Σ*0
uus Σ*+
q = +2
s = −2
dss Ξ*−
uss Ξ*0
q = +1
s = −3
sss Ω−
q = 0
q = −1

(c) The baryon decuplet with total spin 3/2

Figure 1.2: The results of the quark model. The quark content is shown in the upper line of text in each circle, and the conventional name in the lower line. Charge (q) and strangeness (s) quantum numbers are shown by the dashed and dotted lines, respectively. Where multiple particles share the same q/s combination, they appear superimposed, however they differ in other quantum numbers that are not illustrated here. In the case of (b), the π^0, η and η' particles are formed by different linear combinations of $u\bar{u}$, $d\bar{d}$ and $s\bar{s}$.

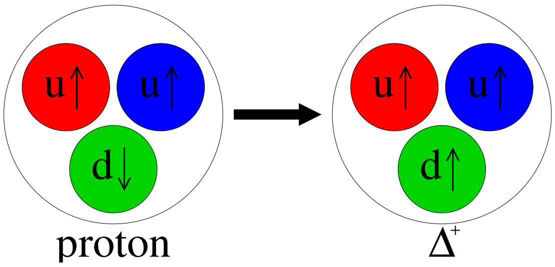
u↑
u↑
d↓
proton
u↑
u↑
d↑
Δ+

Figure 1.3: A simple view of the excitation of a proton to form a Δ^+.

incredible precision (as mentioned in Section 1.3). In the case of a very short-lived resonance, the very tightly defined lifetime (small $\Delta\tau$) limits the precision to which its mass (ΔE) can be determined. Instead of a single value, we find a distribution of values (the Breit-Wigner distribution function [50]), described by the mean value (the mass) and the spread (width) of the distribution.

These short resonance lifetimes cause experimental difficulty. They preclude many of the usual techniques that were used to measure the main properties of the baryon octet, such as spin precession in a magnetic field to determine the magnetic dipole moment of a particle. In consequence, we know very little about the baryon decuplet (other than the Ω^-), save the masses and widths of the lowest lying resonances.

1.8 The $\Delta(1232)$ Testing Ground

The group of four particles with $s = 0$ in the baryon decuplet (Figure 1.2(c)), the Δ^-, Δ^0, Δ^+ and Δ^{++}, are known collectively as the Δ isobar. The $\Delta(1232)$ isobar is an ideal testing ground for theoretical models for a variety of reasons. Each member of the isobar differs (in turn) by a single valence quark, and all are composed entirely of up and/or down quarks (which have very similar masses). This means that differences we observe from Δ to Δ can be accounted for on grounds of quark flavour alone. For example, any differences between the Δ^- and the Δ^0 result from the exchange of a down quark (the Δ^- contains **ddd**) for an up quark (the Δ^0 contains **udd**). Also, the Δ^0 and Δ^+ have the same quark composition as the neutron and proton, respectively, and differ from the nucleons only in their total spin. This allows us to study the effects of changing the quark spin alignment within a baryon.

From Equation 1.3, we can see that we have to supply energy to a nucleon if we want to produce a resonance as the resonances are all heavier than the nucleon. For a specific mass difference, there is a minimum required energy that we have to supply and this is known as the threshold energy for that resonance.

The $\Delta(1232)$ isobar (the isobar under study in this work) is experimentally easy to access, as it has the lowest mass and therefore the lowest energy threshold of the baryon decuplet. The Δ is also well isolated: the peak energy of Δ production occurs below the threshold production energy of most other resonances, so one can be fairly sure that effects observed are due to the Δ, and not complex interferences from other resonances. These properties make the Δ a popular subject of experimental and theoretical study. Despite this, due to its short lifetime, experimental access to most of the fundamental properties of the Δ isobar is very restricted.

1.9 Our Experiment

In 1968 Kondratyuk and Ponomarev proposed a method to indirectly access the magnetic dipole moment of the Δ^{++} by experiment [51]. This experiment was performed [11] first by the UCLA group, using the 184-inch cyclotron at Berkeley

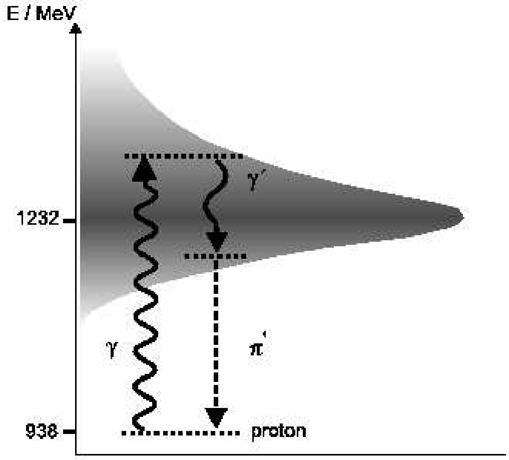

Figure 1.4: Diagrammatic representation of $\gamma + p \rightarrow \Delta^+ \rightarrow \Delta^+\gamma'$, showing the shaded Breit-Wigner mass distribution of the Δ^+, the proton being excited to form a high-mass Δ^+, which subsequently decays, with the emission of a photon, to form a lower mass Δ^+, which decays to form a π^0 meson and a proton. Extracted from [1].

(mentioned in Section 1.1). An extended experiment was also performed at SIN [14, 15]. As a result of these two experiments and subsequent analyses of the data, the Particle Data Group[2] (PDG) now quote a value for the magnetic dipole moment of the Δ^{++} ($\mu_{\Delta^{++}}$) as 3.7 - 7.5 nuclear magnetons (μ_N) [52]. This work is described in Chapter 3.

Model	μ_{Δ^+}/μ_N
SU(3):$\mu_\Delta = Q_\Delta.\mu_p$ [23]	2.79
RQM [53]	2.38
lattice QCD [54]	2.5±0.3
χPT [55]	2.1±0.2
χQSM [56]	2.19
LCQSR [57]	2.2±0.4

Table 1.3: Different quark model predictions for μ_{Δ^+}

The magnetic dipole moment of the Δ^+ has been predicted using several different models (Table 1.3). The results do vary, but it would require a result of much better precision than that obtained for $\mu_{\Delta^{++}}$, to provide any differentiation between models. However, the pioneering measurement of the magnetic dipole moment of the Δ^{++} provided a method [11] which has been adapted for our measurement [2, 58, 59].

We formed Δ^+ resonances by exciting protons in our liquid Hydrogen target using an energy-tagged photon beam. Some of these Δ^+ were at the upper end of their Breit-Wigner mass spectrum. Due to the large width of the Δ^+ (120MeV), a small proportion of these high mass Δ^+ underwent “self-decay”, whereby they decayed to a lower mass Δ^+, with the emission of a photon (Figure 1.4). Due to the short lifetime of the Δ^+, we detected the products of the low mass Δ^+ decay: a proton and a π^0 (which further decayed to a pair of photons before reaching our detector). Thus we reconstructed these events using the information we obtained from the single proton and three photons registered in the detector system described in Chapter 4.

---

[2] The Particle Data Group is a large international collaboration which collates and publishes a biannual summary of the current standing of particle physics.

This process has a probability which depends on the magnetic moment of the Δ^+ and from the final results, and a reliable theoretical interpretation, we intend to extract this value. The experiment measured three different physically observable quantities, and in this thesis we will present and discuss results for two of these. The cross section is a measure of the probability of the reaction occurring expressed as a unit of area - the nanobarn (1 barn $= 10^{-24}cm^2$). The ultimate goal is to produce a five-fold differential cross section $(\frac{d^5\sigma}{d\Omega_{\pi^0}d\Omega_{\gamma'}dE_\gamma})$ where the cross section is shown as a function of the angles of the π^0 and γ' and the energy of the γ, in this work we present the first stage of this determination - the total cross section. Our collaborators are tasked with the production of the fully differential cross section. We used linearly polarised photons to excite the protons in the target, and thus we can measure the effects of this aligned excitation on the final angular distribution of the π^0. We measured at two different linear polarisation orientations, 90° apart, and calculated the linearly polarised photon asymmetry (Σ). This is defined as $\frac{\sigma_\perp - \sigma_\parallel}{\sigma_\perp + \sigma_\parallel}$ where $\sigma_\parallel$ is the cross section for incident photon polarisation parallel to the reaction plane (the plane containing the incoming photon and the outgoing pion) and $\sigma_\perp$ is the cross section for incoming photon polarisation perpendicular to the reaction plane. Of particular interest is the variation of Σ with the outgoing photon energy, presented herein. For more detail on photon asymmetries and polarised photon production see Appendices B and C. The circularly polarised photon asymmetry (analogous to that for linearly polarised photons) was also under study, and will be analysed by other members of the A2 Collaboration. Results for both total cross section and photon asymmetries are reported in Chapter 7.

Prior to our experiment, a proof-of principle experiment had been carried out using the TAPS detector system at MAMI in 2003 (Section 3.2) [1]. This had yielded a result of $\mu_{\Delta^+} = (2.7^{+1.0}_{-1.3}(stat.) \pm 1.5(syst.) \pm 3(theo.))\mu_N$, which has insufficient precision to allow hadron model evaluation. The aim of the experiment was to significantly improve on the precision of this result, by the employment of a more extensive, complex detector system to obtain better statistics, and to study more physical observables and parallel reaction channels. In this work we study the total cross section of the reaction, showing a marked improvement in statistical error, and the linearly polarised photon asymmetry, a hitherto unmeasured observable.

Chapter 2

Relationship of the $\gamma p \rightarrow p\pi^0\gamma'$ Reaction to the Magnetic Dipole Moment of the Δ^+

2.1 Quantum Field Theory and the Effective Lagrangian

In Sections 1.4 to 1.6 we introduced QCD and mediating particles, otherwise known as gauge bosons or force carriers. It is clear from this brief description that to calculate exactly what will happen in a system, purely on the basis of the theory of QCD, is an incredibly difficult task, currently beyond our computational ability. To calculate exactly the internal dynamics of a many-body strongly interacting system such as a baryon would be a massively complex affair. One must take into account particle by particle all the possible individual gluon interactions with individual quarks, not only for the valence quarks, but also for all of the quark-antiquark pairs evolving and annihilating in the surrounding quark sea, and include the effects of gluon self-interaction. The extraordinary strength of the strong force, and hence the "violence" of these many interactions further complicate an already monumental task.

However, in any many-body system of strongly interacting particles we find that to describe the behaviour of the system as a whole, we do not need to describe the behaviour of every single particle in minute detail. We simply need to understand the average behaviour of the particles and can form an "effective" theory which, although not a complete representation of every possible individual interaction within the system, will still yield the overall behaviour of our system [60]. Instead of considering the individual point interactions involving the exchange of quanta, we treat them as a "field", a potential spread throughout space. This type of theory is known as a Quantum Field Theory.

The Lagrangian of a system completely describes the physical behaviour of its constituents in terms of a scalar Lorentz potential and is simply defined as $\mathcal{L} = T - V$ where T is the kinetic energy of the system and V is the potential energy. The QCD Lagrangian contains terms related to both quark and gluon fields and its application is highly complex due to the fact that gluons carry colour charge and are therefore capable of self-interaction. In general, the Lagrangian can be viewed as a sum over all possible paths from one state to another where each path is described by the interaction terms and propagators of the appropriate field(s) weighted with a complex amplitude which determines the phase and magnitude of that particular path. These paths are often represented pictorially as Feynman diagrams and so are frequently referred to simply as diagrams. As the complexity of the diagram topology increases, the probability of a particular process occurring becomes smaller and smaller and so it contributes less and less to the overall Lagrangian. When we create an effective Lagrangian, instead of summing over every single possible path, we limit the sum to those paths or diagrams which contribute significantly to the Lagrangian and hence to the physical behaviour of the system. In so doing we create an "effective" model of the system, which describes the physical behaviour to a given accuracy without the absolute precision and complexity of the full Lagrangian, this is known as an effective field theory.

The variety of QCD-inspired effective Lagrangian models stems from the fact that there are several possible approaches to the construction of an effective Lagrangian and that the diagrams included in the Lagrangian are also a subject of some debate. It should be noted that, as the single most important feature of the effective Lagrangian is the accuracy of the potential it describes, rather than the "absolute truth" of its formulation, there are no grounds, other than personal taste, to chose between two effective Lagrangians of different formulation which describe the same physical system with the same level of accuracy. No one effective Lagrangian in this situation is more correct than another.

The effective Lagrangians of the two models that will be used to extract μ_{Δ^+} from our measurement of $\gamma p \rightarrow p\pi^0\gamma'$, are constructed in two different ways. In Section 2.2 we will look at the unitary effective Lagrangian model of Drechsel, Vanderhaeghen *et al.* [2, 17, 59] which is constructed by extracting the coupling constants for each individual stage or vertex of each diagram from experimental data. In Section 2.3, we study the model of Pascalutsa and Vanderhaeghen in which the effective Lagrangian is formed on the basis of the underlying symmetries of QCD and expressed as a small scale expansion in particle masses and the production photon momentum [9]. In Section 2.4 we will consider and compare the predictions of the models and their agreement with each other for the experimental observables of interest, namely the photon asymmetry and the differential cross section with respect to the centre-of-mass outgoing photon energy.

2.2 The Unitary Effective Lagrangian Model

The basis of this unitary model was first reported by Machavariani, Faessler and Buchmann in 1999 [58], and independently by Drechsel, Vanderhaeghen *et al.* in 2000 [59]. At this stage it contained only the Δ-resonant mechanisms for the $\gamma p \rightarrow p\pi^0\gamma'$ process. It was further developed by Vanderhaeghen and Drechsel who reported the extension of the theory to include non-resonant terms such as the initial and final state charged particle bremsstrahlung and Born terms

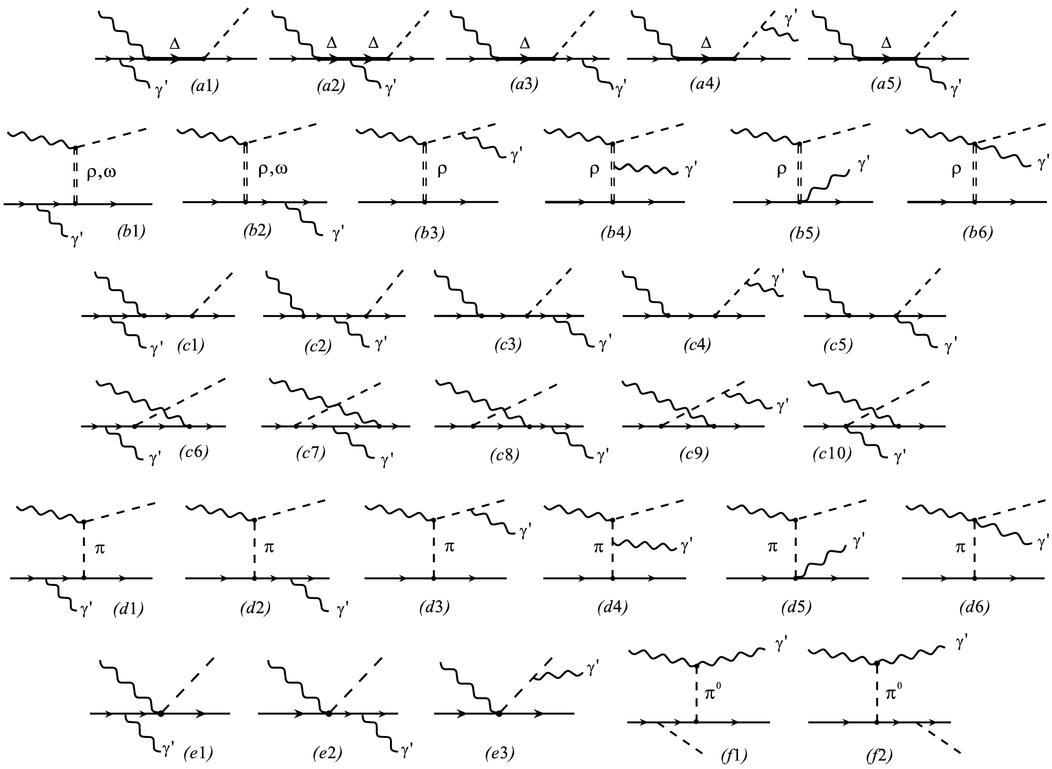

Figure 2.1: Feynman Diagram representation of each of the processes included in [2]. Process (a2) is sensitive to μ_{Δ^+}. Extracted from [2].

in 2001 [17]. In the latest implementation by Chiang *et al.* [2], the model has been broadened to include re-scattering terms and the parallel reaction channel $\gamma p \rightarrow n\pi^+\gamma'$. In this model, the $\gamma p \rightarrow p\pi^0\gamma'$ process is described as the sum of all the processes illustrated in Figure 2.1. Of these processes, only process (a2) has an amplitude dependant on μ_{Δ^+}, and thus one must first determine the amplitudes of all the other process in order to identify the amplitude of the process (a2) and hence infer the magnetic moment of the Δ^+.

To achieve this aim, Chiang *et al.* [2] began by describing the reaction $\gamma p \rightarrow \pi N$ with an effective Lagrangian model, tuned to reproduce the measured cross sections and polarisation observables. The amplitudes of the various processes involved in this $\gamma p \rightarrow \pi N$ effective Lagrangian model (illustrated in Figure 2.2) were constructed using known particle properties (such as κ_N - the anomalous magnetic moment of the nucleon) and coupling constants obtained from various experimental data sets e.g. the vector meson photon couplings $g_{\rho\pi\gamma}$ and $g_{\omega\pi\gamma}$ were extracted from the radiative decays $\rho \rightarrow \gamma\pi$ and $\omega \rightarrow \gamma\pi$. The only free parameters in the final model were the hadronic vector meson coupling constants and the $\gamma N\Delta$ electric and magnetic coupling constants which were obtained by fitting to the available $\gamma p \rightarrow p\pi^0$ and $\gamma p \rightarrow n\pi^+$ data.

In the model, the $\Delta(1232)$ is described by a complex pole $M_\Delta - \frac{i}{2}\Gamma_\Delta$ to take account of the finite Δ width, where both M_Δ and Γ_Δ were taken from the PDG values [52]: $(M_\Delta, \Gamma_\Delta) = (1210, 100)$ MeV. A Breit-Wigner type propagator was

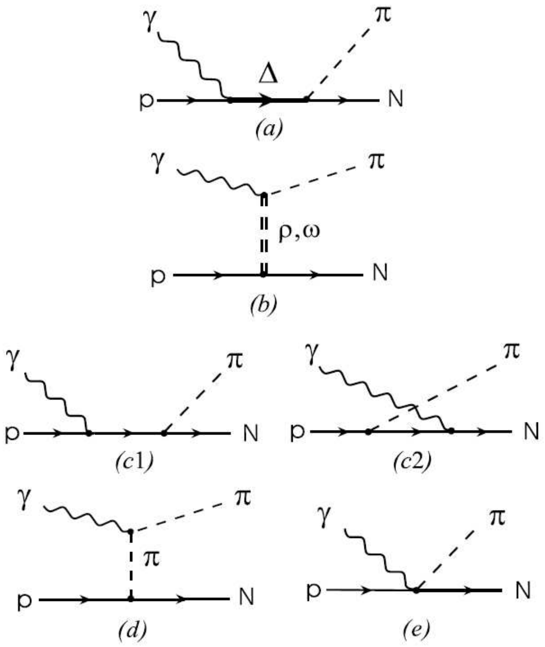

Figure 2.2: Diagrams for the $\gamma p \to \pi N$ reaction in the $\Delta(1232)$ region: Δ resonance excitation (a), vector meson exchange (b), nucleon pole terms (c1-c2), pion pole term (d) and Kroll-Ruderman term (e). Extracted from [2].

not used as the energy dependant width would violate gauge invariance when applied to the resonant parts of the $\gamma p \to \gamma'\pi N$ reaction. The model also applied purely pseudo-vector coupling in the πNN interaction Lagrangian in order to remain consistent with the leading order of chiral perturbation theory. The use of a Breit-Wigner type energy dependent width and the use of mixed pseudo-vector and pseudo-scalar coupling in the πNN interaction Lagrangian would have improved the fit to the experimental data, especially at higher incoming photon energies. However, as the main purpose of this $\gamma p \to \pi N$ model was to provide a basis for the analysis of the $\gamma p \to \gamma'\pi N$ interaction, it was decided to form a model with the fewest parameters necessary to provide a good fit to the abundant $\gamma p \to \pi N$ data.

This simple model describes the data very well for both $\gamma p \to p\pi^0$ and $\gamma p \to n\pi^+$ (as can be seen from Figures 2.3 and 2.4). At higher energies there is some deviation from the data probably due to the low energy tail of the N*(1440) resonance which was not included in the model (Figure 2.4). As the aim of the whole process is to access the magnetic moment of the Δ^+, the main focus of the analysis will be around and below the energy of the $\Delta^+(1232)$ peak, so this high energy deviation is fairly insignificant to our purposes.

Once the $\gamma p \to \pi N$ model was configured to describe the region of interest, a photon was then coupled in a gauge invariant way to each of the charged particles in the processes shown in Figure 2.2, in every possible permutation to produce the set of processes illustrated in Figure 2.1. This forms the complete set of processes which are summed to produce the effective Lagrangian for $\gamma p \to \gamma'\pi N$.

The interaction diagrams for each of the processes in Figure 2.1(b-e) can be

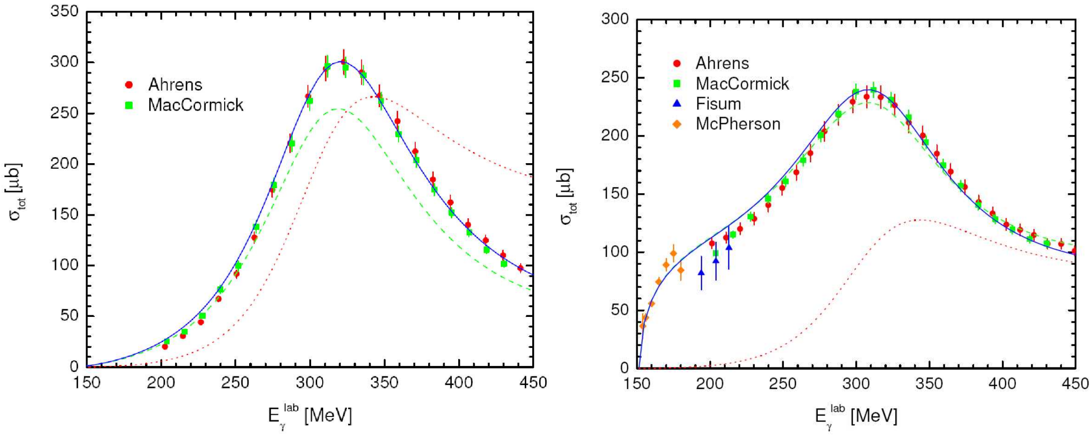

Figure 2.3: Total cross sections for $\gamma p \to p\pi^0$ (left panel) and $\gamma p \to n\pi^+$ (right panel). The solid curve is the result of the full unitary model, the dashed curve indicates the result of the tree-level calculation, and the dotted curve shows the unitarised $\Delta(1232)$ contribution. The data for $\gamma p \to p\pi^0$ are from MacCormick [3] and Ahrens [4]. The data for $\gamma p \to \pi^+ n$ are from McPherson [5], Fissum [6], MacCormick [3] and Ahrens [4]. Extracted from [2].

evaluated from the terms of those used in the successful $\gamma p \to \pi N$ model, or by minimal substitution. The Figure 2.1(a) diagrams can also be described in this way, with the exception of the diagram (a2), which has the interaction Lagrangian defined in Equation 2.1,

$$\mathcal{L}_{\gamma\Delta\Delta} = e_\Delta \bar{\psi}_\Delta^{\beta'} \left\{ g_{\beta'\beta}\left(\gamma_\nu A^\nu - \frac{\kappa_\Delta}{2M_\Delta}\sigma_{\nu\lambda}\partial^\lambda A^\nu\right) + \frac{1}{3}\left(\gamma_\beta\gamma_\nu\gamma_{\beta'} - \gamma_\beta g_{\nu\beta'} - \gamma_{\beta'} g_{\nu\beta}\right) A^\nu \right\} \psi_\Delta^\beta, \tag{2.1}$$

where A^ν is the electromagnetic vector potential, M_Δ is the Δ mass, and κ_{Δ^+} is the anomalous magnetic moment of the Δ^+. Thus, in comparison to the $\gamma p \to \pi N$ model, the only new parameter is κ_{Δ^+}, which relates to μ_{Δ^+} as defined in Equation 2.2.

$$\mu_{\Delta^+} = \left\{ (1 + \kappa_{\Delta^+}) \frac{M_N}{M_{\Delta^+}} \right\} \mu_N. \tag{2.2}$$

In principle $\mathcal{L}_{\gamma\Delta\Delta}$, and hence κ_{Δ^+}, are functions of $\mathbf{k}'^2$, $\mathbf{p_\Delta}^2$ and $\mathbf{p'_\Delta}^2$, which are the squares of the energy-momentum four vectors of the production photon, the initial Δ and the final Δ, respectively. However, as we are dealing with a real photon, $\mathbf{k}'^2$ must be zero. We are analysing the reaction in the $\Delta(1232)$ region, so $\mathbf{p_\Delta}^2$ must be equal to M_Δ^2. In the soft photon limit i.e. in the limit of zero production photon momentum, it follows that $\mathbf{p'_\Delta}^2$ must also equal M_Δ^2. Thus, if κ_{Δ^+} is a slowly varying function of $\mathbf{p'_\Delta}^2$, we can assume that κ_{Δ^+} is a constant in the soft photon region. This leaves our model with only one unknown, adjustable parameter to be altered to fit the data - κ_{Δ^+} which gives us μ_{Δ^+}.

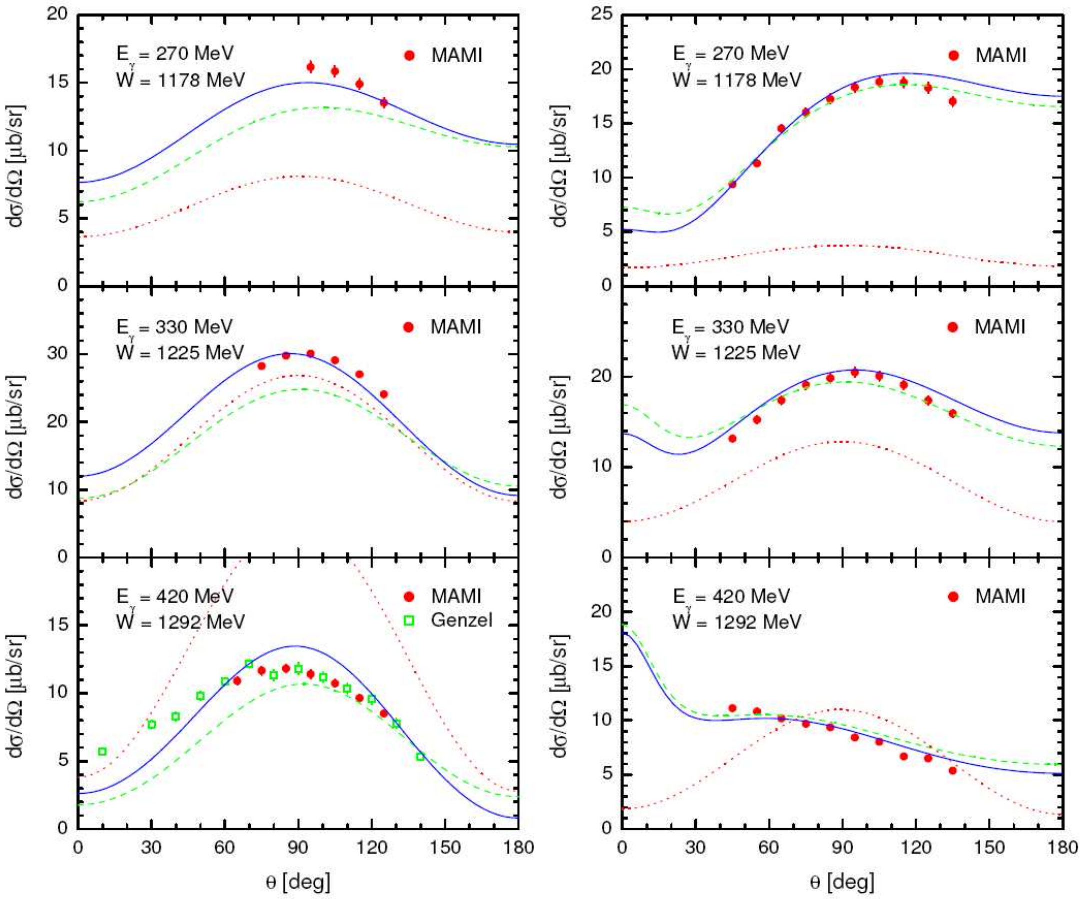

Figure 2.4: Differential cross section for the $\gamma p \to \pi^0 p$ reaction (left panel) and $\gamma p \to \pi^+ n$ reaction (right panel) at different photon lab energies E_γ as a function of the c.m. angle θ. The data are from MAMI [7] and Bonn [8]. See Figure 2.3 for further notation. Extracted from [2].

2.3 The Chiral Effective Field Theory Model

In this model by Pascalutsa and Vanderhaeghen [9], the effective Lagrangian is constructed by exploiting the symmetries of the QCD Lagrangian. As the mass difference between the up and down quarks is small, their hadron spectrum can be organised as a set of approximately degenerate basis states of irreducible isospin with $SU(2)$ symmetry. This can be extended to include the strange quark (which although heavier than the u / d quarks is still significantly lighter than the c, b and t quarks), producing $SU(3)$ symmetry.

Chiral effective field theory (χEFT) has been constructed on the assumption that, as the light quark masses tend to zero (the chiral limit), the left- and right-handed quark fields in the QCD Lagrangian decouple, producing a chiral $SU(3)_L \times SU(3)_R \times U(1)_v$ symmetry (where $U(1)_v$ is related to baryon number conservation). The sixteen generators[1] of the $SU(3)_L \times SU(3)_R$ group can be formed into linear combinations $Q_V^a = Q_R^a + Q_L^a$, and $Q_A^a = Q_R^a - Q_L^a$, where $a = 1 \ldots 8$. The generators Q_A^a are each associated with an idealised massless Goldstone boson. These bosons have zero baryon number, negative parity and transform as an octet under the subgroup $SU(3)_v$. Thus, in the chiral limit, the pseudo-scalar meson octet depicted in Figure 1.2, become candidates for this Goldstone boson role. As, in the physical world, the members of the octet are not massless, they are sometimes referred to as the pseudo-Goldstone bosons.

An effective Lagrangian can then be formed based on Weinberg's theorem [61, and referernces therein] that the most general S-matrix[2] consistent with the fundamental principles of quantum field theory and the assumed symmetry of a system can be yielded by a perturbative expansion of the most general effective Lagrangian containing all possible terms compatible with the assumed symmetry principles. Thus in Chiral Effective Field Theory, the effective Lagrangian becomes an infinite series in terms of small-scale parameters, namely the external momentum and the quark (or Goldstone boson) masses. In the nineteen eighties, χPT was extended [61, and references therein] to situations with one external nucleon line e.g. $\gamma p \rightarrow p\pi^0$. This was more complex to achieve as the nucleon mass (unlike that of the Goldstone bosons) does not vanish in the chiral limit. The effective Lagrangian then became an expansion in terms of powers of inverse nucleon masses (M) as well as the pion mass (m_π) [61].

This in principle allows both extraction of fundamental properties (such as μ_{Δ^+}) from experimental observables and the extrapolation of Lattice QCD calculations (which are necessarily performed with artificially high quark mass) into the physical quark mass region. Both of these functions are performed in [9], however we will restrict ourselves to the study of how χEFT will be used to extract μ_{Δ^+} from our data set.

As in any other perturbative expansion, it is expected that higher order terms in the χEFT Lagrangian will contribute progressively less and that the series will converge. Thus, in order for χEFT to be of use, we must know which terms contribute significantly to the Lagrangian at the order of interest. To this end, χEFT employs a systematic power counting scheme which assesses the impact of each possible diagram as the quark mass or external momenta change. This gives an unambiguous determination as to which order the quark mass and momentum expansion of the Lagrangian must be extended.

---

[1] The generators of a group S are the members of the smallest possible subgroup of S which can reconstruct every member of S by the product of a finite number of the generator subgroup members.

[2] The S-matrix or scattering matrix is a unitary matrix operator which relates the final state at an infinite time in the future to the initial state at an infinite time in the past, that is to say it defines the link between the free particle initial and final states in a given reaction.

In formulating an effective field theory, one "integrates out" or neglects the heavier or more energetic fields that do not contribute significantly at the order of interest in the energy region of interest. For example, when considering the centre of mass energy region substantially below ρ-meson mass, one does not consider the effects of the ρ-meson field, thereby limiting the region of validity of any results to an energy region significantly below that required for ρ-meson production. The scale at which our "integrating out" of the higher energy / mass fields results in an unphysical description of the situation is known as the scale of chiral symmetry breaking, Λ.

In this work, the external momentum concerned is merely that of the incoming photon as we have a fixed target. At low energies (less than the pion mass, $m_\pi \simeq 139 MeV$), an effective Lagrangian taking into account only the pion and nucleon fields is sufficient to produce very convincing and useful results in most interactions, giving a good match for experimentally measured quantities. However, in the higher energy region, χEFT has traditionally fared very badly. This is due in part to the fact that at relatively low incoming photon momenta ($\sim$ 293 MeV) the $\Delta(1232)$ resonance can be produced on the nucleon. If this is not explicitly taken into account by the effective Lagrangian, the results produced by the effective Lagrangian model will become progressively worse as the photon energy approaches this limit, making $\Lambda \simeq 293$ MeV. In the Pascalutsa model [62, 63], this is taken care of using the "δ-expansion" scheme which explicitly includes the Δ-resonance, in an effective Lagrangian containing both pion and nucleon fields. By using this scheme, the chiral symmetry breaking point moves to a much higher scale, in the region of 1 GeV.

$$\Delta \equiv M_\Delta - M_N \approx 293\, MeV. \tag{2.3}$$

The δ-expansion works on the principle that Δ, defined in Equation 2.3, is small scale compared to Λ and that Δ/Λ is similar in size to m_π/Δ (Equation 2.4).

$$\delta = \frac{\Delta}{\Lambda} \sim \frac{m_\pi}{\Delta}. \tag{2.4}$$

Thus if we expand our Lagrangian in terms of δ, only one small scale parameter is required for the expansion and, by Equation 2.4, m_π/Λ scales as δ^2. Thus our power counting scheme also achieves a simpler basis. However, there are two distinct regimes to this model: that where the incoming photon momentum p is in the region of m_π ($p \sim m_\pi$), and thus the Δ resonance does not play a significant role in the reaction behaviour, and that of the Δ-resonance-region, where $p \sim \Delta$ and the $\Delta(1232)$ resonance has a strong influence on reaction proceedings. Due to the differing dominant effects in the two regions, two different power-counting rules are required.

As described, the power counting index n of a diagram indicates that that particular diagram contributes to the total Lagrangian at the level of δ^n. In the region of the Δ resonance, one needs to identify the one-Δ-reducible (OΔR) diagrams as they have terms proportional to $1/(p-\Delta)$ which would become incredibly large as $p \rightarrow \Delta$. To alleviate this difficulty we re-scale these terms so they vary as $1/(p-\Delta-\Sigma)$, where Σ is the self-energy of the Δ and begins at order p^3, thus for $p \sim \Delta$ the dressed OΔR propagator scales as δ^{-3}.

In this $p \sim \Delta$ region, n is given by Equation 2.5,

$$n = n_{\chi PT} - N_{\Delta} - 2N_{O\Delta R}, \tag{2.5}$$

where N_{Δ} is the number of Δ-isobar propagators (not including the $O\Delta R$ propagator terms) and $N_{O\Delta R}$ is the number of dressed $O\Delta R$ propagator terms. The term $n_{\chi PT}$ is given by Equation 2.6,

$$n_{\chi PT} = \Sigma_i i V_i + 4L - N_N - 2N_{\pi}, \tag{2.6}$$

where V_i is the number of vertices with dimension i, L is the number of loops, N_{π} is the number of pion propagators and N_N is the number of nucleon propagators in the diagram of interest. In the lower momentum ($p \sim m_{\pi}$) region, n is given by:

$$n = 2n_{\chi PT} - N_{\Delta}, \tag{2.7}$$

where N_{Δ} is the total number of all types of Δ propagator, and $n_{\chi PT}$ is given by Equation 2.7. For further detail of the δ-expansion see [62, 63].

Using this δ-expansion, the effective Lagrangian for the $\gamma p \rightarrow \gamma' \pi^0 p$ process was formulated including terms up to and including those at next to leading order (and single loop processes). The included diagrams are shown in Figure 2.5. Diagrams 2.5(a), (b) and (c) represent the processes detailed in Equations 2.8, 2.9 and 2.10 and diagrams (d), (e) and (f) show the single-loop corrections that are included, along with the straightforward vertices, in the shaded blobs of (a), (b) and (c). In our situation, the loops we consider are those where the Δ decays to a nucleon and pion combination which subsequently recombine to form a Δ, leaving the final state unchanged. In general, a "loop" describes the situation in which particles appear (by decay or particle / antiparticle emergence from the vacuum) and alter the intermediate path of the diagram, but are gone (either due to recombination or annihilation), before the final state is reached, making a completely closed cycle in the process diagram. These cycles pose problems in the calculation of the final interaction as they introduce infinite terms in the effective Lagrangian which have to be dealt with by the process of renormalisation.

The full effective Lagrangian is a complex sum over many terms. Only those terms from the Lagrangian relating to the spin-3/2, isospin 3/2 field of the Δ isobar are detailed in Equations 2.8, 2.9 and 2.10:

$$\begin{aligned} \mathcal{L}_{\Delta}^{(1)} = & \bar{\psi}_{\mu}(i\gamma^{\mu\nu\alpha}D_{\alpha} - M_{\Delta}\gamma^{\mu\nu})\psi_{\nu} \\ & + \frac{ih_A}{2f_{\pi}M_{\Delta}}\Big\{\bar{N}T_a\gamma^{\mu\nu\lambda}(\partial_{\mu}\psi_{\nu})D_{\lambda}\pi^a + H.c.\Big\}, \end{aligned} \tag{2.8}$$

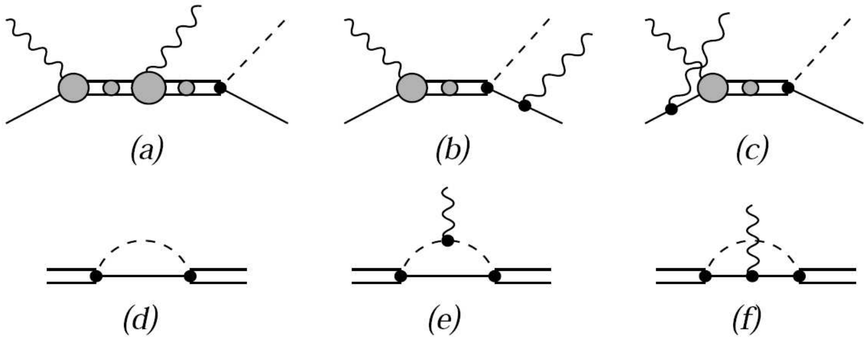

Figure 2.5: Diagrams for the $\gamma p \rightarrow \gamma'\pi^0 p$ interaction in the next-to-leading order of the χEFT calculation presented. Doubled lines represent Δ propagators. Extracted from [9].

$$\begin{aligned}\mathcal{L}_\Delta^{(2)} =& \frac{ie(\mu_\Delta - 1)}{2M_\Delta}\bar{\psi}_\mu \psi_\nu F^{\mu\nu} \\ &+ \frac{3ieg_M}{2M(M+M_\Delta)}\left\{\bar{N}T_3 \partial_\mu \psi_\nu \tilde{F}^{\mu\nu} + H.c.\right\} \\ &- \frac{eh_A}{2f_\pi M_\Delta}\left\{\bar{N}T_a \gamma^{\mu\nu\lambda} A_\mu \psi_\nu \partial_\lambda \pi^a + H.c.\right\},\end{aligned} \tag{2.9}$$

$$\mathcal{L}_\Delta^{(3)} = \frac{-3eg_E}{2M(M+M_\Delta)}\left\{\bar{N}T_3 \gamma_5 \partial_\mu \psi_\nu F^{\mu\nu} + H.c.\right\}, \tag{2.10}$$

where N and π^a are the nucleon and pion fields ($a = 1, 2, 3$); M and M_Δ are the nucleon and $\Delta(1232)$ masses, respectively; D_μ is the covariant derivative; $F^{\mu\nu}$ is the electromagnetic field strength and $\tilde{F}^{\mu\nu}$ its dual; T_a are the isospin 1/2 to 3/2 transition matrices; $H.c.$ stands for the Hermitian conjugate, and the coupling constants f_π, g_M and g_E are 92.4 MeV, 2.94 and -0.96, respectively (see [62, 63] for further detail). The χPT parameter h_A is set, using a resonance width $\Gamma_\Delta \simeq 115$ MeV, to be around 2.85. Thus the only adjustable parameter in the whole Lagrangian is μ_{Δ^+} which appears in the part of the Lagrangian shown in Equation 2.9. This parameter of the effective Lagrangian will be adjusted to find the best fit to the experimental data.

The effective Lagrangian as a whole is formulated and the power counting performed in terms of δ^n, however in Equations 2.8, 2.9 and 2.10 the powers of δ are replaced by the appropriate physical masses in order to facilitate understanding of the physical basis of the Lagrangian.

2.4 Model Predictions and Dependence of the μ_{Δ^+} Result

The experiment was designed to measure three physical observables (differential cross section, linear polarised photon beam asymmetry and circularly polarised photon beam asymmetry) in two channels ($\gamma p \rightarrow p\pi^0\gamma'$ and $\gamma p \rightarrow n\pi^+\gamma'$) in order to provide as broad an experimental basis as possible to test the predictive power of these effective Lagrangian models. Both models are formulated to have μ_{Δ^+} as their only adjustable parameter. We have studied the total cross section and linearly polarised photon asymmetry, and collaborators will study the differential cross section and circularly polarised photon asymmetry of $p(\gamma, \gamma'\pi^0 p)$ and all the $p(\gamma, \gamma'\pi^+ n)$ observables. The extraction of μ_{Δ^+} will then be independently performed with each model, by varying μ_{Δ^+} to find the best fit to the data over all six experimental observables. If the six observables and the two models agree in their final best fit μ_{Δ^+}, while the models provide a good consistent description of those observables more weakly dependant on μ_{Δ^+}, then we will have a fairly model independent extraction of the magnetic moment of the Δ^+.

Of the six observables, those of the $\gamma p \rightarrow \gamma'\pi^0 p$ channel show a far greater sensitivity to μ_{Δ^+} than those of the $\gamma p \rightarrow \gamma'\pi^+ n$ channel, because of the far larger non-resonant final state bremsstrahlung contribution to the cross section in the charged pion channel due to the low pion mass. Although this would limit the value of an independent extraction of μ_{Δ^+} from the $\gamma p \rightarrow \gamma'\pi^+ n$ channel alone, parallel analysis of $\gamma p \rightarrow \gamma'\pi^+ n$ provides an invaluable test of the non-resonant final state bremsstrahlung contributions to the effective Lagrangian, which were the limiting factor in the extraction of $\mu_{\Delta^{++}}$ as described in Chapter 3.

The predictions for the experimental observables are shown in Figure 2.6 and 2.7. The predicted total cross section of the $\gamma p \rightarrow \gamma'\pi^0 p$ reaction shows little sensitivity to μ_{Δ^+}. The predicted differential cross section with respect to $E_{\gamma'}^{c.m.}$ shows a more pronounced dependence on the magnetic moment and the predicted sensitivity of the photon asymmetry (as a function of $E_{\gamma'}^{c.m.}$) to μ_{Δ^+} varies markedly between the two models in their current state. The most promising observable of all is perhaps the circularly polarised photon asymmetry. This is necessarily zero for all two-body processes, thus only the $\gamma\Delta\Delta$ vertex, which causes the dependence on μ_{Δ^+}, can lead to a circularly polarised photon asymmetry. Hence any observed asymmetry should be simply proportional to the amplitude of the $\gamma\Delta\Delta$ vertex and therefore to the magnetic moment of the Δ^+.

For the total and differential cross sections which were previously measured with lower precision in [1], both models show reasonable agreement. However, for the other two new polarisation observables, and their variation with outgoing photon energy and angle and pion theta ($E_{\gamma'}$, $\theta_{\gamma'}$ and θ_π), the models exhibit substantial differences. Thus, the measurement of both photon asymmetry and single-spin asymmetry is essential for the resolution of the ambiguities in the existing theory. In extremis, if we do not achieve a definitive solution for μ_{Δ^+}, our measurement will serve to further refine the models of the interaction, thereby facilitating the future determination of μ_{Δ^+} with sufficient precision to differentiate between the various quark models mentioned in Table 1.3 and to complete our knowledge of the Δ isobar.

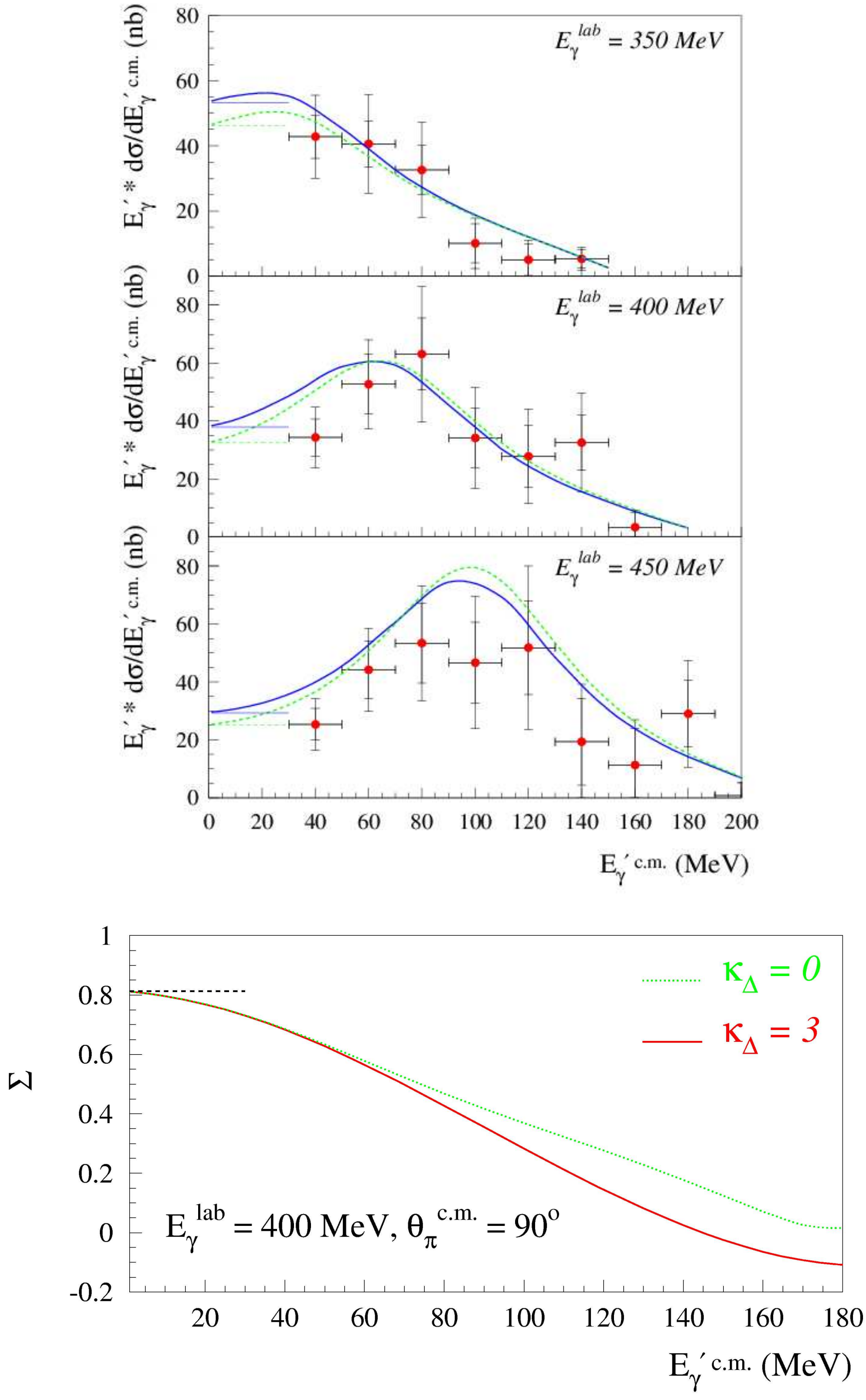

Figure 2.6: Predictions of the Unitary Model [2], described in Section 2.2. Upper panel: outgoing photon energy dependence of the cross section $d\sigma/dE_{\gamma'}^{c.m.}$ multiplied by $E_{\gamma'}^{c.m.}$ for κ_{Δ^+}=3 and at three different beam energies. The dashed curve represents the results of the tree-level approximation and the solid curve the result of the unitary model. Data are from [1]. Lower panel: Prediction of the variation of the photon asymmetry with $E_{\gamma'}^{c.m.}$ at a laboratory frame beam energy of 400 MeV. Dotted curve shows the result for $\kappa_{\Delta^+} = 0$, solid line for $\kappa_{\Delta^+} = 3$. Extracted from [2].

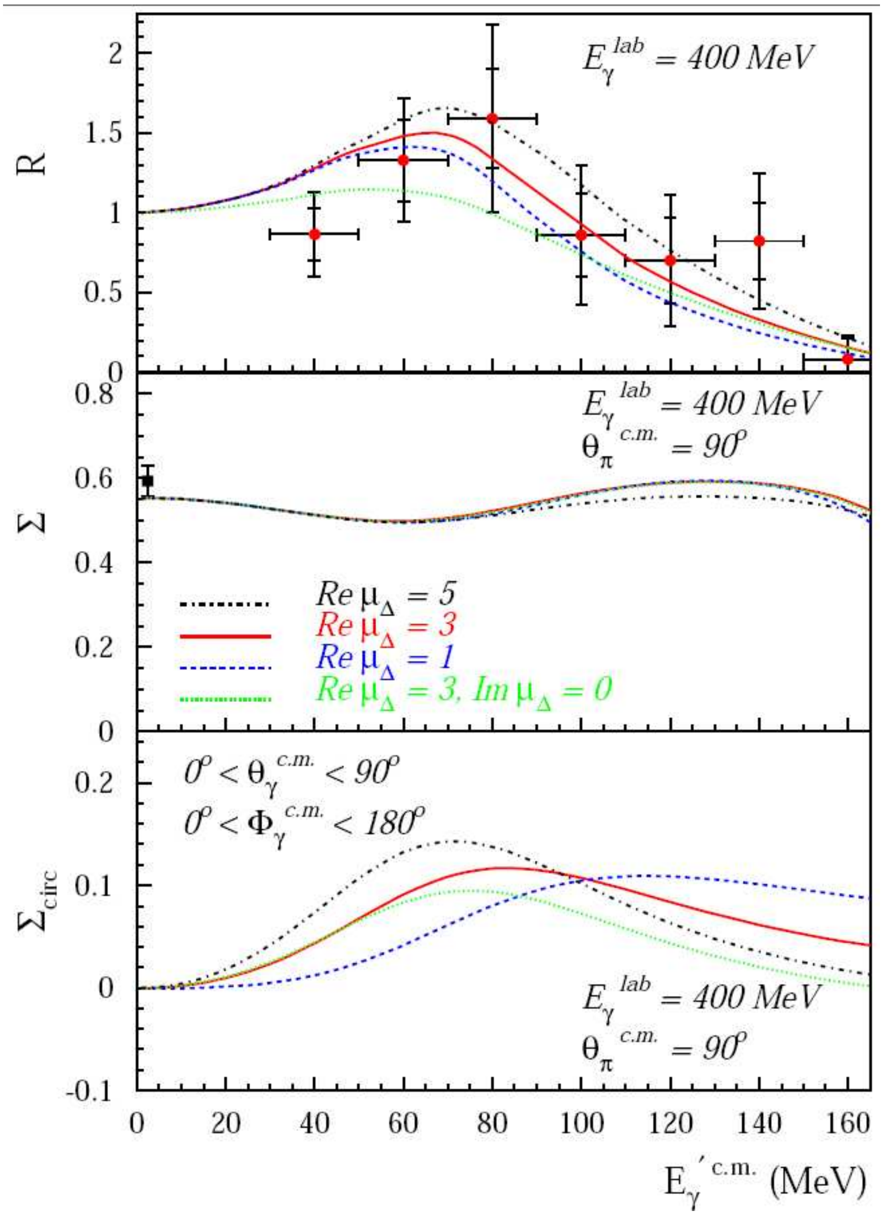

Figure 2.7: The predictions of the χEFT theory [9], described in Section 2.3. Upper panel: the ratio of $\gamma p \to \gamma' \pi^0 p$ to $\gamma p \to p\pi^0$ cross sections. Data are from [1]. Middle panel: the linear-polarisation photon asymmetry of the $\gamma p \to \gamma' \pi^0 p$ cross sections differential w.r.t. $E_{\gamma'}^{c.m.}$ and the pion c.m. angle. The data point at $E_{\gamma'}^{c.m.} = 0$ corresponds to the $\gamma p \to p\pi^0$ photon asymmetry reported in [7, 10]. Lower panel: the circularly polarised photon asymmetry as a function of $E_{\gamma'}^{c.m.}$. Extracted from [2].

Chapter 3

Previous Work

It is extremely difficult to access the magnetic moments of the short-lived members of the baryon decuplet. Thus there are only three previous purpose-designed measurements of any relevance to our experiment. Although we are trying to measure the magnetic moment of the Δ^+, the early experiments designed to measure the magnetic moment of the Δ^{++} are of relevance as they both inspired the method by which we hope to access the magnetic moment of the Δ^+ and they faced similar problems in the analysis of the final data.

Two measurements have been made to establish the magnetic moment of the Δ^{++}. The first measurement by UCLA [11] sought only to establish the differential cross sections for the reactions $\pi^+ p \rightarrow \pi^+ p\gamma$ and $\pi^- p \rightarrow \pi^- p\gamma$. The second experiment at SIN (Schweizerisches Institut für Nuklearforschung) [14,15] looked at both the differential cross section and the polarised target asymmetry of $\pi^+ p \rightarrow \pi^+ p\gamma$. Based on these reactions, the Particle Data Group now quote a value for $\mu_{\Delta^{++}}$ of 3.7 - 7.5μ_N [52]. The large uncertainty in the extraction of the magnetic dipole moment of the Δ^{++} arises from uncertainty in the reaction mechanism. The strength of resonant Δ^{++} production relative to non-resonant processes which produce the same final state was poorly known and bremsstrahlung from the initial and final state charged particles can mimic the γ radiated from the Δ^{++}.

The UCLA $\pi^- p \rightarrow \pi^- p\gamma$ data could conceivably also be used to access the magnetic moment of the Δ^0. However, as the Δ^0 is uncharged and so does not radiate, the data were taken to compare and contrast with the $\pi^+ p \rightarrow \pi^+ p\gamma$ reaction channel data as a check of the reaction model. An additional 808 $\pi^- p \rightarrow \pi^- p\gamma$ events were added to the world data set by the Omicron Collaboration at CERN in the 1980's [64, 65] in parallel with an experimental search for the rare decay $\pi^0 \rightarrow e^+ e^-$. Within the limited precision these data agree with the cross section measurements from UCLA.

In 2003 an experiment was performed by the A2 Collaboration of MAMI (at Mainz, Germany) using the TAPS detector [1] (see Section 4.5). The aim was to measure the differential cross section of the reaction $\gamma p \rightarrow p\pi^0\gamma'$ in order to establish the magnetic moment of the Δ^+. This experiment yielded a result of $\mu_{\Delta^+} = (2.7^{+1.0}_{-1.3}(stat.) \pm 1.5(syst.) \pm 3(theo.))\mu_N$. The present measurement of the same reaction at MAMI, using a detector with much better acceptance, has yielded a factor $\sim$ 50 improvement in counts, and additionally should benefit from better magnetic moment extraction due to improvements in the model and the inclusion of parallel channels ($\gamma p \rightarrow n\pi^+\gamma'$) and more physical observables in the final analysis.

3.1 Measurement of the Magnetic Dipole Moment of the Δ^{++}

In 1968, it was first suggested by Kondratyuk and Ponomarev that the magnetic moment of the Δ^{++} could be determined by radiative π^+p scattering [51]. This was a revolutionary idea as, until that point, no experimental information on the electromagnetic form factors of any of the baryon decuplet (with the exception of the Ω^-) had been obtainable due to their extremely short lifetimes. This suggestion formed the inspiration for two dedicated experiments, one side study and many, many analyses of the resulting data set.

As the method was further studied and the description of the reaction process established and extended, it formed the basis for proposals to investigate the magnetic moment of the Δ^+ in an analogous manner. Thus it is important to understand the $\mu_{\Delta^{++}}$ experiments, as they are the testing ground on which the theoretical models necessary to interpret our experiment were formed.

3.1.1 External Emission Dominance, the Soft Photon Approximation and the Extraction of $\mu_{\Delta^{++}}$

There are two types of radiative event involved in the reaction $\pi^\pm p \rightarrow \pi^\pm p\gamma$: external bremsstrahlung which comes from the incoming or outgoing charged particles, and internal radiation which is coupled to the internal structure of the reaction itself.

Low showed that, in the absence of a resonance, the first two terms of the series expansion of the differential bremsstrahlung cross section:

$$\sigma = \frac{\sigma_0}{k} + \sigma_1 + O(k), \tag{3.1}$$

can be calculated exactly from the on-mass shell elastic scattering amplitudes in the limit of zero photon energy (k) [66]. The first coefficient, σ_0, contains all electric multipoles, and the second, σ_1, involves the magnetic multipoles as well as the electric multipoles of all involved processes. Calculations have been made using two different approximations: External Emission Dominance (EED) [67] and the Soft Photon Approximation (SPA) [12].

EED involves only the first term of the Low expansion and assumes that the bremsstrahlung cross section is dominated by external radiation (that of the incident/outgoing charged particles). The SPA assumes that the description is best given using both of the first two terms of the Low series expansion.

EED has the benefit of being gauge and Lorentz invariant, computationally simple and lacking in adjustable parameters. If EED is accurate, the bremsstrahlung cross section depends in a straightforward way on the elastic scattering cross section. However, there is some discussion as to which values of s (the square of the total πp centre of mass energy), and t (the square of the four momentum transfer) to use in the the evaluation of the elastic cross section. One possibility, $EED(s_0, t_0)$ is to use the elastic scattering limit, where the photon energy is zero and hence the momentum transfer and total centre of mass energy are fixed. Another option is $EED(\bar{s}, \bar{t})$, where the average values of momentum transfer and centre of mass energy are used, as follows:

$$\bar{s} = \frac{1}{2}\Big[(P_1 + P_2)^2 + (P_3 + P_4)^2\Big], \tag{3.2}$$

$$\bar{t} = \frac{1}{2}\Big[(P_1 - P_3)^2 + (P_2 - P_4)^2\Big], \tag{3.3}$$

where P_1 and P_2 are the incident four-momenta, and P_3 and P_4 are the outgoing four-momenta of the pion and proton, respectively.

The only input required by the EED calculations is the elastic scattering cross section. To improve comparisons to $(\pi p \gamma)$ data, rather than simply using the published values, the elastic scattering cross section used in the EED analysis can be experimentally measured with the same detector setup. This reduces the influence of systematic experimental errors on the extraction of the magnetic moment from the data.

For convenience, in the UCLA experiment, detector positions (shown in Figure 3.1) and most other angles were described in an α, β, and d set of coordinates, where α is the horizontal projection of the angle measured clockwise from the beam line, β is the angle of elevation measured upwards from the horizontal plane, and d is the distance from the front face of the detector to the Hydrogen target. Initial EED calculations for planning the UCLA experimental measurement of $\mu_{\Delta^{++}}$ assumed a simple co-planar “point geometry”, where the EED theory was evaluated at different E_γ with the pion scattering at $\alpha = 50.5°$, and $\beta = 0°$ and the photon emerging in the horizontal π-p reaction plane. The predicted external bremsstrahlung cross section was then plotted against α_γ. These plots (see Figure 3.2(a)) had a very similar shape for most of the anticipated photon energies. They all indicated a deep external bremsstrahlung minimum at an outgoing photon angle of 220° to the incident pion beam direction. This minimum was due to destructive interference between the proton and pion backwards bremsstrahlung amplitudes and was not found to be strongly dependent on co-planar geometry.

The UCLA & SIN experiments were designed to exploit the minimum in the external emission cross section to access the internal bremsstrahlung contribution to the overall $\pi^+ p \to \pi^+ p \gamma$ cross section. In the case of $\pi^- p \to \pi^- p \gamma$, the backwards proton and pion bremsstrahlung add constructively at the point of the $\pi^+ p \to \pi^+ p \gamma$ EED minimum. Thus by comparing the π^+ and π^- channels at each of the selected incident pion energies it was possible to investigate: (1) the effect of the $\Delta(1232)$ resonance on the differential cross section, (2) the range of photon energy which the soft-photon approximation can adequately describe, (3) the possibility of determining the electromagnetic multipole moments of the $\Delta(1232)$, and (4) the off-mass shell pion-nucleon interaction [68]. When Kondratyuk and

Pomonarev first suggested the possibility of the magnetic moment determination by radiative pion-nucleon scattering, they predicted that there would be a large enhancement around 60 MeV, due to internal bremsstrahlung, in the otherwise $1/E_\gamma$-dependent E_γ spectrum of the reaction for these special kinematic conditions [51]. The size of this bump would relate to the magnetic dipole moment of the resonance.

3.1.2 The UCLA Measurement

In 1972, Arman gave a preliminary report on the first experimental attempt to quantify the magnetic moment of the Δ^{++} using radiative pion-proton scattering near the $\Delta(1232)$ resonance [69], with a pion beam energy of 294 MeV. The experiment and analysis were fully discussed in 1975 by Sober *et al.* [68]. The experiment was then extended to look at slightly different kinematic regions, with additional beam energies of 269 MeV and 324 MeV. A full analysis of the extended data set, with a summary of the results and analysis at all three beam energies, was reported by Nefkens *et al.* in 1978 [11].

The initial experiment investigated the reaction $\pi^+p \rightarrow \pi^+p\gamma$ with a π^+ beam energy of 294 MeV in the laboratory frame. The subsequent experiment had improved photon detection capability and used π^+ beam energies of 269 MeV, 298 MeV and 328 MeV to extend the study of the original reaction. In addition, they studied $\pi^-p \rightarrow \pi^-p\gamma$ at π^- beam energies of 263 MeV, 298 MeV and 330 MeV.

The experiment used the charged pion beam from the 184 in cyclotron at the Lawrence Berkley Laboratory. The proton beam from the cyclotron was converted to a pion beam using a production target of 48 cm of CH_2 for π^+ or 15 cm thick Beryllium for the π^-. The pion energy was established from range measurements in copper with corrections for multiple scattering (of the order of 3 %). The level of electron contamination in the pion beam was measured using a gas Cerenkov counter. The muon contamination was extracted by a combination of two methods: (1) on-momentum muon contamination was extracted from the range curves. (2) the fraction of off-momentum muon contamination was calculated. The π^- beam composition was checked with a NaI counter and found to agree with the other results.

To minimise the energy loss of the recoiling proton in the liquid Hydrogen, the 6.5 cm long liquid Hydrogen target was inclined at an angle of $20.5 \pm 0.5^\circ$ to the beam line. The liquid Hydrogen was contained in a cylindrical mylar vessel, enclosed in an alumnised mylar and corrugated aluminium flask. The end walls of the target bowed, making the target longer than the original design specifications reported in [68].

The experimental layout is given in Figure 3.1. Incoming pions were monitored by a hodoscope with two layers: one with four vertical scintillator strips, each 1.9 cm wide, and one with six horizontal strips, each 2.5 cm wide (labelled V,H respectively in Figure 3.1). This hodoscope was surrounded by an anticoincidence counter $\bar{A}_H$ which reduced beam halo effects. There was also a small single counter (T) placed in the beam further downstream to provide timing

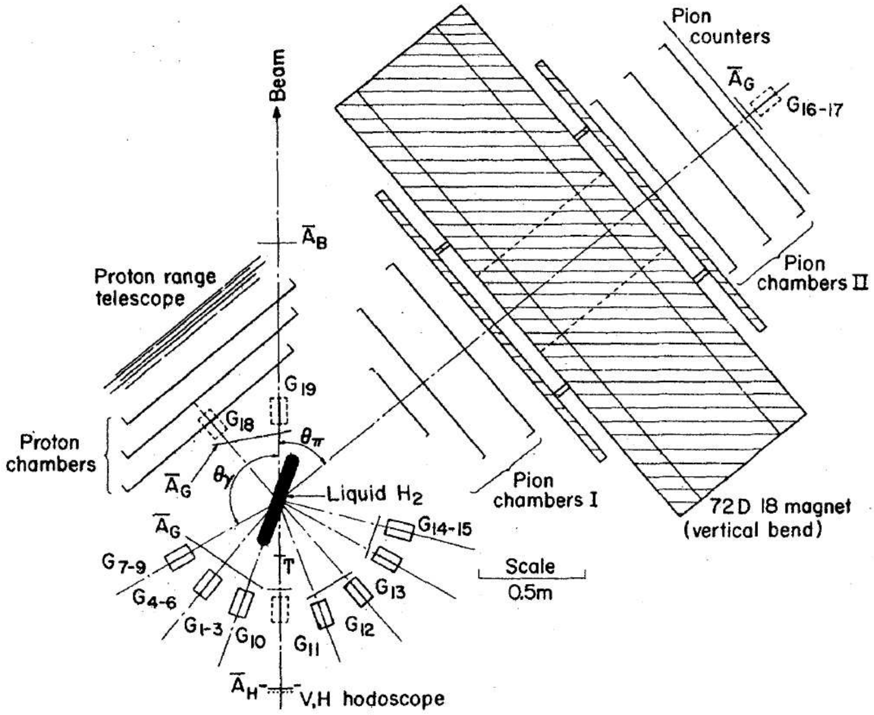
Pion counters
$\bar{A}_G$
G16-17
Pion chambers II
72D 18 magnet (vertical bend)
Beam
$\bar{A}_B$
Proton range telescope
G19
G18
θ_π
Proton chambers
$\bar{A}_G$
θ_γ
Liquid H2
Pion chambers I
$\bar{A}_G$
G14-15
Scale 0.5m
G7-9
G4-6
G1-3
G10
T
G11
G12
G13
$\bar{A}_H$
V,H hodoscope

Figure 3.1: Experimental setup for $\mu_{\Delta^{++}}$ study by UCLA. Reproduced from [11]

information.

Pions were detected in an array of three spark chambers (pion chambers I), passed through a dipole "picture-frame" magnet, and then encountered another layer of three spark chambers (pion chambers II), followed by an array of four scintillators (pion counters). The two spark chamber layers gave tracks before and after the magnetic field, providing bend angle and hence momentum information, and the scintillation counters gave particle identification using time-of-flight. The pion detection system was centred on $\alpha = 50.5°$ and had a solid angle coverage of ~ 120 msr.

Protons were tracked through three layers of spark chambers and then their energy was measured in a range telescope composed of 13 scintillators arranged in 6 planes. The proton energy resolution was $\sim \pm 10$ MeV and the detector system covered nearly 1 sr of solid angle, thus the proton detection did not limit the event acceptance at most photon energies.

The photons were detected in ten lead glass counters in the first experimental round (G1-10). Nine further lead glass detectors were added in the second round of experiments to add photon detection at more forward angles (G11-19). Photon detectors G1, G4, G7 and G11-14 were positioned in-plane ($\beta = 0°$), the others were arranged at various values of negative β, aside from G17 which was positioned at $\beta = 4°$. The initial ten photon counters were centred around an angle of 220° from the outgoing pion beam direction, 170° from the scattered pion direction. All of the photon detectors measured 10 cm by 10 cm by 15 cm thick. Charged particles were vetoed by anti-coincidence counters $\bar{A}_G$ placed in front of the photon counters. With the exception of G_{16} and G_{17}, which were placed behind the pion detectors, the front faces of the photon counters were positioned between 56 cm and 63 cm from the centre of the target.

Prior to the UCLA experiment, the world data set contained only 190 reported (πpγ) events. This experiment measured and accepted over 8000 events. The data were analysed to produce differential cross sections (Figure 3.2), sampling photon angle from 205° to 103° and at 0°, 50° and 320° in α, over a β range from $+9^\circ$ to -36° and for photon energies from 15 MeV to 180 MeV. The cross sections of simple elastic scattering ($\pi^{\pm}p \rightarrow \pi^{\pm}p$) were also measured in order to check for systematic effects. The measured elastic scattering cross sections were consistently 10 % below the literature values, but this difference was within the estimated systematic uncertainty. To mitigate any systematic effects, several cross section ratios were considered and compared to the available models. Ratios P_1, P_2, and P_3 were defined as:

$$P_1 = \frac{d^5\sigma(\pi^- \ at\ 263MeV)}{d^5\sigma(\pi^+ \ at\ 269MeV)}, \tag{3.4}$$

$$P_2 = \frac{d^5\sigma(\pi^- \ at\ 298MeV)}{d^5\sigma(\pi^+ \ at\ 298MeV)}, \tag{3.5}$$

$$P_3 = \frac{d^5\sigma(\pi^- \ at\ 330MeV)}{d^5\sigma(\pi^+ \ at\ 324MeV)}. \tag{3.6}$$

Two further ratios, R_+ and R_-, were calculated to study the relationship between incident pion energy and the cross section:

$$R_+ = \frac{d^5\sigma(\pi^+ \ at\ 269MeV)}{d^5\sigma(\pi^+ \ at\ 324MeV)}, \tag{3.7}$$

$$R_- = \frac{d^5\sigma(\pi^- \ at\ 263MeV)}{d^5\sigma(\pi^- \ at\ 330MeV)}. \tag{3.8}$$

The EED calculation used $\bar{s}$ and $\bar{t}$ as defined in Equations 3.2 and 3.3. Monte Carlo methods (labelled $\overline{EED}$) were employed to average the EED calculations over the finite detector acceptance rather than the previously mentioned "point geometry". Both the elastic scattering cross section measured in the UCLA experiment, and the previously published values, were used in the EED calculations. Those employing the UCLA result are labelled EED^*.

The EED calculations reproduced the cross sections up to the maximum measured photon energy (150 MeV in the lab frame) (see Figure 3.2). Even in the region of destructive interference where internal bremsstrahlung should play a more prominent role, the cross section falls off monotonically with increasing photon energy. However, the EED calculations show some significant disagreement with the P and R ratios (Equations 3.4 to 3.8 and Figures 3.3 to 3.5).

Basic SPA calculations, as detailed in [68], reproduce the data only for the lowest photon energy bin 15 MeV< E_γ <30 MeV. Where E_γ >40 MeV, the SPA results do not show any dip in cross section in the region of destructive interference ($\alpha_\gamma = 220^\circ$). However, a modified SPA calculation by Liou and Nutt [12], where the coefficients of k^{-1} and k^0 (in Equation 3.1) are independent of k, reproduced

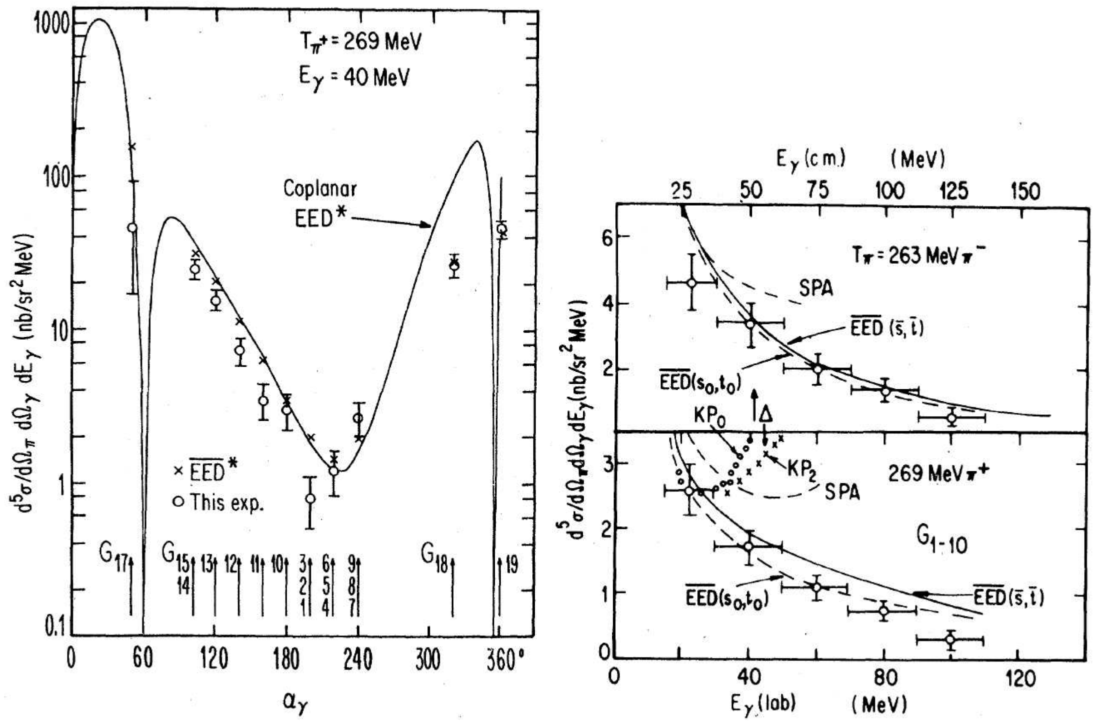

(a) (b)

Figure 3.2: Comparison of measured and calculated cross sections as a function of: (a) α_γ at $E_\gamma = 40$ MeV and $T_{\pi^+} = 269$ MeV, and (b) E_γ, averaged over photon counters $G_1 - G_{10}$ for 263 MeV π^- (upper panel) and 269 MeV π^+ (lower panel). Reproduced from [11].

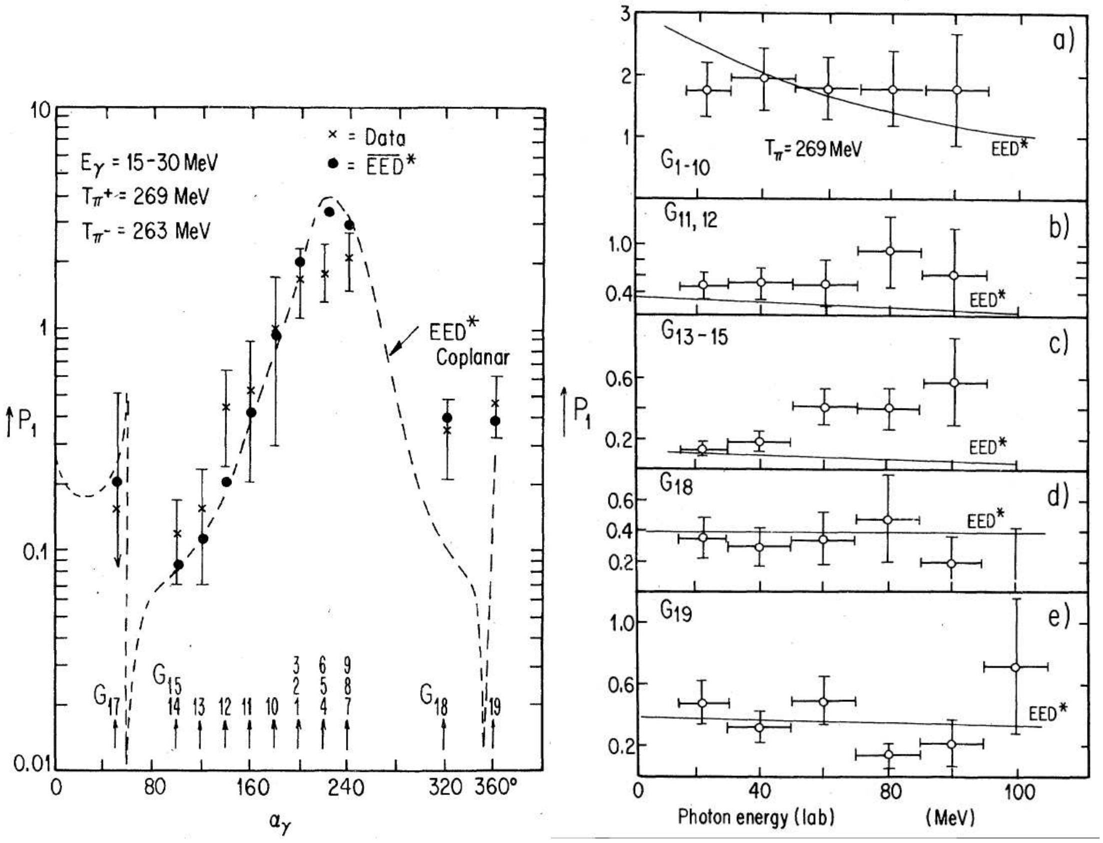

(a) (b)

Figure 3.3: Comparison of measured and calculated ratio P_1 as a function of: (a) α_γ at $E_\gamma = 15 - 30$ MeV and (b) E_γ for several different angles, averaged over neighbouring photon counters. Reproduced from [11].

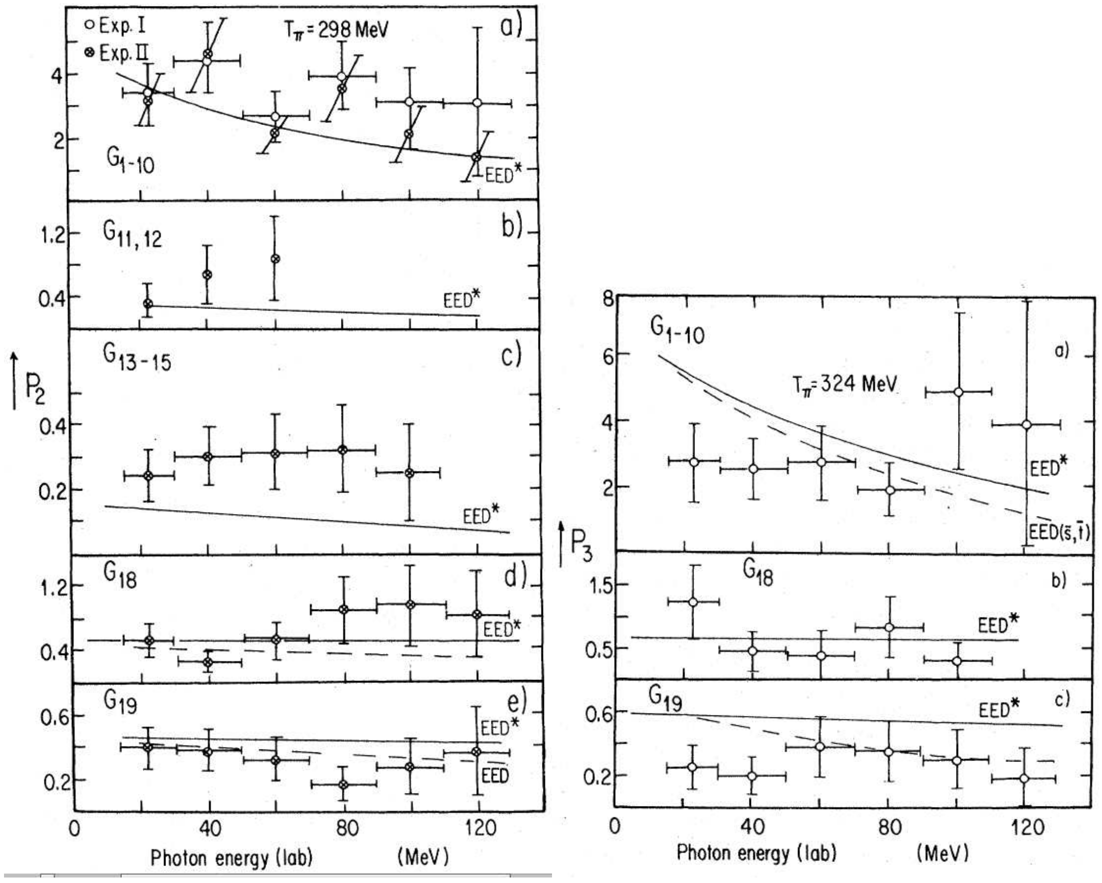

(a) (b)

Figure 3.4: Comparison of measured and calculated ratios: (a) P_2 and (b) P_3 as a function of E_γ for several different angles, averaged over neighbouring photon counters. Reproduced from [11].

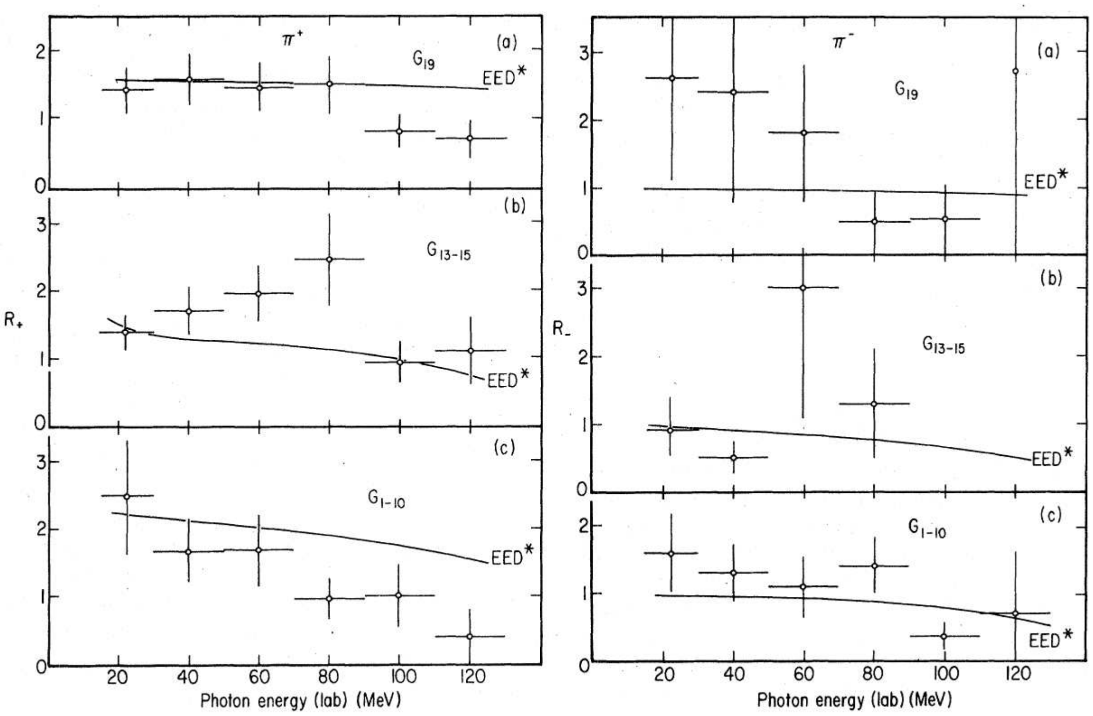

(a) (b)

Figure 3.5: Comparison of measured and calculated ratios (a) R_+ and (b) R_- as a function of E_γ for several different angles, averaged over neighbouring photon counters. Reproduced from [11].

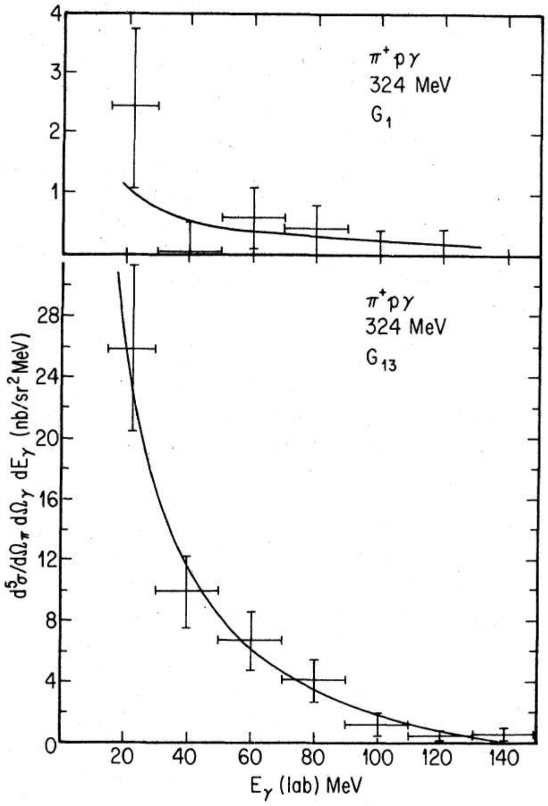

Figure 3.6: Comparison of $\pi^+p \rightarrow \pi^+p\gamma$ cross section in the lab frame as a function of E_γ for $T_{\pi^+} = 324$ MeV for photon counters G_1 (upper panel) and G_{13} (lower panel) with SPA theory by Liou and Nutt [12] and data points from [11]. Reproduced from [11].

the data far better than the EED calculations (see Figure 3.6). Liou and Nutt postulated that this is due to off-shell mass effects being small and that radiation from πp resonant states (such as the Δ^{++}) has negligible effect.

Pascual and Tarrach [13] agreed with this, stating that the $\Delta^{++} \rightarrow \Delta^{++}\gamma$ reaction does not dominate the bremsstrahlung reaction. They made a calculation of the $\mu_{\Delta^{++}}$ contribution at a single photon energy, that which leaves the π^+p final state at the peak of the $\Delta^{++}(1232)$ resonance. At this specific point, the amplitude for the $\pi^+p\gamma$ state can be considered to be the amplitude for $\pi^+p \rightarrow \Delta^{++}\gamma$ multiplied by the amplitude for $\Delta^{++} \rightarrow \pi^+p$ and a propagator related to the finite Δ width. The input parameters for the calculation were the electric charges and magnetic dipole moments of the p, π^+, and Δ^{++}, of which only $\mu_{\Delta^{++}}$ is unknown. Hence the $\mu_{\Delta^{++}}$ contribution to the differential cross section may be expressed as a series in $\mu_{\Delta^{++}}$:

$$\frac{d^5\sigma}{d\Omega_\pi d\Omega_\gamma dE_\gamma} = a + b\mu_{\Delta^{++}} + c\mu^2_{\Delta^{++}}, \tag{3.9}$$

where the coefficients a, b and c are calculable and contained in [70]. Plots of model-calculated $d^5\sigma/d\Omega_\pi d\Omega_\gamma dE_\gamma$ vs $\mu_{\Delta^{++}}$ are parabolic in appearance, and by drawing a line corresponding to the measured cross section at various different

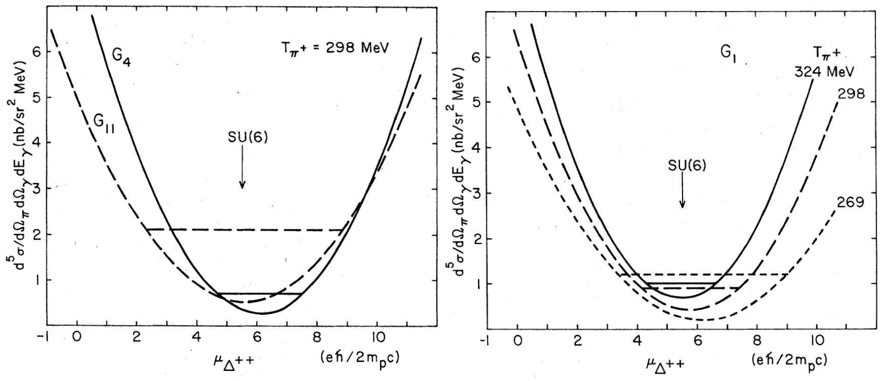

(a) (b)

Figure 3.7: $\pi^+p \rightarrow \pi^+p\gamma$ differential cross section in the lab frame as a function of $\mu_{\Delta^{++}}$, as calculated by [13]. The horizontal lines show the measured laboratory cross section as reported in [11] for: (a) photon counters G_4 and G_{11} at T_π =298 MeV for E_γ =60 MeV and 58 MeV, respectively. (b) photon counter G_1 at T_π = 269 MeV, 298 MeV and 324 MeV with E_γ =43 MeV, 58 MeV and 69 MeV, respectively. Reproduced from [11].

incident pion energies and outgoing photon angles, a series of limits for $\mu_{\Delta^{++}}$ can be derived (see Figure 3.7). This procedure was used to produce the final result by Nefkens *et al.* of $(+4.7 < \mu_{\Delta^{++}} < 6.7)\mu_N$. This limit was derived using only the co-planar counters, as these were the only cases calculated by Pascual and Tarrach.

Bég, Lee and Pais [70] have shown that, by SU(6) symmetry, the magnetic dipole moment of any member of the baryon decuplet is simply the proton magnetic moment multiplied by the baryon charge. The magnitude and sign of $\mu_{\Delta^{++}}$ as extracted from the UCLA experiment are in agreement with the SU(6) model prediction of $5.6\mu_N$. The Pascual and Tarrach model neglected two major factors: the short lifetime of the Δ, and the radiation of the outgoing p and π. As the overall parabola from the calculations was quite steep, these effects were estimated to have only have a minimal influence on the final derived limits.

3.1.3 SIN / PSI Measurement

The measurement at SIN (Schweizerisches Institut für Nuklearforschung now PSI, the Paul Scherrer Institut) covered both the differential cross section $(d^5\sigma/d\Omega_\pi d\Omega_\gamma dE_\gamma)$ [15] and the polarised target asymmetry [14] of the reaction $\pi^+p \rightarrow \pi^+p\gamma$. The target asymmetry (γ) is defined as:

$$\gamma = \frac{d^5\sigma \uparrow /d\Omega_\pi d\Omega_\gamma dE_\gamma - d^5\sigma \downarrow /d\Omega_\pi d\Omega_\gamma dE_\gamma}{d^5\sigma \uparrow /d\Omega_\pi d\Omega_\gamma dE_\gamma + d^5\sigma \downarrow /d\Omega_\pi d\Omega_\gamma dE_\gamma},$$

where $d^5\sigma \uparrow /d\Omega_\pi d\Omega_\gamma dE_\gamma$ is the differential cross section with the proton spin in one particular polarisation state and $d^5\sigma \downarrow /d\Omega_\pi d\Omega_\gamma dE_\gamma$ is the differential cross

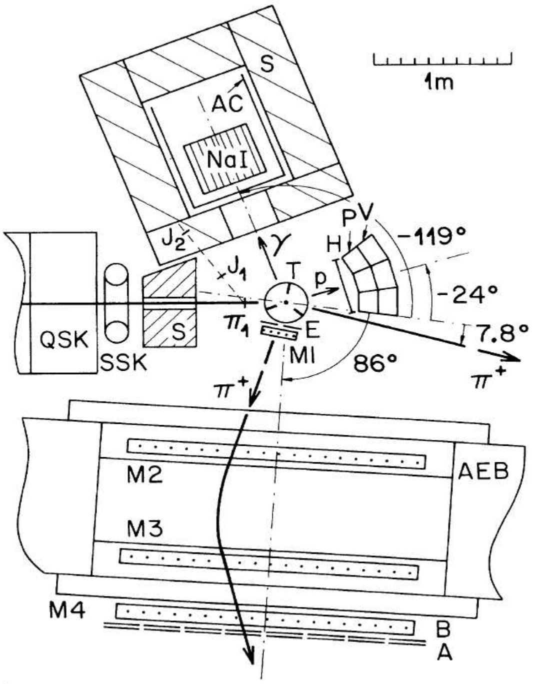

Figure 3.8: Experimental setup for $\mu_{\Delta^{++}}$ study at SIN / PSI. Reproduced from [14].

section for the opposite proton spin polarisation state.

In order to measure both observables, the experiment employed two different targets, liquid Hydrogen for the differential cross section, and a polarised-proton target of frozen Butanol beads ($C_4H_{10}O$) to measure the polarised target asymmetry. The experimental setup for the polarised target part of the experiment is shown in Figure 3.8. Other than the target choice, and the fact that the magnetic field of the polarised target bent the outgoing pion beam by 7.8°, the detector arrangement for the two parts of the SIN experiment was nearly identical. The experimental design was similar to that of the UCLA experiment, save that the SIN experiment covered a range of pion angles, holding the photon angle constant, while the UCLA experiment studied a range of photon angles at a fixed pion angle.

The SIN measurement used a 299 MeV π^+ beam from the proton cyclotron. After the insertion of carbon absorbers into the beam, the beam had a p/π^+ content of 0.005/1, and a muon content (calculated by Monte Carlo methods) of $\mu^+/\pi^+ \approx 0.045/1$. The 26 MHz incident beam, which had a flux of 40×10^6 π^+/sec, was monitored by a two-scintillator telescope (J1 and J2 in Figure 3.8) which was calibrated against the in-beam counter (π_1 in the diagram) at lower fluxes and accelerator frequencies of 0.50 MHz, 1.0 MHz and 2.0 MHz.

Pions were detected in the angular range of $55° \leq \theta^{\pi}_{lab} \leq 95°$. The pion detector again relied on a “picture-frame” dipole magnet (AEB in Figure 3.8) with two pairs of wire chambers, M1 and M2 providing the tracking before the magnet, and M3 and M4 tracking the pion exit from the magnet. Scintillator E identified pions entering the system, and scintillator planes A and B defined the pion exit from the detector system. Pulse height and timing information from E and B was recorded for each event. Time of flight information from B and E was used in conjunction with the pulse-height to distinguish between pions and protons. Pion tracks were measured before and after the magnet, the bend angle was inferred and thereby the pion momenta were extracted.

Protons were detected in a ΔE hodoscope (H in the diagram), consisting of twelve scintillators followed by two layers, each of three plastic blocks to measure energy. The first layer (labelled P) gave the total proton energy, stopping protons of energies up to 150 MeV. The second layer of plastic blocks (labelled V) vetoed anything that reached it, to reject pions and any minimum ionising particles. The proton detector had an energy resolution of 5.2 MeV at 100 MeV, but there was an additional 6.0 MeV energy loss uncertainty due to ambiguity in the target interaction point during the liquid Hydrogen target runs. The proton detectors covered sufficient solid angle to ensure that their physical extent only limited acceptance in the highest photon energy bins, where the protons went forward.

The photons were detected in an array of sixty-four NaI(Tl) crystals, each measuring $63.5\times63.5\times400\,\mathrm{mm}^3$ (NaI on diagram). This NaI array was shielded by successive layers of lead, borated polyethylene, cadmium and more lead (labelled S). It was also surrounded on the top, bottom and sides by plastic scintillator (labelled AC) to veto cosmic rays. A 1 cm-thick plastic scintillator layer in front of the counters vetoed charged particles produced in the target region. The resolution of the NaI was measured to be:

$$R(\%FWHM) = \frac{200}{E_\gamma(MeV)} + 8$$

for $E_\gamma > 10$ MeV. The photon detector covered the region of $\theta^\gamma_{lab} = 119^\circ \pm 10^\circ$, on the opposite side of the target from the pion detector in a co-planar arrangement.

The liquid Hydrogen target was contained in a mylar cylinder of 45 mm diameter and 140 mm length with bowed ends. It presented a thickness of ~ 1 g/cm^2 to the incident π beam, with 75 μm thick mylar walls at the beam entrance and exit and 135 μm walls everywhere else. It was cooled with liquid Helium and contained in a vacuum vessel with 500 μm thick mylar windows.

The polarised target was a more complicated apparatus. It contained 8 cm^3 of frozen Butanol beads, each 1-2 mm in diameter, which were surrounded by and cooled in liquid ^3He to 0.5 K. It was dynamically polarised in a 2.5 Tesla magnetic field, achieving spin polarisations of $+58$ % and -47 % using appropriate microwave frequencies of 70.580 and 70.200 GHz, respectively. In order to correct for background due to the complex structure of the target, a dummy target was also used. It contained 9 g of carbon, also immersed in liquid Helium, and was otherwise identically constructed to the real polarised target. Both targets were housed in a cylindrical cavity, 22 mm in diameter, with 0.05 mm thick copper walls.

When the final results were analysed, some comparison was made to the UCLA data, to check for consistency. Due to the different angular ranges covered by the two measurements, only a small segment of each data set could be directly compared. Only the UCLA data with a similar photon exit angle to that of the

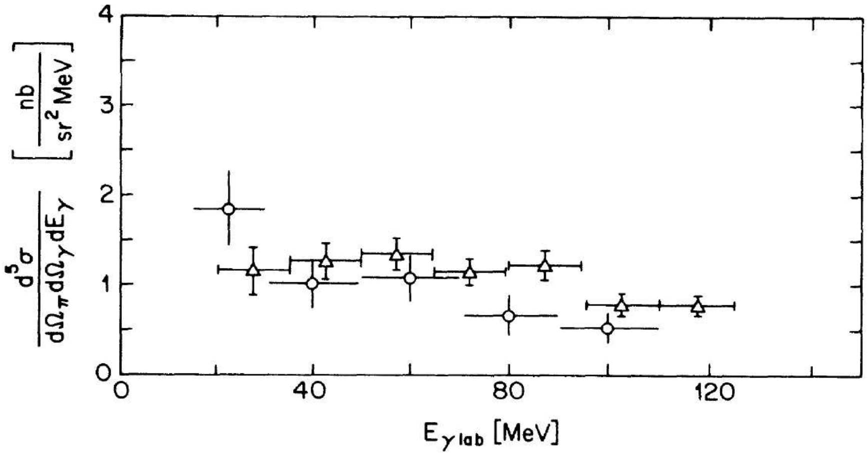

Figure 3.9: Comparison between UCLA data (circles) with the SIN low angle data set (triangles). Reproduced from [15].

SIN data was used, limiting it to the results from photon counter G_7. The SIN data covered a far larger range of pion angles, and so was split into two data sets, those with low ($55° \leq \theta_\pi \leq 75°$) and high ($75° \leq \theta_\pi \leq 95°$) pion angle. The low pion angle data were still at a higher range of pion angles than the UCLA data, but were close enough to bear comparison. Both data sets followed roughly the same shape, although the SIN data values were typically larger than the UCLA results (see Figure 3.9). This is in agreement with the expectation that cross section increases with increasing pion angle (UCLA pions were centred on $\theta_\pi = 52.5°$, whereas SIN pions were measured in the low-angle range from $55° \leq \theta^\pi_{lab} \leq 75°$).

The SIN data were compared to old SPA models [68] (that of [12] was computationally too difficult) and found, as for the UCLA data, to be very good for the lowest photon energies (< 40 MeV), but not outside of that region (Figure 3.10). The low-angle cross section was underestimated by SPA, although the shape of the distribution was correct to $E_\gamma \approx 60$ MeV. For the higher angle data set, SPA agreed with the first data point and then turned sharply upwards, away from the data.

EED in general reproduced the data better than SPA, but failed at high photon energy and at large pion angles. The EED cross section agreed well up to $E_\gamma \approx 70$ MeV for large pion angles, but above this EED predictions lie far above the observed $1/E_\gamma$ drop-off. For the low-angle data set, EED did fairly well, but tended to underestimate the cross section in the middle of the photon energy range. This could be evidence for internal structure or off-mass-shell effects, which are not included in the EED predictions.

In addition to the SPA and EED models considered by UCLA, MIT produced an isobar model which was fitted to experimental phase shifts and considered P_{33}, S_{31} and P_{31} resonances [71]. This MIT model was used to extract $\mu_{\Delta^{++}}$ from the SIN data set. The EED model agreed with the large angle data better than the MIT model. Thus only the low angle data set was eventually included in the MIT-based $\mu_{\Delta^{++}}$ calculations. The MIT result from the SIN data yielded a result

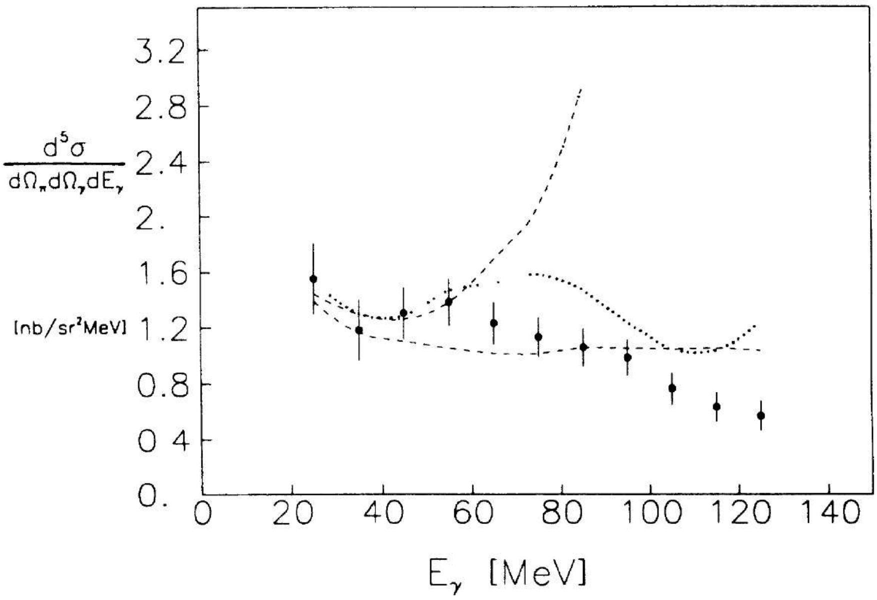

Figure 3.10: Comparison of all-angle SIN differential cross section with different models: SPA (dash/dot), EED (dashes), MIT (dots). Reproduced from [15].

of $\mu_{\Delta^{++}} = (2.8 \pm 0.5)\mu_p$, which is in agreement with the MIT result from their fits to the UCLA data of $\mu_{\Delta^{++}} = (3.0 \pm 0.5)\mu_p$.

The cross sections from the polarised target measurements were compared to those from lH_2 to check consistency, and they were found to agree. As with the cross section data, the asymmetry results were compared to the MIT model [71]. It was found by MIT that the extracted magnetic moment is relatively insensitive to the off-shell model selected for the extrapolation and thus this was a more reliable observable from which to extract $\mu_{\Delta^{++}}$ than the differential cross section. However, at the point of publication of the SIN data, only MIT had offered any prediction of the polarised target asymmetry.

Figure 3.11 shows the polarised-target asymmetry data plotted against photon energy with curves for different values of μ_Δ. A χ^2 minimisation was used to determine which value of $\mu_{\Delta^{++}}$ best fit the data. The model fits best below ≈ 70 MeV. At low E_γ, the model is less sensitive to $\mu_{\Delta^{++}}$ as it is assumed in the Low theorem that the cross section must converge towards that of elastic scattering as $E_\gamma \rightarrow 0$. At high E_γ, the energy of the photon is approaching the width of the Δ and so the model becomes less applicable. In the middle of the E_γ range, around the peak of the Δ resonance, the measurement is at its most sensitive. It is in this region that the MIT model best reproduces the trend in energy dependence shown by the data. The final result extracted from the polarised target asymmetry was $\mu_{\Delta^{++}} = 1.62 \pm 0.18\mu_p$. This does not agree with the UCLA data, or even the analysis of the SIN cross section. In an attempt to resolve this ambiguity, a new fit was performed on the cross section data from SIN. The photon energy was limited to less than 80 MeV (where the model should be more reliable) and the pion angle to between 75° and 95°, overlapping with the range in the polarised target part of the experiment. This yielded a result of $\mu_{\Delta^{++}} = 1.9 \pm 0.3\mu_p$, which

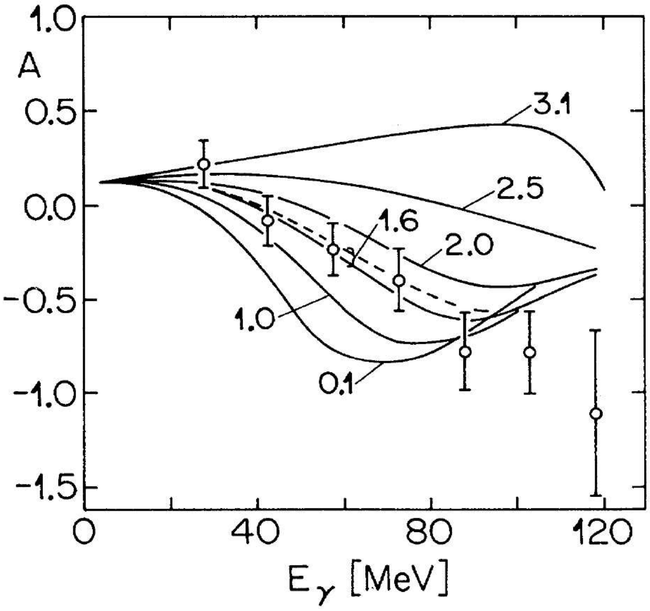

Figure 3.11: Bremsstrahlung polarised-target asymmetry versus photon energy. The curves are predictions from MIT theory for several values of $\mu_{\Delta^{++}}$, with data points from [14]. Reproduced from [14].

is closer to the polarised-target asymmetry value.

3.1.4 Discussion of $\mu_{\Delta^{++}}$ Experiments

The experiments designed to measure $\mu_{\Delta^{++}}$ suffered from several weaknesses. The use of a hadronic probe (the π^+), although providing a high interaction cross section, introduces more complex reaction mechanisms and final state interactions than the simple electromagnetic probe used in this work. The theories used to extract $\mu_{\Delta^{++}}$ considered only resonant effects, and therefore could only provide broad limits on $\mu_{\Delta^{++}}$. Finally, the theories centred on a single observable, that of the differential cross section, with only one attempt to study the polarised-target asymmetry, which was only considered in one theoretical model.

To gain a more precise value for μ_{Δ^+} than that obtained for $\mu_{\Delta^{++}}$, we must use a better understood experimental probe, use more developed theoretical models which incorporate non-resonant effects, and we must test those models with a wider range of experimentally observed constraints.

3.2 Measurement of the Magnetic Dipole Moment of the Δ^+ by $p(\gamma, p\pi^0\gamma')$

The first attempt to measure the magnetic moment of the Δ^+ using the reaction $\gamma p \rightarrow \gamma' p\pi^0$ [1, 16, 23] was made at the Glasgow tagged photon facility at Mainz between 1999 and 2001. The main process of interest was again the resonance de-excitation photon, produced by the two-step process $\gamma p \rightarrow \Delta^+ \rightarrow \Delta^+\gamma' \rightarrow p\pi^0\gamma'$,

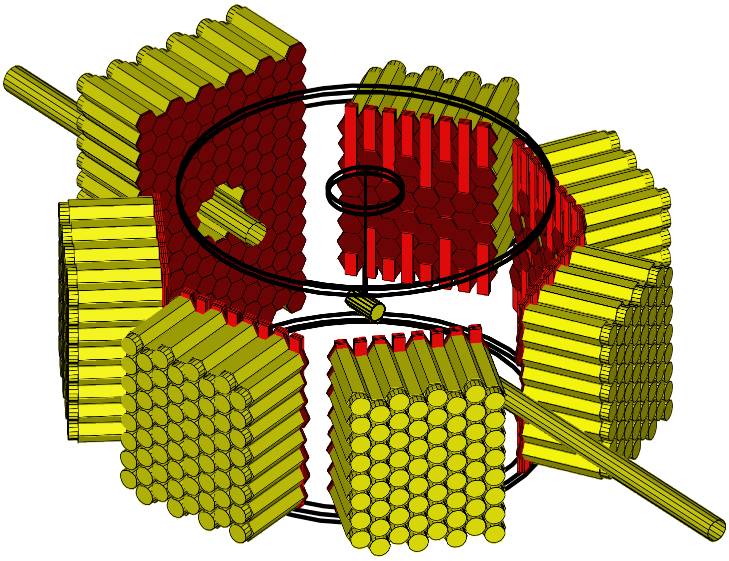

Figure 3.12: The TAPS experimental setup at MAMI, showing the six smaller TAPS blocks and the larger forward wall.

as this has an amplitude dependent on μ_{Δ^+} (see Chapter 2).

The experiment was performed in the A2 Tagged Photon Hall at the Institut für Kernphysik at Johannes Gutenberg University in Mainz, Germany under the auspices of the A2 and TAPS collaborations. The experiment made use of the energy-tagged bremsstrahlung photon beam provided by the Glasgow Tagger in conjunction with the electron accelerator MAMI (see Section 4.2) to provide a photon beam of energies between 205 MeV and 820 MeV with an energy resolution of $\sim$ 2 MeV. This was incident on a 10 cm long, 3 cm diameter, liquid Hydrogen target.

The photons and protons were detected in the TAPS BaF_2 array (see Section 4.5), which was arranged in a seven-block geometry as seen in Figure 3.12. There were six blocks of 64 detector elements, each arranged in an 8 by 8 matrix, and a single forward wall containing 138 crystals arranged in an 11 by 14 rectangle. The smaller blocks were arranged in a horizontal plane around the target at angles of $\pm 54^\circ$, $\pm 103^\circ$, and $\pm 153^\circ$ from the beam line, with their front faces 55 cm from the centre of the target. The larger forward wall was 60 cm from the centre of the target. All of the TAPS detector elements were faced with 5 mm thick plastic veto counters as described in Section 4.5.2. The inscribed circles shown in Figure 3.12 indicate the dimensions of the carbon-fibre walled, vacuum filled, scattering chamber which occupied the space between the liquid Hydrogen target vessel and the TAPS detector blocks, limiting unwanted energy losses and particle interactions.

TAPS was used to detect all species of particle. The π^0 was detected via its two decay photons. The production photon was separated from the π^0 decay

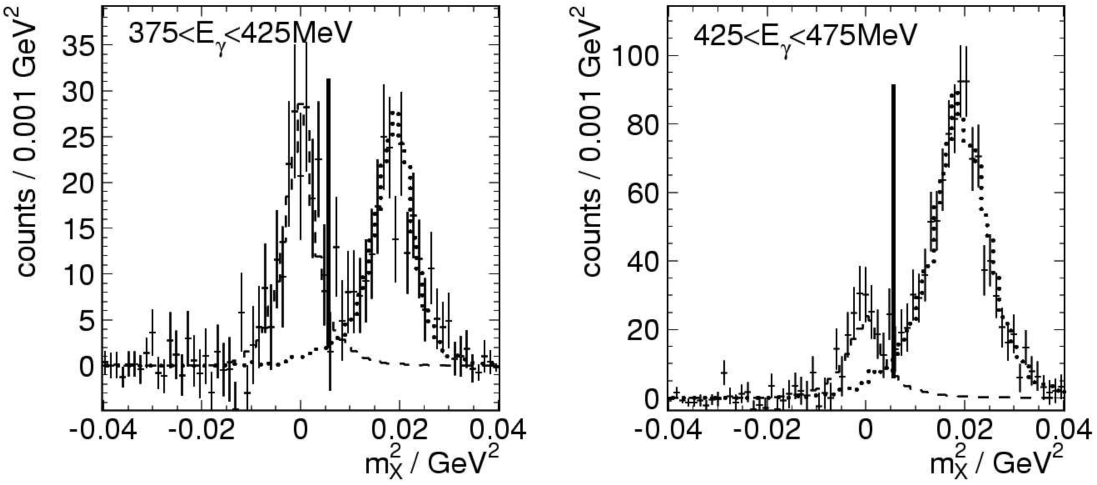

Figure 3.13: The missing mass of the $(\pi^0 p)$ system in the final state for two different photon beam energies. The peak near 0.02 $(\mathrm{GeV/c^2})^2$ is from $2\pi^0$ production and is cut away, that at 0.00 $(\mathrm{GeV/c^2})^2$ shows the true $\gamma'\pi^0 p$ production. The dotted and dashed lines are the respective lineshapes from a GEANT 3 simulation. Extracted from [1].

photons by invariant mass analysis. The two-photon combination having the invariant mass closest to the true π^0 mass were assigned to be the decay photons, and the remaining one was assumed to be a γ'. The protons were detected in the TAPS blocks and identified by a combination of time-of-flight and pulse-shape analyses.

Background contributions were largely removed by checking for momentum conservation and energy balance, and reconstructing invariant masses from the kinematically over-determined data. The largest background problem came from $\gamma p \rightarrow \pi^0\pi^0 p$, as the solid angle covered by the detector was only 40% of 4π sr. Thus, frequently, one of the four π^0 decay photons escaped detection, thereby producing what appeared to be a three-photon, single-proton final state. This was overcome by constructing the square of the missing mass (M_x^2), as defined in Equation 3.10 to separate the $\gamma p \rightarrow p\pi^0\pi^0$ events (which peak near $0.018(\mathrm{GeV/c^2})^2$) and the true $\gamma p \rightarrow p\pi^0\gamma'$ events, which peak at $0.00(\mathrm{GeV/c^2})^2$ (see Figure 3.13). This is calculated as:

$$M_x^2 = ((E_{\pi^0} + E_p) - (E_{beam} + m_p))^2 - ((\vec{p_{\pi^0}} + \vec{p_p}) - (\vec{p_{beam}}))^2, \qquad (3.10)$$

where E_{π^0}, E_p and E_{beam} are the total energies of the π^0, final state proton and photon beam, respectively, $\vec{p_{\pi^0}}$, $\vec{p_p}$ and $\vec{p_{beam}}$ are the momenta of the π^0, final state proton and photon beam, respectively and m_p is the proton rest mass. In the higher photon energy bins where the double π^0 photo-production cross section becomes large compared to that of $p\pi^0\gamma$, the edges of the two peaks overlap due to finite detector resolution. To deal with this, the experiment was simulated using Geant 3 [72] and the M_x^2 distribution reconstructed. The line shape of the two peaks in the simulation reproduced closely that of the data, thus the level of contamination could be estimated with reasonable confidence from the simulation and subtracted from the final data set (see Figure 3.13).

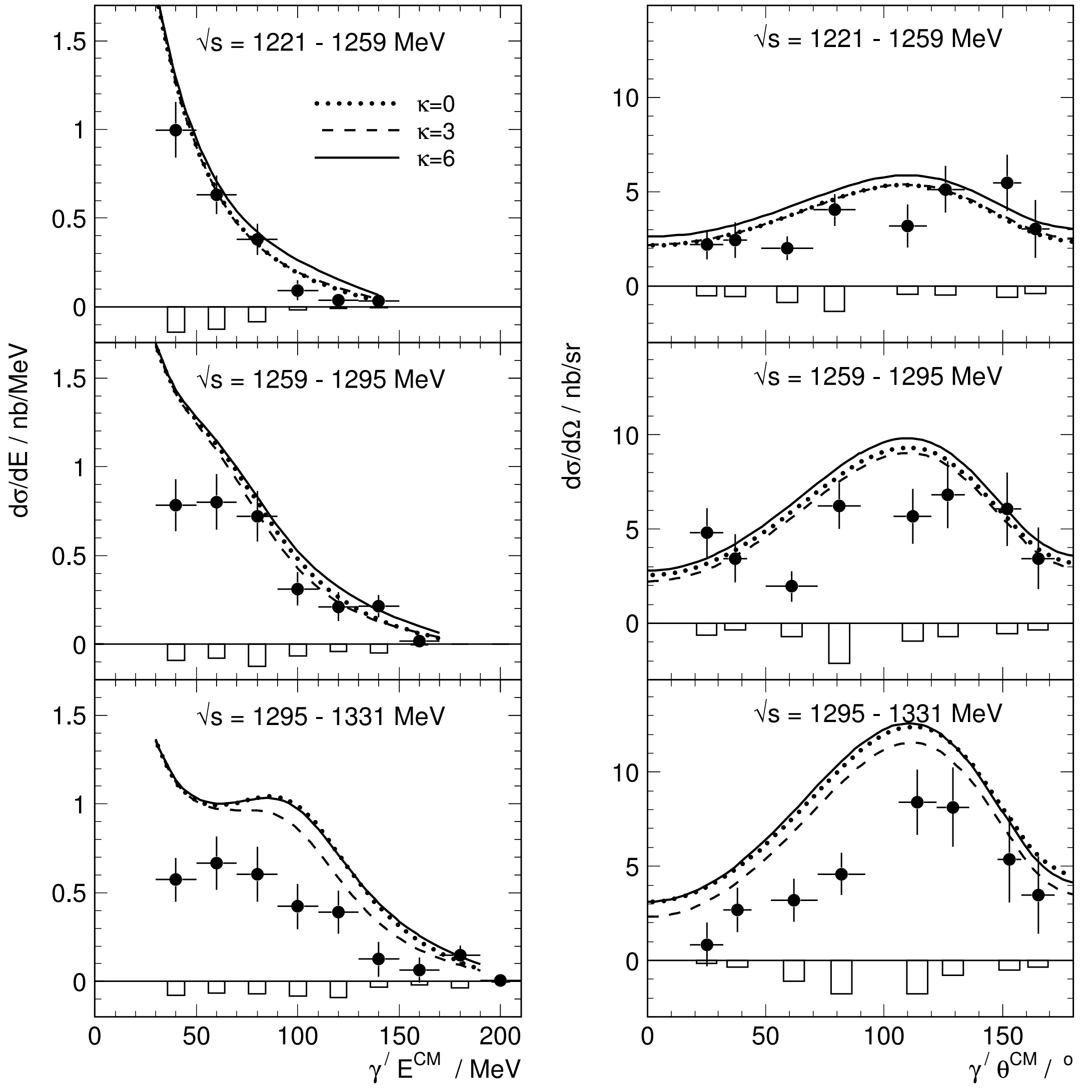

Figure 3.14: The reaction cross section for $\gamma p \rightarrow \gamma' p \pi^0$, as measured by the TAPS & A2 Collaborations [1, 16]. The three lines are predictions of the cross section based on different values of μ_{Δ^+} from [17].

The final measured cross sections are shown in Figure 3.14 plotted against $E_{\gamma'}^{CM}$ and $\theta_{\gamma'}^{CM}$ for several values of $\sqrt{s}$ (the total γp centre of mass energy). The lines shown on the plot are theoretical predictions of the cross section by Drechsel and Vanderhaeghen [17] for different values of the magnetic dipole moment of the Δ^+.

It can be seen that the model reproduces the shape of the data. However, at higher values of $\sqrt{s}$, the model over-predicts the cross section. This was attributed to the lack of πN re-scattering terms in the model for $\gamma p \rightarrow p\pi^0$, which was later remedied [2]. As the same over-estimation is in the model for both $\gamma p \rightarrow p\pi^0$ and $\gamma p \rightarrow p\pi^0\gamma'$, the ratio of the cross sections is less sensitive to the model, and this showed better agreement to it.

In this experiment, the TAPS detector system covered only 40% of the full solid angle. The detector system also suffered from systematic effects which occurred at the edges of each of the separate detector blocks, making it difficult to exactly calculate the detector acceptance. These drawbacks to the experimental setup limited the accuracy of the final measurement, which also suffered from low statistics, with approximately 500 accepted events. As can be seen from Figure 3.14, the resulting uncertainty in the cross section measurements is large, and thus the extracted magnetic dipole moment had a correspondingly large uncertainty. The theoretical understanding and interpretation of the reaction was also at an immature stage, resulting in large uncertainties and model dependencies in the extraction of the magnetic dipole moment from the reaction cross section. Thus the final extracted value was $\mu_{\Delta^+} = (2.7^{+1.0}_{-1.3}(stat.) \pm 1.5(syst.) \pm 3(theo.))\mu_N$.

There are some obvious revisions that can be made to any future experiment in order to improve upon this measurement. The first is in the measurement equipment itself: a contiguous detector system covering the majority of the solid angle would minimise $\gamma p \rightarrow p\pi^0\pi^0$ background and maximise the chance of detecting all four final state particles. Contiguity would reduce the systematic uncertainty in detector acceptance related to the edge effects experienced in the TAPS experiment. The second requirement is that of theoretical improvement. In order to improve the extraction of the magnetic dipole moment from the final data set, model dependencies must be minimised. To provide more rigorous tests of any theoretical prescription we should require the simultaneous reconstruction of more than one observable, and also more than one reaction channel. As will be seen from the following chapters, our experiment was designed to meet these challenges and provide a clear reduction in the uncertainties surrounding both the experimental measurement and the theoretical extrapolation of the magnetic dipole moment from the final data set.

Chapter 4

Experimental Equipment

4.1 Overview

Our experiment was carried out in the A2 experimental hall in the Institut für Kernphysik of the Johannes Gutenberg University, in Mainz, Germany over several beam allocations, through July to October 2004 and in January 2005. In order to obtain the accuracy required by our experiment, we used the high quality electron beam from the MAMI (MAinzer MIcrotron) accelerator in combination with the Glasgow Tagged Photon Spectrometer (Tagger) to provide an energy-tagged bremsstrahlung photon beam. The photon beam interacted with a liquid Hydrogen target.

In order to cleanly separate events involving our reaction of interest, we had to detect three photons and a proton in the final state with high efficiency and with accurate energy, particle track, and timing information. As these requirements are, to some extent, contradictory, this was achieved by assembling a three-component detector system, which covered overlapping ranges of phase-space: the Crystal Ball (CB) to provide accurate spectroscopic information over a large part of the solid angle; the Multi-Wire Proportional Chambers (MWPCs) to provide accurate position information for charged particles impinging on the CB; and the Particle Identification Detector (PID) to provide particle identification and trigger timing for different charged particle species detected by the CB. This was supplemented by the Two-Arm Photon Spectrometer (TAPS) to provide particle calorimetry, tracking and identification in the forward region. The arrangement of these detectors can be seen in Figure 4.1.

4.2 Photon Beam

In order to measure a reaction with such a low cross section, we required a large number of incoming photons and a good energy resolution to facilitate the identification of the reaction of interest. To achieve this we used the electron beam of MAMI B, which provides an energy of 883.25 MeV with an energy resolution of $\sim$0.02 % and a duty factor of 100 %. To produce an energy-tagged photon beam we passed the electron beam through a thin diamond radiator where some of the electrons were slowed by producing bremsstrahlung photons. Post-radiating

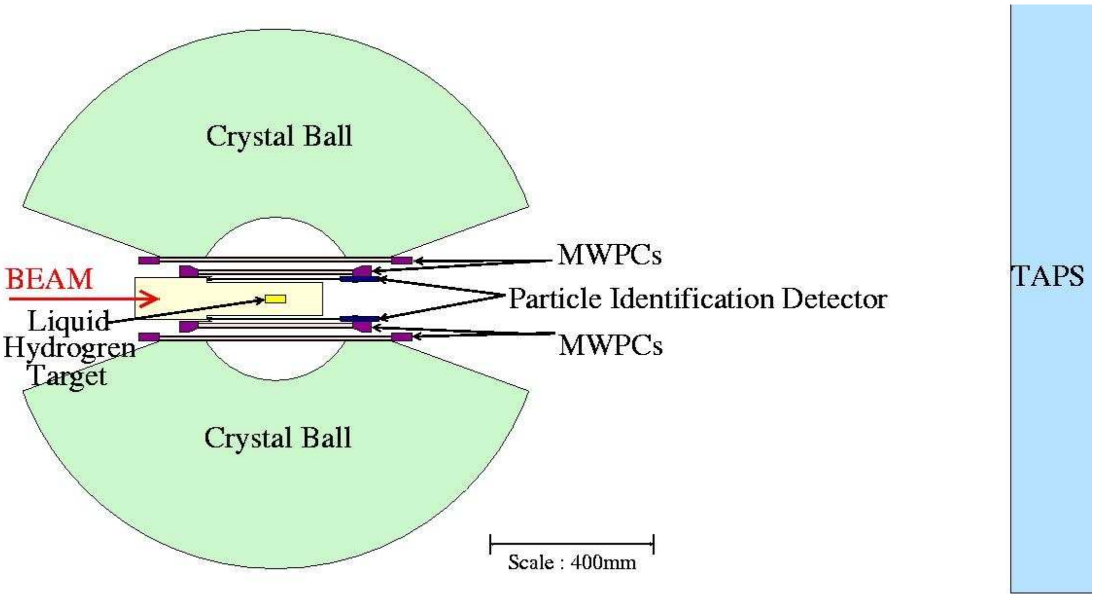

Figure 4.1: The experimental setup, showing the MWPCs and PID inside the Crystal Ball, and TAPS covering the downstream region.

electrons were deflected by the magnetic field of the Glasgow Tagger onto the Tagger's focal plane detector to provide energy information (on the basis of hit position) and thereby 'tag' the energy of photons passing down the beam line to the experimental area. The choice of a diamond rather than an amorphous radiator gave a linearly polarised photon beam. It was necessary to orient the diamond accurately to select specific crystal planes for maximum polarisation (see Appendix B), and this was achieved by mounting the diamond on a computer-controlled 5-axis goniometer. When analysing the data, it is vital to know the exact photon flux at the target in the experimental hall. This information was repeatedly gathered by continual 'Tagging Efficiency' measurements, obtained from the scalers counting the output of the focal plane detectors in conjunction with the lead glass detector setup described in Section 4.2.3.

4.2.1 MAMI

MAMI, the MAinzer MIcrotron [73, 74], is a three-stage racetrack microtron (RTM), beginning with an injector linac supplying electrons with 3.96 MeV total energy and ending with an 883 MeV output beam. MAMI-B produces a continuous wave electron beam current of up to 100 μA. It supplies the electron beam to any of the experimental halls (A1, A2, A4, X1) shown on the schematic diagram in Figure 4.2. A new accelerator section (MAMI-C), the harmonic double-sided microtron (HDSM) in Figure 4.2, is being installed to raise the maximum electron beam energy to 1.5 GeV. The Photon Tagger is also being upgraded to accommodate this increase.

A microtron is an accelerator in which the electron beam is re-circulated many times through a single linac using constant-field dipole magnets (Figure 4.3). As the electron energy increases, the radius of curvature of the path through the

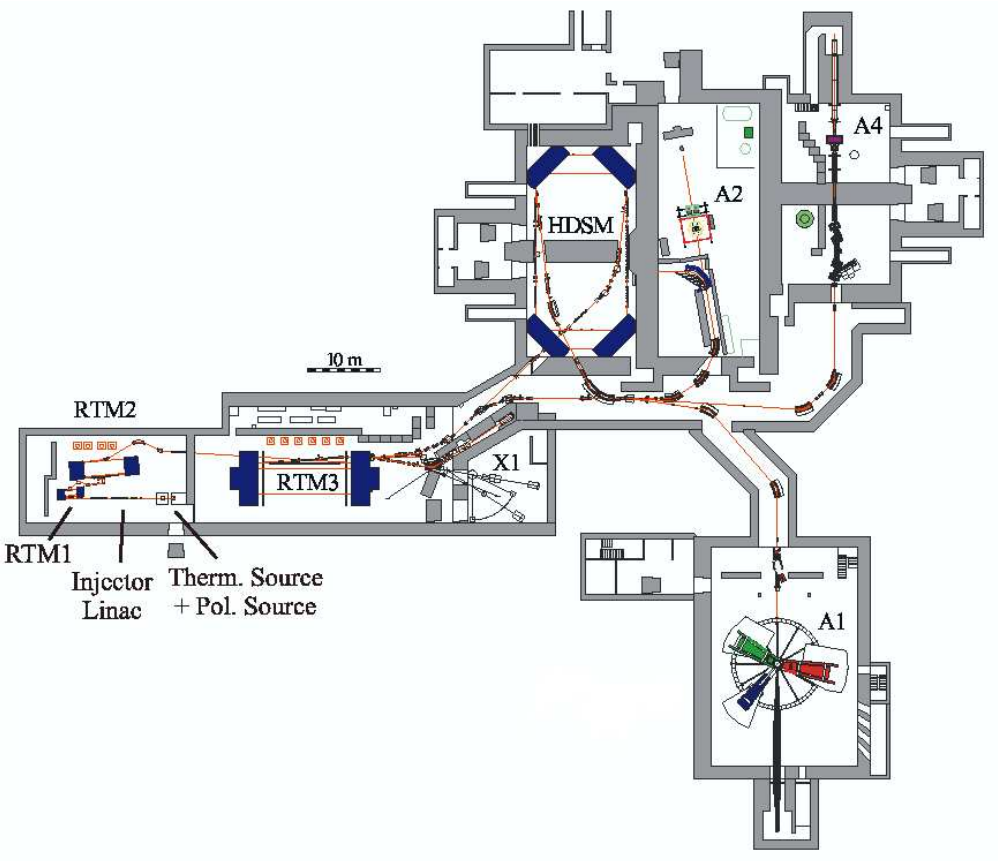
A4
A2
HDSM
10 m
RTM2
RTM3
X1
RTM1
Injector
Linac
Therm. Source
+ Pol. Source
A1

Figure 4.2: The MAMI facility, showing RTMs 1, 2 and 3 (MAMI-B) which were in use for this experiment, the Harmonic Double Sided Microton (HDSM – MAMI-C), planned to raise the electron beam energy to 1.5 GeV, and the A2 experimental hall where the experiment took place.

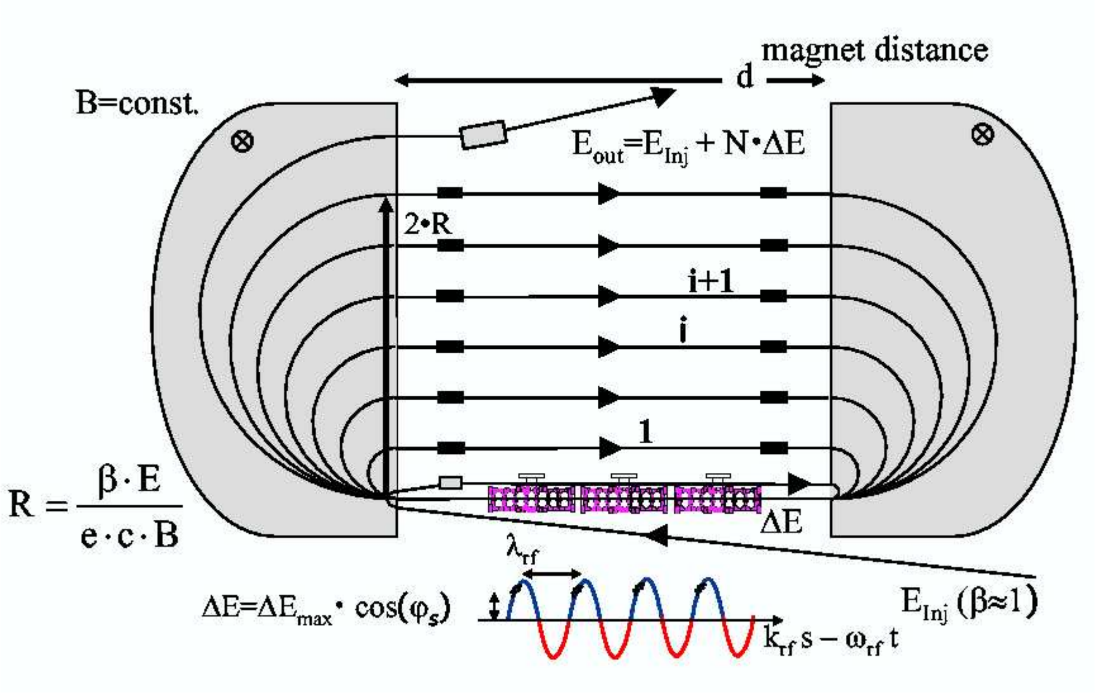
magnet distance
d
B=const.
$E_{out}=E_{Inj}+N\cdot\Delta E$
2•R
i+1
i
1
$R=\frac{\beta\cdot E}{e\cdot c\cdot B}$
ΔE
λ_{rf}
$\Delta E=\Delta E_{max}\cdot\cos(\varphi_s)$
E_{Inj} ($\beta\approx1$)
$k_{rf}s-\omega_{rf}t$

Figure 4.3: A racetrack microtron showing the increased path radius with increasing energy and the relationship between ΔE for the electron and the phase of the cavity oscillation.

bending magnets increases. Thus, each successive recirculation loop becomes larger, with the common point of contact being the path through the accelerating section of the microtron [75]. When the beam has been accelerated to the desired energy, a small “kicker” magnet ejects it out of the recirculation pathway and into the beam handling system. The difference in time taken between each successive recirculation loop has to be an exact integer multiple of the period of the RF supply to the accelerating section in order that the particle bunches always see the same phase of the alternating voltage in the accelerating section.

The microtron provides exceptional phase stability and small energy spread of the final beam due to its inherent phase correction. Particles travelling in the bunch that have higher than the designed energy will have a longer path through the bending magnets and will arrive at the accelerating section later than the rest of the bunch and so be under-accelerated in the next re-circulation. Particles of lower than the designed energy follow a slightly shorter orbit back to the accelerating section, arrive early and so are over-accelerated. The continual under/over acceleration of particles, coupled with continual energy loss due to synchrotron radiation, keeps the energy spread to a minimum, compressing the final energy spread to only 60 keV full width at half maximum (FWHM).

The initial racetrack microtron (RTM1) of MAMI first operated in 1975. It increases the beam energy from the 3.97 MeV injector linac energy to 14.86 MeV by 18 turns through its accelerating section. RTM1 then acts as the injector for RTM2 which increases the beam energy from 14.86 MeV to 180 MeV by 51 recirculations through its accelerating section. RTM 1 & 2 were first used together as MAMI A in 1983. RTM2 now acts as the injector for RTM3. Together they are known as MAMI B, and they first operated in 1990. RTM3 takes the beam energy from 180 MeV to 855 MeV in 7.50 MeV steps by 90 turns through its accelerating section when operating to design specifications. In recent years, the accelerator staff at Mainz have raised the maximum output energy from 855 MeV to 883.25 MeV. This has been achieved without any change to the physical geometry of the microtrons.

We used a beam current of 11.5 nA at an energy of 883.25 MeV. As we wanted to study the beam spin-asymmetry of various reactions, as well as the differential cross section and photon asymmetry, a polarised electron beam was required. MAMI has a (highly refined) polarised electron source, based on the photoelectron emission from III-V semiconductors (circularly polarised photons from a Ti:Saphire laser applied to a strained GaAsP cathode), to provide ~75 % polarised electrons to the injection linac [76]. We used this, switching from positive to negative electron polarisation throughout the experiment in order to reduce systematic errors.

4.2.2 Glasgow Tagger

The Glasgow Tagger (see Figure 4.4) consists of a large dipole magnet [77] with a focal plane detector system [78]. The 883 MeV MAMI electron beam passes through a thin radiator, producing photons by the bremsstrahlung process, at energies up to that of the electron beam. These photons travel downstream to the target. Once through the radiator, electrons which have not radiated are bent by the Tagger's magnetic field into the Faraday cup of the beam dump which records total beam charge. Those that have radiated have less momentum and so are bent through larger angles to impinge on the Tagger's focal plane detection system. The position at which the electrons are detected corresponds to their energy (E_{e^-}) and, since the beam energy (E_0) is known, the energy of the radiated photon is obtained from the relation in Equation 4.1:

$$E_\gamma = E_0 - E_{e^-}. \tag{4.1}$$

A timing coincidence is then used to match the photon Tagger hit, and hence photon energy, with corresponding hits in reaction-product detectors.

The focal plane detector system [78] consists of an array of 353 plastic scintillators, each approximately 2 cm wide, 8 cm long and 2 mm thick. Using programs such as RAYTRACE, the electron optics of the spectrometer were calculated for all of the electron momenta within the Tagger's acceptance. This information was used to position the 353 elements along the focal plane of the detector. Each element is angled perpendicular to the anticipated electron path for the electron momentum corresponding to that particular position in the focal plane array. Each scintillator overlaps with both of its neighbours in such a way that any true tagging electron (following a trajectory from the beam spot on the radiator) should trigger two scintillators (Figure 4.4). Thus the photon Tagger has 352 coincidence channels. All events involving only a single element are rejected, thereby reducing the background.

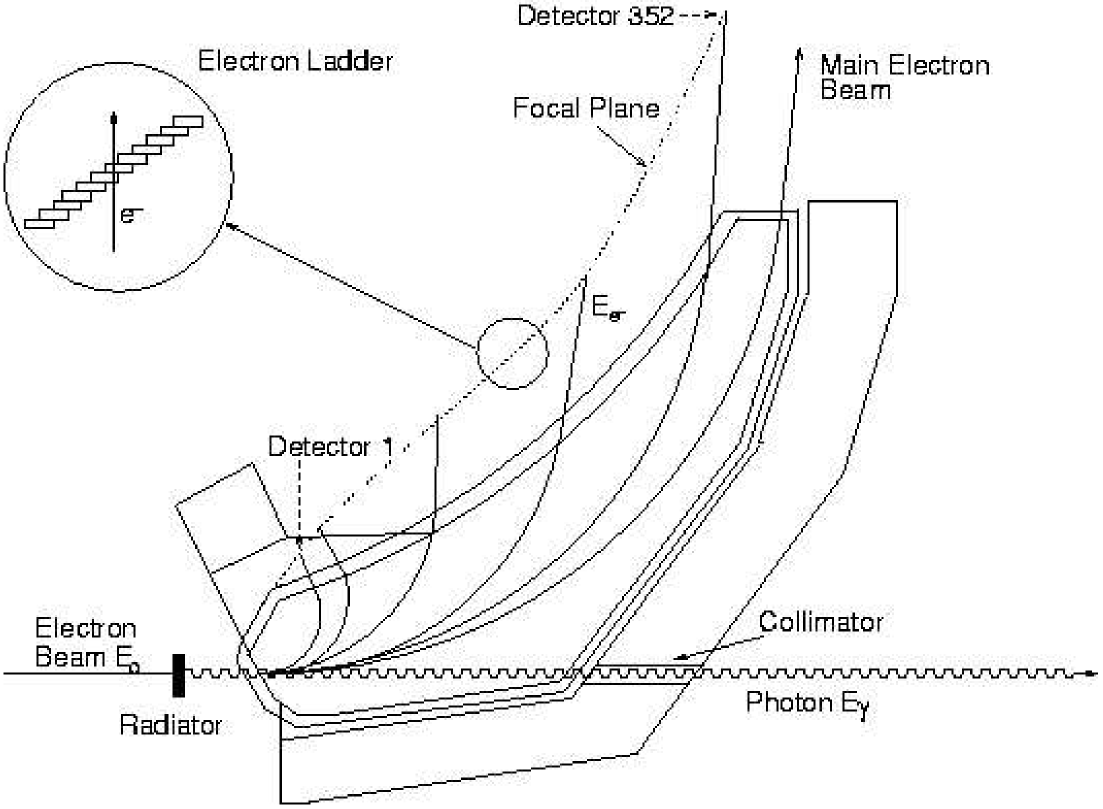

Figure 4.4: The Glasgow Tagger. Adapted from [18].

When the Tagger was constructed, the number of focal plane elements was determined by the physical space occupied by a single photomultiplier. The 353 elements gave the maximum comfortable packing density for the photomultiplier tubes, covering an electron energy range of 62 MeV to 814 MeV with an energy resolution of around 2 MeV (determined by the width of each individual scintillator). However, the intrinsic resolution of the magnetic spectrometer is far superior to this, of the order of 120 keV. It was decided to slightly displace the detector array from the true focal plane of the magnet. It runs on a curve parallel to the true focal plane, but 41 mm further from the effective field boundary. Due to the 2 MeV channel width of the focal plane array, the slight defocussing makes very little difference to the energy resolution of the system.

A supplementary, high resolution focal plane detector (the Tagger Microscope [79]) was later constructed in order to better exploit the potential of the magnetic spectrometer. It is a scintillating fibre detector which inserts at approximately the true focal plane of the magnet and gives an energy resolution of around 400 keV over a limited range of photon energies. This is very useful for experiments where a small energy range has to be examined in greater detail, for example when determining reaction thresholds. However, in our experiment, we used only the main Tagger.

Due to the $\sim 1/E_\gamma$ shape of the Bremsstrahlung distribution, a large number of low energy photons (high energy tagging electrons) are produced. In order not to saturate the focal plane detection system, the detector elements at the extreme high electron energy (low photon energy) area of the focal plane were switched off. This permitted a higher electron beam current and thus a larger photon rate in the middle of the Tagger's energy range which was the region of interest in this experiment. Thus we tagged photons in the energy range 206 MeV to 820 MeV.

Each individual photon Tagger channel has a small electronics card connected directly to its photomultiplier tube. This card contains two discriminators and coincidence logic (AND with neighbouring elements). The discriminators have two thresholds: a low one which determines signal time; and a higher one which determines if the signal is sufficiently large to result from an incident electron. This dual threshold setup in principle provides an individual Tagger channel with a timing resolution of ~0.5 ns FWHM.

Signals from the cards are then fed to the main rack of Tagger electronics. The first stage of the main electronics system involves a delay of ~500 ns. The on-board electronics attached to the focal plane system receive their signal from the electrons earlier than the experimental detector systems around the target. Hence the signal from the 'electron side' of the experiment must be delayed in order to be combined with the experimental trigger (X-trigger). The individual Tagger signals are fed to live-time gated scalers, through a latch to TDCs (Time to Digital Converters) and a logical OR of all 352 channels. The scalers are used to determine the number of tagged photons in the beam. The latch provides a bit-pattern indicating which Tagger elements are hit and the TDC provides the time difference between each focal plane hit and the X-trigger to enable more detailed and precise offline analysis. The OR of all 352 channels (Ladder-OR) is supplied to the main experimental trigger logic unit and may optionally be ANDed with the X-trigger to ensure that there is always a corresponding Tagger signal for all of the experimental data read out.

The major electronics units in this system, the Scaler, Latch and TDCs, all follow the IEEE FASTBUS[1] standard. In line with the rest of the A2 Data Acquisition (DAQ) systems, the Tagger FASTBUS electronics system is controlled and read out by a VMEbus[2] single-board computer (SBC). This single-board VME CPU then supplies all of the data it has accumulated for each event to the Master VME CPU in the Crystal Ball DAQ system for recording to memory with the rest of the experimental data stream.

4.2.3 Beam Monitoring & Tagging Efficiency Measurement

In order to perform a precise cross section measurement, it is necessary to know the number of tagged photons in the beam incident on the target. It is also essential to know that the beam spot is contained within the target diameter (so all photons in the beam pass through the target). To constrain the radius of the beam spot on the target, the photon beam passes through a lead collimator before leaving the Tagger magnet return yolk. This gives a photon beam radius of ~2.5 mm, 2.5 m downstream of the radiator (the electron beam spot size on the radiator is <1 mm in diameter). During experimental running, the beam spot shape and intensity distribution can be observed in real time using an in-beam CsI scintillator viewed by a CCD camera. The position of the electron beam on the radiator was adjusted to ensure that the bright cone of forward bremsstrahlung was centred on the collimator axis.

---

[1] ANSI/IEEE STD 960-1986

[2] VME stands for VERSAmodule Eurocard bus, a computer bus standard developed largely by Motorola and then standardised as ANSI/IEEE 1014-1987.

The collimation does prevent some of the photons that have been 'tagged' from reaching the experimental area. In order to know how many of the photons tagged by a particular Tagger channel reach the experimental area, we performed tagging efficiency measurements. This is done using lower beam intensity than normal running in order not to saturate the lead glass detector which is driven into the beam for the measurement. At low beam intensity, this large volume Cerenkov detector has $\sim$100 % efficiency for registering energetic photons. If the photons are counted in coincidence with the electron counters on the Tagger, a ratio can be defined:-

$$\varepsilon_{tagg}^{n} = \frac{N_{\gamma}^{n}}{N_{e}^{n}}, \tag{4.2}$$

where N_{γ}^{n} is the number of hits in the lead glass detector coincident with hits in Tagger channel n and N_{e}^{n} is the number of counts in the focal plane scaler of channel n. This ratio (ε_{tagg}) is known as the tagging efficiency. Tagging efficiency is measured for each Tagger channel and used to normalise the counts in the focal plane electron scalers to give the number of photons from each Tagger channel reaching the target.

As the lead glass detector would be damaged by running at normal experimental beam currents, we take it out of the beam and monitor the photon beam with an ionisation chamber which measures the overall bremsstrahlung flux during normal running.

4.2.4 Polarised Photon Production

In order to produce linearly polarised photons from the electron beam, it is necessary to use a crystalline radiator. We used a **100** diamond radiator. As explained in Appendix B, the crystal must be aligned precisely in order to ensure that the [022] or [02$\bar{2}$] lattice vector is correctly orientated with respect to the electron beam direction, while also ensuring the other lattice vectors are manoeuvred carefully out of the allowable 'momentum pancake' [80,81]. This is achieved using a five-axis goniometer, with each of the axes driven by computer controlled motors. The zero point of the diamond is considered to be when the three basis vectors, $\mathbf{b_1}$,$\mathbf{b_2}$, and $\mathbf{b_3}$ are parallel to the beam, vertical and horizontal axes, respectively. The goniometer can rotate round all three of those axes in order to position the diamond. As well as orientating the diamond, the goniometer is used to change the radiator to other materials such as nickel and iron and to remove all radiators from the electron beam path during initial steering of the beam from the accelerator into the experimental hall (see Figure 4.5). The goniometer can move both horizontally and vertically, in addition to the three axes of rotation, in order to achieve this.

The diamond crystal is aligned using methods described in references [81,82].

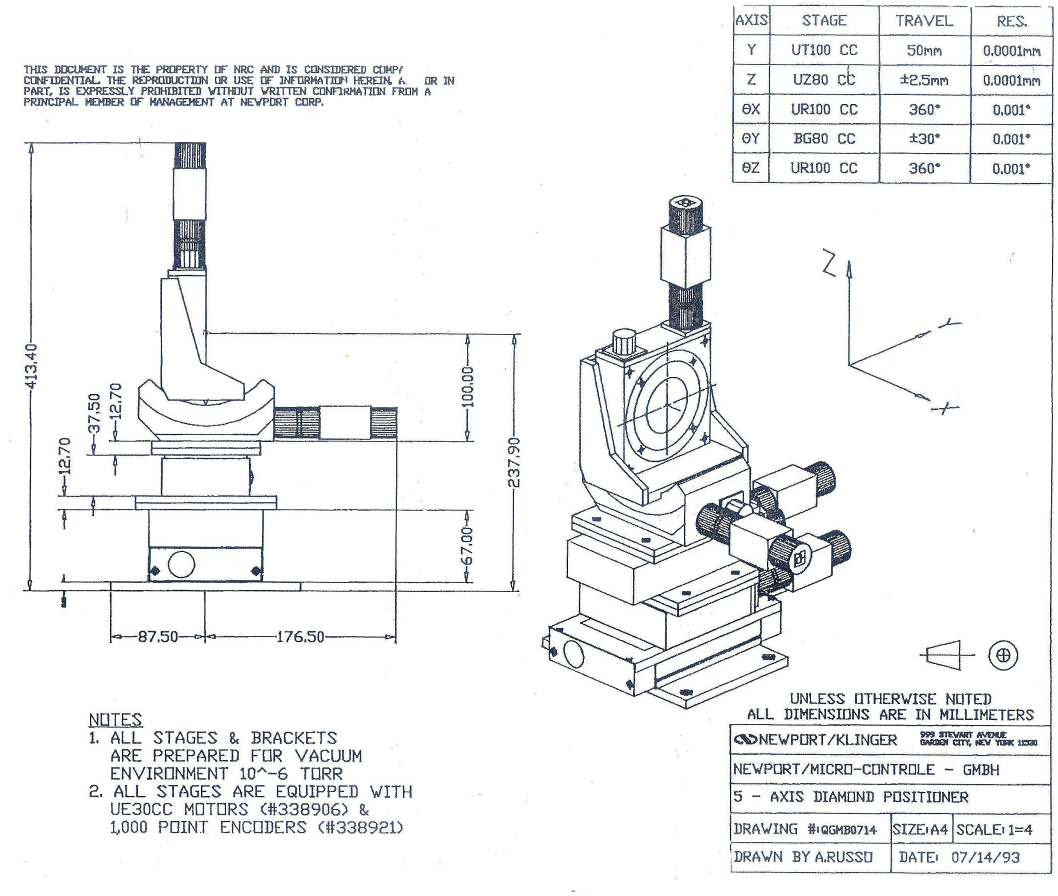
THIS DOCUMENT IS THE PROPERTY OF NRC AND IS CONSIDERED COMP/ CONFIDENTIAL. THE REPRODUCTION OR USE OF INFORMATION HEREIN, & OR IN PART, IS EXPRESSLY PROHIBITED WITHOUT WRITTEN CONFIRMATION FROM A PRINCIPAL MEMBER OF MANAGEMENT AT NEWPORT CORP.
413.40
37.50
12.70
12.70
100.00
237.90
67.00
87.50
176.50
NOTES
1. ALL STAGES & BRACKETS ARE PREPARED FOR VACUUM ENVIRONMENT 10^-6 TORR
2. ALL STAGES ARE EQUIPPED WITH UE30CC MOTORS (#338906) & 1,000 POINT ENCODERS (#338921)
AXIS
STAGE
TRAVEL
RES.
Y
UT100 CC
50mm
0.0001mm
Z
UZ80 CC
±2.5mm
0.0001mm
θX
UR100 CC
360°
0.001°
θY
BG80 CC
±30°
0.001°
θZ
UR100 CC
360°
0.001°
Z
Y
X
UNLESS OTHERWISE NOTED ALL DIMENSIONS ARE IN MILLIMETERS
NEWPORT/KLINGER
999 STEWART AVENUE GARDEN CITY, NEW YORK 11530
NEWPORT/MICRO-CONTROLE - GMBH
5 - AXIS DIAMOND POSITIONER
DRAWING #:QGMB0714
SIZE:A4
SCALE: 1=4
DRAWN BY A.RUSSO
DATE: 07/14/93

(a) A schematic diagram of the goniometer

(b) A technical drawing showing axes

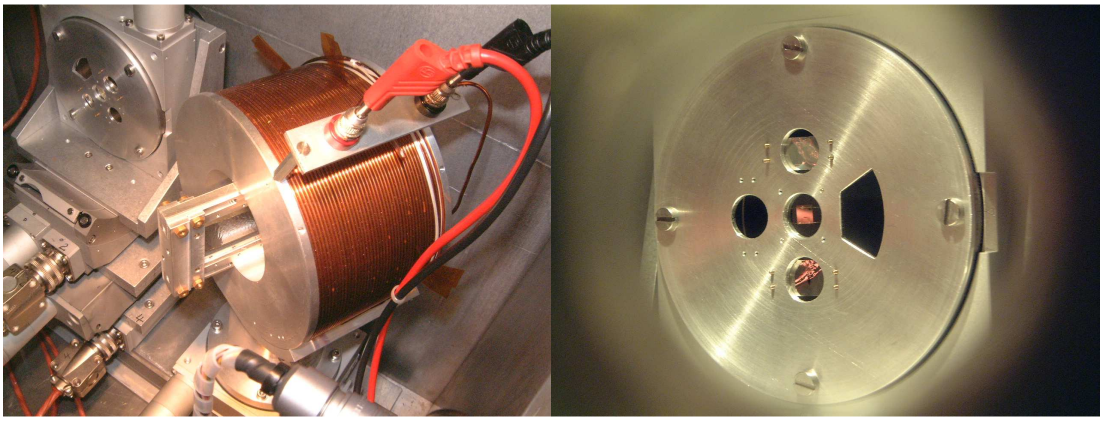

(c) The goniometer with the Moeller coil

(d) The radiator choices, diamond in the centre with, clockwise from left, blank, nickel, blank, iron

Figure 4.5: The A2 Goniometer

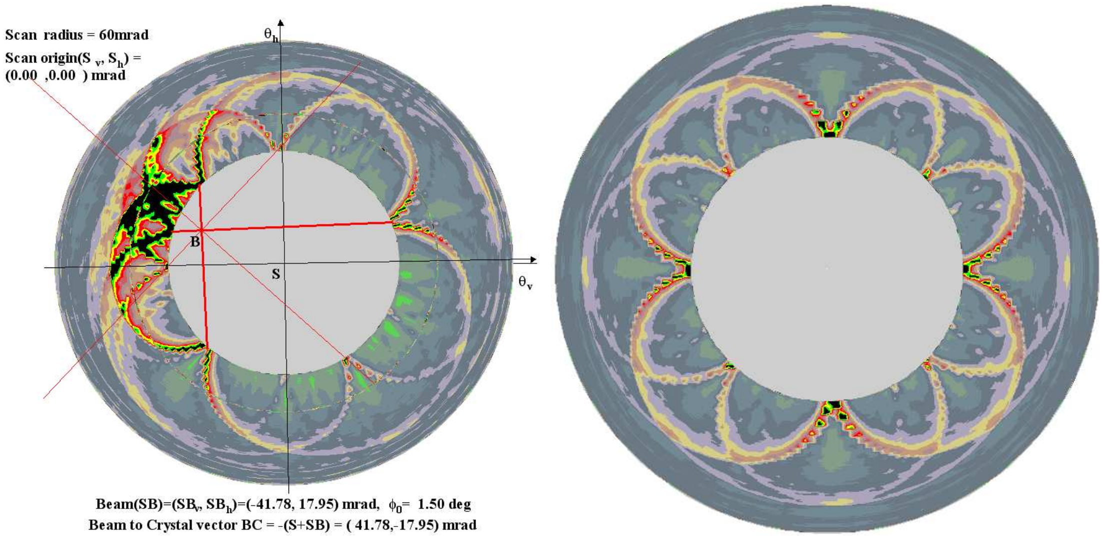

Figure 4.6: Goniometer Alignment Scan Results: the photon energy is plotted radially from the centre of the ring and the azimuthal angle indicates the angular position at which the energy spectrum was sampled. Left panel: An initial goniometer scan showing asymmetry, which indicates crystal misalignment. The superimposed lines show the fit results which locate the proper alignment position. Right panel: A goniometer scan after the diamond crystal has been aligned using the scan results shown on the left. Four-fold symmetry indicates successful alignment.

A series of scans are taken, where spectra of Tagger scaler counts as a function of electron energy are accumulated for a series of small angular steps of the crystal. The electron "energy spectra" are plotted against angle and the four-fold symmetry shows where the curves of maximum intensity meet at $E_\gamma = 0$ MeV as the [022] and [02$\bar{2}$] lattice vectors were lying parallel to the beam axis (Figure 4.6). The zero point of the crystal can then be identified and any crystal orientation, and hence any polarisation edge energy, can then be obtained by suitable rotations about the horizontal and vertical axes.

The photon beam was collimated with a 4 mm collimator for the July experimental run and a 3 mm collimator for all subsequent runs to enhance the degree of linear polarisation as described in [83]. In order to calculate the degree of linear polarisation achieved, the analytical bremsstrahlung calculations described in [84] were used. These provided a good match to the observed energy spectrum and yielded a maximum degree of linear polarisation of ~ 37 %.

4.3 Liquid Hydrogen Target

In our experiment, we used liquid Hydrogen as a proton target (Figure 4.7). The liquid Hydrogen is contained in a cylindrical vessel 4.8 cm long and 2 cm in radius formed from 125 μm thick Kapton. This is surrounded by eight layers of super-insulation foil (formed from 8 μm Mylar with 2 μm Aluminium) to assist in the maintenance of the 21 K temperature. This assembly is then contained in a 1 mm thick carbon fibre vacuum tube, with a Kapton exit window, to protect the target cell and to act as a scattering chamber to contain the Hydrogen in the event of target cell leakage.

The target was maintained at a pressure of 1080 millibar (slightly above atmospheric pressure) to minimise the risk of air leaking into the target. It presented an areal density to the beam of 2.01×10^{23} protons per cm^2.

4.4 Crystal Ball System

The Crystal Ball System (Figure 4.1) is composed of the NaI spectrometer, Multi-Wire Proportional Chambers (MWPC) and the Particle Identification Detector (PID) which all cover the same solid angle range viewed from the target at the centre. The information from these three detectors combines to provide accurate energy, angle and particle identification in the region from 0° to 360° in azimuthal angle (ϕ), and 21° to 159° degrees in polar angle (θ).

4.4.1 The Crystal Ball

The Crystal Ball (CB) [85] (Figures 4.1, 4.8) is a segmented Sodium Iodide detector covering 94 % of 4π steradians. The spherical shape is approximated by an icosahedron with each of its twenty triangular faces (major triangles) divided into 4 minor triangles. These 4 minor triangles are then subdivided into 9 triangular crystal faces. The projections of each crystal face are extended radially outwards until they intercept the smallest sphere which completely encases the icosahedron. There are eleven slightly different crystal shapes but all are truncated triangular pyramids 40.6 cm in height pointing towards the centre of the target. The triangular side lengths are 12.7 cm at the external surface and 5.1 cm at the internal surface. The Crystal Ball is divided into two hemispheres which may be separated to access the central region. At both the front and rear of the Ball, 24 crystals have been removed to form the beam entrance and exit leaving 672 crystals and a θ coverage of 21° to 159°.

Each of the 672 crystals is optically isolated by wrapping it in reflective paper and alumnised mylar. The scintillation light travels through a 5 cm air gap and a glass window before reaching a 5.1 cm diameter photomultiplier. The thickness of NaI is almost one hadron interaction length and typically 98 % of all the deposited energy from the electromagnetic shower created by a photon or electron is contained within a thirteen crystal cluster. Due to its high segmentation, the Crystal Ball achieves an angular resolution for electromagnetic showers of $\sigma = 2^\circ - 3^\circ$ in θ and $\sigma = \frac{2^\circ}{sin\theta}$ in ϕ. A minimum ionising particle passing through the Ball deposits ~197 MeV and the energy resolution for photons is given by $\frac{\sigma}{E} = \frac{2.7\%}{E(GeV)^{1/4}}$ [85].

The NaI crystals are extremely hygroscopic and so the Crystal Ball has to be vacuum sealed. The Crystal Ball is divided into two hemispheres, separated by a 0.8 cm air gap between two 1.6 mm stainless steel disks on which the crystals rest. The inner wall of each hemisphere is formed by 1.5 mm (0.09 radiation lengths) of stainless steel. The energy resolution for low energy particles is worsened by

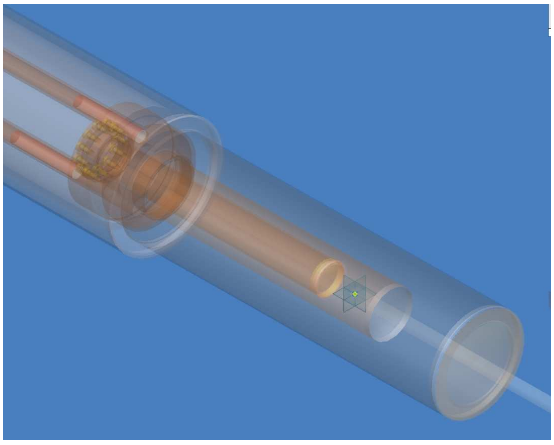

(a) AutoCad representation of the target.

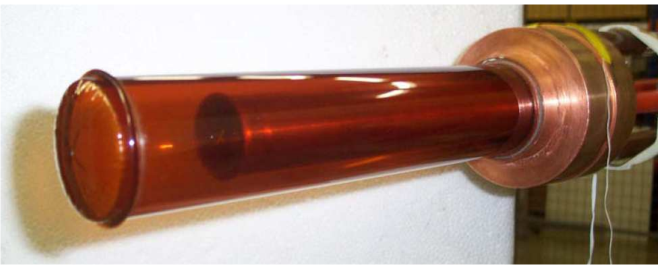

(b) Photo of the Kapton target cell.

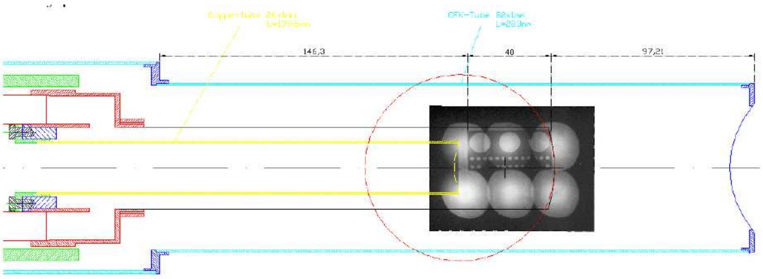
CFK-Tube 82x1mm
L=283mm
146,3
40
97,21

(c) Schematic diagram of the target showing an X-ray picture of the target cell when cold.

Figure 4.7: The liquid Hydrogen target. Figures reproduced from [19].

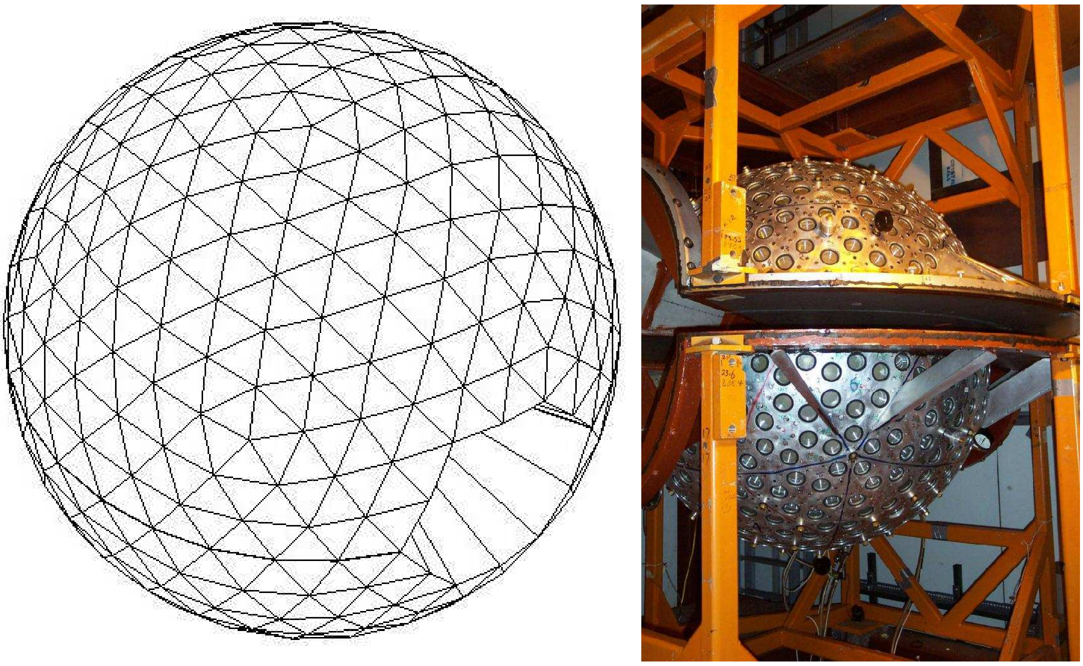

(a) Diagram of the NaI Crystal Array (b) Photograph of the Detector

Figure 4.8: The Crystal Ball

the air gap between the NaI crystals and the PMTs. However, due to the complex and delicate nature of the internal structure of the Crystal Ball it is completely unfeasible that any modifications to the internal light couplings might be effected. Some (around 2 %) of the crystals have also been damaged during the lifetime of the Crystal Ball which reduces optical transmission somewhat.

The HV supply to all of the PMTs is common so gain setting of the Crystal Ball is achieved by adjusting the voltage dividers of each PMT individually. The crystals were tested with a 4.438 MeV γ source (^{241}Am/^{9}Be contained in borated polyethylene to suppress the neutron background) and their gains were aligned as far as possible with the source. The physical gain alignment ensures that hardware voltage thresholds correspond to similar energies for each crystal in the Ball.

The source calibration has a long extrapolation to the E_γ of experimental interest. Thus it was necessary to perform a calibration using the kinematically overdetermined reaction p(γ,π^0). This is described in Section 5.3.1.

4.4.2 Particle Identification Detector

The Particle Identification Detector (PID) is a ~10 cm diameter barrel formed by twenty four plastic scintillators. Each scintillator is 31 cm long, 13 mm wide, and 2 mm thick. The design and construction of the Particle Identification Detector formed a large proportion of the author's work during 2002 to 2004, a more detailed account can be found in Appendix A.

This detector (Figure 4.9) was built specifically for the experimental series of which our study forms a part. Particle identification was needed in the CB to veto electrons (to cleanly identify photons), detect protons, and, in the case of the $n\pi^+\gamma'$ channel, detect charged pions. The particle flight path from the target to the NaI is too short and the NaI timing resolution too poor to provide particle identification by time-of-flight methods. This made it necessary to implement some other method of separating the various charged particle species. The PID identifies charged particles by differential energy loss in the thin plastic scintillator. The design of the detector was complicated by the tight physical constraints laid down by pre-existing detector geometries. The final PID location was between the target and the MWPCs. This is an unusual arrangement as most detector systems have the tracking elements closest to the target in order to get accurate information on particle direction without degrading the signal by multiple scattering. However, as there was insufficient space to fit the PID outside of the MWPC, it was accepted that we would have to sacrifice some position resolution in order to gain particle identification. After simulation using a Geant-3 based model of the detector, it was decided to construct the barrel of 2 mm thick plastic scintillator as a reasonable compromise between multiple scattering and a functional energy loss signal.

The PID provides identification of different particle species by a comparison of the energy deposited in the Crystal Ball (assumed to be approximately the total energy of the particle) and the energy deposited in the PID scintillators. The energy deposited in the PID scintillators is comparatively small (of the order 400 keV for a minimum ionising particle), but is measurably different for particles of the same total energy, but different ionisation density, such as protons and charged pions. The lighter particles deposit a smaller fraction of their total energy in the PID, so a plot of energy deposited in the PID (ΔE) against the energy deposited in the Crystal Ball (E) reveals distinct bands corresponding to particle species as shown in Figure 4.10. To select a certain species of particle, one then simply defines a polygon enclosing the locus of the ΔE, E combinations of the desired particle and accepts only particles which produce a ΔE, E combination which lies within this polygon, as illustrated in Figure 4.10. There the red polygon defines the proton region and the blue polygon selects charged pions.

The calibration of the Particle Identification Detector was Glasgow's responsibility and full details can be found in Section 5.3.2.

4.4.3 Multi-Wire Proportional Chambers

We used the inner two Multi-Wire Proportional Chambers (MWPCs) of DAPHNE (Detecteur a grande Acceptance pour la PHysique photoNucleaire Experimentale) [86] to provide charged particle tracking for protons and charged pions. The Crystal Ball segmentation is sufficient to provide position information for photons as they fire multiple NaI elements, allowing for location of the photon hit position by determination of the "centre of gravity" of the energy distribution. However, for charged particles, which usually fire only one or two NaI elements, far superior position information is obtained using Multi-Wire Proportional Chambers.

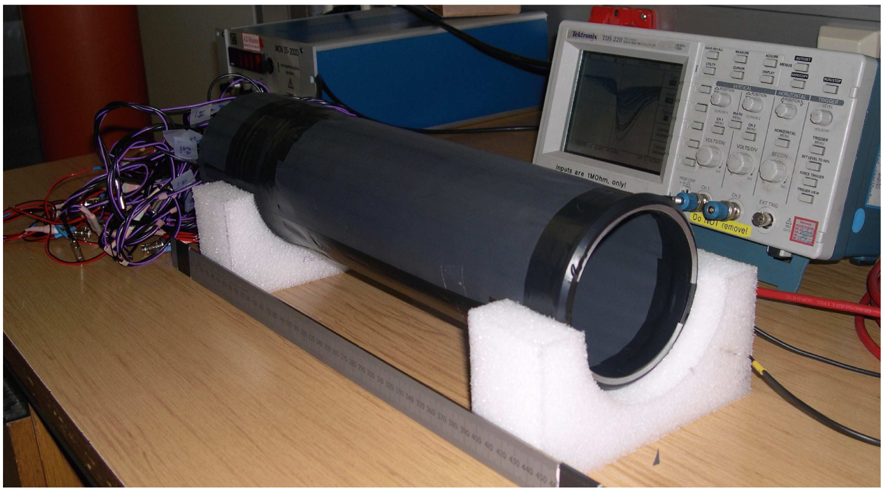

(a) The Particle Identification Detector, fully assembled in Mainz for testing, before installation.

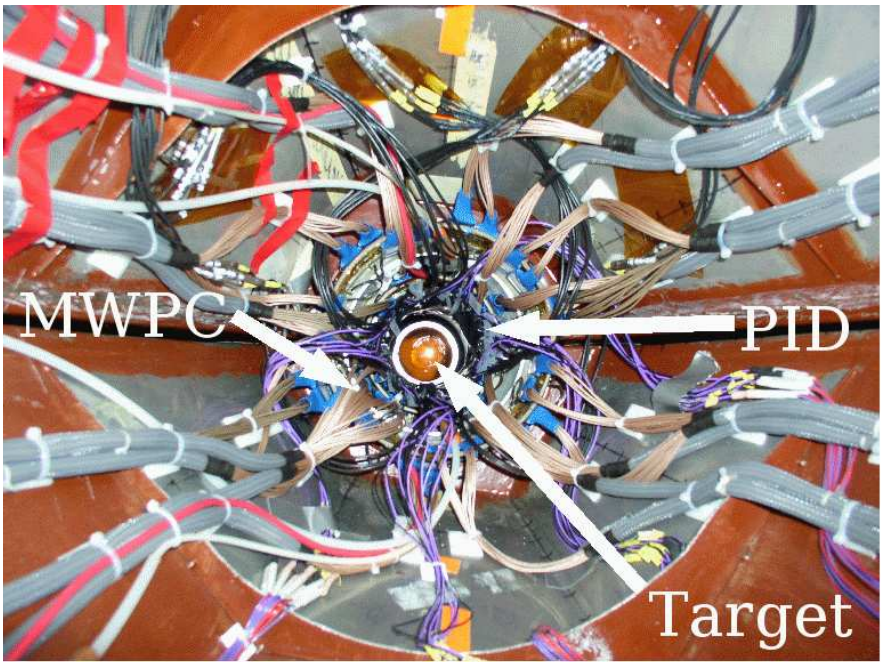

(b) Final detector position, looking into the CB beam pipe, towards the Photon Tagger.

Figure 4.9: The Particle Identification Detector

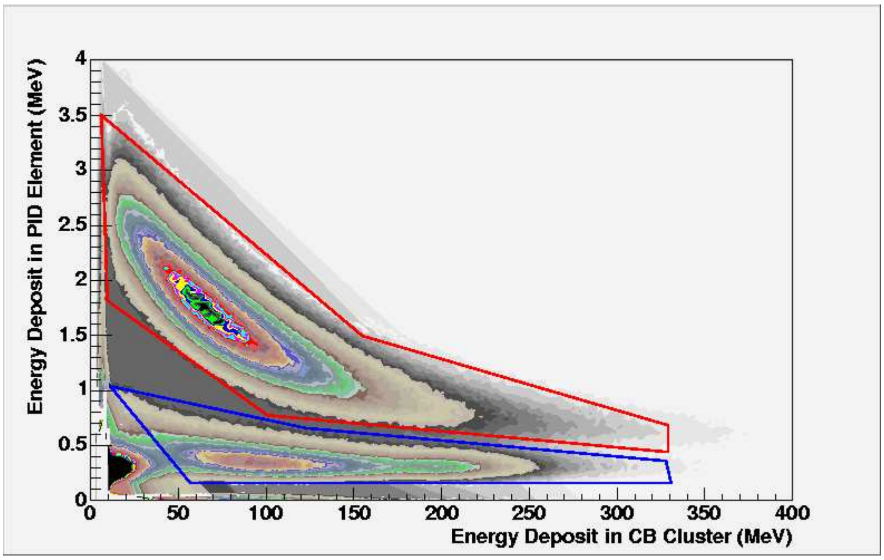

Figure 4.10: ΔE / E plot from experimental data showing particle separation. The red band shows a typical selection region for protons, the blue band for charged pions. An electron peak can be seen near the origin.

The MWPCs are filled with a mixture of Ar (74.5 %), ethane (25 %) and freon (0.5 %) and collect the charge deposited in their substrate gas by travelling charged particles in a combination of fine wire anodes and thin strip cathodes which locate the precise position of the particle's passage through an individual chamber. When such a position is obtained in two or more wire chambers, the particle track can be deduced. Although having three such chambers would have improved our track reconstruction efficiency and accuracy, we were limited to the inner two by spatial constraints and the intensity limit imposed by the sensitivity of the largest of the three chambers.

Each of the wire chambers is contained within two coaxial 1 mm thick cylindrical Rohacell [87] walls coated in 25 μm Kapton film. Electrical screening is achieved via a 0.1 μm thick Al coating on the external surfaces of the chamber

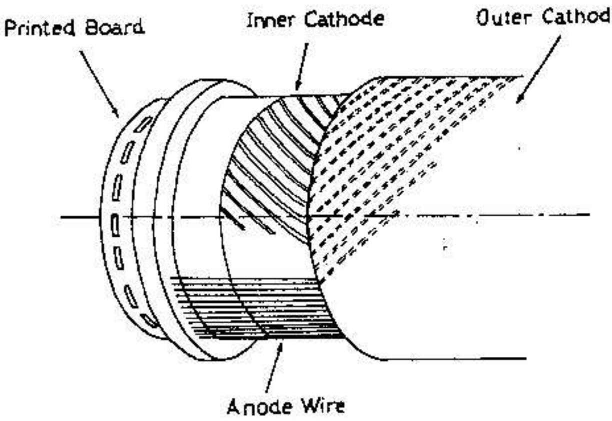

Figure 4.11: Wire chamber diagram, showing anode wires and cathode winding.

walls. The 20 μm diameter Tungsten anode wires are positioned at 2 mm intervals round the circumference, parallel to the cylinder axis. These are read out on a binary basis (hit or not). There is a 4 mm anode to cathode gap. The cathodes are formed by 0.1 μm thick, 4 mm wide Al strips (with 0.5 mm separation) deposited on the internal surfaces of the Rohacell cylinders. The cathode strips are wound helically at angles of $\pm 45°$ to the anode wires (Figure 4.11). The centre of gravity of the charge induced on the, generally three or four, strips can locate the hit position to better than the strip pitch. Each of the inner and outer cathode strips cross each other twice along the length of the chamber and it is necessary to establish which anode wires have also fired in order to uniquely identify the hit position.

Due to the cylindrical symmetry of the wire chambers, they cover 360° in ϕ. The θ range is from 21° to 159° due to the openings at the front and rear of the cylinders, giving coverage of 94 % of 4π steradians. Each hit on a wire chamber is evaluated to give an azimuthal coordinate (α) and a longitudinal coordinate (z). The larger the angle to perpendicular incidence, the wider the charge distribution on the cathode strips becomes and, hence, the poorer the z-resolution becomes. Z-resolution was measured to be around 200 μm with a collimated β source at 90°. However this resolution worsens with angle (as discussed above) and also due to physical imperfections in the wire chambers such as misalignments in the anode wires and variation in the anode to cathode gap. Reconstruction of cosmic ray muons which pass through each chamber twice gives an average θ resolution of 1.88°, and a constant azimuthal resolution of $\Delta\phi = 2°$.

4.5 The TAPS Forward Angle Spectrometer

TAPS [88], which had previously been configured as a “Two/Three Arm Photon Spectrometer”, is a 510 element Barium Fluoride Photon Spectrometer, configured as a forward wall for our experiment. Each BaF_2 element is capped with a 0.5 mm thick plastic veto detector to identify charged particles. As the Crystal Ball was originally designed for colliding beam experiments there is a large hole in the CB’s forward angle acceptance between 0°and 21° in θ when used in a fixed target experiment. TAPS is used to detect photons, protons and pions in this forward angle region, which is important due to the Lorentz boost provided by the photon beam. As there are no other detectors covering this area of phase space, TAPS must provide tracking, calorimetry and identification of particles in this region.

4.5.1 BaF_2

The forward wall made up of 510 TAPS BaF_2 detector elements [88] is shown in Figure 4.12. Each individual element is 250 mm long and has a hexagonal cross section of inner radius 29.5 mm (see Figure 4.13). TAPS elements have an energy resolution of $\frac{\sigma}{E} = \frac{3.7\%}{E(GeV)^{(1/4)}}$ [88].

As the angular region covered by TAPS was not also covered by the wire chambers (see Section 4.4.3) or the Particle Identification Detector (see Section

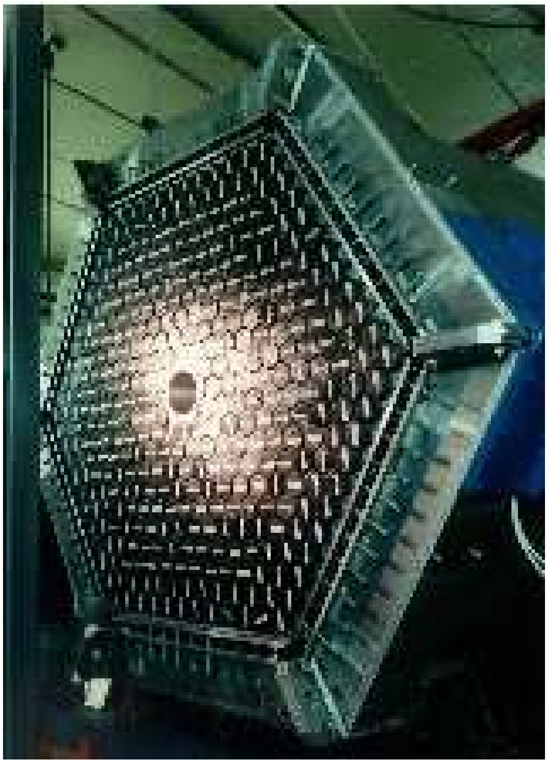

Figure 4.12: The TAPS forward wall configuration.

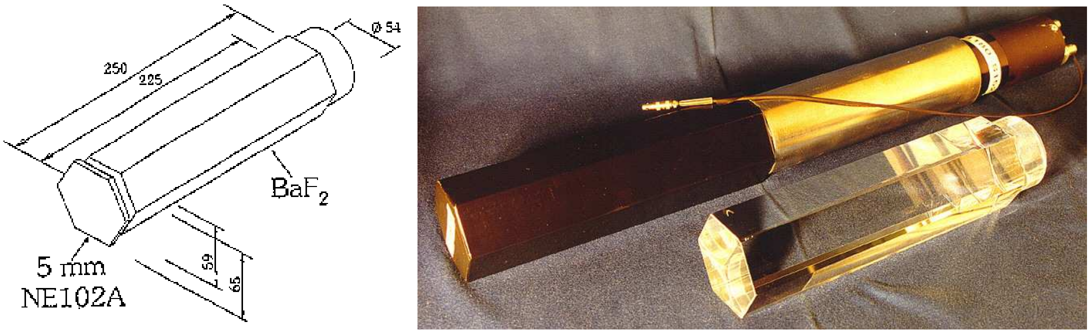
250
225
Ø 54
BaF$_2$
5 mm
NE102A
59
65

(a) Technical drawing of a TAPS element, showing hexagonal plastic veto counter

(b) A Barium Fluoride crystal and assembled detector element

Figure 4.13: A TAPS element.

4.4.2), the granularity and particle identification characteristics of the detector were vital. BaF_2 is an excellent choice of scintillator for this role as the the relative intensity of the components of its scintillation emission (λ= 195 nm and 220 nm, τ= 0.6 ns; λ= 310 nm τ= 620 ns) [89] is strongly dependent on the velocity of the incident particle. The ratio of fast light output to total light output decreases with increasing ionisation density (decreasing velocity) of the incoming particle [90]. As with the CB, the electromagnetic shower induced by an incident photon fires several adjacent crystals and by taking the "centre of gravity" of the signal amplitudes a position resolution of ~3 cm may be obtained. The detector was placed 1.8 m downstream of the target, giving an angular resolution of ~0.7°.

Due to the fast rise time of its scintillation pulse, TAPS has a timing resolution of approximately 200 ps except at very low photon energies (around 10 MeV). This means that time-of-flight particle identification methods can also be used. If the time-difference between the signal in TAPS and the Tagger is plotted against the energy deposit in TAPS, distinct bands are seen corresponding to the different particle masses. This can be used in parallel with pulse shape analysis to separate out charged pions and protons, or photons and neutrons.

4.5.2 Veto

All TAPS elements are capped with a 5 mm thick hexagonal plastic scintillator which is read out with an optical fibre. Since the light collection is poor, the size of the energy deposit is not recorded, but the hit is registered as a binary digit of a pattern unit. Thus the vetos can differentiate charged and neutral particles (for example, protons and neutrons) which give a similar pulse shape signature.

4.6 Experiment Electronics

4.6.1 Crystal Ball and Trigger Electronics

The Crystal Ball, MWPC and PID were all equipped with new electronics systems for the beginning of the CB@MAMI experimental series. As this was foreseen to be a long-term proposition and involved substantial investment of time and resources, it was decided to make use of the new CERN standard electronics. This should ensure long-term support for the newly refurbished Data Acquisition (DAQ) system, while providing a flexible, scalable and sustainable DAQ system.

The Crystal Ball trigger electronics are shown in Figure 4.14. Crystal Ball photomultiplier tubes (PMT) were connected to Uppsala-designed active fan-out units in groups of sixteen channels. The fan-out copied the signal to both an ADC (Amplitude to Digital Converter) branch of the electronics and a TDC/Trigger branch. It also provided an analogue sum of the sixteen inputs. These sixteen-input sums were then summed through a cascade of LeCroy 428F NIM analogue Fan In/Out modules to provide an analogue sum of all CB deposited energy signals. This analogue sum was then passed to a pair of LeCroy 621 NIM discriminators, one with a low threshold (30 mV) to provide timing for the CB total

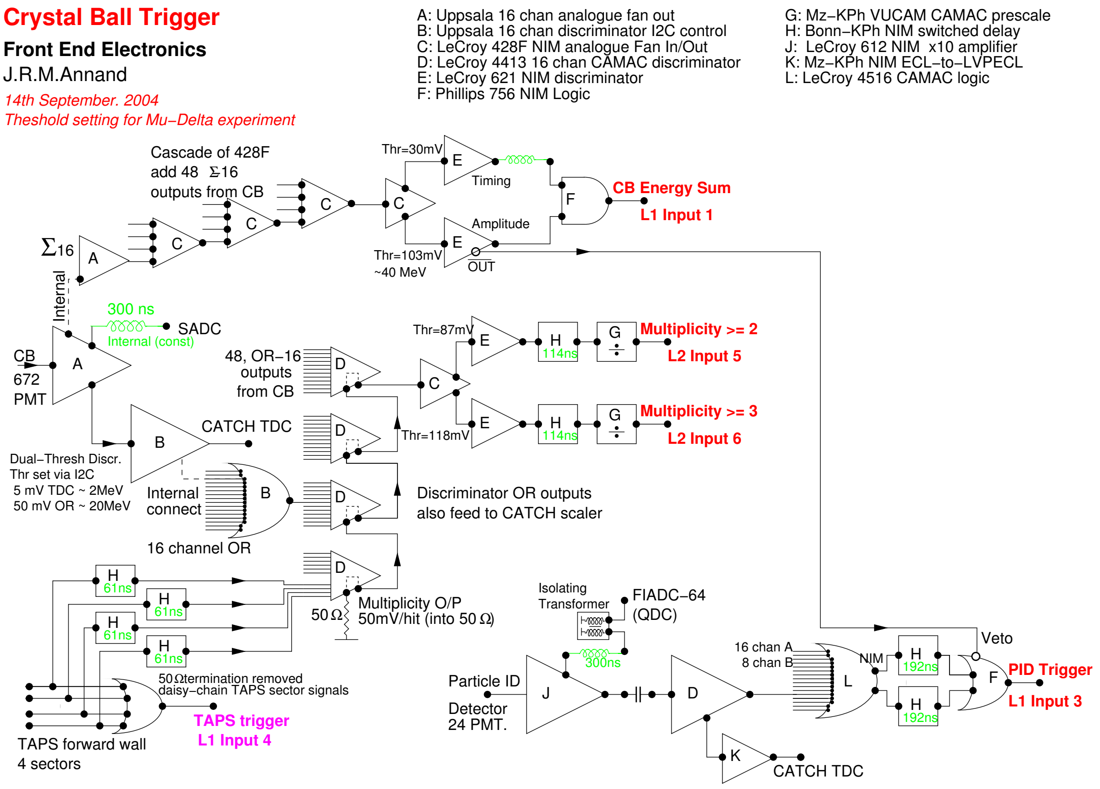
Crystal Ball Trigger
Front End Electronics
J.R.M.Annand
14th September. 2004
Theshold setting for Mu–Delta experiment
A: Uppsala 16 chan analogue fan out
B: Uppsala 16 chan discriminator I2C control
C: LeCroy 428F NIM analogue Fan In/Out
D: LeCroy 4413 16 chan CAMAC discriminator
E: LeCroy 621 NIM discriminator
F: Phillips 756 NIM Logic
G: Mz–KPh VUCAM CAMAC prescale
H: Bonn–KPh NIM switched delay
J: LeCroy 612 NIM x10 amplifier
K: Mz–KPh NIM ECL–to–LVPECL
L: LeCroy 4516 CAMAC logic
Cascade of 428F
add 48 Σ16
outputs from CB
Σ16
Internal
Thr=30mV
Timing
Amplitude
Thr=103mV
~40 MeV
OUT
CB Energy Sum
L1 Input 1
300 ns
SADC
Internal (const)
CB
672
PMT
48, OR–16
outputs
from CB
Thr=87mV
Thr=118mV
114ns
Multiplicity >= 2
L2 Input 5
Multiplicity >= 3
L2 Input 6
CATCH TDC
Dual–Thresh Discr.
Thr set via I2C
5 mV TDC ~ 2MeV
50 mV OR ~ 20MeV
Internal
connect
16 channel OR
Discriminator OR outputs
also feed to CATCH scaler
61ns
Multiplicity O/P
50mV/hit (into 50 Ω)
50 Ω
50 Ω termination removed
daisy–chain TAPS sector signals
TAPS trigger
L1 Input 4
TAPS forward wall
4 sectors
Isolating
Transformer
FIADC–64
(QDC)
300ns
Particle ID
Detector
24 PMT.
16 chan A
8 chan B
NIM
192ns
Veto
PID Trigger
L1 Input 3
CATCH TDC
A B C D E F G H J K L

Figure 4.14: The layout of the Crystal Ball trigger electronics.

energy trigger and one with a high threshold (103 mV - corresponding to approximately 40 MeV energy deposit in the Crystal Ball) to provide the CB total energy deposit threshold. The AND logical combination of the discriminator outputs, made in a Philips 756 NIM logic unit, provides the CB total energy trigger, with good timing (due to the low threshold branch) and a total deposited energy threshold of 40 MeV in the Crystal Ball (due to the high threshold branch).

4.6.1.1 ADC Branch

The ADC signal branch from the splitter was fed to an array of 32-channel sampling ADCs (i-SADC 108032 from i-tr0nics GmbH [91]). These ADCs continuously sample signals applied to the inputs at a rate of 40 MHz, and buffer the digital data. The SADCs offer the possibility of reading out all samples produced over a 2 μs period, allowing the reconstruction of the NaI pulse-shapes. As the large volume of data would have overloaded the DAQ system, we opted to use on board integration of the samples. The boards are programmed to produce integrals over three windows: a baseline integral of samples before the scintillation pulse, a signal integral of the main body of the scintillation pulse, and an integral of the tail of the signal. The timing of the samples to integrate is derived from the experimental trigger. Use of these integrals reduced the volume of data by a factor of $\sim 10^2$ and allowed dynamic pedestal subtraction (subtraction of the baseline integral from the signal integral per event) and checking enhancement of the tail region for ‘pile-up’ effects.

The i-SADCs make extensive use of field programmable gate array (FPGA) technology and so can be re-programmed in the field to allow for changes in read-out mode, sampling frequency and trigger latency. When a trigger pulse is received, the ADC looks to the pre-programmed point in the multi-hit buffer and produces the desired integrals for each channel. It is then possible to read out the three integrals from every channel, or to use zero-suppression and read out only the channels in which the signal integral is greater than the baseline by a set threshold. We used zero-suppression in the read-out, and read out the three integrals only for channels with a signal corresponding to an energy greater than approximately 0.5 MeV above baseline.

The i-SADCs were 6U VMEbus modules, however they only used the power supply from the VME crate. All communication and control was done via an optical I2C link by a GeSiCA controller which interfaced with the VMEbus CPU. The GeSiCAs communicate either via an optical "S-Link", as in CERN, or using the GeSiCA VME interface spy buffer. The spy buffer was originally designed for use in testing the ADCs during development, but as S-Link read-out was not yet fully implemented in Mainz and the data volume was comparatively small (by CERN standards), we used the VME spy buffer for experimental data read-out.

4.6.1.2 TDC Branch & Triggers

The TDC branch from the Uppsala-designed fan-out unit was fed to an array of PM98 [92] 16-channel discriminators. These discriminators were programmed to have a low threshold (5 mV - around 2 MeV) for output to the TDCs and a high threshold (50 mV - approximately 20 MeV). The high threshold signals from each group of 16 inputs were 'OR'ed and the results from all 48 logical OR outputs from the Crystal Ball were combined with the four sector outputs from TAPS. The multiplicity of the 52 CB / TAPS sector signals was determined using the multiplicity outputs (50 mV per hit) of four LeCroy 4413 16 channel CAMAC discriminators. The summed multiplicity outputs were fanned out into two discriminators: one with a threshold of 87 mV for the "level two" multiplicity two trigger and one with a threshold of 118 mV to give the "level two" multiplicity three trigger. These signals were both fed through CAMAC programmable prescale modules to allow prescaling of the multiplicity triggers, before final trigger decisions.

The individual discriminator channel outputs were fed to CATCH (Compass Accumulation, Transfer and Control Hardware) TDCs, originally designed for the COMPASS experiment at CERN [93, 94]. The CATCH TDCs are free running, each having a ~10 GHz oscillator, giving a channel to time conversion of ~117 ps per channel. They are synchronised by a CERN-standard trigger control system (TCS), with one TDC channel (the 'reference TDC') connected to the trigger. Each time a TDC registers a hit, it simply stores the corresponding oscillator count in a buffer. To obtain the timing of a TDC hit, one simply subtracts the number stored in the reference TDC from the number stored in the TDC of interest and uses the constant channel to time conversion given by the ~10 GHz oscillation frequency to provide the time, with respect to the trigger signal, in seconds. They have a double hit resolution of around 20 ns and, apart from this, are essentially without dead-time, having multi-hit storage capacity.

4.6.1.3 PID & MWPC Electronics

The original PID electronics were laid out as shown in Figure A.5. The signal from the photomultiplier tubes was fed through a 10× amplifier and fanned out to a Fast Integrating ADC (FIADC) as described in [93] and to LeCroy 4413 discriminator modules. One of the two available discriminator outputs from each channel was then passed to CATCH TDCs (as used for the CB) after undergoing ECL to LVPECL conversion. The other discriminator outputs were passed to a LeCroy CAMAC logic unit where they were combined in a logical OR. The output from the logic unit was then connected to the CB trigger unit, to offer the possibility of a charged particle trigger, which was not used in our experiment.

The MWPC strip-ADCs were replaced with the same i-tr0nics ADCs as used for the Crystal Ball. The anode wire signals were digitised in CATCH TDCs.

4.6.2 TAPS Electronics

The TAPS electronics were implemented in custom designed CAEN VME modules [95]. The 6U VMEbus units contained 4 ADC channels and a TDC for each BaF_2 element. The TDC was started by an internal constant fraction discriminator (CFD) for precise time pick off to optimise time of flight particle identification. Two internal leading edge discriminators allow for different trigger conditions. The four ADC channels per detector element allowed for signal integration over different time periods and with different charge to channel conversion gains. The “short gate” ADCs integrate the first fast component of the scintillator light ($\tau \sim 40$ ps) and the “long gate” ADCs integrate over the whole pulse ($\tau \sim 200$ ps). There are also short gate sensitive and long gate sensitive ADCs, but these have not yet been calibrated and so were not used in our data analysis. The TAPS veto counter hit patterns were recorded in LeCroy CAMAC pattern units. With 510 channels, reading out so many signals per channel is a very CPU intensive task. The TAPS electronics are housed in 9 VME crates controlled by nine VMEbus single board computers.

The TAPS DAQ data stream was read in separately from the Crystal Ball DAQ data stream and both streams were merged by the main DAQ computer. The only direct interaction between the Crystal Ball DAQ and the TAPS DAQ was for trigger purposes. TAPS was divided into four quarters for cluster triggering purposes, and those four logical OR outputs were fed to the CB DAQ and combined with the other 48 logical OR outputs from the CB to provide the cluster multiplicity signal as described in Section 4.6.1.

4.6.3 Overall Control

As electronic setups in Mainz have traditionally been controlled by a VMEbus single-board computer running the LynxOS operating system and the ACQU data acquisition program [96] (see Section 5.1), it was desirable to build on that expertise. Thus the entire array of ADCs, TDCs and scalers which formed the

CBDAQ were controlled and read out by two VME CPUs, one master, one slave, communicating by VICbus which is essentially a parallel 32-bit cable extension of VMEbus. The information directly received from TAPS was restricted to an event stamp, the four sector segments and a TAPS busy inhibit which was ORed with the corresponding CB busy signal.

The VME machines acquired the CB digital data and performed the slow control functions (such as programmable threshold setting and starting and stopping data runs). The master VME machine then passed the acquired data via Ethernet to a PC running AcquRoot [20] (see Section 5.1) located in the A2 counting room. The TAPS DAQ data stream was also communicated to the same PC over the Ethernet. AcquRoot, which recognises both CB and TAPS data formats, merged the separate CB and TAPS data streams and stored them on a 2TB raid array. It simultaneously performed basic online analysis of the data. This allowed real-time checking of basic things such as the detector hit patterns and total energy deposits alongside more complex physics variables such as the total invariant mass of all 2-hit events. This allowed us to continually monitor detector condition and data quality and check that synchronisation between the CB and TAPS DAQ systems was maintained.

Chapter 5

Event Reconstruction

To convert the data from a series of stored digital pulse heights and times to a physical description of a hadronic interaction requires much thought and effort in calibration. This work was divided between the various members of the collaboration. We seek to give an impression of the method of calibration rather than a blow-by-blow account of the process, only going into detail when describing calibrations performed specifically by the author.

We will begin by describing the analysis software which was used at every stage of the experiment and analysis, and then proceed to describe the calibration of each detector component, with emphasis on the particle identification detector calibrations and the proton energy corrections which were performed by the author.

5.1 Analysis Software

All of the online running and offline analysis of data in the A2 collaboration has been historically handled by ACQU, a data acquisition and analysis suite mainly written by J. R. M. Annand [96] and used in several European Laboratories. Versions of ACQU prior to version 3v4 were formed from a mixture of mainly C and Fortran routines which interfaced via shared memory and semaphores. In recent times, ACQU has been upgraded and has now become the multi-threaded purely C++ program known as AcquRoot [20]. AcquRoot is based on the CERN ROOT [97, 98] system of high energy physics software that is used in HEP labs worldwide. AcquRoot combines full ROOT functionality, including things as diverse as matrix manipulation and 3D histogramming graphics classes, with A2-authored classes designed to specifically control the A2 electronics, data acquisition, storage, retrieval and analysis. Each of the different functions of AcquRoot runs as a separate thread within the one container program, as shown in Figure 5.1. This allows the four separate threads to access the same area of memory while running independently from each other with different levels of priority.

The aim in conversion to C++ was to provide standardisation and modularity to the code. C++ is an object-orientated programing language. This allows the production of basic templates for functions and data objects, that will be required many times over in a system, to be grouped together and defined once as a class.

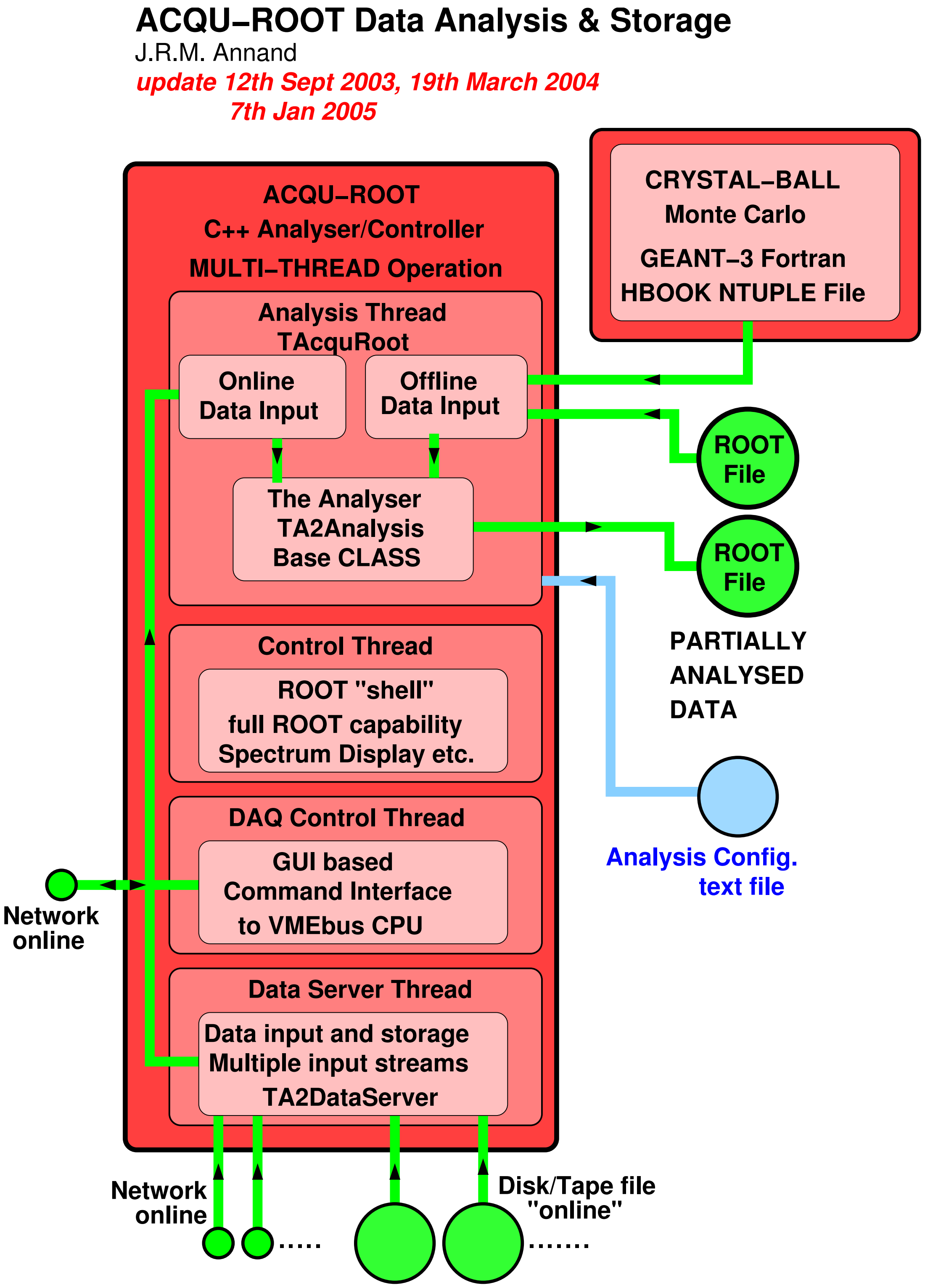
ACQU–ROOT Data Analysis & Storage
J.R.M. Annand
update 12th Sept 2003, 19th March 2004
7th Jan 2005
ACQU–ROOT
C++ Analyser/Controller
MULTI–THREAD Operation
Analysis Thread
TAcquRoot
Online
Data Input
Offline
Data Input
The Analyser
TA2Analysis
Base CLASS
Control Thread
ROOT "shell"
full ROOT capability
Spectrum Display etc.
DAQ Control Thread
GUI based
Command Interface
to VMEbus CPU
Data Server Thread
Data input and storage
Multiple input streams
TA2DataServer
CRYSTAL–BALL
Monte Carlo
GEANT–3 Fortran
HBOOK NTUPLE File
ROOT
File
ROOT
File
PARTIALLY
ANALYSED
DATA
Analysis Config.
text file
Network
online
Network
online
Disk/Tape file
"online"

Figure 5.1: The AcquRoot data storage and analysis system. Extracted from [20].

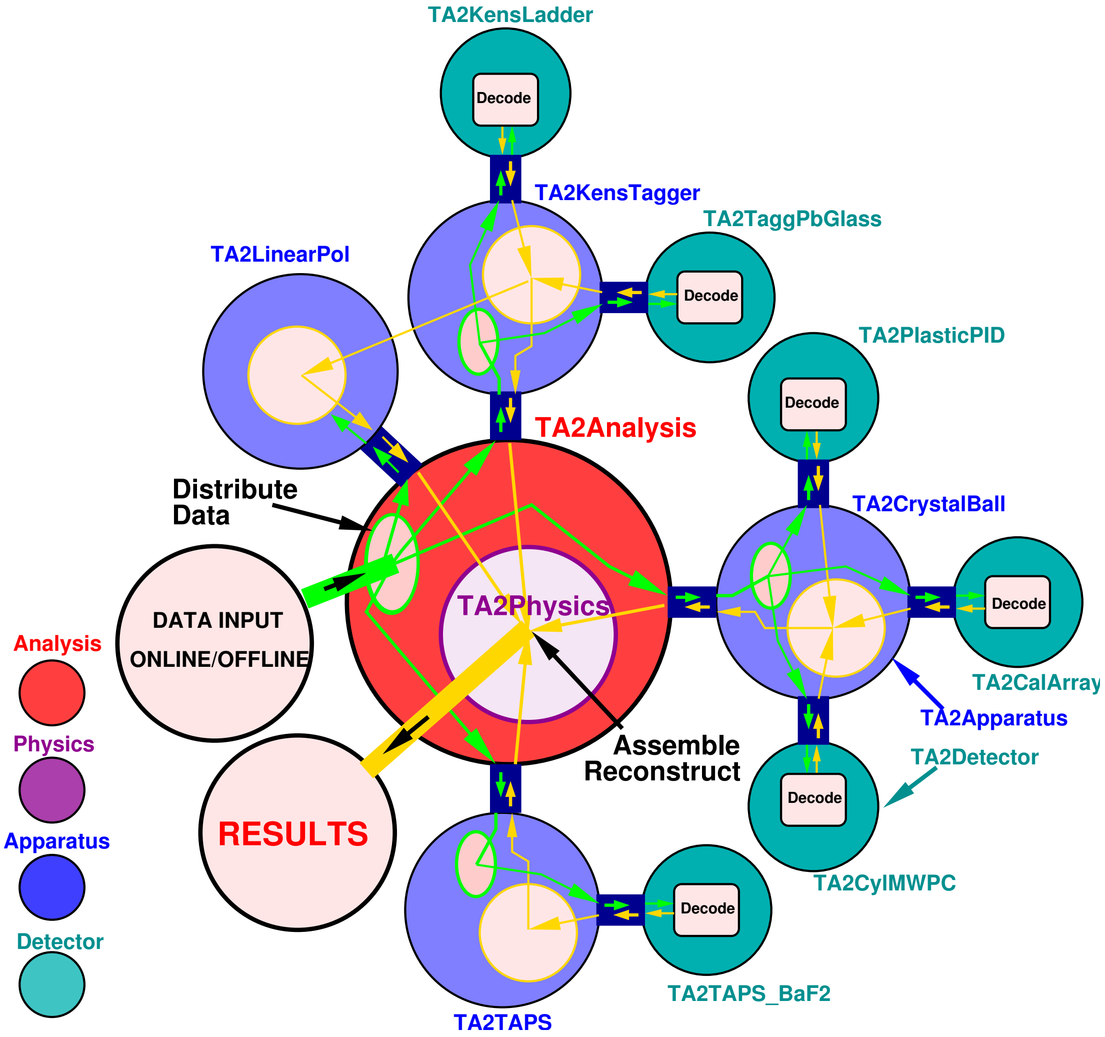
TA2KensLadder
Decode
TA2KensTagger
TA2TaggPbGlass
Decode
TA2LinearPol
TA2PlasticPID
Decode
TA2Analysis
TA2CrystalBall
Distribute
Data
DATA INPUT
ONLINE/OFFLINE
TA2Physics
Decode
TA2CalArray
TA2Apparatus
TA2Detector
Decode
Assemble
Reconstruct
Analysis
Physics
Apparatus
Detector
RESULTS
TA2CylMWPC
Decode
TA2TAPS_BaF2
TA2TAPS

Figure 5.2: The analysis architecture applied in this work. Adapted from [20].

This class can subsequently be 'inherited from' and the functionality accessed by diverse inherited classes. For example, the conversion of digitally stored electronic pulse heights to energies and times is needed in some format to interpret the data from every single detector in the system. These functions (along with several other detector standards) are defined in the *TA2Detector* class which forms part of the 'System Code' of AcquRoot (otherwise and hereafter known as *acqusys*). This class is then inherited by detectors as diverse as *TA2ClusterDetector* (a photon-spectrometer interpretation class) and *TA2WireChamber* (an MWPC interpretation class), which utilise the basic functions in *TA2Detector*, but add to them to produce vastly different results. The structure of the analysis used in this work is shown in Figure 5.2, which illustrates very clearly the benefits of the inheritance system.

The enforceable standards are laid down both by the requirements of the ROOT system basis and also by the base classes (such as *TA2Detector*) which form part of the *acqusys* code. All of the classes in AcquRoot inherit from the ROOT TNamed class which means that they must posses certain functions and behave in a specifically constrained way. Any user-authored AcquRoot classes inherit from the *acqusys* base classes and therefore must contain the data members and functions specified by the parent class.

The modularity of AcquRoot is analogous to the modularity of the detector system that it describes. For each physical detector component in the experimental hall, there exists an AcquRoot detector class (inherited from *TA2Detector*). Each of these detector classes is logically grouped into a set according to which physical apparatus they belong and an appropriate apparatus class is defined (inheriting from *TA2Apparatus* in *acqusys*) which converts the energies and times into particle types and four-vectors. The *TA2CrystalBall* apparatus class, for example, takes information from the NaI, the PID and the MWPC and produces particle four-vectors that come from identification by the PID & NaI combination, energy from the NaI, and angle (in the case of the charged particles) from the MWPC information. Thus, from the basic detector energies and times, the apparatus classes evolve a list of four-vectors and corresponding PDG particle ID numbers. In the current setup, we have three such apparati: *TA2CrystalBall*, *TA2TAPS* and *TA2KensTagger*. The fourth apparatus class shown in Figure 5.2 is *TA2LinearPol* which supplies information relating to the photon beam polarisation. This is the only apparatus with no directly owned detectors (it takes data from the Ladder class(es) associated with the Tagger, and an ADC which contains the polarisation orientation information) and also the only apparatus which directly analyses raw data.

The four-vectors, particle identities and polarisation information are then passed to a single 'Physics' class which combines this information to form physical variables such as missing energies and masses, to identify specific particles from their decay products, and reconstruct the physics processes which have occurred. The whole system is controlled by a pyramid of ASCII text setup files which stipulate - for a given analysis - which detectors, apparati and physics classes are to be used and with which parameters they are to be initialised.

The *acqusys* code contains not only the base classes for all of the above mentioned class categories, but also classes which handle all of the housekeeping functions of data retrieval and transfer between various classes and data display.

During experimental running, the DataServer thread of AcquRoot communicates with the two VME machines that control experimental running, accumulating and storing the data. The Sort and Control threads provide online analysis to assess data quality and online diagnostic tools for any problems encountered during running. The two VME machines run an older version of ACQU which contains classes that communicate with each of the many electronics modules that comprise the A2 data acquisition system. This is a complicated task due to the many hardware standards in simultaneous operation:- CAMAC, FASTBUS, CATCH, and NIM.

5.2 Photon Tagger Calibrations

All Tagger energy and time calibrations were performed by colleagues in Glasgow and the tagging efficiency analyses were performed by A. Nikolaev of Mainz [99].

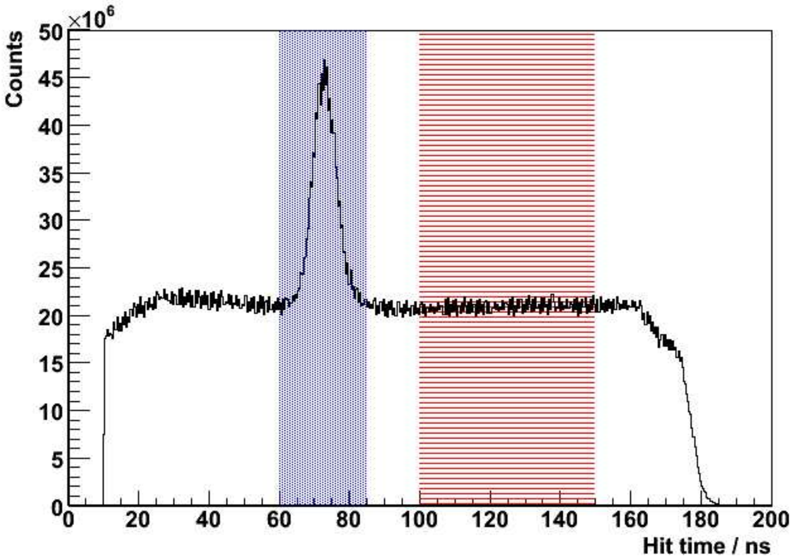

Figure 5.3: Spectrum indicating the blue dotted "prompt" and the red lined "random" region of the Tagger time OR spectrum.

5.2.1 Random Subtraction

As, during normal experimental running, more than one electron is detected by the Photon Tagger for each experimental trigger, we require a way of distinguishing the "real" or "prompt" photons (those that cause the event under study) from the "random" events, where the photon tagged is not the one that caused the event of interest. To do this we look at the Tagger TimeOR spectrum - that is the plot showing the timing of every single Photon Tagger hit in every channel relative to the experimental trigger (Figure 5.3). It can be seen that this spectrum is composed of two parts: an almost flat background of random coincidences for the whole ~170 ns wide event window and a prompt peak (in this case at ~70 ns) which is related to the experimental trigger and the "real" coincident photons. If we assume that the random background under the prompt peak is simply a continuation of the background on either side, we can recover the "true" coincidence results by sampling events for two regions: (1) the prompt region containing the prompt peak and the random background underneath it (illustrated by the blue dotted region in Figure 5.3); (2) the random background - our sample region is shown by the red lined area in Figure 5.3. We then scale the random region sample by the relative widths of the prompt and random regions (0.5 in our case) to give us a sample equivalent to what we expect to find under the prompt peak. In the production of any physical spectrum, e.g. particle energy, this scaled random sample is subtracted from the prompt region sample to give us results due to the prompt photons.

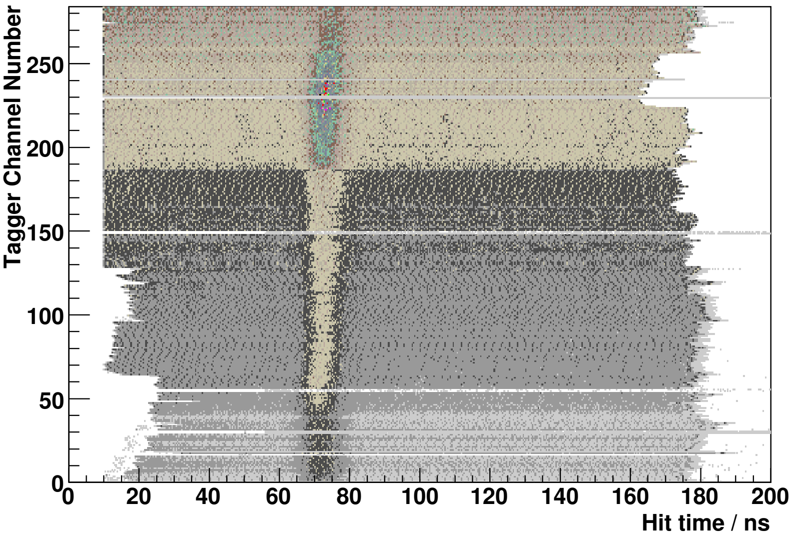

Figure 5.4: Spectrum showing Tagger time alignment for all of the July data.

5.2.2 Timing Calibration & Alignment

The timing calibration for the ladder is a simple affair. Each Tagger TDC channel has a time conversion of ~0.18 ns / channel (based on a calibration done when the Tagger was first installed). It is desirable that all of the Tagger channels are aligned so that their "prompt" peaks (the peak related to the experimental trigger) occurs at the same point in each TDC time spectrum. The channels are aligned by fitting a Gaussian distribution to the prompt peak of each channel (obtained in a low-intensity tagging efficiency run to minimise random coincidences). The mean of this Gaussian is determined and a constant time offset applied to shift the mean of each channel to the same arbitrary time. This means that, when analysing data, a single set of "prompt" and "random" time windows can be applied to the entire Tagging Spectrometer rather than being selected channel-by-channel. A single alignment can be used for a whole run period, as can be seen in Figure 5.4, where the time spectrum is plotted against Tagger channel for the entire July run data set. Although using the same alignment for an entire beam period gives a wider prompt peak than that observed immediately after the initial alignment, one can still see the clear prompt region - around 70 ns - which can be used for each channel and is sufficient for our purposes. Tagger time alignments were performed by R. Codling from the University of Glasgow [100].

5.2.3 Energy Calibration

The energy of the tagged photons is completely derived from the measured final electron energy E_{e^-} and the initial electron beam energy E_0 as given in Equation 4.1. The energy of the degraded electron (E_{e^-}) is derived from the position at which it impinges on the Tagger's focal plane. To calibrate the correspondence between this position and the electron energy, ray tracing in an equivalent uniform field is performed using a computer program called TagCal, originally written by I. Anthony [79, 101].

TagCal applies an equivalent uniform field constructed on the basis of a field map measured along the main beam trajectory. This uniform field is scaled according to the magnetic field measured by the NMR probe which is permanently positioned inside the Tagger magnet. Using a map of the positions and angles of the individual scintillators in the focal plane detector array (which are completely determined by the structure of the focal plane detector frame), TagCal follows a χ-squared minimisation routine to find the degraded electron energy which passes directly through the centre of each Tagger scintillator.

This calibration is redone for each individual beam time. The NMR measurements are monitored throughout each beam time to ensure that there is no drift in the Tagger calibration.

5.2.4 Tagging Efficiency

The tagging efficiency measurements as described in Section 4.2.3 were performed daily throughout the experiment. In order to account for activation, which causes a build up of background radiation, a “beam off” measurement was made of the background counts in the Tagger Scalers before and after each tagging efficiency measurement was made. It was soon realised that the initial activity in these background measurements fell away very swiftly and so the activity measured after the tagging efficiency measurement was performed was scaled according to the length of the tagging efficiency run to give the background to the measurement. Thus Equation 4.2 could more accurately be rendered as Equation 5.1 where N_{bg}^{n} is the number of background counts in scaler n:

$$\varepsilon_{tagg}^{n} = \frac{N_{\gamma}^{n}}{N_{e}^{n} - N_{bg}^{n}}. \tag{5.1}$$

This tagging efficiency was calculated for each channel and for each tagging efficiency measurement a text file was created containing a lookup table of the tagging efficiency values by A. Nikolaev of Mainz [99]. To use the tagging efficiency values in this data analysis, we took the average of these measurements for each beam time, channel-by-channel.

This method could be improved upon by using the tagging efficiency lookup tables to normalise the data on an event-by-event basis using the tagging efficiency measurements made either side of the event in question. However, tagging efficiency remained stable throughout the experiment and was similar for both parallel and perpendicular photon beam polarisations as can be seen in Figure 5.5. Hence we felt that the average tagging efficiency was adequate - the effect of the simplification is further discussed in Chapter 7.

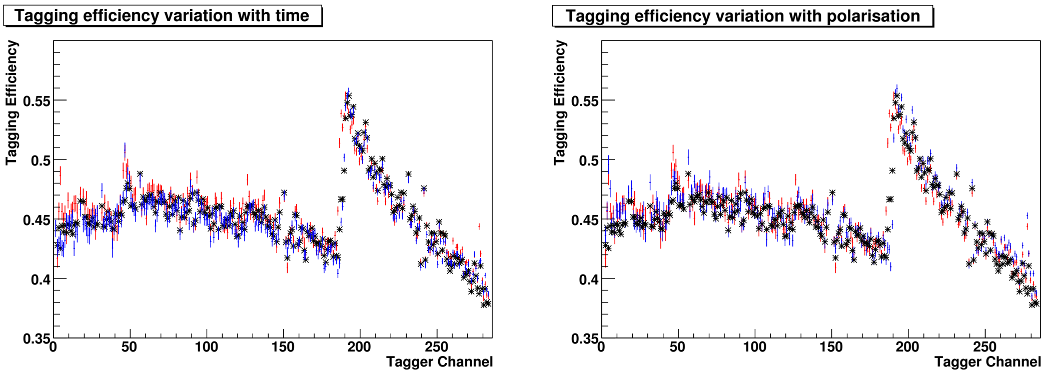

Figure 5.5: The tagging efficiency as a function of Tagger channel, illustrating the variation with time and polarisation orientation. The sudden change in tagging efficiency near channel 200 is due to the Diamond radiator. As coherent bremsstrahlung is more strongly forward-peaked than normal bremsstrahlung, a large increase in tagging efficiency is observed at the coherent edge (see Appendix B). Left panel: Tagging efficiency variation throughout the run period, red crosses show tagging efficiency for $\parallel$ run 2852 (early in the experimental run period), blue crosses for $\parallel$ run 3398 (late in the run period) and black crosses show the average tagging efficiency values used in this work. Right panel: red crosses show tagging efficiency for $\parallel$ run 2852, blue crosses for $\perp$ run 2853 and black crosses show the average tagging efficiency values used in this work.

5.3 CB System Calibrations

5.3.1 NaI Crystals

The initial hardware gain alignment of the CB was performed by illuminating individual crystals with an ^{241}Am/^{9}Be source and adjusting the individual potentiometers (which control the HV supply) of the PMT bases to place the 4.438 MeV γ-decay peak in the same region of the ADC spectra. This provided a rough alignment to allow the experimental hardware thresholds (which are in mV) to be set at a similar level for all crystals. This alignment is performed at far lower energies than those we use in our experiment. Thus, although sufficient for threshold alignment, a further, more refined, calibration was required for reaction-product particles which have much higher energy.

During experimental running, an individual MeV per channel calibration was formed for each detector element using the kinematically overdetermined $\gamma p \rightarrow p\pi^0$ reaction. The measured energy of the π^0 decay photons was compared to the energy calculated on the basis of the incoming photon beam energy and the π^0 emission angle (θ_{π^0}). In a typical event, the energy deposited by a photon is spread between several neighbouring crystals which form a hit "cluster". Only clusters in which 70 % or more of the photon energy was deposited in the central crystal were used in the calibration. The calibration constant (or conversion gain) of the central crystal was then scaled according to the results of the analysis. As adjusting the calibration constant of one crystal will change the results for the surrounding ones, this calibration procedure had to be iterated until the

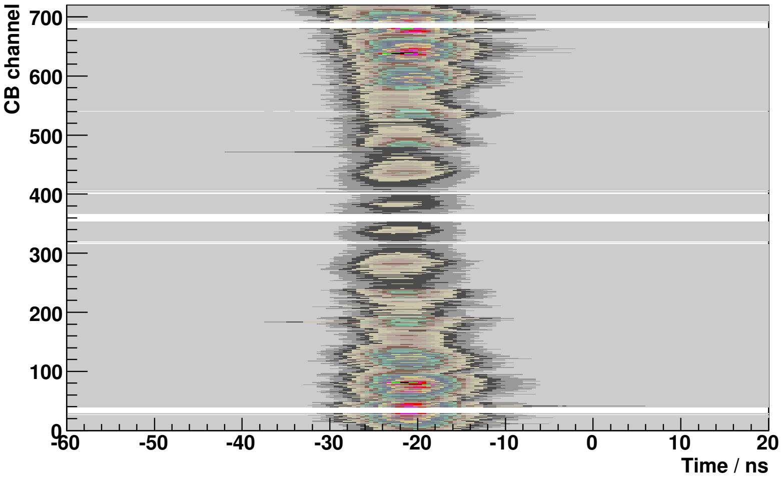

Figure 5.6: Crystal Ball element time alignment results for the entire July data set.

calibration constants converged. In this case four iterations were found to be necessary. The calibration of the CB was performed by J. Brudvik from UCLA and M. Unverzagt of Mainz [102, 103].

As explained in Section 4.6.1, the timing of each individual crystal signal was also recorded by a CATCH TDC. Due to the nature of the CATCH TDCs, there was a fixed channel to time conversion of ∼117 ps / channel. However, to use the Crystal Ball timing information, it was desirable that the CB time signals were aligned. To achieve this D. Krambrich of Mainz [104] looked at the CB time spectra, fitted a Gaussian distribution to them channel-by-channel to find the mean value and then applied a constant offset to each of them individually to shift their timing peak to a common arbitrary point in the timing spectra.

For more accurate timing, once all of the individual elements of a single detector are time-aligned with each other, it is sometimes beneficial to further align them on the basis of a timing sum, usually in combination with the Photon Tagger. The electronic trigger which starts / stops detector timing has a finite timing width which gets folded in with the detector times. As the Tagger timing is stopped by the trigger and the CB timing is started by it, by summing the detector times we remove this trigger width and are aligning only the individual detector elements, with an overall resolution determined by a combination of both detectors. This was done with the CB, with the aligned Tagger plus CB element time plotted for each CB element and then aligned by D. Krambrich in the same way as the single detector times [104], see Figure 5.6 .

5.3.2 Particle Identification Detector Calibrations

PID calibration procedures were designed and tested by the author and then carried out by R. Codling of Glasgow [100].

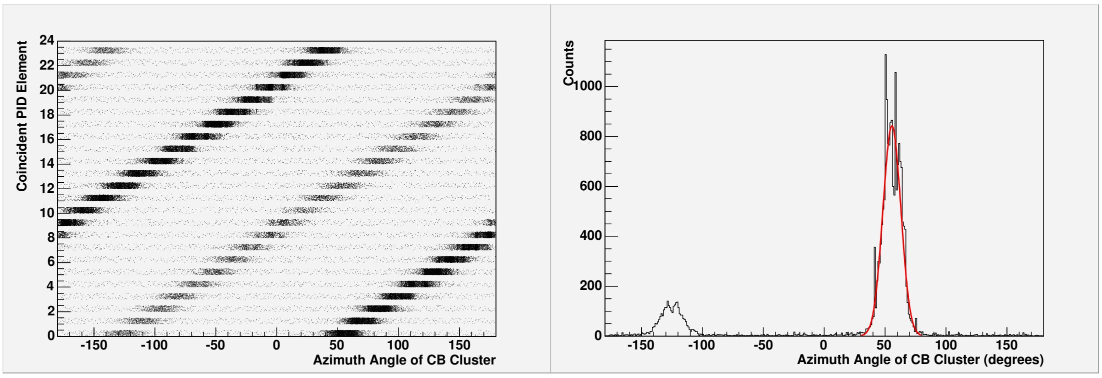

Figure 5.7: Azimuthal position calibration of Particle Identification Detector. Left panel: Azimuthal angle of CB clusters in coincidence with PID elements for events with one hit in each detector. Right panel: Projection of left panel for PID element 0. The strong peak results from charged particles (such as electrons) passing from the target, through the PID and into the CB creating a signal in both detectors. We use this to identify the ϕ position of each PID element. The weaker peak $\sim 180°$ from the stronger one results from reactions emitting particles 180° apart in ϕ, such as $p(\gamma,\pi^+n)$, where the neutral particle makes a detectable signal in the CB, but the charged particle stops in the PID.

5.3.2.1 Position Calibration

The PID position calibration determined the azimuthal angle (ϕ) of each element, relative to the Crystal Ball. This is necessary in order to link the energy deposits in the PID with the appropriate clusters in the Crystal Ball NaI crystals and thereby form the $\Delta E/E$ plots that provide the basis for charged particle identification in the Crystal Ball system.

These ϕ positions can be clearly seen by looking at a plot of the ϕ angles of clusters detected in the Crystal Ball vs the identity of any PID element that fires in coincidence (see Figure 5.7 (left)). We applied cuts to data to display only events with a single hit in the PID and a single cluster in the Ball. After doing this, it was possible to discern by eye the darker regions of the histogram, and use this as a first approximation of PID element position.

To improve the accuracy of this procedure and make the results more reproducible, we wrote a ROOT macro which takes projections of this 2D histogram for each PID element and fits a Gaussian distribution around the highest point in the resulting 1D spectra (see Figure 5.7 (right)). The macro then fills a histogram with the mean of each of the twenty-four fits and fits a straight line to it, constraining the gradient to represent a clearly defined 15 degree change between each neighbouring pair of PID elements. From the results of this straight line fit, the mean ϕ position of each individual element is calculated.

This procedure was carried out for the beginning, middle and end of each experimental run period in order to ensure that the detector positions are accurately known at all times.

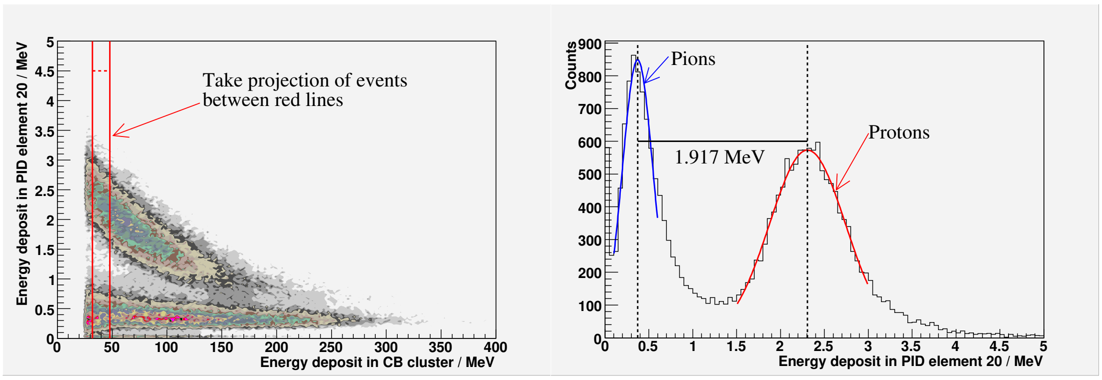

(a) DE/E Plot for a single PID element.

(b) DE/E plot projection with fit.

Figure 5.8: Energy calibration of Particle Identification Detector.

5.3.2.2 Energy Calibration

During the design and construction of the PID, the energy resolution was anticipated to be modest as the long, thin, low density, plastic scintillators do not absorb very much energy and therefore produce relatively few scintillation photons. However it was more than adequate to enable separation of minimum ionising particles, charged pions, protons and occasional deuterons. In order to facilitate this identification and make it easier to deal with the small percentage of cases where a particle traverses the join between two neighbouring scintillators (and we have to sum the energy deposits), we aligned the output of individual PID elements, guided by the Monte Carlo model of the CB which gives energy loss distributions for various particles.

If we take the ΔE/E plots and look at a projection of events which deposit between 32 MeV and 48 MeV in the Crystal Ball (E), we can see two separate ΔE peaks: a lower energy peak (around 0.4 MeV) due to charged pions and a second, higher energy, peak appearing around 2.3 MeV due to protons (see Figure 5.8). We took projections such as this from each PID element ΔE/E plot and one from the simulation results. We fitted a Gaussian distribution to each of the energy peaks in the simulated projection and found that there was a difference of 1.917 MeV in energy between the means of the two distributions. We then performed the same fitting procedure on each of the twenty-four element projections and calculated a new energy calibration MeV/ADC channel factor for each element using Equation 5.2,

$$c' = c\frac{m_p^{sim.} - m_\pi^{sim.}}{m_p^{meas.} - m_\pi^{meas.}}, \tag{5.2}$$

where c' is the new MeV/channel factor, c the old one, $m_p^{sim.}$ and $m_\pi^{sim.}$ are the mean of the proton and pion Gaussian fits to the simulated data, respectively, and $m_p^{meas.}$ and $m_\pi^{meas.}$ are the measured proton and pion distribution means. This method was swift, successful and reproducible and so was adopted as the standard calibration procedure.

This method has been applied to PID data from all beam times in order to ensure accurate particle identification. A selection of 10 or so data files (around four hours of data) is analysed for the beginning, middle and end of each data run. It has been found that, for the most part, the calibration remains stable to the order of ~1 % for a given continuous run period.

However, this procedure is limited by the requirement that there be proper separation between protons and pions. This has not remained the case throughout the lifetime of the detector. There were problems with the liquid Hydrogen target and it was dismounted between the first and second beam times for the experiment of interest. As space is so limited inside the Crystal Ball, the target dismount procedure was difficult and resulted in two of the twenty-four PID elements sustaining damage to the light guide-PMT join which has severely affected their light output. As a result, these two elements no longer produce sufficient light to discern between pions and protons and thus this calibration method does not apply to them. The present solution is simply to align the upper edge of the smeared triangular shape on the ΔE/E plot with the upper edge of the aligned and clear ΔE/E plots. This is a highly inaccurate and unreliable method and thus the selection of pions and protons (as described in Section 5.3.3) from any information involving the damaged elements is not recommended. However the remaining detector elements continued to perform well until the decommissioning of the first phase of CB@MAMI experiments.

5.3.2.3 Time Calibration

Timing calibration of the PID is simplified by the use of CATCH TDCs for which more complete operational detail is given in Section 4.6.1. These TDCs have a fixed channel to time conversion. As all of the PID signals pass through an identical electronic setup and the pulses from plastic scintillators are very sharp (having an intrinsic timing resolution of ~0.5 ns) they are very easy to align in software and a "PID trigger" (an OR of all twenty-four PID elements) has a FWHM of only ~3 ns.

As the conversion factor is standard, all that has to be achieved to produce a time-aligned detector signal is to obtain the current position of the timing peak of each element (by fitting a Gaussian distribution to the time spectrum) and shift it using software offsets to the desired location in time.

As described above, it is sometimes beneficial to further align detector element times on the basis of a timing sum in combination with the Photon Tagger. The Tagger timing is stopped by the trigger and the PID timing is started by the trigger, so we summed the detector times to remove the finite trigger timing width and aligned each of the elements based on this timing sum. However, for the PID, we found that this summed time alignment made very little difference to the quality of the final result and doubled the length of time required for each calibration. Thus we decided to adopt only the internal alignment as the standard time calibration method.

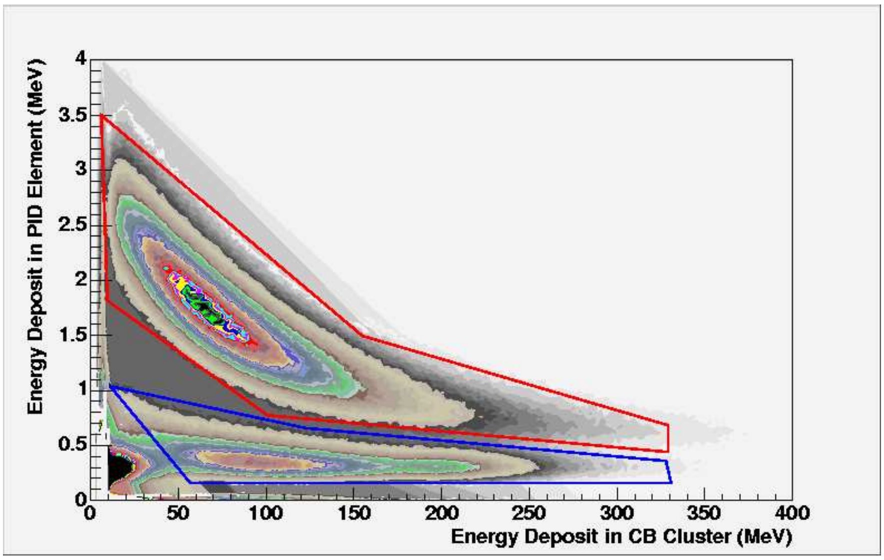

Figure 5.9: ΔE/E Plot for all PID elements showing the pion cut (Blue Line) and the proton cut (Red Line) for all PID scintillators and all CB cluster energy deposits >5 MeV, using the 883.25 MeV beam and liquid Hydrogen target.

5.3.3 Particle Identification

From the plot shown in Figure 5.9 it can be seen that there is a clear separation of protons and pions in the PID. To convert this into code and use it to identify particles on an event-by-event basis we currently apply the ROOT *TMath* library *IsInside()* function [97] to a pair of polygons illustrated in Figure 5.9. If the E,ΔE combination is inside the proton polygon, we set the four-vector output by the Crystal Ball apparatus class to have a kinetic energy defined by the energy deposit in the CB NaI crystals, an angle as dictated by the MWPCs (or the CB in the case where there is no corresponding track information from the wire chambers) and a mass of 938 MeV. If the E,ΔE combination lies inside the pion cut, we set the four-vector output similarly, but this time applying a mass of 139 MeV to the particle.

It is possible to define a single pair of cuts that are used for all PID elements, but for analysing real data, we define a proton and pion cut for each individual PID element on the basis of each E,ΔE plot. This allows us to take advantage of the narrow ridges in the detector elements with better resolution, without throwing away data from the elements with poorer resolution unnecessarily. In the case of simulated data, where the performance of every PID element is identical, we define a single pair of cuts that applies equally well to all PID elements.

5.3.4 Multi-Wire Proportional Chambers

The MWPC handling code was adjusted from its original Fortran format to C by V. Lisin of INR, Moscow and then adapted to AcquRoot compatible C++ by J. Annand. S. Schuman [105] subsequently performed all alignment and efficiency measurements in collaboration with P. Pedroni of INFN, Pavia.

Intrinsic angular resolutions were determined by analysing cosmic ray data, where the passage of muons through the MWPCs create four intersection points (a signal caused by the track meeting a single wire chamber) and two tracks (pairs of intersection points which can be linked to define a line or track through the detectors, one in each MWPC). These two tracks should be collinear as the cosmic muons travel in a straight line. The difference in angle between these two tracks gives a ϕ resolution of 1.33° and a θ resolution of 1.88°. The cosmic muons were also used to study the efficiency of the chambers, by looking at the number of events having two interaction points in both chambers divided by the number of events having two interaction points in one chamber. This gave a track reconstruction efficiency of 81.2% for minimum ionising particles.

Proton efficiencies were accessed by using the kinematically overdetermined reaction $\gamma p \rightarrow p\pi^0$ as a source of tagged protons. Events with three clusters, one of which was identified as a proton by the $\Delta E/E$ plots, and two of which were neutral, were analysed. Those which had a difference in ϕ of $180° \pm 15°$ between the reconstructed pion and the identified proton, and where the invariant mass of the two neutral clusters was determined to be 135 ± 20 MeV, were used to asses the efficiency of the MWPC proton track reconstruction. This yielded a track reconstruction efficiency of 89.7% for protons based on the July data.

Charged pion efficiencies were tested using the reaction $\gamma p \rightarrow n\pi^{\pm}$. Events were identified by looking for two clusters in the CB, one with a corresponding PID hit indicating that it was a $\pi^{\pm}$. Only events where the charged cluster involved only one crystal and the difference in ϕ between the two detected clusters was $180° \pm 15°$ were accepted. An additional constraint, that the neutron θ be less than 60°, was applied to limit background. This gave an MWPC efficiency for pion track reconstruction of 79.3%. This difference in proton / pion efficiency is due to the higher proton ionisation density which produces a more strongly ionised trail in the MWPC gas.

5.4 TAPS Calibrations

5.4.1 Barium Fluoride Energy Calibration

The TAPS Barium Fluoride elements were calibrated in two stages. The crystal pedestal (zero energy) channels were determined by observing the strong peak in the lowest energy region of the ADC spectra. The channel with the highest value before the first decrease was determined to be the pedestal value. This narrow peak was due to the TAPS pedestal pulser which forced a readout of all the TAPS ADCs once per second, to obtain this zero energy deposit pedestal value.

The individual crystal MeV/channel factors were aligned by studying the energy distribution formed by the passage of cosmic muons through the crystals using cosmic data that was taken both before and after each experimental run. The channel-space to MeV conversion factors were determined element-by-element by fitting a Gaussian plus exponential distribution to the higher energy (above pedestal) region of the ADC spectra as shown in Figure 5.10. The mean of the Gaussian distribution gave the channel where the 37.7 MeV muon peak

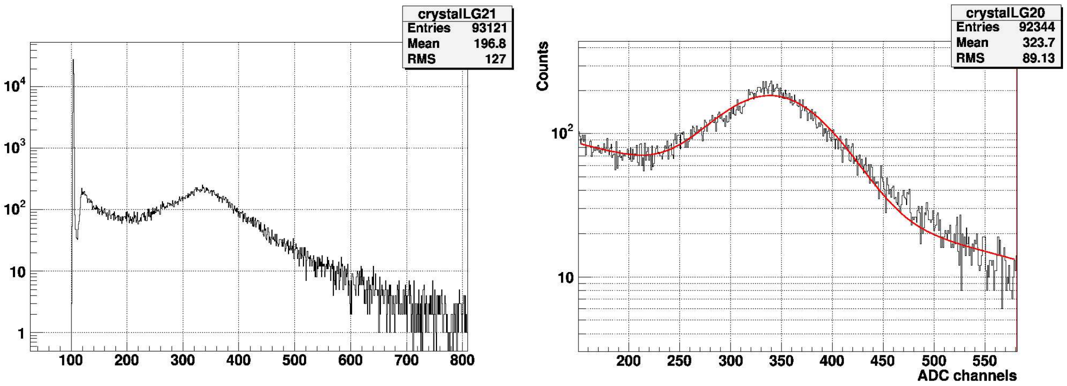

Figure 5.10: The TAPS BaF_2 energy calibration. Left panel: TAPS energy spectrum showing pedestal peak and cosmic muon energy deposit. Right panel: TAPS energy spectrum showing exponential + Gaussian distribution fit used to obtain the cosmic muon peak position in channel space. Extracted from [21].

lay, which (in combination with the zero-energy channel) completely determines the MeV/channel conversion. This part of the calibration was performed by B. Boillat from Basel for all of the TAPS ADCs [21].

As the crystal response to photons differs somewhat from their response to cosmic muons, the cosmic calibration aligns the crystal outputs, but does not completely determine the MeV / channel conversion for photons. After the crystals were aligned we identified the $\gamma p \rightarrow p\pi^0$ reaction and plotted the π^0 invariant mass for the case with one π^0 decay photon in TAPS and one in the Crystal Ball (after the CB alignment and calibration). We then adjusted the π^0 invariant mass by simply multiplying the individual BaF_2 detected energies by a factor close to 1 until the measured π^0 invariant mass agreed with the PDG value. This factor was determined to be 1.10 for the July data, 1.11 for September and 1.14 for the January data.

5.4.2 Barium Fluoride Time Calibration

The time difference between each BaF_2 crystal and a single Photon Tagger channel was plotted for all hits in the BaF_2. Each of the 510 spectra was fitted with a Gaussian distribution to determine its mean, and an offset applied to put the timing peaks for each detector element at an arbitrary common time. This calibration was performed by F. Zehr of Basel [106].

5.4.3 TAPS Veto Calibrations

The TAPS veto elements are read out on a binary basis - hit or not - into a pattern unit. As there is no timing or energy information derived from the veto detectors, it was sufficient to simply adjust their high voltage supply so that the energy deposit of a minimum ionising particle is above threshold and the PMT “dark current” is below.

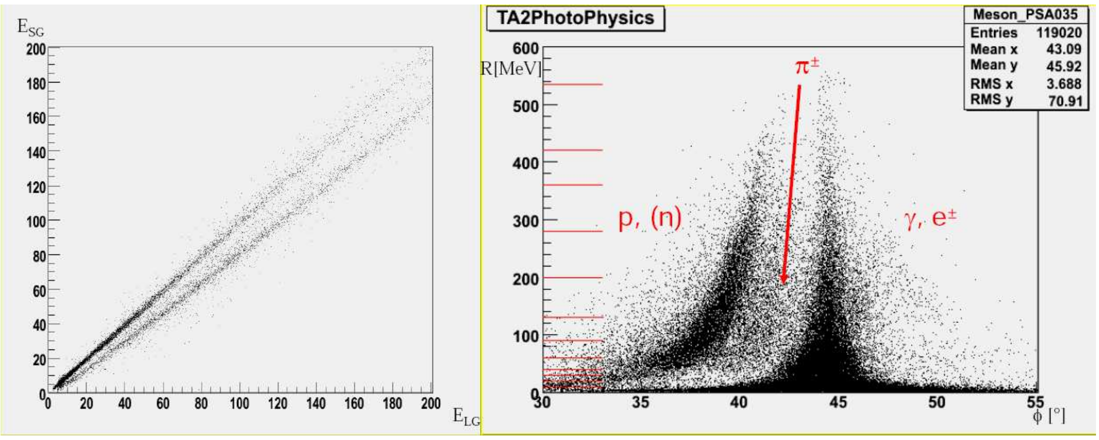

Figure 5.11: Pulse shape analysis of BaF_2 crystal output. Left panel: the energy deposit in the short gate ADC is plotted against that in the long gate. Right panel: the information is converted to polar coordinates then projected in the slices indicated by the red lines on the y-axis to allow selection. Extracted from [22].

5.4.4 TAPS Particle Identification

The particle identification in TAPS is achieved by combining pulse shape analysis from the BaF_2 with the signals from the veto detectors. The veto detectors simply indicate whether the corresponding particle was charged (e.g. differentiating between protons and neutrons). The pulse-shape analysis is possible as each BaF_2 signal is recorded by more than one ADC and these ADCs have two different integration times (gate widths): - the short gate for 30 ns and the long gate for 2 μs. Once the energy deposits in both of these gates had been calibrated, S. Lugert and R. Gregor of Giessen calibrated the pulse shape response of the BaF_2 scintillator to differentiate between photons and protons [107, 108].

The pulse shape response can be seen in the left panel of Figure 5.11. E_{SG} (the energy measured by the short gate ADC) and E_{LG} (the energy registered in the long gate ADC) were then transformed using the following equations:-

$$R = \sqrt{E_{SG}^2 + E_{LG}^2} \tag{5.3}$$

$$\phi = \arctan\left(\frac{E_{SG}}{E_{LG}}\right)\frac{180^\circ}{\pi} \tag{5.4}$$

to produce the plot shown on the right hand side of Figure 5.11. This plot is then sliced up according to the red lines shown on the y axis to produce a series of 1d plots as illustrated in Figure 5.12. These plots are then fitted with a Gaussian distribution to find the mean and width of the photon distribution. A cut is then set at the distance of 3σ from the mean of the distribution as illustrated. Anything creating a signal which lies to the left of this cut is deemed to be a proton (or neutron if there is no corresponding veto hit), anything to the right of this is deemed a photon (or electron - again depending on whether there is a corresponding veto hit).

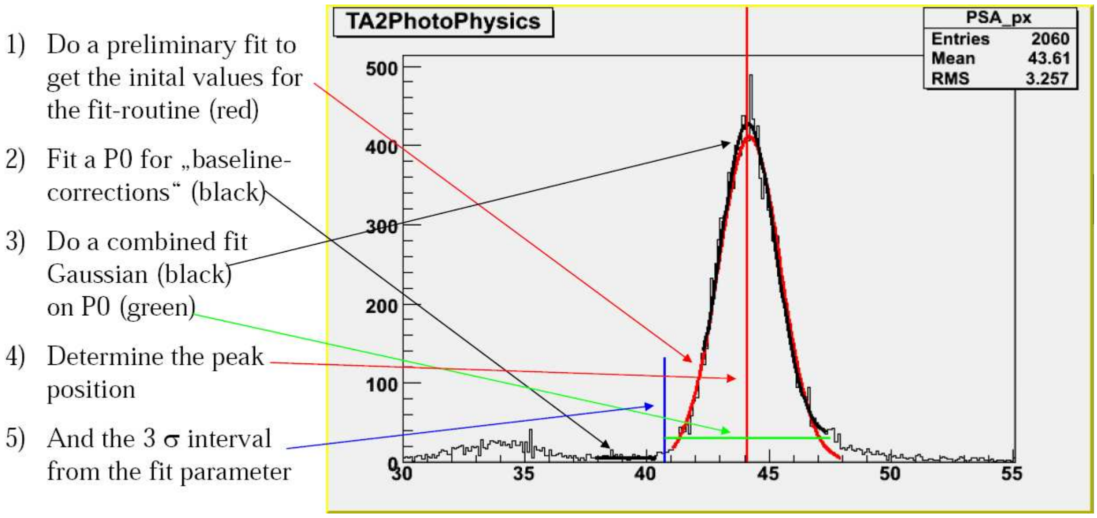

1) Do a preliminary fit to get the inital values for the fit-routine (red)
2) Fit a P0 for „baseline-corrections“ (black)
3) Do a combined fit Gaussian (black) on P0 (green)
4) Determine the peak position
5) And the 3 σ interval from the fit parameter

Figure 5.12: Explanation of the fitting procedure applied to the BaF$_2$ pulses to separate the proton and photon peaks. The large peak results from photon energy deposits, the smaller peak on the left results from protons. Extracted from [22].

5.5 Calorimeter Clustering Algorithm

As mentioned in both the Crystal Ball and TAPS calibration sections, a single particle does not in general deposit energy in a single detector crystal. Instead, a single particle creates a shower that spreads the energy deposit over several neighbouring crystals. Thus a method of linking together detector element energy deposits which result from the same shower (and hence the same particle) is required.

To do this, the detector setup files for both the CB NaI crystals and the TAPS BaF$_2$ crystals contain a list of the “nearest neighbours”, that is a list for each of the detector elements which details the twelve (six) surrounding crystals for the CB (TAPS) detector element. When an AcquRoot detector class processes the array of detector element energy deposits, it makes a temporary copy. It then scans through the array of energy deposits to find the maximum energy deposit. The crystal in which that energy deposit occurs is assumed to be the central crystal in a cluster. The remaining energy deposits in the array are then scanned to find if any of them occurred in a neighbouring crystal to the cluster centre. All energy deposits in neighbouring crystals are added to the central crystal energy to form the cluster energy, and the cluster angle is determined by an $\sqrt{E}$-weighted average of the position vectors of all the contributing crystals. Once the cluster is defined, all of the energy deposits involved in that cluster are deleted from the copy of the energy deposit array, a search begins for the next maximum energy deposit in the array, and a new cluster is processed. This procedure continues until the pre-set maximum number of clusters is reached (determined from the setup text files), or until there are no energy deposits large enough to meet the software cluster centre energy threshold (again read in from the setup text files).

It was found that this process quite often led to false clusters being found centred on the next nearest neighbours of real ones. To solve this problem and

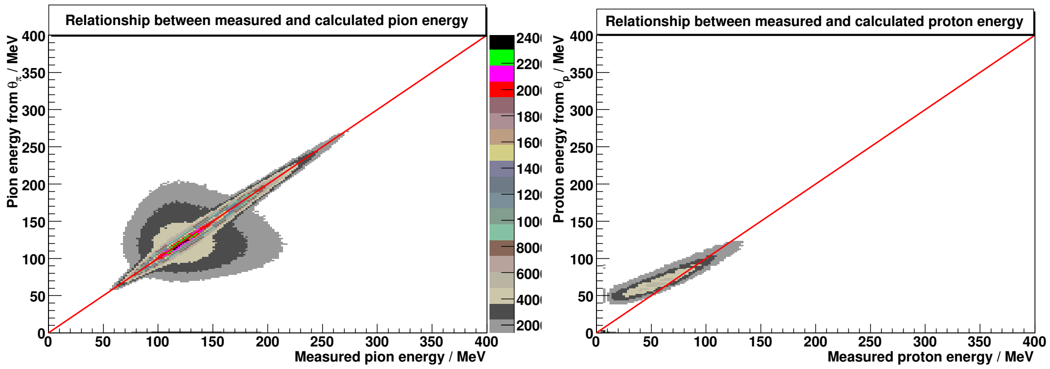

Figure 5.13: The result of the energy calibration for photons and protons. Left panel: π^0 energy calculated from θ_p and incoming beam energy plotted against measured π^0 energy from NaI pulse height (all π^0 variables are obtained from reconstruction of the π^0 from its two decay photons). Right panel: proton energy calculated from θ_p and incoming beam energy plotted against measured proton energy.

"mop up" this missed energy, the cluster algorithm was extended to search through the next-neighbours of next-neighbours until it runs out of neighbouring energy deposits or exceeds a pre-determined (from the setup files) maximum distance from the central cluster crystal. This almost completely removes the false cluster formation, but does increase the possibility that two clusters near to each other may be artificially merged into one.

5.6 Proton Energy Correction

In Figure 5.13 we show the result of testing the calibrations by analysing the kinematically overdetermined $\gamma p \rightarrow p\pi^0$ reaction. We can calculate the expected values of the π^0 and proton kinetic energies using the incoming beam energy, known proton target mass and the polar angle of the final proton trajectory. Plotting the calculated values of these observables against those measured by pulse height reveals a problem. For the π^0 energy, which is entirely reconstructed from the decay photon energies, we find excellent agreement between measured and expected values. For the proton, we find that at low energies (less than ~80 MeV) the measured energy is markedly smaller than that which we calculate. At higher proton energies, we find that the measured proton energy is more than that which we calculate.

This phenomenon can be explained by two different effects. At low energies, the protons lose a large proportion of their energy while travelling through the air and other materials between the target cell and the detector system - thus the detectors record less than the calculated proton energy. At higher energies, the protons appear to deposit too much energy in the detectors as both the Crystal Ball and TAPS are calibrated using photons. Photons create a large electromagnetic shower, depositing energy throughout a large cluster of crystals, with additional energy losses between crystals. This "shower loss" is implicitly

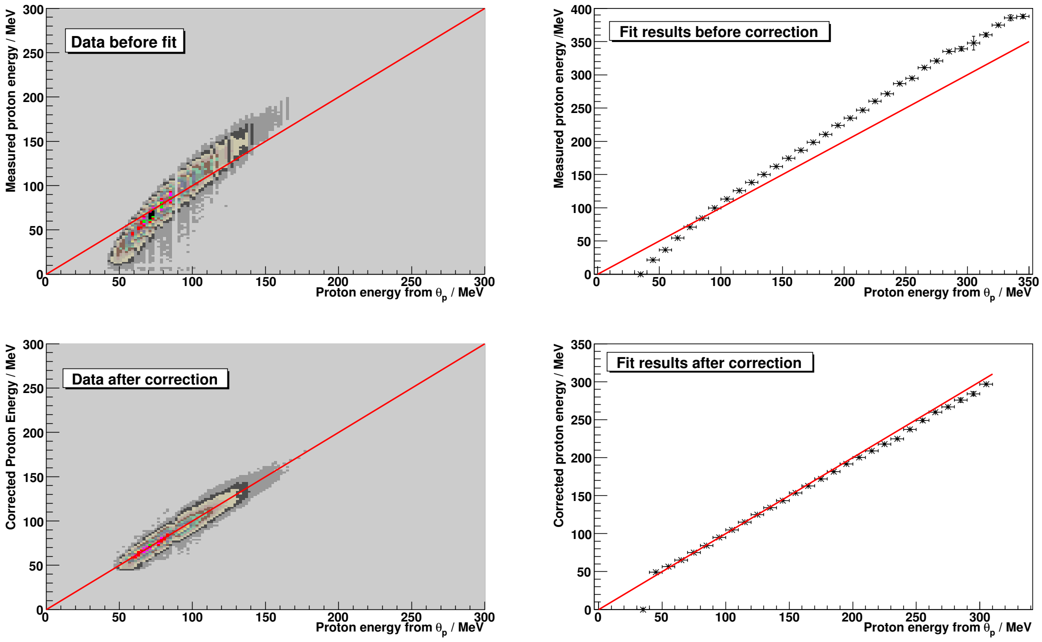

Figure 5.14: Proton energy correction for $30° < \theta_p < 32°$. Upper left panel: Plot showing measured proton energy vs that calculated from θ_p and E_γ. Upper right panel: Graph showing fit results for measured proton energy projections of the 2D plot vs proton energy calculated from θ_p and E_γ. Lower panels: As above panels, but after proton energy correction has been applied. It can be seen that the proton energy correction improves the proton energy determination significantly.

corrected when we apply the energy scaling factors to shift the π^0 invariant mass peak to the PDG value after the photon calibration of the detectors. As protons generally deposit energy in only one or two crystals, there is less “shower loss” and so the energy scaling factor over-corrects, making the “measured” energy too high.

It is possible to correct for both of these effects separately by simulating the proton energy losses and applying this correction to the real data to correct the low energy portion of the proton energy spectrum and then calibrating the proton response of the two calorimeters. However, if we assume that the proton calibration will be isomorphically related to the photon calibration (for a given point θ and ϕ combination), we can work out a way to map the results of the photon-calibration based energy measurement to the actual proton energy and correct for both effects simultaneously.

We assumed that all energy corrections were independent of the azimuthal angle (ϕ) as the detector system is azimuthally symmetric, but varied with polar angle (θ) (due to discrete components such as detector readout electronics which affect the energy losses), and proton energy. We made plots of measured against calculated proton energy for 0° to 160° in θ_p, in 2 degree-wide θ_p bins (see Figure 5.14, LHS). We then took projections of these plots in 10 MeV-wide calculated energy slices. These projections were each fitted with a Gaussian distribution to determine the measured energy for each calculated energy bin (see Figure 5.15).

This was sufficient to give a good representation of the relationship between measured and calculated proton energy. The mean of each Gaussian distribution was recorded in a text file, with the mean value of each of the calculated energy bins and their correspondence to θ_p. Thus to determine the corrected proton energy where we know the measured energy, E_p, we first pick the correction values from the appropriate θ_p bin, then we search through the measured energy samples to find the two measured energy values, E_1 and E_2 closest to E_p such that $E_1 < E_p < E_2$. We then calculate the corrected $E_p^{corr.}$ using the two calculated energy values E_1^c and E_2^c (corresponding to measured energy samples E_1 and E_2 respectively) as shown in Equation 5.5.

$$E_p^{corr.} = E_1^c + (E_2^c - E_1^c)\frac{(E_p - E_1)}{(E_2 - E_1)}. \tag{5.5}$$

This worked well for 2° $< \theta_p <$ 10° and 24° $< \theta_p <$ 66°, but between 10° and 24° the MWPC and PID electronics caused azimuthally asymmetric energy losses that resulted in a large variation in measured proton energy within the same calculated proton energy and θ_p bin (see Figure 5.16). At $\theta_p >$ 66°, we found that there were insufficient statistics to form a proton energy correction, and as θ_p increased from 24° to 66° we found the energy range over which we could formulate an energy correction decreased, due to diminishing statistics.

This energy correction was also determined using two-body breakup data from the liquid Deuterium target that was taken in experimental runs interspersed with the μ_{Δ^+} experiment. It should have allowed us to access a larger range of proton energies and polar angles due to the different reaction kinematics. However, the overall statistics from these runs were poorer, making 20 MeV-wide calculated energy slices necessary. As the θ_p and E_p distributions for our reaction bear more resemblance to those of $\gamma p \rightarrow p\pi^0$ than $\gamma d \rightarrow pn$, we selected the better E_p resolution in preference to extended E_p and θ_p range and we applied the $\gamma p \rightarrow p\pi^0$ correction in our final data analysis. That said, the correction factors from the liquid Deuterium data (where there was sufficient data to form the same E_p and θ_p bins) agreed very well with those we obtained from the liquid Hydrogen data.

5.7 Determination of the Degree of Linear Photon Polarisation

The bremsstrahlung spectrum from a crystalline radiator is composed of two parts:- an incoherent part (due to lattice vibrations - $\sigma_{incoh.}$) and a coherent part due to the diffractive effect of the crystal lattice - σ_{coh} (Equation 5.6):

$$\sigma = \sigma_{coh.} + \sigma_{incoh.}. \tag{5.6}$$

The degree of linear polarisation (P) at any point in the bremsstrahlung spectrum can be determined from the ratio of intensities described in Equation 5.7 where $I_{coh.}$ is the intensity resulting from $\sigma_{coh.}$ and $I_{incoh.}$ is the intensity resulting from

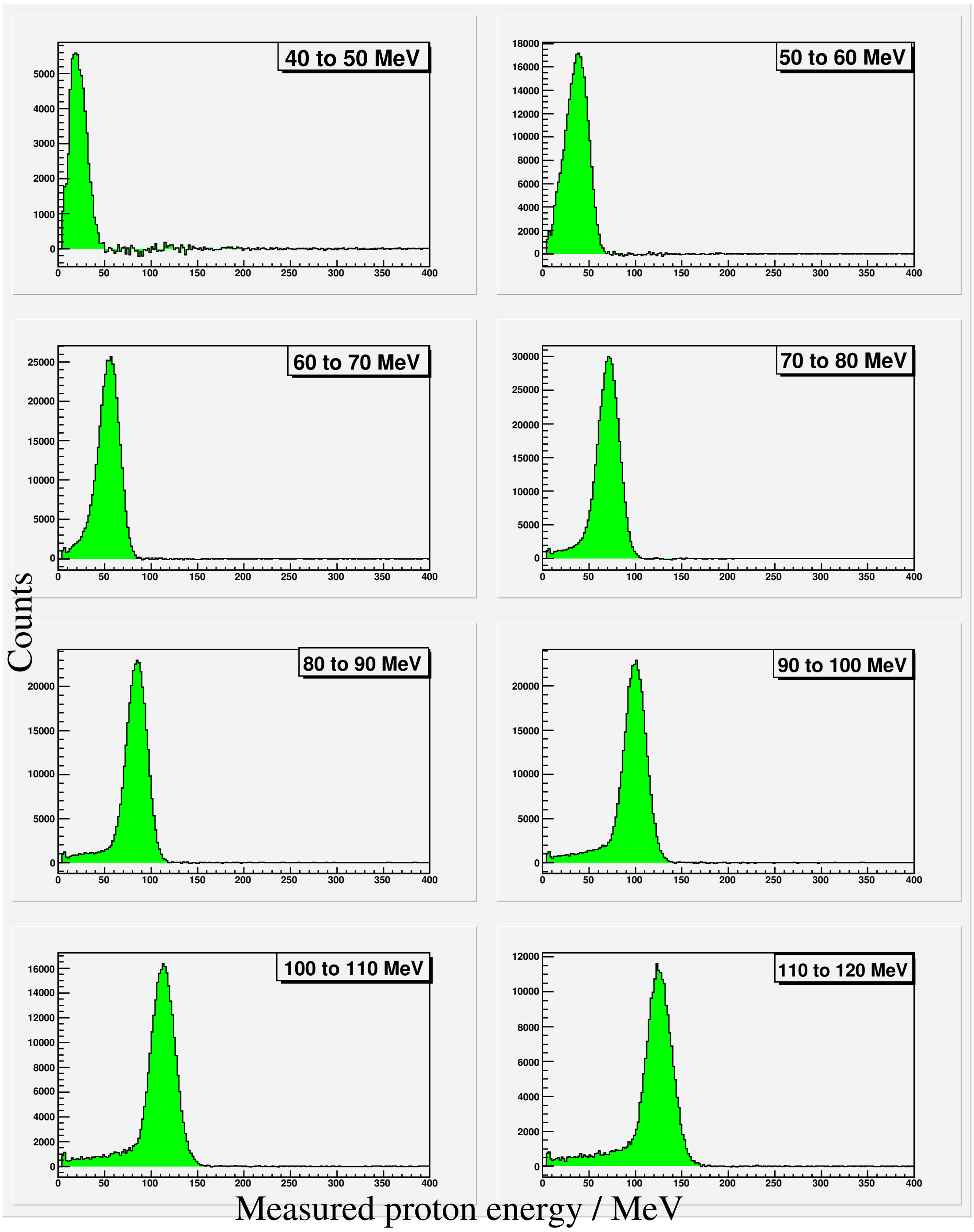

Figure 5.15: The first eight $E_p(E_\gamma\theta_p)$ slice projections for $30° < \theta_p < 32°$. The $E_p(E_\gamma\theta_p)$ range is shown in the upper right hand corner of each plot. Fitting Gaussian distributions to each plot produced a representative measured energy value for each bin, only failing at higher $E_p(E_\gamma\theta_p)$ due to low statistics.

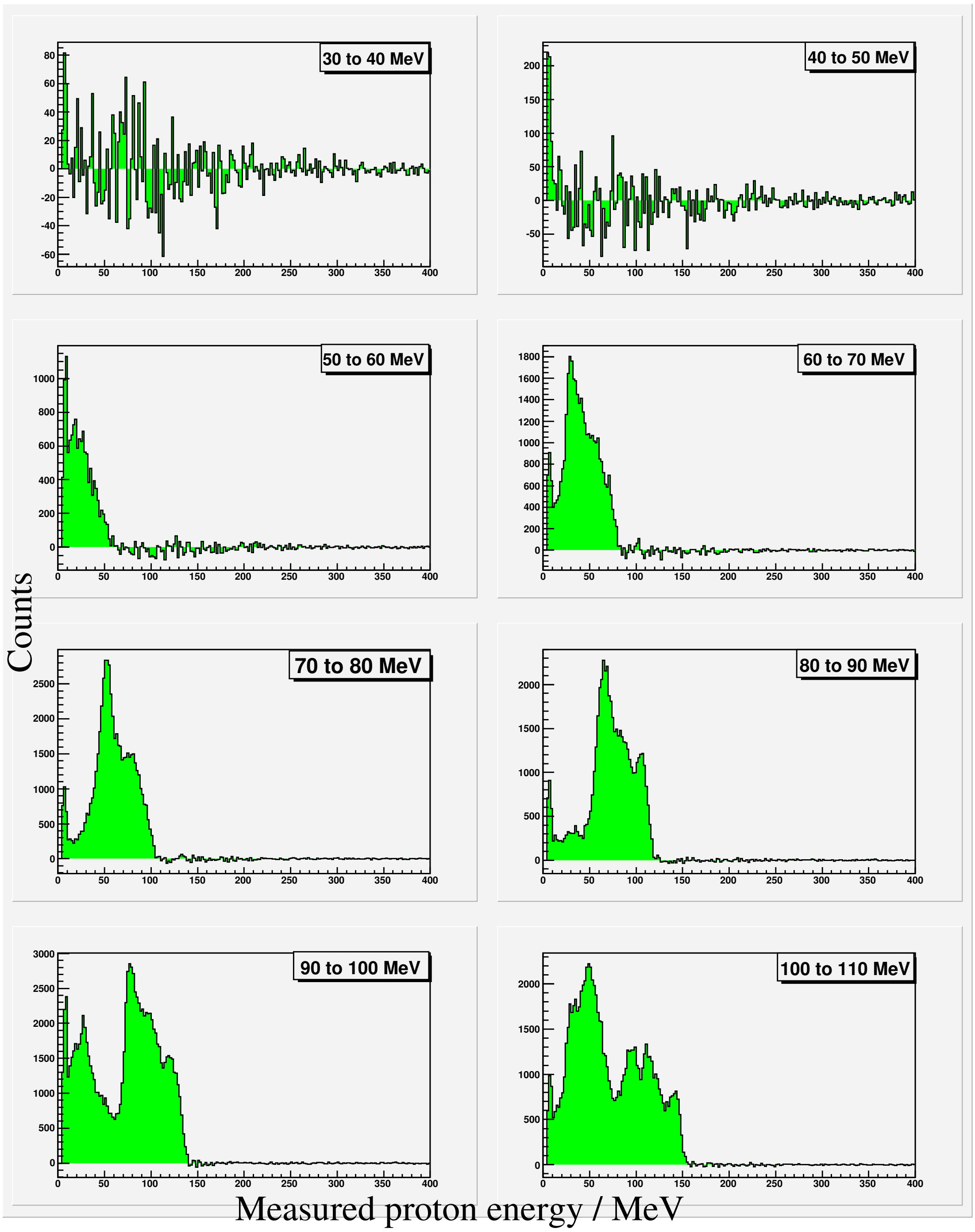

Figure 5.16: First eight $E_p(E_\gamma\theta_p)$ slice projections for $20^\circ < \theta_p < 22^\circ$. The $E_p(E_\gamma\theta_p)$ range is shown in the upper right hand corner of each plot. It was impossible to produce a representative measured energy value for each plot.

$\sigma_{incoh.}$:

$$P = \frac{I_{coh.}}{I_{incoh} + I_{coh.}}. \tag{5.7}$$

Thus we can calculate the degree of linear polarisation by separating out the coherent and incoherent parts of the bremsstrahlung spectrum. For a more detailed description of coherent bremsstrahlung production see Appendix B.

To calculate the degree of linear photon polarisation, we use the program *anb* which is discussed more fully in [84]. *Anb* calculates the degree of linear polarisation and the shape of the resulting enhanced Tagger spectrum[1] analytically on the basis of several inputs (seen in the sidebar of Figure 5.17), which relate to the electron beam parameters, photon beam collimation parameters and the atomic numbers of the radiators involved. We know from Equation 5.7 that if the *anb* calculation accurately reproduces the experimental enhanced Tagger spectrum, then it will accurately deduce the degree of linear polarisation as a function of photon energy [84]. As can be seen in the upper image in Figure 5.17, the calculated enhanced Tagger spectrum (blue line) matches the real data (black line) very well. The lower spectrum in Figure 5.17 shows the resulting degree of linear polarisation.

The *anb* calculation outputs several tables with the degree of linear polarisation as a function of tagged photon energy (in ~1 MeV-wide bins) for a series of different polarisation edges (see Appendix B). In the future, these will be used as lookup tables which the data analysis will use to extract the degree of linear polarisation for each photon using linear interpolation on the basis of the most recent edge position (which is redetermined every 1000 events) and the exact photon energy. At present, this full functionality is still under development.

To provide a degree of linear polarisation for this analysis, we took these polarisation tables, and combined them in such a way as to agree with the average edge position over each of the data runs, producing a histogram indicating the degree of linear polarisation in each of the 1 MeV-wide photon energy bins. We then normalised all of the final photon asymmetries by taking the spectrum of photon beam energies for each histogram, multiplying each photon beam energy channel by the appropriate degree of linear polarisation and then taking the average polarisation to be the integral of the polarisation-weighted histogram divided by the total number of incoming photons. We then used this to normalise the photon asymmetries as detailed in Appendix C.

5.8 Photon Asymmetry of $\gamma p \rightarrow p\pi^0$

When we planned and tested our setup for the initial data-taking run for this experiment, it was anticipated that the collaboration would be measuring both the photon asymmetry and the five-fold differential cross section of the $\gamma p \rightarrow \gamma' N\pi$ reactions in order to access μ_{Δ^+}. It was later postulated that the circularly

---

[1] An enhanced Tagger spectrum is simply a Photon Tagger scaler or TDC spectrum measured with a crystalline radiator divided by the same spectrum produced using an amorphous radiator, usually normalised to have a baseline of 100. This shows the coherent bremsstrahlung peaks very clearly.

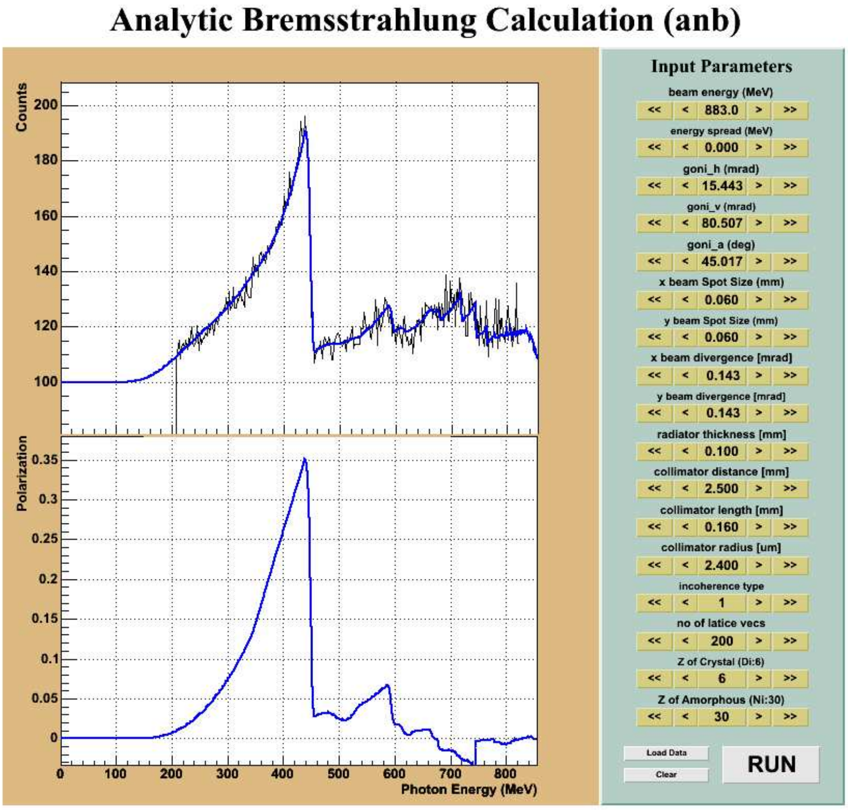
Analytic Bremsstrahlung Calculation (anb)
Counts
200
180
160
140
120
100
Polarization
0.35
0.3
0.25
0.2
0.15
0.1
0.05
0
0
100
200
300
400
500
600
700
800
Photon Energy (MeV)
<<
<
>
>>
Load Data
Clear
RUN

Input Parameters

beam energy (MeV) 883.0
energy spread (MeV) 0.000
goni_h (mrad) 15.443
goni_v (mrad) 80.507
goni_a (deg) 45.017
x beam Spot Size (mm) 0.060
y beam Spot Size (mm) 0.060
x beam divergence [mrad] 0.143
y beam divergence [mrad] 0.143
radiator thickness [mm] 0.100
collimator distance [mm] 2.500
collimator length [mm] 0.160
collimator radius [um] 2.400
incoherence type 1
no of latice vecs 200
Z of Crystal (Di:6) 6
Z of Amorphous (Ni:30) 30

Figure 5.17: Illustration of the *anb* calculation. Upper panel: enhanced Tagger spectrum showing agreement between data (black line) and calculation (blue line). Lower panel: polarisation output from *anb*. Right panel: input parameters for part of July data.

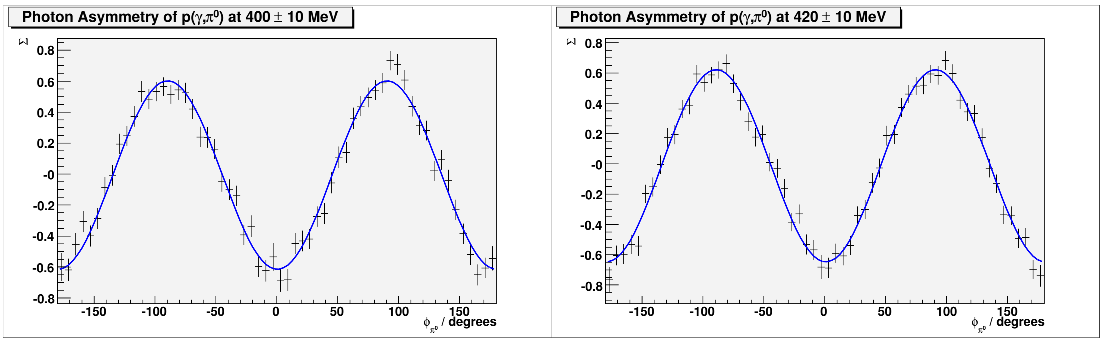

Figure 5.18: Measured photon asymmetry of $\gamma p \rightarrow p\pi^0$ for $\theta_p^{c.m.} = 90^\circ \pm 5^\circ$ and photon beam energies of 400 ± 10 MeV (left) and 420 ± 10 MeV (right).

polarised photon asymmetries of these channels would show greater sensitivity to the MDM than the other two observables and thus it was decided to run the experiment with both linearly and circularly polarised photons simultaneously. To achieve this we used a longitudinally polarised electron beam in combination with the diamond radiator. This meant that, at high photon energy (above the coherent peak) where the photons would normally be unpolarised, the photons were circularly polarised (due to the longitudinally polarised electron beam), allowing the measurement of circularly polarised photon beam asymmetries.

There was some concern that this combination of crystalline radiator and polarised electron beam would interact in such a way as to affect the degree of linear polarisation or change the orientation of the polarisation plane. In order to test for this effect, it was decided to analyse the well-studied reaction channel $\gamma p \rightarrow \pi^0 p$. This channel exhibits a fairly large photon asymmetry that was easily observable using our 4π detector setup. We planned to check that the magnitude of the $\cos(2\phi)$ structure that we observed did not alter with electron beam polarisation and that there was no systematic change in the phase or linear offset of the $\cos(2\phi)$ distribution. Also, as the photon asymmetry of this channel had been previously measured [24], we compared the magnitude of the asymmetry to the known values to check for any systematic error in the new detection system.

For the first tests, we looked at the photon asymmetry for $\gamma p \rightarrow p\pi^0$ in two incoming photon energy bins, 410 ± 10 MeV and 420 ± 10 MeV for $\theta_{\pi^0} = 90^\circ \pm 5^\circ$. We found these events by selecting only events with three detected clusters. We then selected the best π^0 candidates by reconstructing the π^0 and proton in each of the three possible combinations. We chose the combination which gave the difference in ϕ between the proton and pion momentum closest to 180 degrees (as it should be, due to conservation of momentum) and placed a cut on π^0 invariant mass of between 115 MeV and 155 MeV. Looking at the proton missing mass spectra, we saw a clear and clean peak around 938 MeV indicating that this method of analysis was sufficiently good to give us a very clean event sample. We also selected on a θ_{π^0} of between 85° and 95° in the centre of mass frame in order to match the conditions of the previously measured asymmetry with which we wanted to compare.

We plotted ϕ_{π^0} against incoming E_γ separately for eight categories of event,

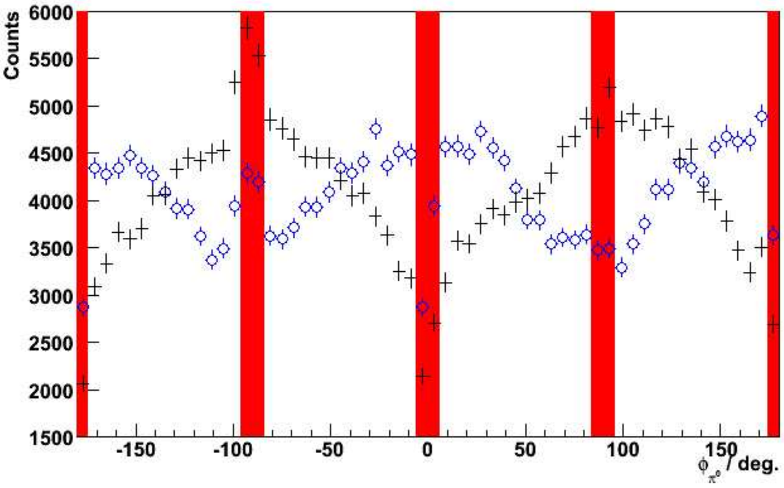

Figure 5.19: Random subtracted para (black crosses) and perp (blue circles) data showing why only counts outside of the shaded area were included in the normalisation of the $\gamma p \rightarrow p\pi^0$ data. The CB acceptance is very low at $\phi = \pm 180°$ and $\phi = 0°$, as can be seen by the dip in the data at these points. We artificially force the acceptance to zero (for the purposes of the normalisation) in the dotted regions to give the acceptance a 90°-symmetry in order that the acceptance changes affect both samples equally.

dividing them according to whether they were 'prompt' or 'random' and 'para' or 'perp' and whether the beam polarisation bit-pattern (which corresponded to the electron beam polarisation) was 1 or 2. We then took slices of these plots in 20 MeV E_γ bins and performed random subtractions as appropriate.

To calculate a photon asymmetry correctly, it is necessary to ensure that one has equivalently sized samples of para and perp events and that they have equal polarisation. However, in achieving this normalisation we have to take account of the fact that there is imperfect azimuthal symmetry in the Crystal Ball. As there are two metal plates between the hemispheres of the Ball (between 0°and ±180° in ϕ), at 0°and ±180° the acceptance for protons falls dramatically. As this effect has 180° symmetry, it affects one of the two polarisation orientations more dramatically than the other as can be seen in Figure 5.19. Thus it would not be accurate to simply normalise the histograms by dividing through by the integrated total number of counts in each. In order to handle this acceptance problem properly, we decided to give the normalisation acceptance a structure that was 90°-symmetric and so would affect both polarisations equally. This was achieved by ignoring the angular ranges of $0 \pm 6°$, $\pm 90 \pm 6°$ and $\pm 180 \pm 6°$ i.e. in order to calculate the normalisation factors, we simply integrated the histograms from $-174°$ to $-96°$, $-84°$ to $-6°$, $6°$ to $84°$ and $96°$ to $174°$. After dividing through by the normalisation factor, we calculated the asymmetry (Σ) as $\Sigma = \frac{N_{\pi^0 \parallel} - N_{\pi^0 \perp}}{N_{\pi^0 \parallel} + N_{\pi^0 \perp}}$. This results in a distribution proportional to $\cos(2\phi)$ with an amplitude that is the product of the degree of linear polarisation and the magnitude of the photon asymmetry (see Appendix C for more details on asymmetry calculations). As

E_γ	BeamPol	Offset	Amplitude (%)	Phase (deg)	Σ (This Work)
400	1	-0.000 ± 0.003	15.77 ± 0.47	-0.32 ± 0.84	0.584 ± 0.017
400	2	-0.003 ± 0.003	17.06 ± 0.47	-0.40 ± 0.77	0.632 ± 0.017
420	1	-0.036 ± 0.004	20.37 ± 0.51	-0.96 ± 0.73	0.647 ± 0.016
420	2	-0.005 ± 0.004	19.58 ± 0.51	-0.83 ± 0.71	0.622 ± 0.016

Table 5.1: The results of the initial beam polarisation check.

this was only a preliminary check and the software required to calculate linear polarisation on an event-by-event basis was not available at the time of these calculations, we used an average polarisation calculated from the *anb* analytic bremsstrahlung code which gave us an average degree of linear polarisation of 27 % at 400 MeV and 31.5 % at 420 MeV.

The results (shown in Table 5.1) are in reasonable agreement with the previous measurement by Leukel [24] in which the absolute photon asymmetry was calculated to be 0.592 ± 0.036 at 400 MeV and 0.591 ± 0.033 at 420 MeV. It can also be seen that the electron beam polarisation does not appear to have affected the degree of linear polarisation adversely as, although the amplitude results in the 400 MeV bin are not in perfect agreement, they differ in the opposite direction to those in the 420 MeV bin. Also, both the offset and the phase seem to be almost consistent with zero for all of the above cases.

However, these results should be accepted only with care. The normalisation due to the degree of linear photon polarisation is averaged over the full 20 MeV width of each energy bin and was not performed Tagger channel-by-channel as our $\gamma p \rightarrow p\pi^0\gamma'$ results were.

Although the previous results appeared promising, it was decided to extend the study further into regions of lower polarisation. The polarisation edge in the data under study was at 440 MeV, the degree of linear polarisation drops the further that one moves from this value. It was felt that the discrepancy at 400 MeV, should it be real, would worsen the lower the degree of photon polarisation became. So the study was extended to encompass E_γ from 300 MeV to 420 MeV. The degree of linear polarisation is almost identical for both beam polarisations and, as we are only concerned with the agreement of the results rather than their absolute value, the results (summarised in Table 5.2) are not normalised by the degree of linear polarisation. These results indicate very clearly that changing the electron beam polarisation has no systematic effect on the photon asymmetry of the $\gamma p \rightarrow p\pi^0$ reaction channel and thus on the measurement of photon asymmetries in general. Hence, the electron beam polarisation has been neglected in the analysis of the linearly polarised photon asymmetry of the $p(\gamma, \gamma'\pi^0 p)$ channel.

E_γ	BeamPol	Offset	Amplitude (%)	Phase (deg)
300	1	0.003 ± 0.004	3.05 ± 0.52	-8.42 ± 5.01
300	2	0.003 ± 0.004	2.95 ± 0.54	1.82 ± 5.03
320	1	0.002 ± 0.002	5.58 ± 0.35	1.06 ± 1.78
320	2	0.001 ± 0.002	5.88 ± 0.36	-0.02 ± 1.69
340	1	0.000 ± 0.003	8.40 ± 0.37	0.45 ± 1.24
340	2	0.000 ± 0.003	7.85 ± 0.37	-0.55 ± 1.33
360	1	-0.003 ± 0.002	10.65 ± 0.34	-1.52 ± 0.91
360	2	-0.003 ± 0.002	10.98 ± 0.34	-1.66 ± 0.88
380	1	-0.002 ± 0.003	14.18 ± 0.39	0.75 ± 0.78
380	2	-0.001 ± 0.003	13.66 ± 0.39	-0.52 ± 0.81
400	1	-0.000 ± 0.003	15.77 ± 0.47	-0.32 ± 0.84
400	2	-0.003 ± 0.003	17.06 ± 0.47	-0.40 ± 0.77
420	1	-0.036 ± 0.004	20.37 ± 0.51	-0.96 ± 0.73
420	2	-0.005 ± 0.004	19.58 ± 0.51	-0.83 ± 0.71

Table 5.2: The results of the extended beam polarisation check.

Chapter 6

Event Selection and Analysis

6.1 Simulation

In order to properly analyse the $\gamma p \to p\pi^0\gamma'$ data and assess such essential things as the background contributions to the measurement and the acceptance of the detector system, one needs a simulation of the experiment.

When the CB@MAMI series of experiments began, as there was a pre-existing GEANT 3 [72, 109, 110] Monte Carlo package (*cbsim*), and as the Crystal Ball was by far the most geometrically complex of our detector systems, it made sense to simply build on the existing GEANT 3 *cbsim* package. We added the MWPCs and the PID to the simulated detector geometry, and colleagues from UCLA added TAPS.

To run the simulation, one supplies the program with a file of pre-generated events containing particle trajectories, identities and energies and reaction vertex location. The simulation then processes this file, event-by-event, tracking the individual particles through the detector system and monitoring the detector response. It produces an HBOOK format output ntuple containing the identities of the struck detector elements, the size of the energy deposit and (for TAPS alone) the time of the energy deposit.

6.1.1 Event Generation

To accurately gauge the acceptance of the detector system for a particular reaction it is important to have a generated event set which matches the kinematic distributions of the various particles involved. At present, there is no available up-to-date event generator for either of our two models. Instead we used *mcgen* which is the new event generator produced by J. R. M. Annand.

We made simple uniform phase space distributions of both $\gamma p \to p\pi^0$ and $\gamma p \to p\pi^0\pi^0$ reactions to test the background suppression of our analysis. We also made two different simulated data sets for the $\gamma p \to p\pi^0\gamma'$ process. Both data sets applied a 300 MeV to 500 MeV incoming photon beam with a 1/E-type distribution. The production of the data sets differed only in the choice of the production photon energy distribution. The first, gppi0a, simulated the Δ to Δ decay, producing an $E_{\gamma'}$ distribution which resulted from the transition

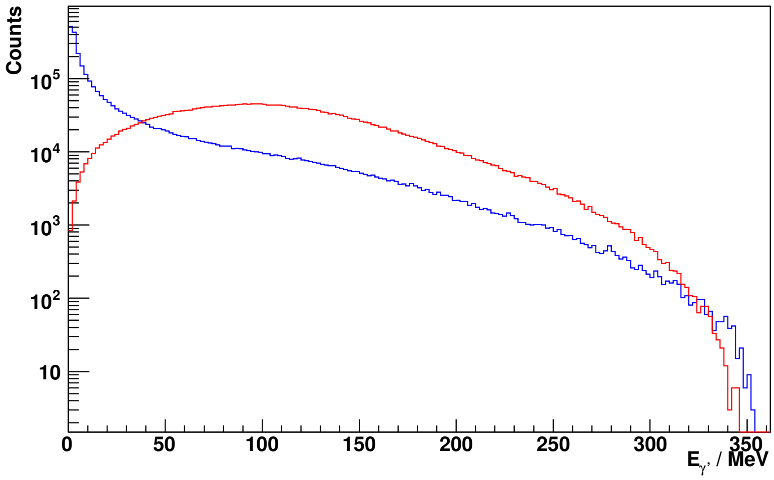

Figure 6.1: $E_{\gamma'}$ distributions from the two $p(\gamma, \gamma'\pi^0 p)$ simulation event generators. The red line shows the distribution from gppi0a, and the blue line shows the $1/E_{\gamma'}$ dependent gppi0b distribution.

within the Breit-Wigner width of the Δ. The second, known as gppi0b, applied a $1/E_{\gamma'}$ bremsstrahlung-type distribution to the outgoing photon energy (see Figure 6.1). These two different $E_{\gamma'}$ distributions affect the shape of the simulated data analysis results quite markedly in some cases, so we will show both sets of simulated data points alongside our experimental results. All four event files contained around 3×10^6 events.

6.1.2 Analysis of Simulated Data Sets

To analyse the simulated data, each of the AcquRoot detector classes has a ReadDecoded() function, which translates the simulation output ntuple (after conversion to ROOT format) into the same energy and time arrays that would be constructed from the pulse heights in the physical detector ADCs and TDCs. From that point on, the simulated data is treated in the same manner as the regular experimental data with a few exceptions.

The energy deposit recorded by the simulation is exact, so we smear the energy deposit in the individual calorimeter elements according to the resolutions reported in [85] (for the Crystal Ball) and [88] (for TAPS) when reading the simulated data into AcquRoot for analysis. This works fairly well and the widths of the various energy distributions agree with those observed in the experiment.

However, the simulation does suffer from some limitations. Due to the spatial constraints of locating the PID and MWPCs inside the Crystal Ball, it was necessary to have the electronics for both detectors forward of the target, an important region due to the forward boost provided by the beam momentum. This affects the region around $10° < \theta < 20°$. We tried to reflect this in the simulation geometry, however the electronics are complex arrangements of capacitors, resistors and chips and it would be impractical to model precisely the various

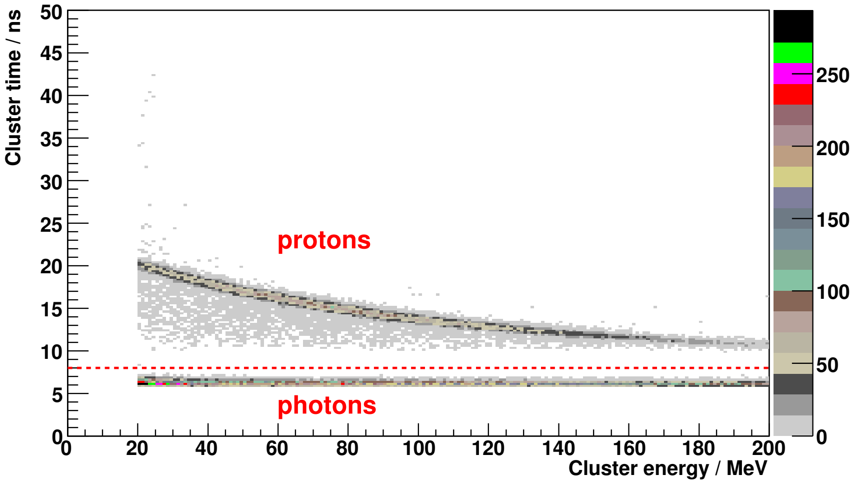

Figure 6.2: Simulated TAPS cluster time vs. cluster energy plot showing the identification of photons and protons in the AcquRoot analysis of simulated $\gamma p \rightarrow \gamma' \pi^0 p$ events.

components. Instead, we approximate the electronics in the simulation geometry with a 1mm-thick cardboard tube. This covers the correct region, but has a far more uniform effect on the energy deposits for charged particles in that region than the physical detector electronics.

As the simulation produces only a single recorded energy for each TAPS element and does not consider pulse form, it is not possible to perform particle identification on the basis of pulse shape analysis. Instead, we utilise the simulated hit timing of TAPS, bearing in mind that TAPS is sufficiently far from the target to allow particle identification by time-of-flight. The reconstructed cluster time vs cluster energy plot (Figure 6.2) has a straight ridge for photons (which have constant velocity). Above this straight photon ridge, we observe a curved ridge corresponding to non-relativistic detected protons. We use this to make a very clean and efficient proton selection by identifying any particle which has a cluster time greater than 8 ns as a proton. In the handling of real data, we used pulse shape analysis to identify particles in TAPS, unfortunately, this is far less efficient than the idealised simulated time-of-flight analysis.

The Crystal Ball elements in the simulation do not store a hit time, only a hit energy. Hence the use of the time relationship between hits to identify coincident photons is not possible for simulated data.

All twenty-four scintillators of the simulated Particle Identification Detector behave identically. In the case of the real detector, there was always some slight variation from element to element, and there were two detector elements which had poorer light collection, and therefore poorer energy resolution and particle identification efficiency. These elements were damaged during the target dismount as described in Section 5.3.2. Overall, the simulated PID may be slightly more efficient than the physical detector. Also, runs occurring after the damage to the PID took place produce systematically lower cross sections resulting from a drop in PID efficiency which is not reflected in the simulations. This drop in efficiency is less than 5% (assuming a halving of efficiency in each of the two elements: $0.5 \times \frac{2}{24}$) and will be corrected by applying measured detector element resolutions and efficiencies within the simulation, but was not achieved during this work due to time constraints.

6.2 Conventions

As we have performed a fairly complex analysis involving several stages of kinematic cuts[1], we felt it was advisable to study the effect of each cut independent of the others. To this end, after defining our final analysis, we re-analysed the data, systematically removing one cut at a time to observe its effect. When we discuss each cut, the plots shown will represent the results of an analysis where every cut (Section 6.4) is applied save the cut under investigation. Thereby we are able to see exactly what that cut removes, in terms of signal and the background upon which the signal sits. The comparison of simulated to experimental data requires that the simulated data undergo (as far as possible) the same analysis as the real data. Therefore, for each data analysis (with different cuts omitted) we have run the simulation analysis in exactly the same way. Subsequent plots compare experimental with equivalent simulated distributions.

Hereafter, the black crosses shown on all data plots represent the "one cut removed" experimental data sets, the red crosses represent the equivalent results from the gppi0a generated simulated data and the blue crosses represent that from the gppi0b simulated data. The incoming photon energy is always quoted in the lab frame, all other variables are in the centre of mass frame unless otherwise stated. The employed symbols are explained in Table 6.1.

Symbol	Meaning
E_γ	incoming photon energy
$E_{\gamma'}$	production photon energy
E_{π^0}	π^0 kinetic energy
E_p	proton kinetic energy
$\theta_{\gamma'}$	polar angle of production photon
θ_{π^0}	polar angle of π^0
θ_p	polar angle of proton
$\phi_{\gamma'}$	azimuth angle of production photon
ϕ_{π^0}	azimuth angle of π^0
ϕ_p	azimuth angle of proton

Table 6.1: Conventional symbols. All values are as measured in the centre of mass frame, save for E_γ which is always reported as measured in the lab frame.

---

[1] A "cut" is the selection of data that meet certain physical criteria.

6.3 Background Channels

There are two main reactions which can produce background to obscure the $p(\gamma, \gamma'\pi^0 p)$ signal: $p(\gamma, \pi^0 p)$ and $p(\gamma, \pi^0\pi^0 p)$. All data cuts described herein were designed to remove these background events, leaving only $p(\gamma, \gamma'\pi^0 p)$ events for the final evaluation of cross section and photon asymmetry.

6.3.1 Background Due to $\gamma p \rightarrow p\pi^0$

If perfectly detected, the $\gamma p \rightarrow p\pi^0$ reaction produces a two-photon, single-proton final state which could be eradicated from our data set by the simplest of cuts. Unfortunately, our detectors are not perfect and, as the $\gamma p \rightarrow p\pi^0$ cross section peaks at $\sim$318 μb within our region of interest [23] while the $\gamma p \rightarrow p\pi^0\gamma'$ cross section is four orders of magnitude smaller [23], even a small proportion of $\gamma p \rightarrow p\pi^0$ events resembling our desired final state can significantly affect our final result.

This reaction may mimic our three-photon, single-proton final state due to a failure of the cluster reconstruction, whereby energy deposits left at the edges of a reconstructed cluster from a single photon are interpreted as a second adjacent cluster by the reconstruction algorithm (hereafter referred to as "pseudo-split-off", see Section 5.5 for a description of the clustering algorithms). Alternatively a real split-off, where the EM shower caused by one photon produces a second separate cluster can mimic the final state of $p(\gamma, \gamma'\pi^0 p)$.

6.3.2 Background Due to $\gamma p \rightarrow p\pi^0\pi^0$

There are two ways in which the $\gamma p \rightarrow p\pi^0\pi^0$ reaction can enter our data set. The first is simply that one of the four π^0 decay photons goes undetected by our detector system and thereby produces an apparent three-photon single proton final state. The second is that our cluster finding algorithm for the calorimeters may merge two of the π^0 decay-photon showers into a single cluster in our analysis, again producing our three-photon single proton final state.

To deal with a missed photon, we simply apply cuts on missing energy, mass and momentum. We can easily separate out events with a missing particle and use simulation to correct for the remaining contamination from our data set. This was a far more significant cause of background in the pioneering μ_{Δ^+} measurement using TAPS [1] due to the relatively small solid angle covered by their detector system. With almost 4π coverage, the possibility of undetected photons is far lower in our CB/TAPS detector setup.

The artificial merging of clusters is a far more insidious problem. The energy of the two photons remains within the detector system and the angle of the merged cluster is a combination of the two real cluster angles. Thus, although the position is somewhat smeared, we cannot remove the contamination purely by looking at missing energy, momentum or mass distributions as these are all still centred on the correct position, they are merely slightly wider. Instead we looked at methods to gauge the level of contamination and correct for it, this will be discussed in Section 6.5.

6.4 Data Cuts

6.4.1 Initial Selection

We begin by selecting events with a total of four detected clusters. We demand that one of these four particles has been identified as a proton and the remaining three as photons.

6.4.2 Clustering Algorithm and Photon Angles

Some of our biggest background contamination results from ambiguities in our cluster identification algorithm. If our main concern is the artificial merging of neighbouring clusters, we use our initial algorithm for cluster determination, looking only at the nearest neighbours of the central cluster crystal (that with the highest energy). If we are more concerned by the creation of extra false clusters at the edges of the real ones (pseudo-split-off) we iterate outwards looking at the neighbours of the neighbours and so on.

To observe the effect of the clustering algorithm, we look at the angle difference between each of the possible combinations of two of the three photons in our event sample. As can be seen in Figure 6.3, the basic, nearest neighbours, clustering algorithm leads to a large peak at low angular difference where a single cluster has been interpreted as two adjoining clusters, while the iterative clustering algorithm leads to a reduction in the number of events with small angular differences.

To reduce this pseudo-split-off and thereby reduce the $\gamma p \rightarrow p\pi^0$ contamination which results from the spurious detection of an extra cluster, we decided to use the iterative cluster algorithm. Although this increases the likelihood of merging neighbouring real clusters, and thereby introducing more $\gamma p \rightarrow p\pi^0\pi^0$ background into our data set, it was decided that reducing the $\gamma p \rightarrow p\pi^0$ background was a higher priority as the cross section for $\gamma p \rightarrow p\pi^0$ is several orders of magnitude larger than that of $\gamma p \rightarrow p\pi^0\pi^0$. Also, the pseudo-split-offs can make real four-cluster $\gamma p \rightarrow \gamma' p\pi^0$ events appear to have five or more clusters and thereby be rejected by our analysis, worsening the statistics of the final event sample.

Having decided to adopt the iterative clustering algorithm in order not to lose events, we further reduced the chance of $\gamma p \rightarrow \pi^0 p$ entering our data set due to pseudo split-off by placing limits on the allowed angular difference between photon pairs. We only accepted events that had an angular difference between all possible photon pairs of greater than thirty degrees (see Figure 6.4). Without this cut, the simulation shows that $\gamma p \rightarrow \pi^0 p$ reaction contamination is three times more likely to enter our final data set.

6.4.3 Removal of TAPS Background

As the central TAPS elements subtend an angle of only 2° from the centre of the target along the beam line, they are very close to the photon beam. There is a substantial random background of electrons and photons produced by atomic

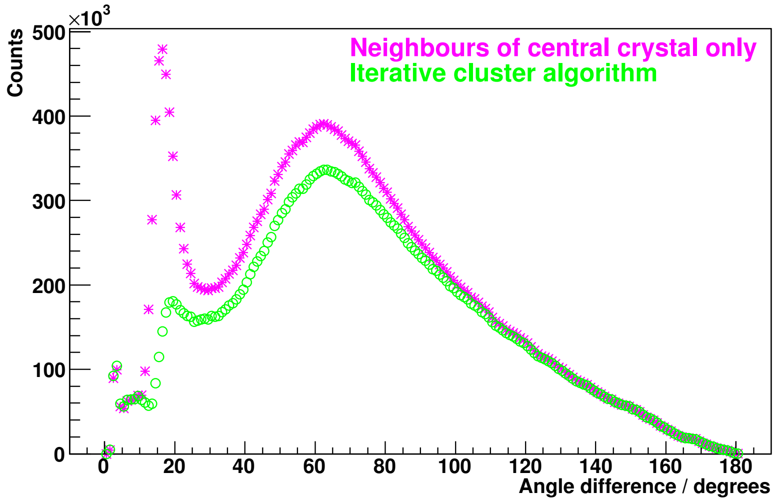

Figure 6.3: The angle difference between photon pairs showing the effect of the clustering algorithm on photon cluster distributions. The crosses show the difference in angle between all possible pairs of photons reconstructed using the basic clustering algorithm, while the circles show the result for the iterative cluster algorithm.

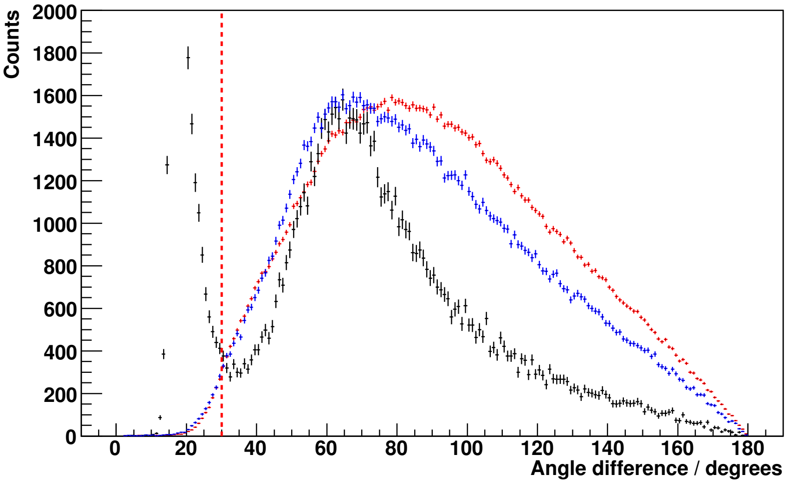

Figure 6.4: The angle difference between photon pairs showing the effect of requiring that the angle difference between all photons must be greater than 30° to ensure no pseudo-split-off contamination. The black points show July data with all cuts save the one under study, the red crosses show analysed gppi0a simulated data and the blue crosses show analysed gppi0b simulated data.

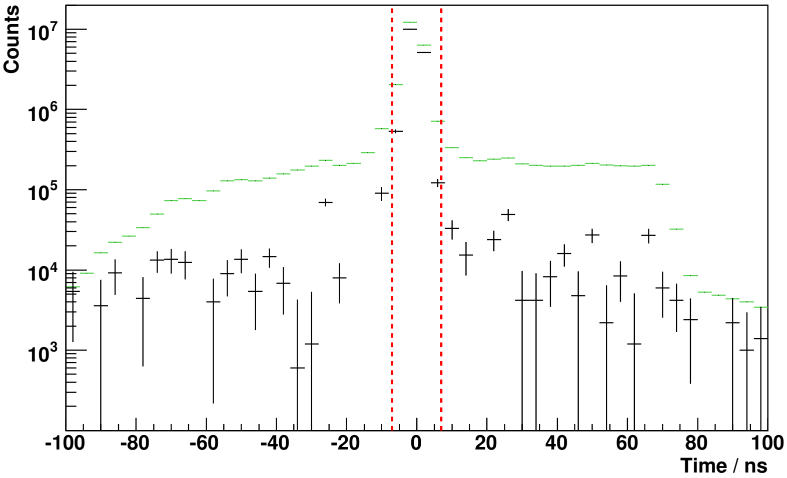

Figure 6.5: The time difference between photon pairs showing the effect of requiring that the magnitude of the time difference between all photons must be less than 7 ns. This removes events having four clusters due to random coincident electromagnetic background in TAPS early in the analysis, but has little effect on the final event sample. The green points show the time difference between all possible photon pairs after only the initial particle identification and number cut has been made. There is a large peak around zero corresponding to coincident photons in the CB and TAPS. The low level EM background in TAPS throughout the TDC time window can be seen. The black points correspond to the final event sample without the application of the timing cut, showing that the constant background is effectively removed by the other cuts.

interactions of the photon beam with the target and surrounding materials. This background is strongly forward peaked and strikes the inner elements of TAPS.

Although these events may be removed from our analysis by other cuts (see Figure 6.5), it is useful to remove them early in our analysis by looking at the time difference between each possible photon pair, thereby increasing the speed with which the data is processed. We loop over all three possible photon combinations and remove any events from our sample that have a photon pair with a time difference of greater than 7 ns.

However, after the timing is cut, some coincident electromagnetic background remains within the 14 ns-wide window. It can be seen in Figure 6.6 that, after all other cuts, if we do not explicitly remove this EM background, it would remain in our event sample. Thus we are forced to demand that all photons (both π^0 decay photons and the γ') have a polar angle of greater than 8° in the laboratory frame .

6.4.4 Identification of π^0

After removing the large electromagnetic backgrounds, we once again loop through all possible combinations of two of the three photons. We look at the invariant

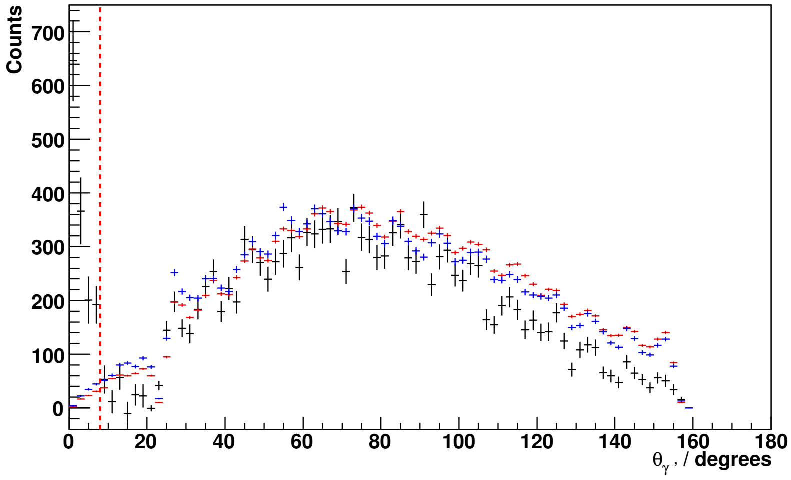

Figure 6.6: The polar angle of γ' in the lab frame showing the effect of the cut requiring all photon angles be greater than 8° (in the lab frame) on the polar angle of the γ'. Without this cut, $\theta_{\gamma'}$ displays an unphysical peak below 8° where the small angle random electromagnetic background in TAPS dominates the real event sample. The black points show July data with all cuts save the one under study, the red crosses show analysed gppi0a simulated data and the blue crosses show analysed gppi0b simulated data.

mass of each of the possible photon pairs and assign the pair with the invariant mass closest to that of the accepted π^0 mass (134.9766 MeV [52]) to be the π^0 decay photons. The π^0 four-vector is defined simply as the sum of the two photon four vectors, we do not perform any mass corrections or other such alterations. The third photon is then identified as the γ'.

6.4.5 Proton Energy Correction

As we require the best possible energy resolution in order to minimise the background contribution to our final event sample, we then apply the proton energy correction as described in Section 5.6 to the experimental data. We reject any "uncorrectable" events in order to ensure consistency in resolution throughout our final event sample.

Due to time constraints, it was not possible to construct a proton energy correction from simulated $p(\gamma, \pi^0 p)$ events to apply to the simulated data. Instead, we used a proton correction constructed by D. Glazier [111]. This correction table was formed by calculating the average difference between the input and registered energy for an input uniform phase space distribution of protons in a series of energy and angle bins. As D. Glazier's correction covers a larger energy and angle range than the experimental proton energy correction, we try to match the experimental correction acceptance by rejecting simulated events with $10° < \theta_p^{lab} < 26°$ or $\theta_p^{lab} > 66°$.

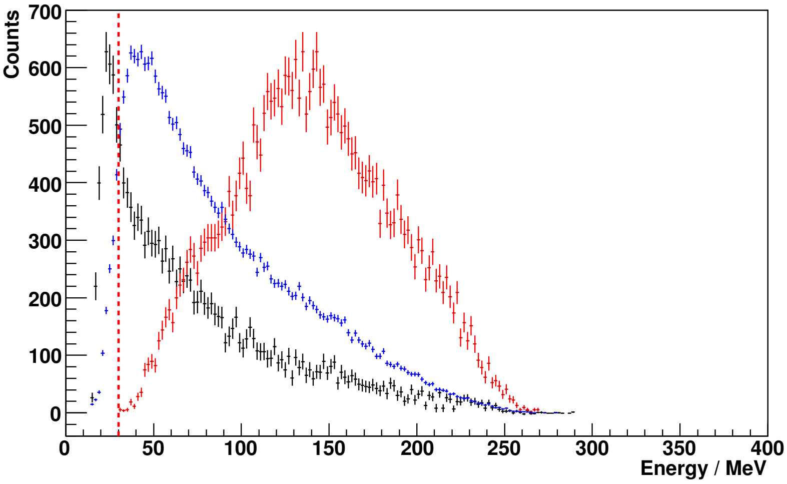

Figure 6.7: The energy of γ' in the centre of mass system, showing the effect of a cut requiring $E_{\gamma'}^{c.m.} > 30$ MeV. Black points show July data with all cuts save the one under study. The black points show July data with all cuts save the one under study, the red crosses show analysed gppi0a simulated data and the blue crosses show analysed gppi0b simulated data.

6.4.6 Beam Energy

As we are interested in $\gamma p \rightarrow \gamma' p \pi^0$ events that proceed via $\Delta(1232)$ production, there is little point in studying events with a photon energy below that of the $\Delta(1232)$ production threshold. Also, to allow the $\Delta \rightarrow \Delta\gamma$ transition, we require more than the threshold energy, so we set our lower beam energy boundary at 300 MeV. At higher beam energies, $\gamma p \rightarrow p \pi^0 \pi^0$ begins to dominate proceedings, so we limit the beam energy to be below 500 MeV. Thus for our total cross section data we analyse events with a photon beam energy between 300 MeV and 500 MeV.

To see photon asymmetries, we require to look at data from a photon energy range with a reasonable degree of linear photon polarisation. Thus, when we produce photon asymmetries, we analyse data with a photon beam energy of between 340 MeV and 440 MeV for the July beam time (where the polarisation edge was ~440 MeV) and between 300 MeV and 400 MeV for the September beam time (where the polarisation edge was ~400 MeV).

6.4.7 Real Split-Off Removal

To reduce the risk of $\gamma p \rightarrow p \pi^0$ events which undergo real split-off entering our event sample, we set a lower bound on the acceptable γ' energy of 30 MeV when evaluated in the centre of mass frame of the initial photon and target (see Figure 6.7). This also allows us to compare directly with the previous result of M. Kotulla, as all of the cross sections reported in [1] are for $E_{\gamma'}^{c.m.} > 30$ MeV.

6.4.8 Momentum Conservation

If our hypothesis is correct, and the event under study is a $\gamma p \rightarrow \gamma' p \pi^0$ event, when we look at the momentum balance in x, y and z coordinates independently (defined in Equations 6.1 to 6.3), we should see Gaussian distributions which are symmetrical around zero, as illustrated in Figure 6.8.

$$p_x^{miss} = p_{x\pi^0} + p_{x\gamma'} + p_{xp} - p_{x\gamma} \tag{6.1}$$

$$p_y^{miss} = p_{y\pi^0} + p_{y\gamma'} + p_{yp} - p_{y\gamma} \tag{6.2}$$

$$p_z^{miss} = p_{z\pi^0} + p_{z\gamma'} + p_{zp} - p_{z\gamma} \tag{6.3}$$

We apply cuts to remove the few events in the tails of the Gaussian distributions of -45 MeV $< p_x^{miss.} <$ 45 MeV, -40 MeV $< p_y^{miss.} <$ 40 MeV and -75 MeV $< p_z^{miss.} <$ 75 MeV. The $p_z^{miss.}$ distribution is not centred on zero, we believe this to be due to a slight target / detector misalignment of the order of 10mm.

6.4.9 Removal of $\gamma p \rightarrow p\pi^0$ by Pion Energy

As the cross section for $\gamma p \rightarrow p\pi^0$ is large, relative to that of our process of interest, we need to be very stringent in our criteria for the rejection of $\gamma p \rightarrow p\pi^0$ events. One way we can do this is to use the kinematic over-determination of $\gamma p \rightarrow p\pi^0$ to test the π^0 kinetic energy. If we make the assumption that the event under study is $\gamma p \rightarrow p\pi^0$, we can calculate the anticipated π^0 energy using the equations:-

$$E_{\pi^0} = \frac{(s + m_{\pi^0}^2 - m_p^2)}{2 \times \sqrt{s}}, \tag{6.4}$$

$$s = 2E_\gamma m_p + m_p^2, \tag{6.5}$$

where m_{π^0} and m_p are the masses of the π^0 and proton, respectively, E_{π^0} is the calculated kinetic energy of the π^0 in the centre of mass frame, and s (the square of the total centre of mass frame energy) is as defined in Equation 6.5 where E_γ is the photon beam energy in the laboratory frame.

If we look at the difference between E_{π^0} calculated using the beam energy and particle masses and the measured E_{π^0}, we see the results displayed in Figure 6.9. The green points show the data half-way through our analysis to illustrate the shape of the $\gamma p \rightarrow p\pi^0$ contamination peak. By demanding that the difference between the measured π^0 energy and that calculated on the basis of the $\gamma p \rightarrow p\pi^0$ hypothesis be less than -25 MeV we reduce the probability of $\gamma p \rightarrow p\pi^0$ events entering our $\gamma p \rightarrow \gamma' p\pi^0$ event sample by removing the small enhancement around zero that can still be seen in our data set (black points) after all other cuts have been performed.

6.4.10 Invariant Mass Difference

If the event under study is a $p(\gamma, \gamma'\pi^0 p)$ event, then evaluating the difference between the total invariant mass of the π^0 and γ' and the missing mass calculated

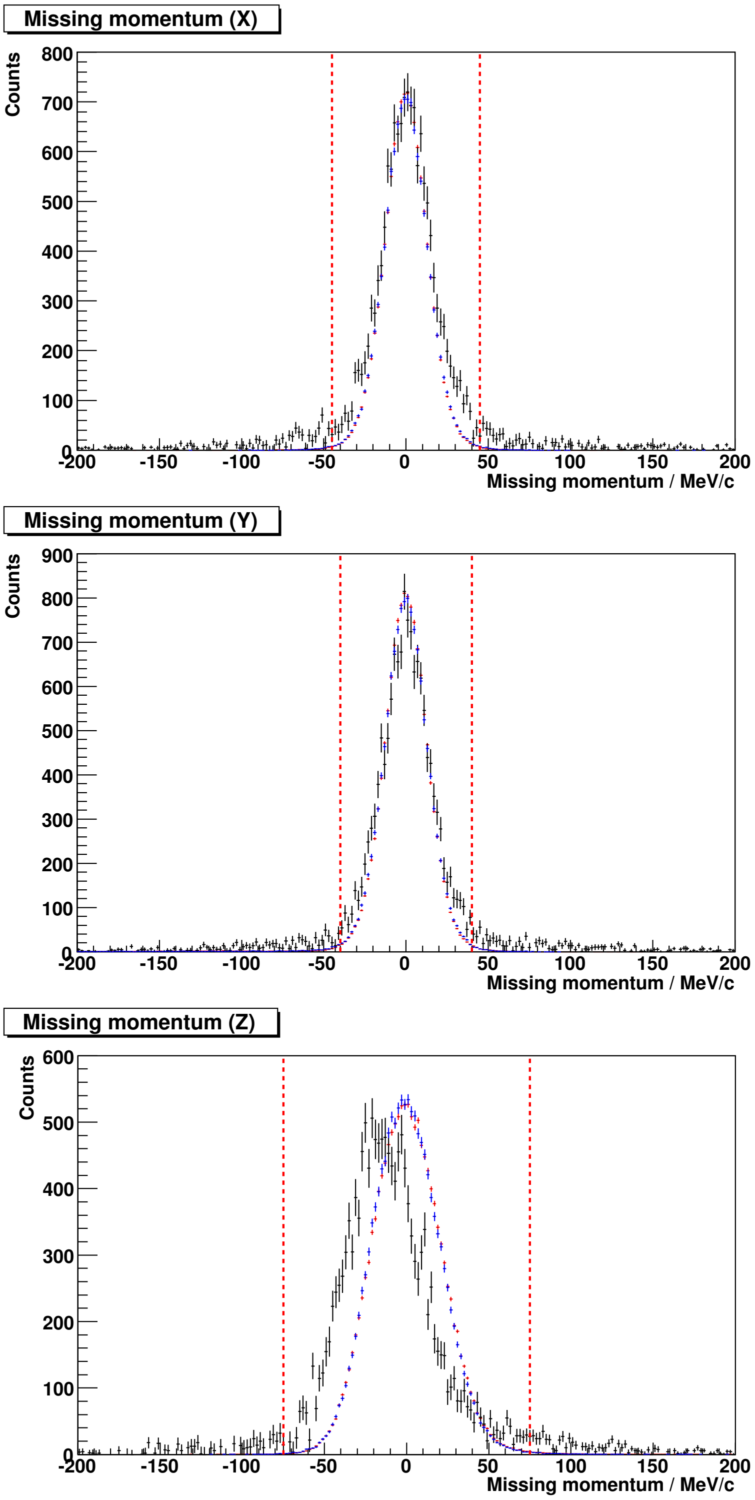

Figure 6.8: The momentum balance in x-, y- and z-directions in the laboratory system showing the effect of the missing momentum cuts (Section 6.4.8). The black points show July data with all cuts save the one under study, the red crosses show analysed gppi0a simulated data and the blue crosses show analysed gppi0b simulated data. The simulation results agree well with the measured distributions. The discrepancy in the centre of the z-distribution should be remedied by incorporating the slight target misalignment (~10mm) into the simulation.

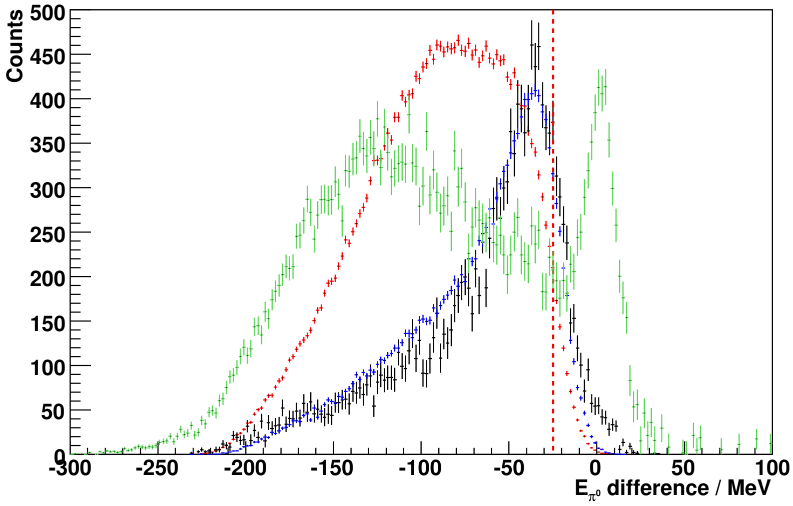

Figure 6.9: The difference between the measured energy of the π^0 and that calculated using $p(\gamma, \pi^0 p)$ kinematics in the centre of mass system, showing the cut requiring the difference be less than -25 MeV. Green points show data before all cuts are made to illustrate clearly the width of the zero-centred $\gamma p \rightarrow p\pi^0$ events. The black points show July data with all cuts save the one under study, the red crosses show analysed gppi0a simulated data and the blue crosses show analysed gppi0b simulated data. A small enhancement can be seen around zero in the final data, this is removed by our cut, without sacrificing too large a proportion of our final event sample. The gppi0b simulation results agree well with the final distribution and therefore is used for the final cross section normalisation.

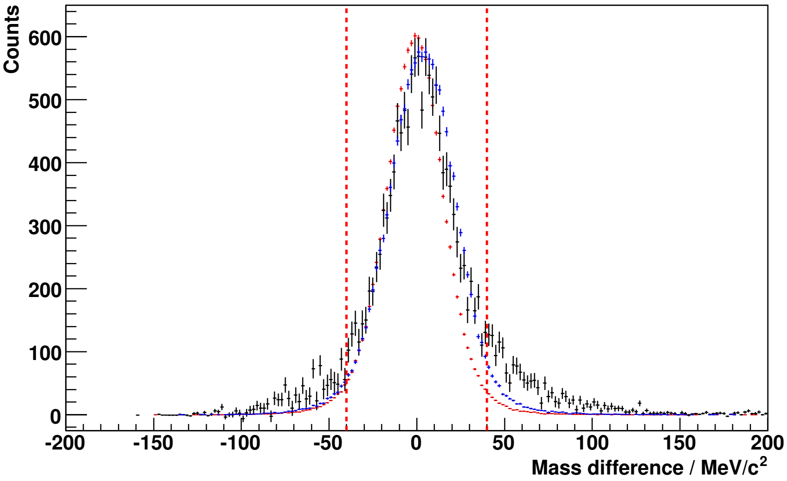

Figure 6.10: The missing mass evaluated as the difference between the invariant mass of the π^0 and γ' and the missing mass calculated using the beam, target and proton (Equation 6.6). The black points show July data with all cuts save the one under study, the red crosses show analysed gppi0a simulated data and the blue crosses show analysed gppi0b simulated data.

using (beam + target - outgoing proton) as defined by Equation 6.6

$$\Delta M = \sqrt{(E_{\gamma'} + E_{\pi^0})^2 - (\mathbf{p}_{\gamma'} + \mathbf{p}_{\pi^0})^2} - \sqrt{((E_\gamma + E_{p_i}) - E_p)^2 - (\mathbf{p}_\gamma - \mathbf{p_p})^2}, \tag{6.6}$$

where E_γ, E_{p_i}, $E_{\gamma'}$, E_{π^0} and E_p are the total energies of the incoming photon, target proton, outgoing photon, π^0 and final proton respectively; and $\mathbf{p}_\gamma$, $\mathbf{p}_{\gamma'}$, $\mathbf{p}_{\pi^0}$ and $\mathbf{p_p}$ are the momentum three-vectors of the beam, outgoing photon, π^0 and outgoing proton respectively, should give a distribution centred on zero. We applied the limit -40 MeV $< \Delta M <$ 40 MeV (Figure 6.10).

6.4.11 Missing Mass of the γ'

$$M^2_{miss.}(\pi^0 p) = ((E_\gamma + E_{p_i}) - (E_{\pi^0} + E_p))^2 - (\mathbf{p}_\gamma - (\mathbf{p_p} + \mathbf{p}_{\pi^0}))^2 \tag{6.7}$$

The square of the missing mass defined in Equation 6.7 (where the symbols carry the same meaning as in Equation 6.6) should be the square of the invariant mass of the production photon and as such should form a peak centred on zero. Any $\gamma p \rightarrow p\pi^0\pi^0$ events entering the event sample due to a missed photon (the biggest background contribution in the previous experiment) will form a peak centred around 0.018 (GeV/c^2)^2 $= m^2_{\pi^0}$. As can be seen from Figure 6.11, the contribution around 0.018 (GeV/c^2)^2 is small, but non-negligible, and as such we impose the limit that -0.01 (GeV/c^2)^2 $< M^2_{miss}(\pi^0 p) <$ 0.01 (GeV/c^2)^2 to remove the missing photon $p(\gamma, \pi^0\pi^0 p)$ background.

As can also be seen from the green simulated $p(\gamma, \pi^0\pi^0 p)$ distribution in Figure 6.11, we have a more insidious problem (as previously explained in Section 6.3.2). The majority of the $p(\gamma, \pi^0\pi^0 p)$ contamination entering our event sample results

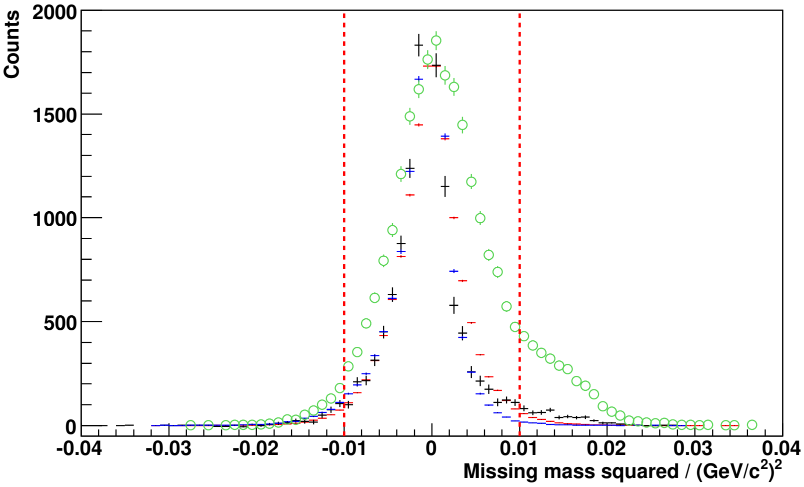

Figure 6.11: The missing mass of the γ', as defined in Equation 6.7. The green circles show the results of the simulated $\gamma p \rightarrow p\pi^0\pi^0$ data. The black points show July data with all cuts save the one under study, the red crosses show analysed gppi0a simulated data and the blue crosses show analysed gppi0b simulated data.

from artificial cluster merging, which places the $p(\gamma, \pi^0\pi^0 p)$ background in the same region of the $M^2_{miss.}(\pi^0 p)$ distribution as the true $p(\gamma, \gamma'\pi^0 p)$ events.

6.4.12 Invariant Mass of the π^0

A cut on the invariant mass of the reconstructed π^0 seems one of the most simple and hence one of the first cuts we should perform on our data. However, from the simulation results for $p(\gamma, \pi^0\pi^0 p)$, it is obvious that we cannot totally remove the $p(\gamma, \pi^0\pi^0 p)$ contamination due to cluster merging from our data set by kinematic cuts alone. After examination, we found that only the invariant mass of the π^0 was sensitive enough to show the results of this $p(\gamma, \pi^0\pi^0 p)$ contamination either side of the real data peak after all the other cuts had been applied to the data as can be seen in Figure 6.12. Thus we applied this cut to our data last, in order that we might use a fit to the background either side of the peak to establish the background underneath it. To remove the background that clearly does not belong to the event sample, we applied a cut of ±20 MeV either side of the accepted π^0 mass.

6.5 $2\pi^0$ Background Subtraction

To remove the $p(\gamma, \pi^0\pi^0 p)$ background after all the kinematic cuts had been applied to the data, we chose to apply two different methods, described in Sections 6.5.1 and 6.5.2. This allowed us to check the consistency of the final $\gamma p \rightarrow \gamma'\pi^0 p$ cross section.

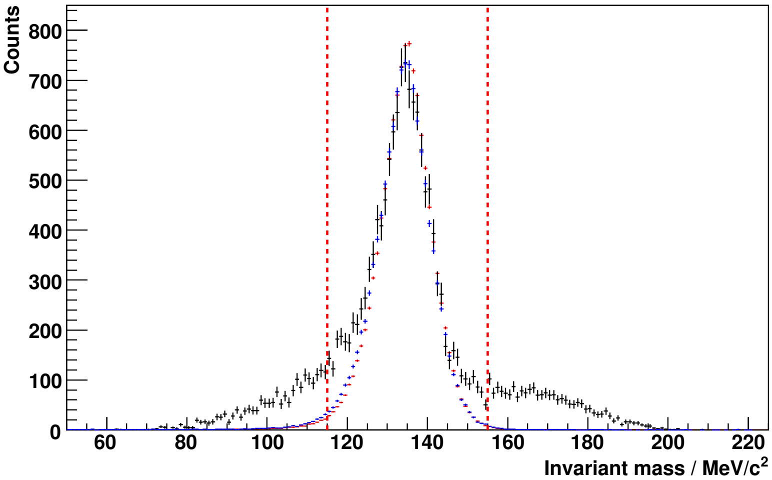

Figure 6.12: The invariant mass of the π^0 after all other cuts have been made, showing the final invariant mass limits. The $p(\gamma,\pi^0\pi^0p)$ background can be clearly seen either side of the true event peak. The black points show July data with all cuts save the one under study, the red crosses show analysed gppi0a simulated data and the blue crosses show analysed gppi0b simulated data. The correction for this background is discussed in Section 6.5.

6.5.1 π^0 Invariant Mass-Based Subtraction

As can be seen in Figure 6.12, there is a distribution either side of the π^0 peak which results from the $p(\gamma,\pi^0\pi^0p)$ contamination. The shape of the high mass tail is very similar to the shape of the π^0 invariant mass distribution produced by the simulated $p(\gamma,\pi^0\pi^0p)$ events (Figure 6.13). The distribution of gppi0a and gppi0b events in Figure 6.12 suggests that the real $p(\gamma,\gamma'\pi^0p)$ events do not contribute significantly above an invariant mass of 155 MeV, and so the events above 155 MeV should be predominately due to the $p(\gamma,\pi^0\pi^0p)$ contamination. We fitted the invariant mass distribution from the $p(\gamma,\pi^0\pi^0p)$ simulation to the data by scaling the $p(\gamma,\pi^0\pi^0p)$ π^0 invariant mass distribution to have the same integral as that of the data between 155 MeV and 180 MeV. The scaled simulation result was then subtracted from the data to correct the number of events.

The sum of simulated $p(\gamma,\pi^0\pi^0p)$ and $p(\gamma,\gamma'\pi^0p)$ events matches the data in Figure 6.13 very well both at and above the true π^0 invariant mass. At lower masses, it can be seen that there is a slight enhancement in the data relative to the simulation. This we assume is due to a combination of $p(\gamma,\pi^0p)$ contamination and the simple model used to simulate the $p(\gamma,\gamma'\pi^0p)$ event distributions. However, the discrepancy is relatively small inside the invariant mass cut that we apply. Unfortunately, the acceptance of $p(\gamma,\pi^0p)$ events is so low that it is impractical to produce a sufficiently large simulated event sample to perform a solely-simulation-based subtraction within the time constraints of this work. From Figure 6.14, it can be seen that the level of background increases with increasing beam energy, with very little background below 450 MeV which is the region of interest.

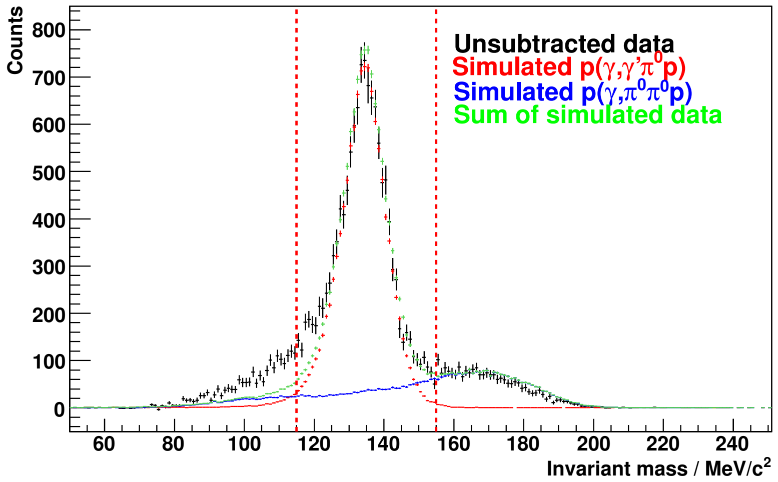

Figure 6.13: The invariant mass of the π^0 after all other cuts have been made, showing the applied cuts. The blue points correspond to the results from the $p(\gamma, \pi^0\pi^0 p)$ simulation, the red from gppi0b simulation results and the green points show the sum of the two simulated contributions. The green trace matches the black experimental data points at and above the true π^0 invariant mass.

6.5.2 $p(\gamma, \pi^0\pi^0 p)$ Cross Section-Based Subtraction

From the simulated $p(\gamma, \pi^0\pi^0 p)$ events, we can calculate the rate of acceptance for these events in the same way as for our desired reaction. We can then use this to normalise the cross section measured in [23], to produce the effective contamination cross section due to $p(\gamma, \pi^0\pi^0 p)$. First, we plotted the measured $p(\gamma, \pi^0\pi^0 p)$ cross section (σ^i in photon energy bin i), averaged over the same E_γ bins as our final cross section (see Figure 6.15). We then plotted the acceptance of $p(\gamma, \pi^0\pi^0 p)$ events ($\epsilon^i_{p(\gamma, p\pi^0\pi^0)}$ in bin i) by taking the the number of simulated $p(\gamma, \pi^0\pi^0 p)$ events surviving all of the cuts in each E_γ bin (N^i_s for bin i) divided by the total number of simulated events from that E_γ bin (N^i_e in bin i) (Equation 6.8, Figure 6.16).

$$\frac{N^i_s}{N^i_e} = \epsilon^i_{p(\gamma, p\pi^0\pi^0)} \tag{6.8}$$

$$\sigma^i_c = \sigma^i \epsilon^i_{p(\gamma, p\pi^0\pi^0)}. \tag{6.9}$$

Applying Equation 6.9 gives the level of contamination in our data set (σ^i_c in bin i), to be subtracted from the final $p(\gamma, \gamma' p\pi^0)$ cross section (Figure 6.17).

6.6 $p(\gamma, \pi^0 p)$ Background Subtraction

Unlike the $p(\gamma, \pi^0\pi^0 p)$ background subtraction, only a tiny fraction of $p(\gamma, \pi^0 p)$ events pass all of the cuts as described in Section 6.4 (67 events from a 3×10^6 input event set). However, due to the fact that the $p(\gamma, \pi^0 p)$ total cross

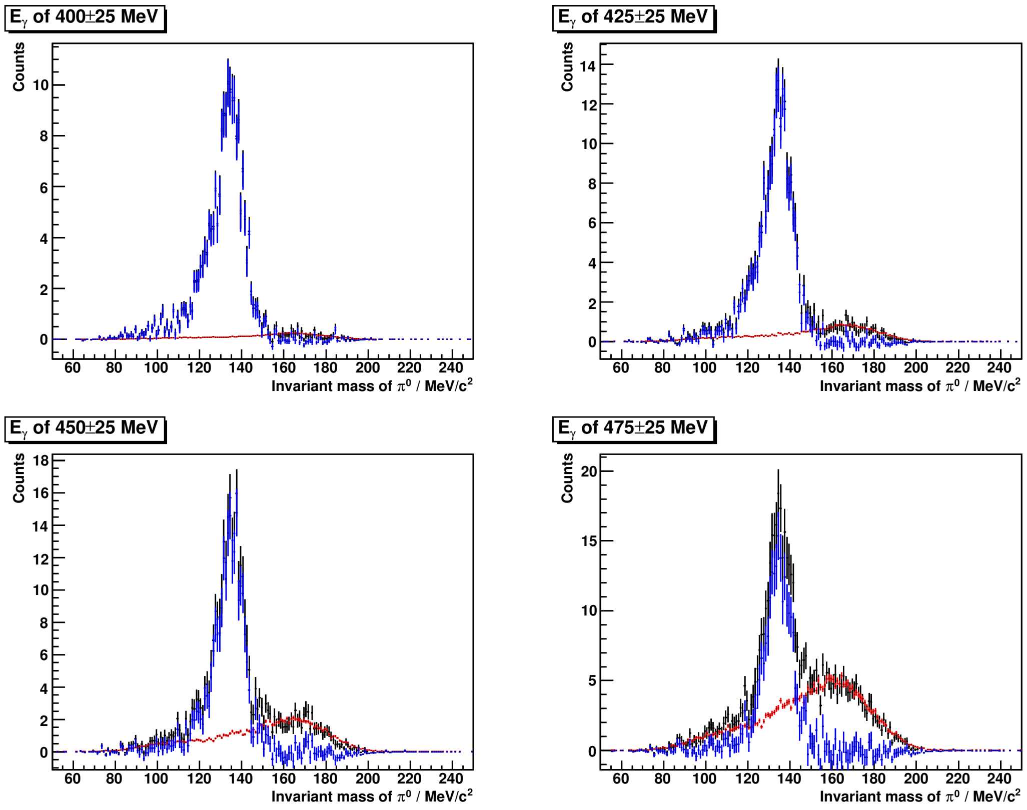

Figure 6.14: The subtraction of $p(\gamma,\pi^0\pi^0 p)$ background based on the invariant mass of the π^0 after all other cuts. The four panels show the variation in background with increasing E_γ in 50 MeV-wide E_γ bins. The black points show the original unsubtracted data, the red shows the $p(\gamma,\pi^0\pi^0 p)$ contribution to be subtracted and the blue shows the final subtraction result. It can be seen that only minimal subtraction is required at $E_\gamma < 450$ MeV where the photon asymmetries and μ_{Δ^+} are evaluated.

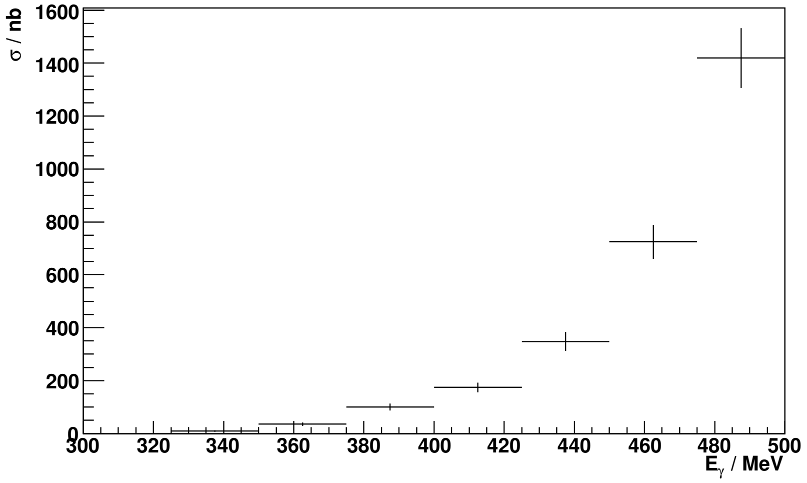

Figure 6.15: The cross section of $p(\gamma,\pi^0\pi^0 p)$ from [23].

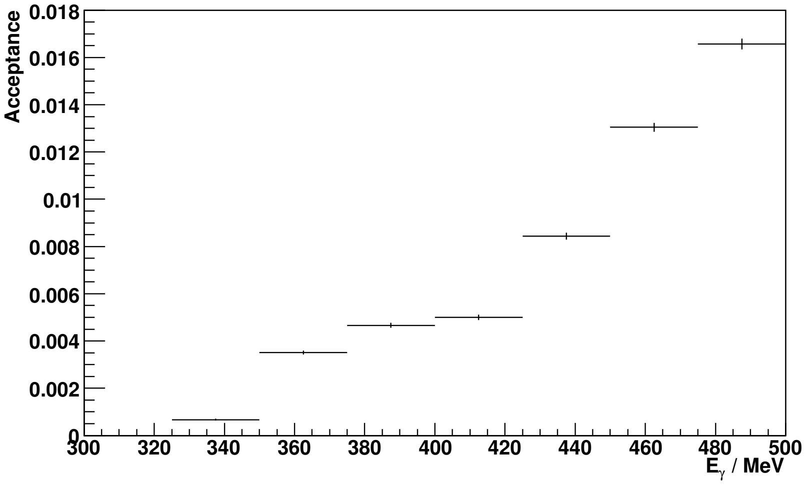

Figure 6.16: The acceptance of $p(\gamma, \pi^0\pi^0 p)$ calculated from the simulation.

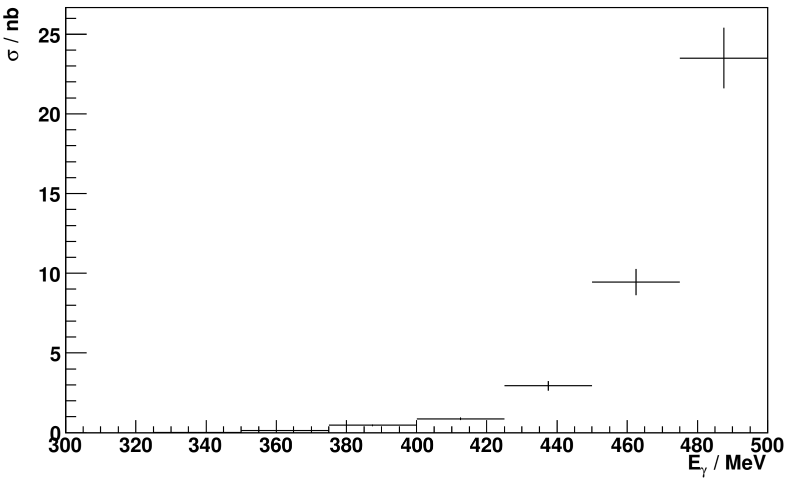

Figure 6.17: The effective cross section due to $p(\gamma, \pi^0\pi^0 p)$ contamination.

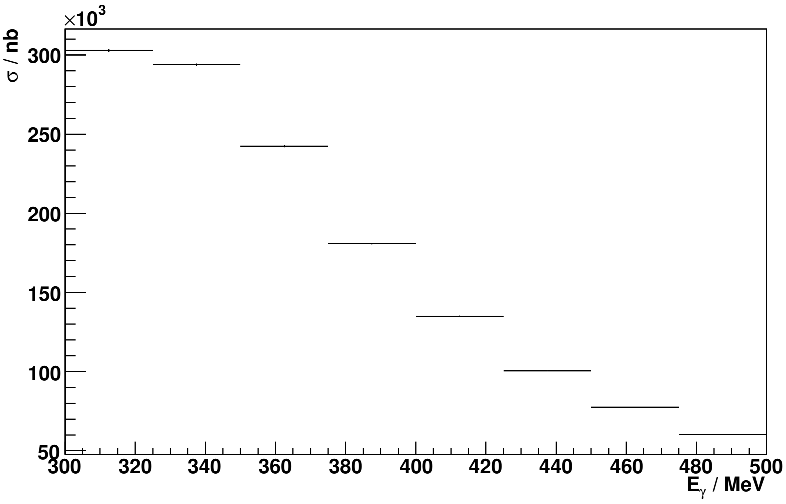

Figure 6.18: The cross section of $p(\gamma, \pi^0 p)$ from [23].

section is several orders of magnitude larger than that of $p(\gamma, \pi^0\pi^0 p)$, the resulting contamination was comparable in magnitude to that of $p(\gamma, \pi^0\pi^0 p)$. We found no single variable that would allow us to cleanly separate and gauge the level of the $p(\gamma, \pi^0 p)$ contamination as the π^0 invariant mass did for $p(\gamma, \pi^0\pi^0 p)$. Instead we formed an estimate of the $p(\gamma, \pi^0 p)$ contamination using the $p(\gamma, \pi^0 p)$ cross section measured in [23] in combination with the event acceptance level obtained from the simulation, as for $p(\gamma, \pi^0\pi^0 p)$ in Section 6.5.2.

First, we calculated the mean value of the cross section from [23] for each of our final $p(\gamma, \gamma'\pi^0 p)$ cross section E_γ bins, shown in Figure 6.18. We then worked out the fraction of $p(\gamma, \pi^0 p)$ events surviving all of our $p(\gamma, \gamma'\pi^0 p)$ event selection cuts for each E_γ bin (Figure 6.19), using the 3×10^6 event uniform phase space based $p(\gamma, \pi^0 p)$ simulated data set. By multiplying these two histograms, we found our final $p(\gamma, \pi^0 p)$ contamination to be as shown in Figure 6.20. This is far smaller than the $p(\gamma, \pi^0\pi^0 p)$ contamination at high E_γ, but provides a ~10% correction to the cross section in the lowest E_γ bin.

6.7 Cross Section

The total cross section of a reaction is the probability that, given a single proton and a single photon, the reaction under study would take place. It is expressed in terms of an area, usually in barns[2]. To produce a reaction cross section, one simply has to calculate the number of events that occurred in the experiment and divide that number by the product of the number of protons and photons available to the reaction. In our case, the Equation takes the form given in Equation 7.1.

$$\sigma = \frac{N_{events}}{S\epsilon_{tagg.}(\Gamma_{\pi^0}/\Gamma_{\pi^0\to\gamma\gamma})\rho_{target}\epsilon_{CBTAPS}} \tag{6.10}$$

---

[2] $1\ \text{cm}^2 = 1 \times 10^{24}$ barns

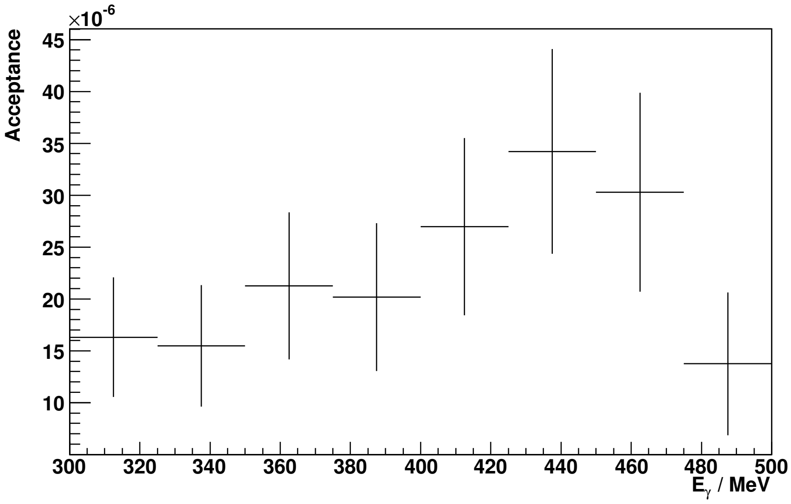

Figure 6.19: The acceptance of $p(\gamma, \pi^0 p)$ calculated from the simulation.

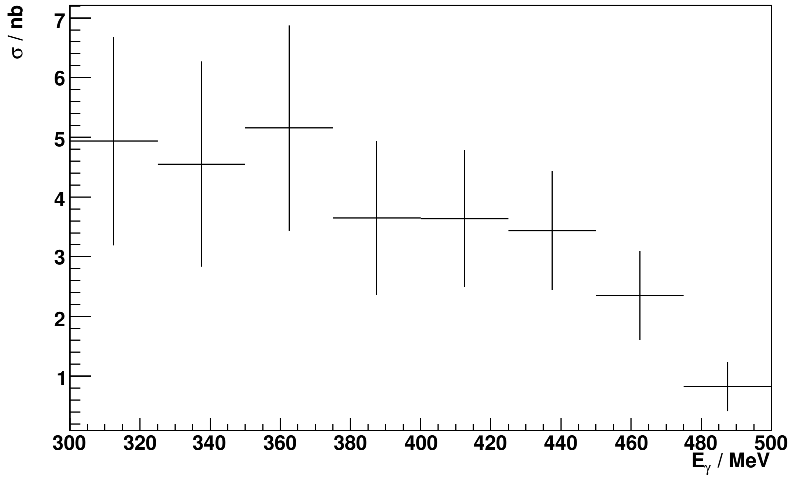

Figure 6.20: The effective cross section due to $p(\gamma, \pi^0 p)$ contamination.

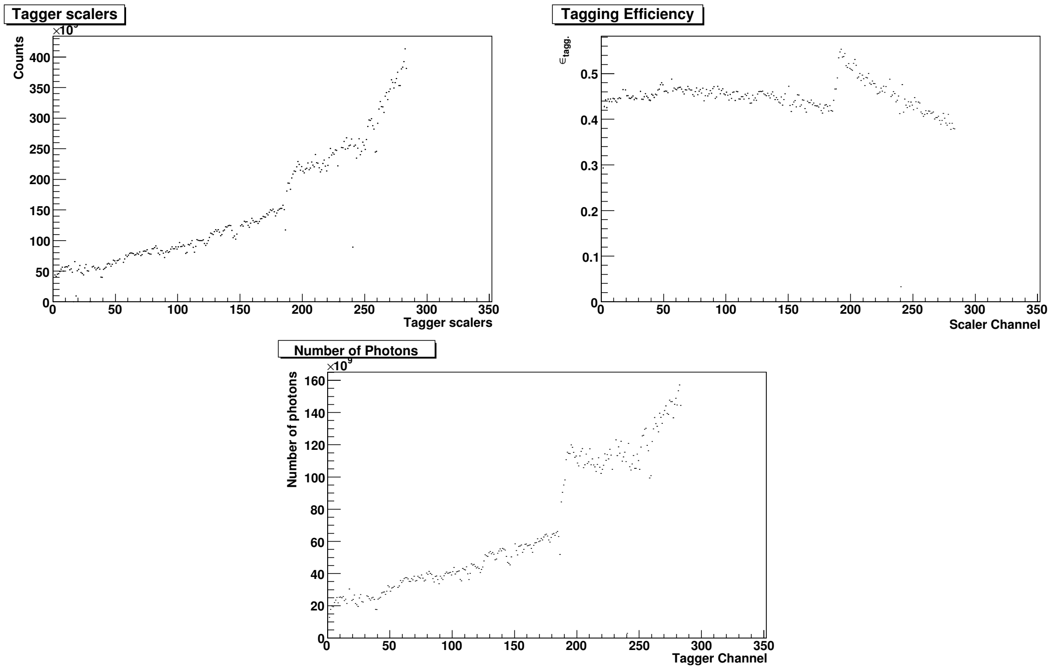

Figure 6.21: Tagger scalers (upper left), multiplied by the tagging efficiency (upper right) give the number of photons impinging on the target from each Tagger channel (lower histogram).

We calculate the number of photons available to the reaction by multiplying the total number of counts in the Tagger scalers (S) by the tagging efficiency ($\epsilon_{tagg.}$). The number of protons is given by the target areal density (ρ_{target}), expressed as nuclei per barn. We then scale the number of detected events according to the detector efficiency (ϵ_{CBTAPS}) and the branching ratio for $\pi^0 \to \gamma\gamma$ decay (($\Gamma_{\pi^0}/\Gamma_{\pi^0 \to \gamma\gamma}$) = 0.98798 [52]) to give the total number of π^0 producing reactions of interest that occurred.

To calculate the total cross section experimentally, as a function of the incoming beam energy, we have to calculate Equation 7.1 for each E_γ bin. Firstly we make a histogram of the Tagger scaler counts for each Tagger channel and the mean tagging efficiency (Section 5.2.4) for each channel as shown in Figure 6.21. The product of these two histograms (also shown in Figure 6.21) gives the number of photons impinging on the target in coincidence with the electron hits, Tagger channel by Tagger channel. We then sum the number of photons in each photon energy bin as shown in Figure 6.22 using the ladder energy calibration as described in Section 5.2.3 to give the correspondence between Tagger channel number and incident photon energy.

To determine the number of protons in the target, we use the known target temperature (21 K) and pressure (1080 millibar) to give us the target density of 70.55 kg/m^3 [19]. The target length was found to be 47.6 ± 0.3 mm by a combination of X-raying the target apparatus when cold and studying the deformation of the inside window (which cannot be seen on the x-ray) under cooling before the target was installed. We then divide the product of the density and target length by the known mass of a hydrogen atom (1.67×10^{-27} kg) to give us a target areal

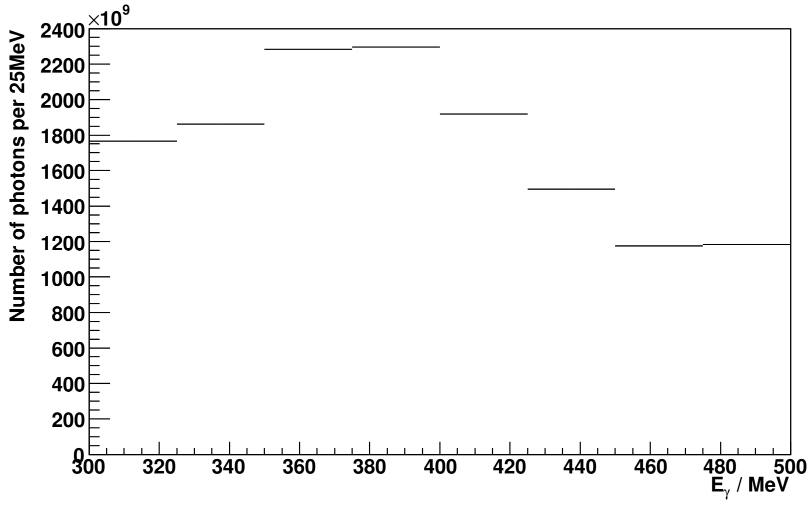

Figure 6.22: The total number of tagged photons in each E_γ bin for all beam times.

density of 0.20064 nuclei (protons) per barn.

To calculate the number of events, we begin by making a histogram of the total number of detected events of interest for each E_γ bin as shown in Figure 6.23. As the detector system is not 100% efficient, we must scale the number of detected events by the efficiency of the detector system to get the total number of events of interest that occurred during the experiment. To calculate this, we simply divide the number of simulated $p(\gamma, \gamma'\pi^0 p)$ events in each E_γ bin passing all of our analysis cuts by the number of events in that E_γ bin in the initial generated event file, giving the efficiency (ϵ_{CBTAPS}) as shown in Figure 6.24. To get the total number of events which occurred we must also scale by the branching ratio for $\pi^0 \rightarrow \gamma\gamma$ decay (($\Gamma_{\pi^0}/\Gamma_{\pi^0 \rightarrow \gamma\gamma}$) = 0.98798 [52]) as not all of the produced π^0s will decay by the $\pi^0 \rightarrow \gamma\gamma$ route that our analysis selects. This then gives us the total number of events that occurred during our experiment, as shown in Figure 6.25.

To obtain the total cross section, we divide the number of detected events by the target areal density (scaling Figure 6.25 by 1/0.20064), and divide the result by the number of photons impinging on the target (Figure 6.22) E_γ bin by E_γ bin, to give the results which are presented and discussed in Chapter 7.

6.8 Photon Asymmetry

The photon asymmetries and associated errors were calculated as described in Appendix C. We only calculated asymmetries for the July and September data sets as the January set was far smaller, had a slightly different Tagger energy calibration and a polarisation edge ~10 MeV lower than the September data set. Thus combining the January data with that from September would have caused an increase in systematic error greater than the decrease in statistical error due to the larger event sample.

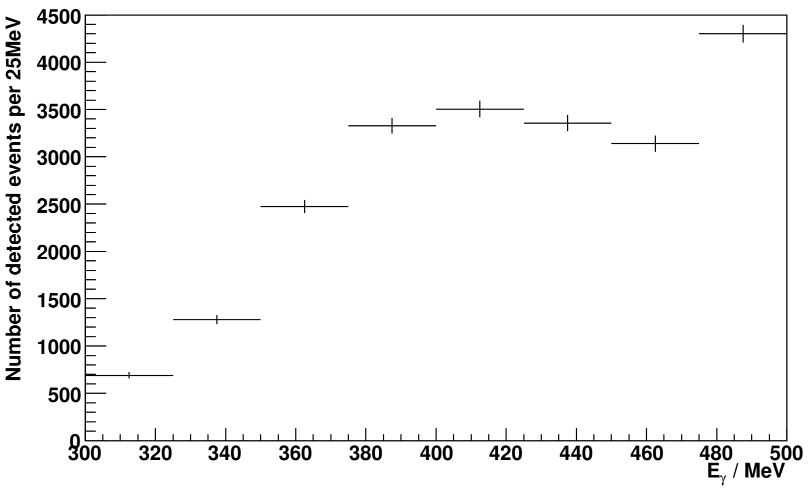

Figure 6.23: The total number of detected $p(\gamma, \gamma' \pi^0 p)$ events in each E_γ bin for all beam times.

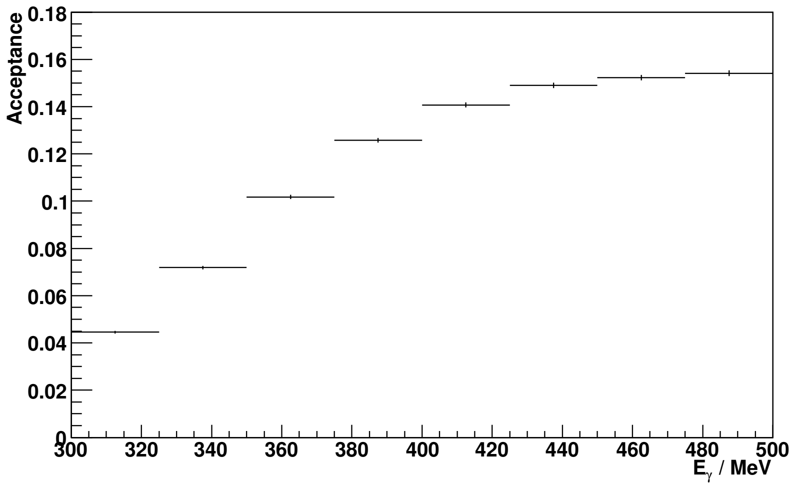

Figure 6.24: The efficiency of the CBTAPS system for $p(\gamma, \gamma' \pi^0 p)$ events as a function of E_γ.

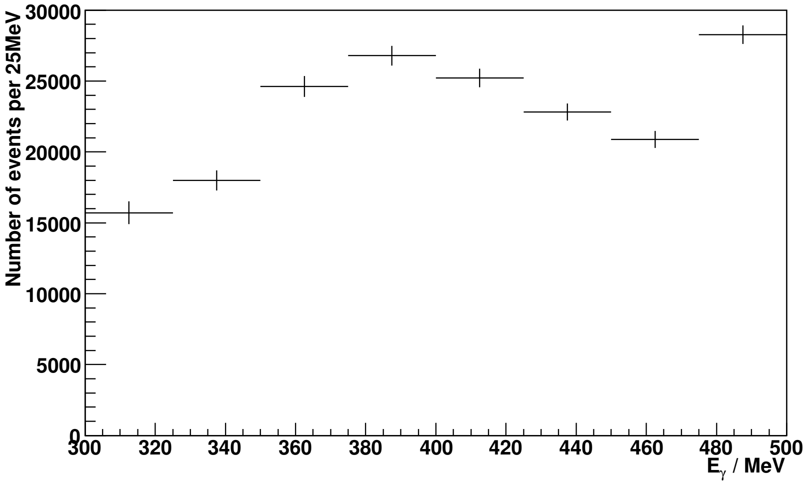

Figure 6.25: The total number of $p(\gamma, \gamma' \pi^0 p)$ events in each E_γ bin for all beam times.

As seen in Figure 6.14, very little $p(\gamma, \pi^0 \pi^0 p)$ contamination is observed below an incident photon energy of 450 MeV. To perform a full $p(\gamma, \pi^0 \pi^0 p)$ subtraction on each of the E_γ, $E_{\gamma'}$ and ϕ_{π^0} bins required for our asymmetry calculation would have required a far larger event sample than was feasible during the time scale of the present project. Instead, we rely on the fact that by fitting to the π^0 invariant mass distribution, we estimate the level of $p(\gamma, \pi^0 \pi^0 p)$ contamination to be 2.93% for the July data set (where we analyse E_γ from 340 MeV to 440 MeV), and 0.2% for the September data (where we analyse E_γ from 300 MeV to 400 MeV). The effect of this contamination will be discussed more fully in Chapter 7.

6.9 Analysis of $p(\gamma, \pi^0 p)$

In order to test for various systematic effects and to provide a cross check of our $p(\gamma, \gamma' \pi^0 p)$ analysis, we also examined $p(\gamma, \pi^0 p)$ for the same data set. The analysis was simple. We selected events with three clusters. We then looped through all three possible combinations of particles to reconstruct a π^0 and proton pair. We selected the combination which gave the azimuthal angle between the π^0 and proton closest to 180° and required that the two particles which reconstructed the best π^0 both be identified as photons. We then cut on a reconstructed π^0 invariant mass between 115 MeV and 155 MeV and a π^0 missing mass of between 898.2 MeV and 978.2 MeV.

We first analysed the set of all events which passed the above basic cuts. We then looked at three overlapping subsets of the selected data: (1) events in which the proton had been identified as a proton by the detector particle identification; (2) events for which it was possible to apply the proton energy correction; and (3) events in which both the proper proton identification and the proton energy correction had been made. Subset (3) had passed conditions closest to those required of our $p(\gamma, \gamma' \pi^0 p)$ data set, so should provide a good testing ground for our $p(\gamma, \gamma'\pi^0 p)$ analysis. Subsets (1) and (2) and the overall data set will be analysed to test our hypotheses on the possible causes of any observed systematic effect, but this was not possible within the time constraints of this work.

We produced a normalised excitation function for subset (3) which will be discussed in Chapter 7.

Chapter 7

Discussion of Results and Conclusions

7.1 Total Cross Section Results

Using the event reconstruction and selection techniques described in Chapters 5 and 6 we obtained our final event sample. We then determined the total cross section for $\gamma p \to \gamma' \pi^0 p$ and a normalised yield for $\gamma p \to \pi^0 p$ using Equation 6.10 (restated below for ease of reference):

$$\sigma = \frac{N_{events}}{S\epsilon_{tagg.}(\Gamma_{\pi^0}/\Gamma_{\pi^0\to\gamma\gamma})\rho_{target}\epsilon_{CBTAPS}}.$$

7.1.1 Total Cross Section of $\gamma p \to \gamma' \pi^0 p$

The total cross section of $p(\gamma, \gamma'\pi^0 p)$ was found using the method described in Section 6.7. The $p(\gamma, \pi^0\pi^0 p)$ background subtraction methods described in Section 6.5 were applied. In Figure 7.1, it is clear that the two methods of $p(\gamma, \pi^0\pi^0 p)$ background subtraction produce total $p(\gamma, \gamma'\pi^0 p)$ cross sections that agree up to around 450 MeV. Above that point, the two correction results diverge. However the region up to 450 MeV is the most important for both μ_{Δ^+} extraction and the accuracy of our final photon asymmetry results, so the divergence beyond this point is not of great concern in this work.

As the π^0 invariant mass-based subtraction (Section 6.5.1) produces smaller subtraction-related errors and relies only on the simulation and its fit to data – while the $p(\gamma, \pi^0\pi^0 p)$ cross section-based subtraction (Section 6.5.2) relies on the simulation and a previously measured cross section – we decided to adopt the π^0 invariant mass-based subtraction as our standard method of cross section determination.

We then subtracted the $p(\gamma, \pi^0 p)$ contamination using the method described in Section 6.6. The effect of the subtraction is shown in Figure 7.2. The increase in the final error due to the $p(\gamma, \pi^0 p)$ background subtraction can be minimised by increasing the size of the simulated background event sample.

Cross section determination and the subtraction of the two major background processes produced the results shown in Figure 7.3, where the cross section deter-

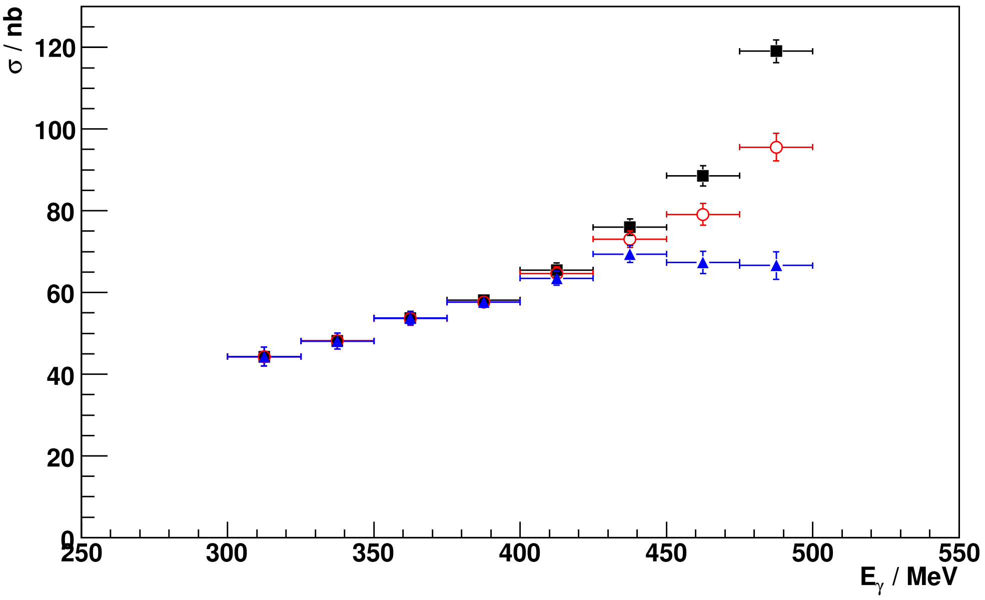

Figure 7.1: The $p(\gamma,\gamma'\pi^0p)$ cross section, before $p(\gamma,\pi^0p)$ subtraction, for the entire data set, illustrating the methods of $p(\gamma,\pi^0\pi^0p)$ subtraction. The square markers represent the raw $p(\gamma,\gamma'\pi^0p)$ cross section before $p(\gamma,\pi^0\pi^0p)$ subtraction, the open circles indicate the cross section after subtraction using the $p(\gamma,\pi^0\pi^0p)$ cross section measured in [23], and the triangles represent the cross section after subtraction by fitting to the π^0 invariant mass distribution. The subtraction methods agree well in the region $E_\gamma < 450$ MeV where both photon asymmetries and μ_{Δ^+} are evaluated.

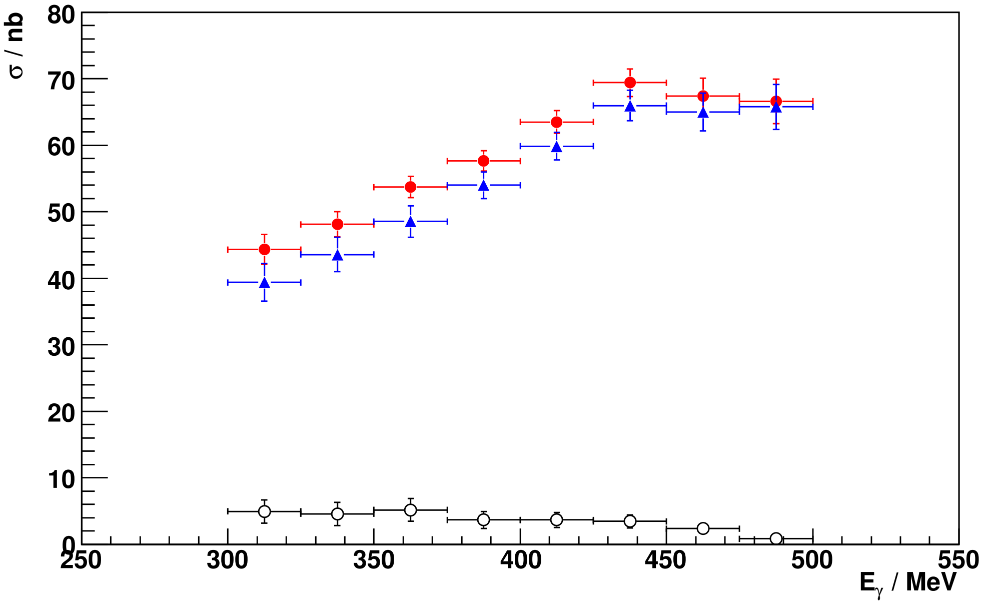

Figure 7.2: The $p(\gamma,\pi^0p)$ background subtraction from our $p(\gamma,\gamma'\pi^0p)$ cross section determination. Filled circles and triangles show the $p(\gamma,\gamma'\pi^0p)$ cross section for the full data set before and after $p(\gamma,\pi^0p)$ subtraction, respectively, and open circles show the $p(\gamma,\pi^0p)$ contamination calculated as described in Section 6.6.

mination is shown for each individual beam time and the full data set combined. The data from the short January beam time has relatively poor statistical accuracy and although the July and September data agree within errors, the July cross section is systematically higher than that from September. This bears further investigation. However, as all three beam period results agree within their statistical error bars, we combined the data from all three data sets to produce a cross section using the full ~20,000-event data set. Figure 7.4 shows this final total cross section for $p(\gamma,\gamma'\pi^0p)$ as compared to the previous measurement and the prediction of the χEFT model [9]. Full results are listed in Appendix D.

7.1.2 Normalised Yield for $\gamma p \rightarrow \pi^0 p$

$$\sigma = \frac{N_{events}}{S\epsilon_{tagg.}(\Gamma_{\pi^0}/\Gamma_{\pi^0\rightarrow\gamma\gamma})\rho_{target}\epsilon_{CBTAPS}} \tag{7.1}$$

The normalised yield of $p(\gamma,\pi^0p)$ was constructed using Equation 7.1. We used the same N_p, S, $\epsilon_{tagg.}$, $(\Gamma_{\pi^0}/\Gamma_{\pi^0\rightarrow\gamma\gamma})$, ρ_{target} and ϵ_{CBTAPS} values as the $p(\gamma,\gamma'\pi^0p)$ measurement. N_{events} represented the number of events selected using the methodology described in Section 6.9. The ϵ_{CBTAPS} was based on an analysis of the uniform phase space based $p(\gamma,\pi^0p)$ simulated event set using the selection criteria defined in Section 6.9. The normalised yield was measured purely as a check of our cross section normalisation and to see if the systematic effects observed in the $p(\gamma,\gamma'\pi^0p)$ channel were replicated here. We found that the July data set once again gave a systematically higher cross section than the September

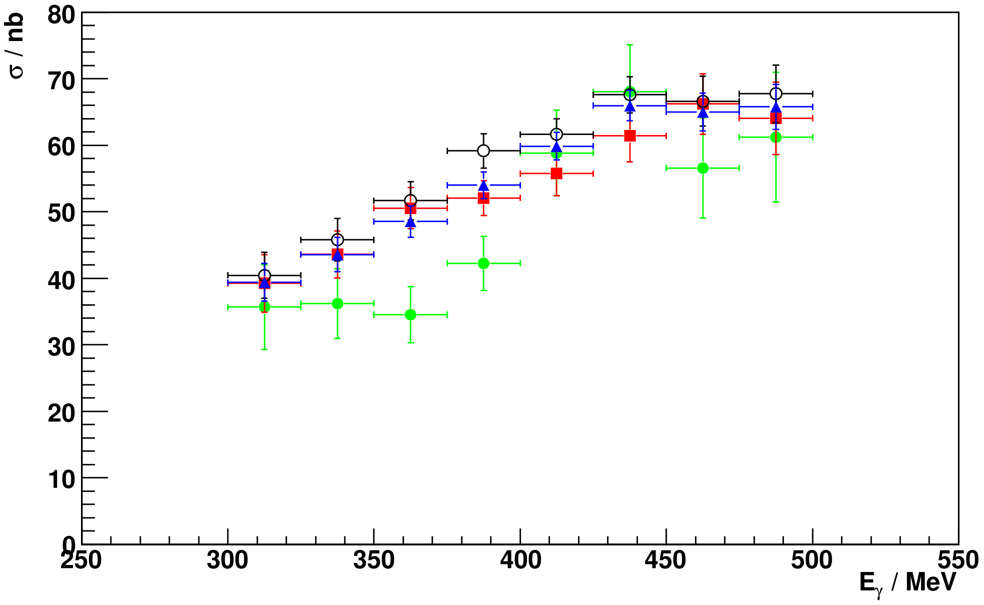

Figure 7.3: The $p(\gamma, \gamma'\pi^0 p)$ cross section for each of the beam times. Open circles show the $p(\gamma, \gamma'\pi^0 p)$ cross section for the July beam time, filled squares show that from September, filled circles show that from January, and triangles show the cross section calculated from the entire data set from all three beam times combined.

data set. The normalised excitation function reproduced the expected shape of the $p(\gamma, \pi^0 p)$ cross sections reported in [23, 24] (Figure 7.5). At high E_γ, our normalised yield agrees well with the previous cross section measurements by Kotulla [23] and Leukel [24]. However, at low E_γ it can be seen that our normalised yield is around 20 % smaller than the prior results due to deficiencies in the acceptance calculation which are discussed below.

7.1.3 Systematic Error in Cross Section Measurements

As the target length when cold was established by making an X-ray image of the target when it was at the standard temperature of 21 K, the target length is known with a precision of ±1%. During experimental running the pressure in the target cell was never more than 20 mbar away from the standard value (1080 mbar). A 20 mbar fluctuation would cause a density fluctuation of ±0.1%. Allowing $\sim$ 1% for temperature fluctuations, we estimate the uncertainty in N_p (Equation 7.1) to be of the order of ±2%.

To truly test the effect of the tagging efficiency variation, we constructed a minimum and maximum tagging efficiency by running through all of the tagging efficiency measurements for the July run and recording the extreme values for every single channel (Figure 7.6). We then used the artificially constructed minimum and maximum tagging efficiency data sets in place of the average and found the artificially low/high cross sections to be 94.9%/105.1% of the cross section val-

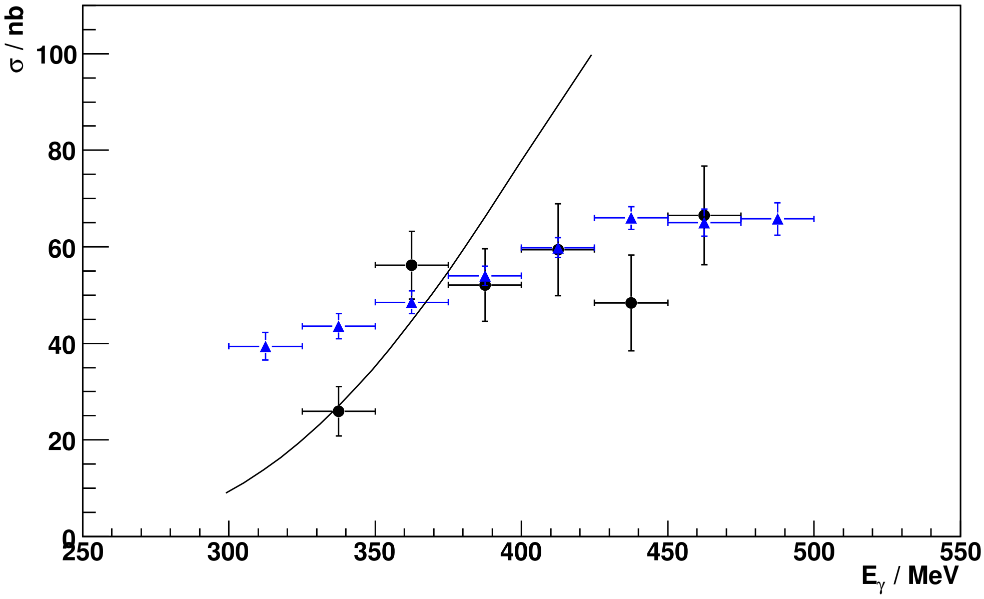

Figure 7.4: The final $p(\gamma, \gamma' \pi^0 p)$ cross section. Triangles show the cross section from this work and circles show that determined in [23]. The solid line shows the prediction of the χEFT model [9]. The χEFT model is currently undergoing further development, which should bring the model prediction closer to the measured cross section. The final results from this work represent a vast improvement in statistical error over the previous measurement.

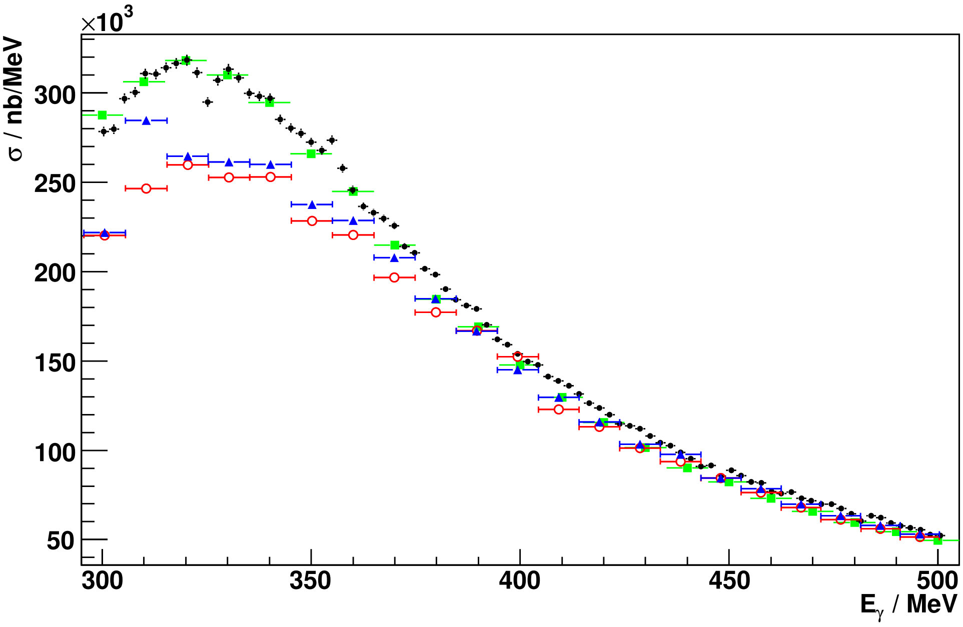

Figure 7.5: The normalised yield for $p(\gamma,\pi^0p)$ from this work compared to the cross section measured in [24] (squares) and [23] (filled circles). Triangles show the yield from the July data set, open circles show that from the September data set. After the simulation is extended to include trigger effects we expect the low E_γ discrepancy to vanish (see Section 7.1.3).

ues obtained using the mean tagging efficiency measurement. As these extremes of tagging efficiency combined the extremes of every channel in one measurement and so would not normally occur, we estimate that a systematic error of $\leq 2.5\%$ is more representative of the true variation.

In order to correct the cross section for acceptance effects, we used a detection efficiency based on the gppi0b simulated event data set as described in Section 6.1. The gppi0b-derived ϵ_{CBTAPS} was selected as the simulation results produced from the gppi0b input file agreed with the final experimental kinematic distributions more closely than those derived from the gppi0a input file (see Figures 7.7, 7.8 and 7.9). In order to investigate the effect of this choice, we evaluated the cross section using the efficiencies derived from both simulated event sets separately. We then looked at the result of dividing the cross section derived from the gppi0a by the cross section derived from gppi0b (Figure 7.10). From this we estimate that the "toy" models used to generate simulated events induce a cross section error of <5 %.

In addition to the systematic error of ±4.5% resulting from the target areal density and the photon flux, we believe that there is considerable uncertainty in our cross section measurements due to the detector acceptance normalisation (ϵ_{CBTAPS}) from the simulation. This uncertainty results from several factors:

1. As explained in Section 6.1, for the simulation to produce an accurate ϵ_{CBTAPS} it requires a generated event set which matches the kinematic

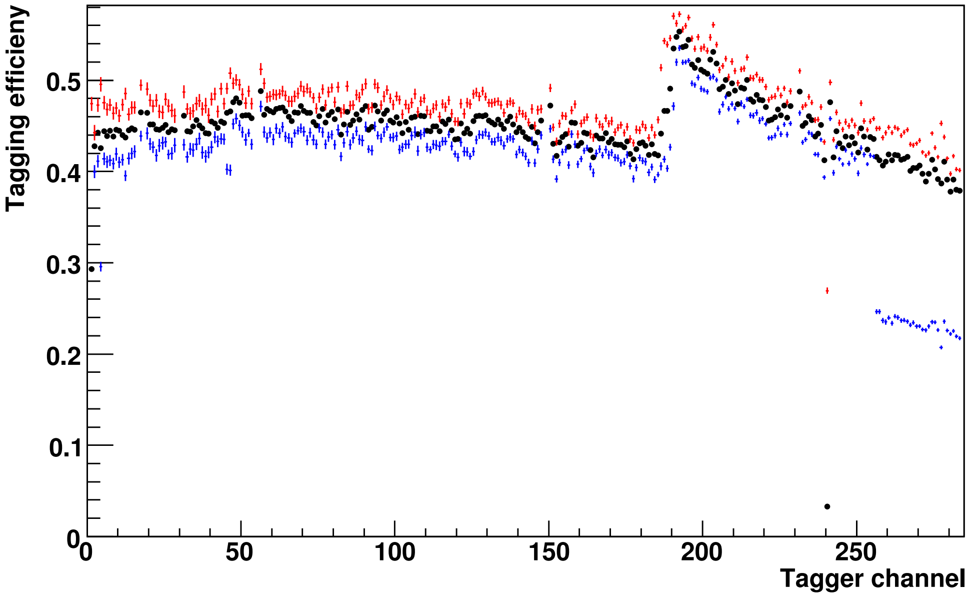

Figure 7.6: Systematic tagging efficiency error evaluation. Crosses show the maximum and minimum recorded tagging efficiencies for each channel and the circles show the mean tagging efficiency for each channel used in the final cross section calculations. The enhancement in tagging efficiency around channel 200 is due to the forward-peaking of the coherent bremsstrahlung which results in a sharp increase in tagging efficiency at the coherent edge.

distributions of the final data set well. As can be seen from Figures 7.7, 7.8 and 7.9, the simulation results don't match the observed energy and polar angle distributions as well as they should for $p(\gamma, \gamma'\pi^0 p)$. This can be partly explained by our input generated event set which was based on very simple principles for $p(\gamma, \gamma'\pi^0 p)$ (Section 6.1). The full model-based $p(\gamma, \gamma'\pi^0 p)$ event generator was not available when the simulations were run, and we estimate that it will alter the final cross section by <5 % as discussed above. This effect is even greater for $p(\gamma, \pi^0 p)$ as this was normalised using only a very basic uniform phase space distribution.

2. The Crystal Ball simulation was mature when the CB-TAPS detector setup began operation, however it had only been used for photon-based Crystal Ball-only experimental simulations. The charged particle response of the Crystal Ball had not been extensively studied and the exit tunnel geometry had never been important, so was not developed to the level of accuracy required to evaluate the combined CB-TAPS acceptance properly.

3. The other detectors: TAPS, the PID and MWPC, have been added to the simulation, but their responses are not yet fully developed, and some areas of their geometry such as the PID and MWPC electronics are not adequately modelled (see Section 6.1.2). The forward angle electronics and TAPS particle identification are areas in urgent need of study, as can be seen in Figure 7.9 where the simulated TAPS proton detection exceeds that observed by more than a factor of three. We were unable to improve upon this situation before the production of these results, however further study and improvement is underway.

4. The final issue is that of the experimental trigger. This is not yet incorporated in the detector simulation. In Section 4.6.1 we explain how the highest level multiplicity triggers are constructed by counting the number of sectors (logical ORs of 16 crystals in the CB or 90° sectors in TAPS) which meet the required energy thresholds. The experiment ran with a multiplicity 3 (M3) trigger in conjunction with a prescaled multiplicity 2 (M2) trigger (reduced by a factor of 48). The software clustering algorithm does not group the detector elements in the same way as the experimental multiplicity triggers, and to reduce the rate due to the low angle background in TAPS the three innermost TAPS detector rings were not included in the cluster multiplicity trigger. Therefore, although we may require events with a minimum of three software-determined clusters to form $p(\gamma, \pi^0 p)$ events in our analysis, there is a possibility that a large fraction of these events were read out due to an M2 rather than an M3 trigger and so were downscaled by a factor of 48. This is less important for the main $p(\gamma, \gamma'\pi^0 p)$ analysis as we require four clusters, three of which have a spacing of greater than 30° so this makes it highly unlikely that events surviving our software cuts (which are also applied to the Monte Carlo data) have resulted from an M2 trigger.

Although the systematic effect due to the poorly known ϵ_{CBTAPS} is currently far larger than that due to either that tagging efficiency or target density, this error has a far greater potential for improvement. We believe that, with careful improvement of the simulation, the uncertainty in ϵ_{CBTAPS} may be reduced to the same order as the other systematic contributions.

7.1.4 Discussion of Total Cross Sections

We see a systematic difference between the July and September results for both $p(\gamma, \gamma'\pi^0 p)$ cross sections and $p(\gamma, \pi^0 p)$ normalised yield. This effect is small, and, for $p(\gamma, \gamma'\pi^0 p)$, smaller than the statistical error. This difference may be due in part to the damage caused to the PID during the target dismount which occurred after the July beam times and so would affect the September and January data sets. This effect may be corrected for when we adjust the PID scintillator efficiencies in the simulation, this was not possible within the scope of the present work due to time constraints. However, the effect is sufficiently smaller than the statistical uncertainty to allow combination of all three data sets for the evaluation of the $p(\gamma, \gamma'\pi^0 p)$ total cross section.

The $p(\gamma, \pi^0 p)$ normalised yields are significantly lower than previous measurements for $E_\gamma < 375$ MeV. As explained above, these yields are much more strongly affected by the inadequacies of the ϵ_{CBTAPS} calculation than the $p(\gamma, \gamma'\pi^0 p)$ measurement. This effect is strongest at low E_γ where the probability of the event causing an M3 trigger is lower due to the lower cluster energies involved. Thus low energy events are more likely to be caused by an M2 trigger and hence be prescaled. This is not accounted for in the simulation.

More work must be done both on the event-generator models and on the detector models in the simulation code in order to produce a sound absolute normalisation for the data and therefore a credible cross section for $p(\gamma, \pi^0 p)$ over the whole E_γ range. Only once these corrections are complete will the $p(\gamma, \pi^0 p)$ cross sections be truly ready for comparison with the published data.

The ϵ_{CBTAPS} calculation is better for $p(\gamma, \gamma'\pi^0 p)$, and the resulting cross section agrees well with the total cross section from [1, 23]. However, we anticipate that the final cross sections may change by up to $\sim 10\%$ as the ϵ_{CBTAPS} calculation is improved. The subtraction of $p(\gamma, \pi^0 p)$ contamination from our data set could also be improved by increasing the size of the simulated event set. Forming the simulation input event set on the basis of a realistic model of the $p(\gamma, \pi^0 p)$ reaction rather than the simple uniform phase-space distribution would further improve the accuracy of the subtraction. The χEFT model prediction does not agree well with the data, however, this model is in an earlier stage of development than the Unitary model (for the latest iteration of which model predictions of total cross section were not available). For the final extraction, the ratio of the $p(\gamma, \gamma'\pi^0 p)$ to $p(\gamma, \pi^0 p)$ cross sections will be compared to the model predictions as this removes some of the systematic differences between both models and the data. As can be seen in Figure 7.5, we are not yet at a stage where this can be calculated with any confidence from the measured cross sections.

However, although the absolute normalisation of the cross sections still requires some work, the main point we can draw from our cross section studies is

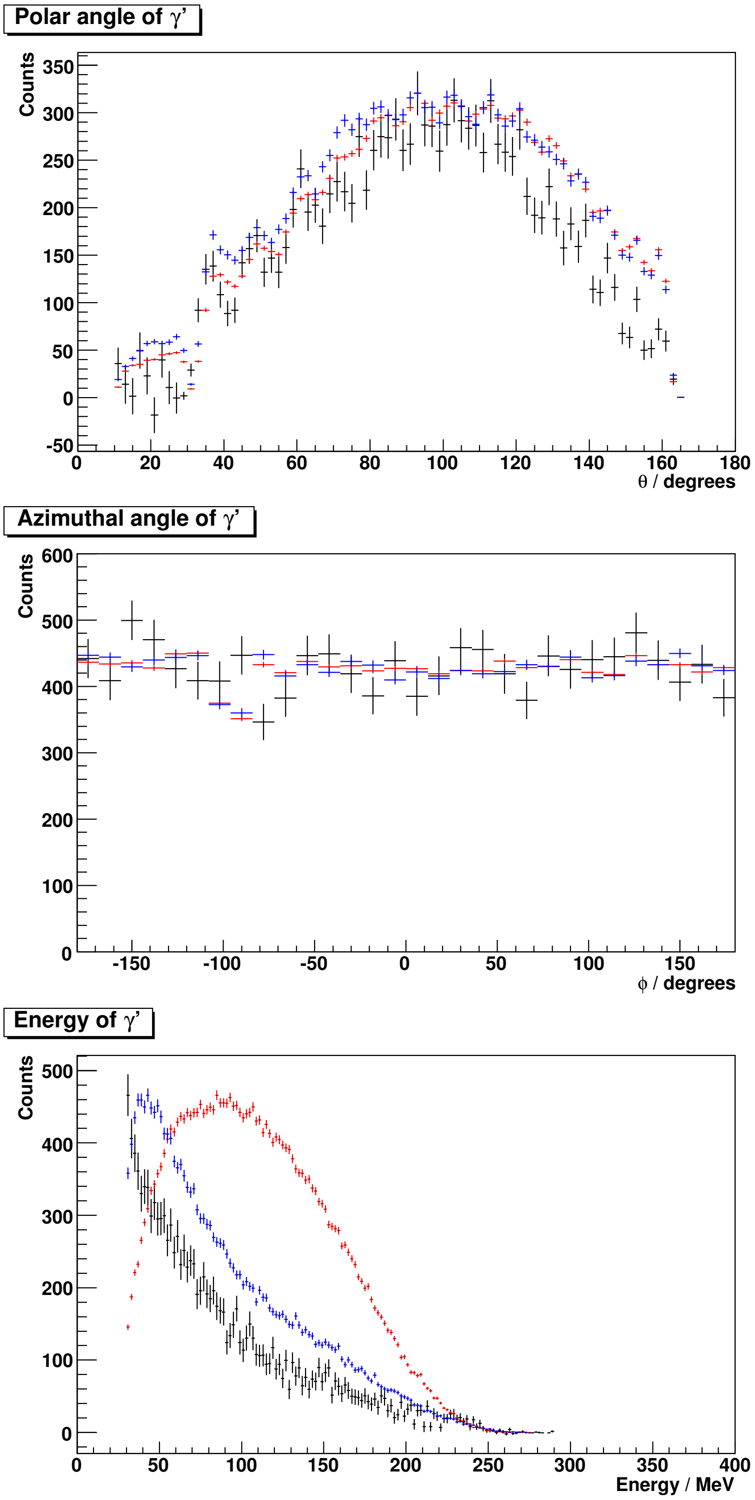

Figure 7.7: Kinematic distributions of final state γ' in the centre-of-mass frame for the July data set: polar angle (upper panel), azimuthal angle (middle panel) and energy (lower panel). Black crosses correspond to the final July data set, red to the gppi0a simulated data set and blue to the simulated gppi0b data set. The gppi0b simulation results agree well with the real data, with only slight disagreement in the $E_{\gamma'}$ spectrum, which should be remedied by the adjustments to the simulation listed in 7.1.3.

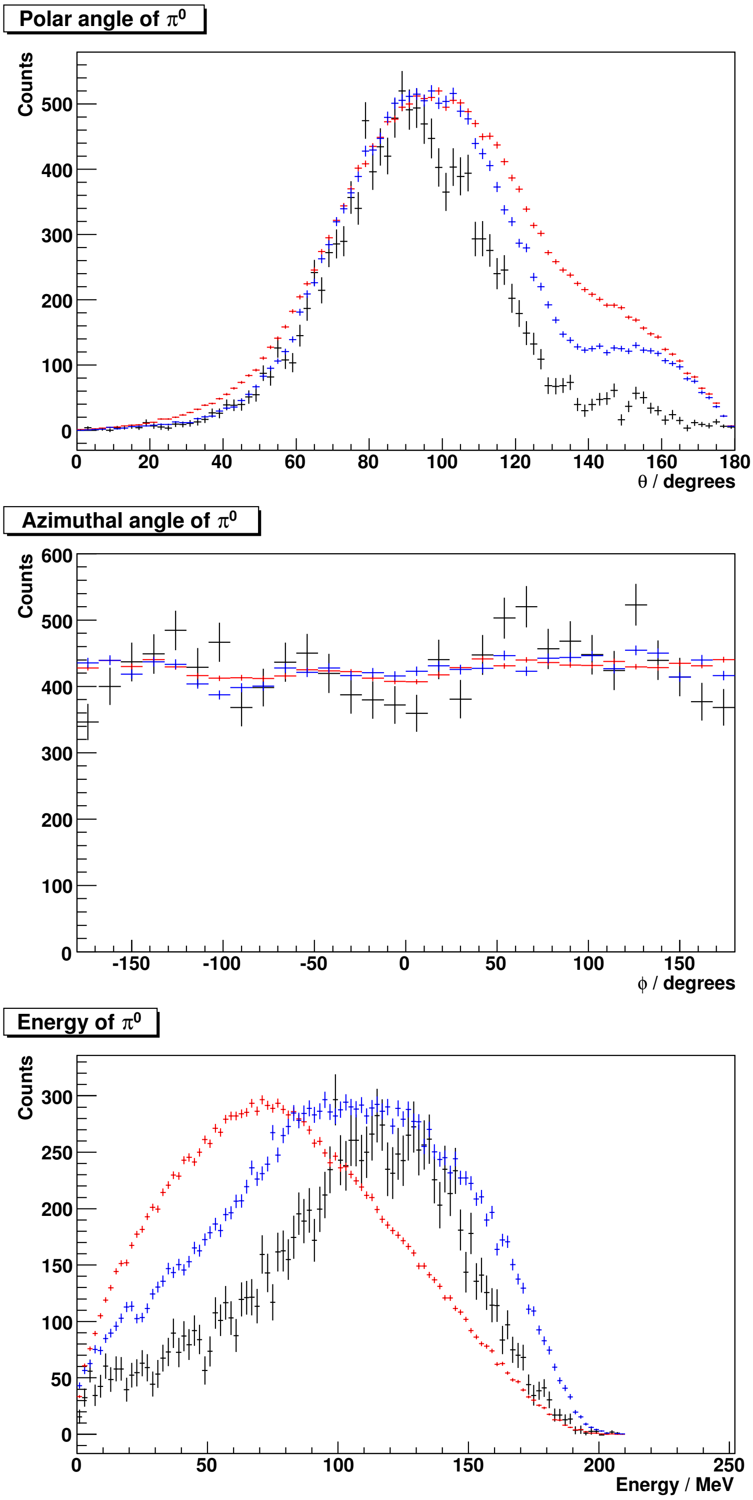

Figure 7.8: Kinematic distributions of final state π^0 in the centre-of-mass frame for the July data set: polar angle (upper panel), azimuthal angle (middle panel) and energy (lower panel). For further notation see Figure 7.7. The gppi0b simulation results agree with the experimental data better than gppi0a. The slight disagreement in the θ_{π^0} and E_{π^0} spectra should be remedied by the adjustments to the simulation listed in 7.1.3.

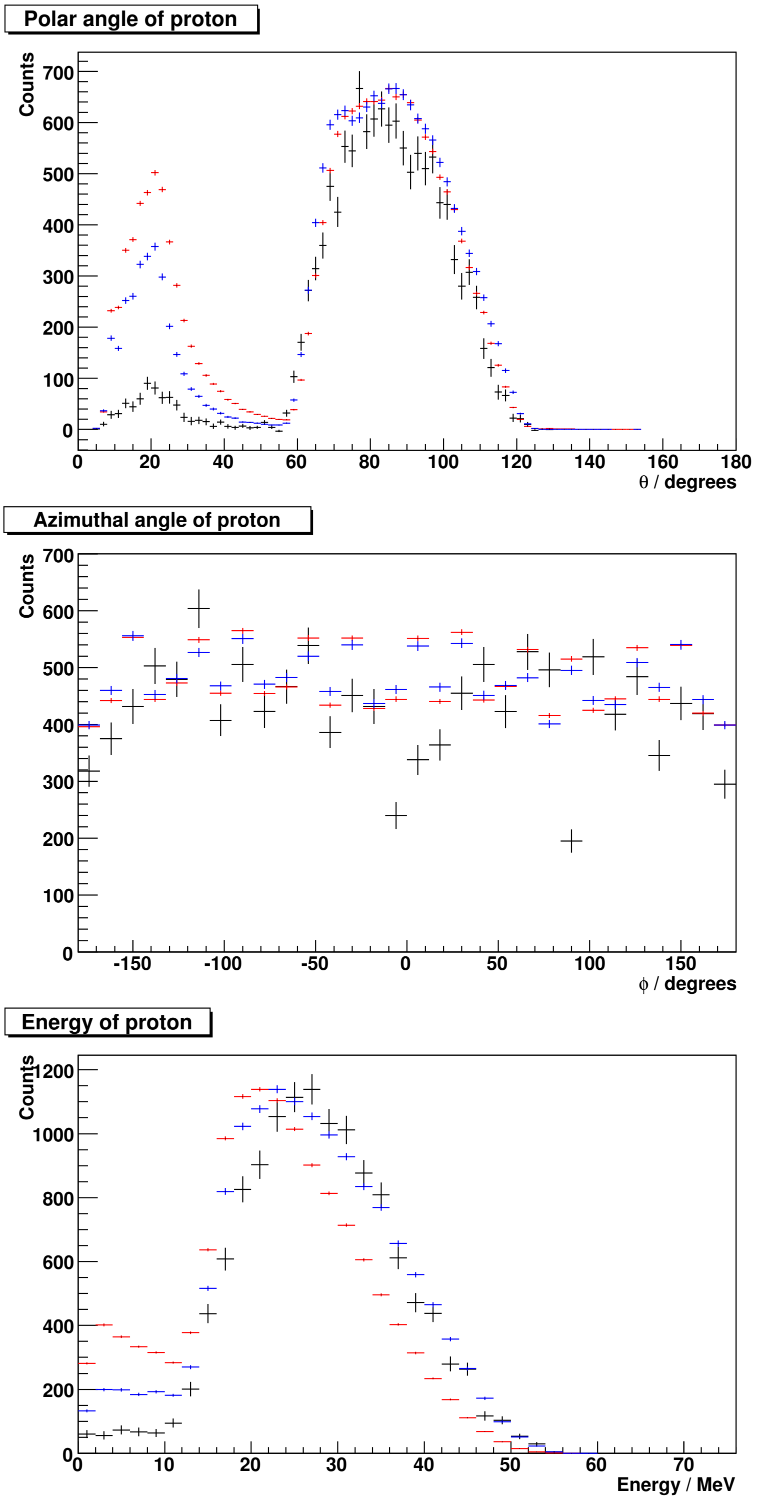

Figure 7.9: Kinematic distributions of final state proton in the centre-of-mass frame for the July data set: polar angle (upper panel), azimuthal angle (middle panel) and energy (lower panel). For further notation see Figure 7.7. Again the gppi0b simulation results agree with the experimental data better than gppi0a. The disparity between the simulation results and experimental data at low θ_p should be remedied by the adjustments to the simulation listed in 7.1.3.

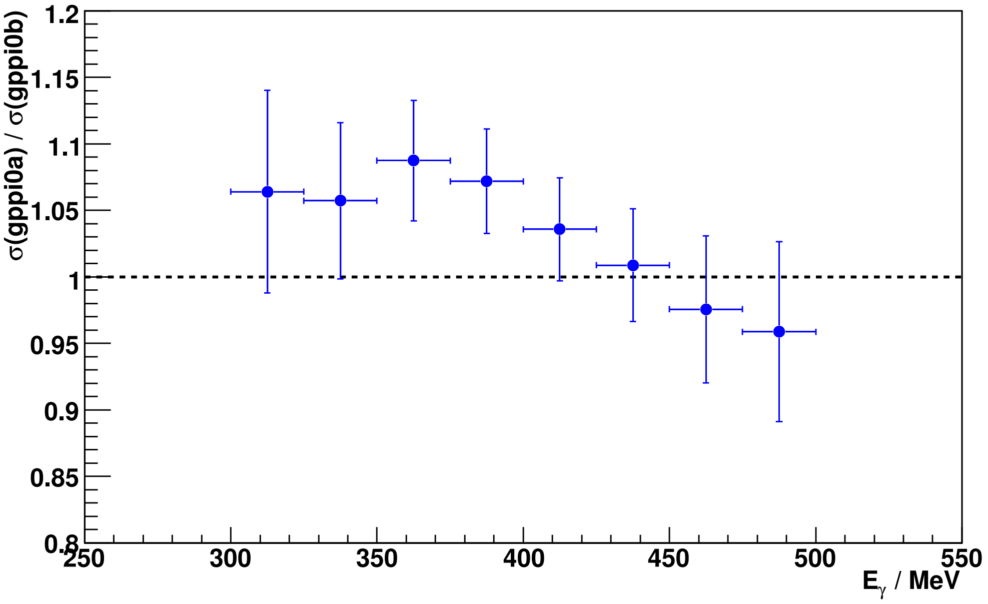

Figure 7.10: Ratio of cross sections derived using event generator models gppi0a and gppi0b. The gppi0a-derived cross section is divided by that from gppi0b. The difference between the gppi0a and gppi0b simulation models is far larger than the difference between the gppi0b simulated data and the experimental results (as can be seen in Figures 7.7, 7.8 and 7.9), thus we expect the uncertainty due to the input generated event set to be smaller than the deviations observed here.

that our two methods of $p(\gamma,\pi^0\pi^0p)$ background subtraction agree in their resulting $p(\gamma,\gamma'\pi^0p)$ total cross sections for E_γ up to 450 MeV. Thus we can conclude that we understand this contamination well and can make proper estimate of its effect on the resulting photon asymmetries.

It should also be noted that the main purpose of this work is to observe the photon asymmetry of $p(\gamma,\gamma'\pi^0p)$. The absolute normalisation coefficients cancel out in an experimental photon asymmetry measurement, as explained in Appendix C. Thus, although of some concern, the uncertainty in the absolute cross section normalisation due to the underdevelopment of the simulation package does not remove the validity of our final resulting asymmetries and therefore does not prevent us achieving the primary goal of this work.

7.2 Photon Asymmetry of $\gamma p \to p\pi^0\gamma'$

We obtained the $\cos(2\phi)$ distributions shown in Figure 7.11 using the event reconstruction and selection techniques described in Chapters 5 and 6 and the asymmetry construction detailed in Appendix C. We then fitted the function

$$\Sigma(\phi) = A\cos(2\phi - 0.5625^\circ) + c$$

(as described in Appendix C) to the resulting distributions. The photon asymmetry for all θ_{π^0} and all $E_{\gamma'}$ was found to be 0.404 ± 0.087 for 340 MeV $< E_\gamma <$ 440 MeV and 0.571 ± 0.097 for 300 MeV $< E_\gamma <$ 400 MeV (Figure 7.11).

After evaluating the photon asymmetry for the whole data set, we subdivided it into $E_{\gamma'}$ bins in order to evaluate the variation of photon asymmetry with $E_{\gamma'}$. The results are shown in Figure 7.12.

In the calculation of our systematic error we accounted for two factors: (1) errors in the absolute degree of linear polarisation and (2) contamination by $p(\gamma,\pi^0\pi^0p)$ events. It was not reasonable to subtract the $p(\gamma,\pi^0\pi^0p)$ contamination from each event sample bin-by-bin as this would involve subtracting the contamination individually for each para/perp, $E_{\gamma'}$ and ϕ_{π^0} combination. This would rely on the $p(\gamma,\pi^0\pi^0p)$ simulation to an even greater extent than the cross section determination. As the acceptance for $p(\gamma,\pi^0\pi^0p)$ was estimated using an event set generated as a uniform-phase-space distribution, this would result in a massive model-based error. Instead, we observed that the shift in the photon asymmetry caused by any background process can be calculated as

$$\Delta(\Sigma_\alpha) = \frac{N_\beta}{N_\alpha + N_\beta}(\Sigma_\beta - \Sigma_\alpha) \tag{7.2}$$

where Σ_α and N_α are the photon asymmetry and number of events of the desired type (α) in the event sample and Σ_β and N_β are the equivalent variables for background channel β. The worst case scenario occurs when α and β have an asymmetry of 1, but with opposite sign. In that case, the maximum $\Delta(\Sigma)$ is twice the proportion of the final event sample which results from the background process under consideration, e.g $2 \times (N_\beta/(N_\beta + N_\alpha))$. Thus, to evaluate the maximum possible influence of $p(\gamma,\pi^0\pi^0p)$ contamination, we have to work out the

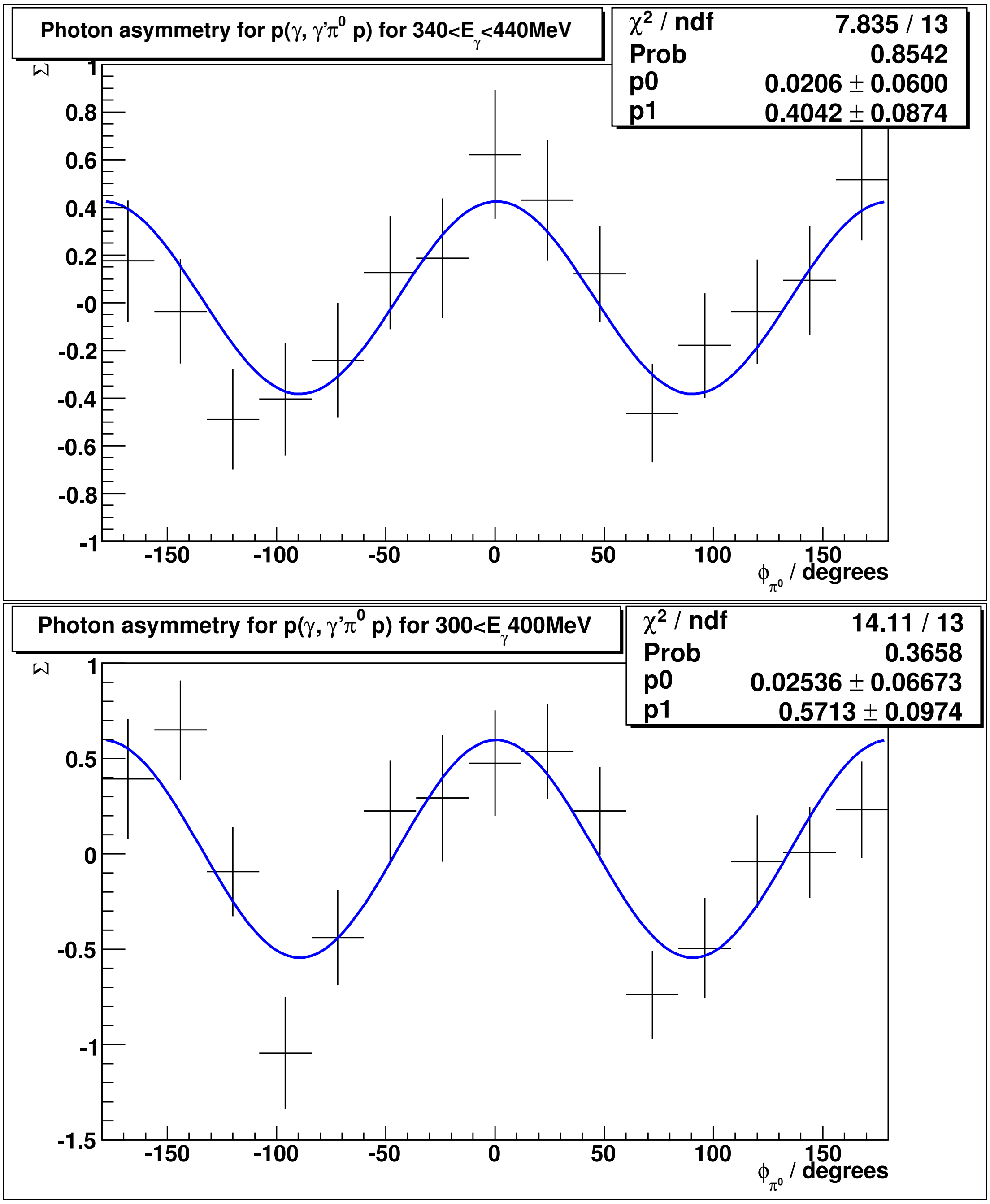

Figure 7.11: Cos(2ϕ) fit to the $p(\gamma, \gamma'\pi^0 p)$ azimuthal distribution for all θ_{π^0} and $E_{\gamma'}$ using: July data set with 340 MeV $< E_\gamma <$ 440 MeV (upper panel) and September data set with 300 MeV $< E_\gamma <$ 400 MeV (lower panel). Plots show statistical error only.

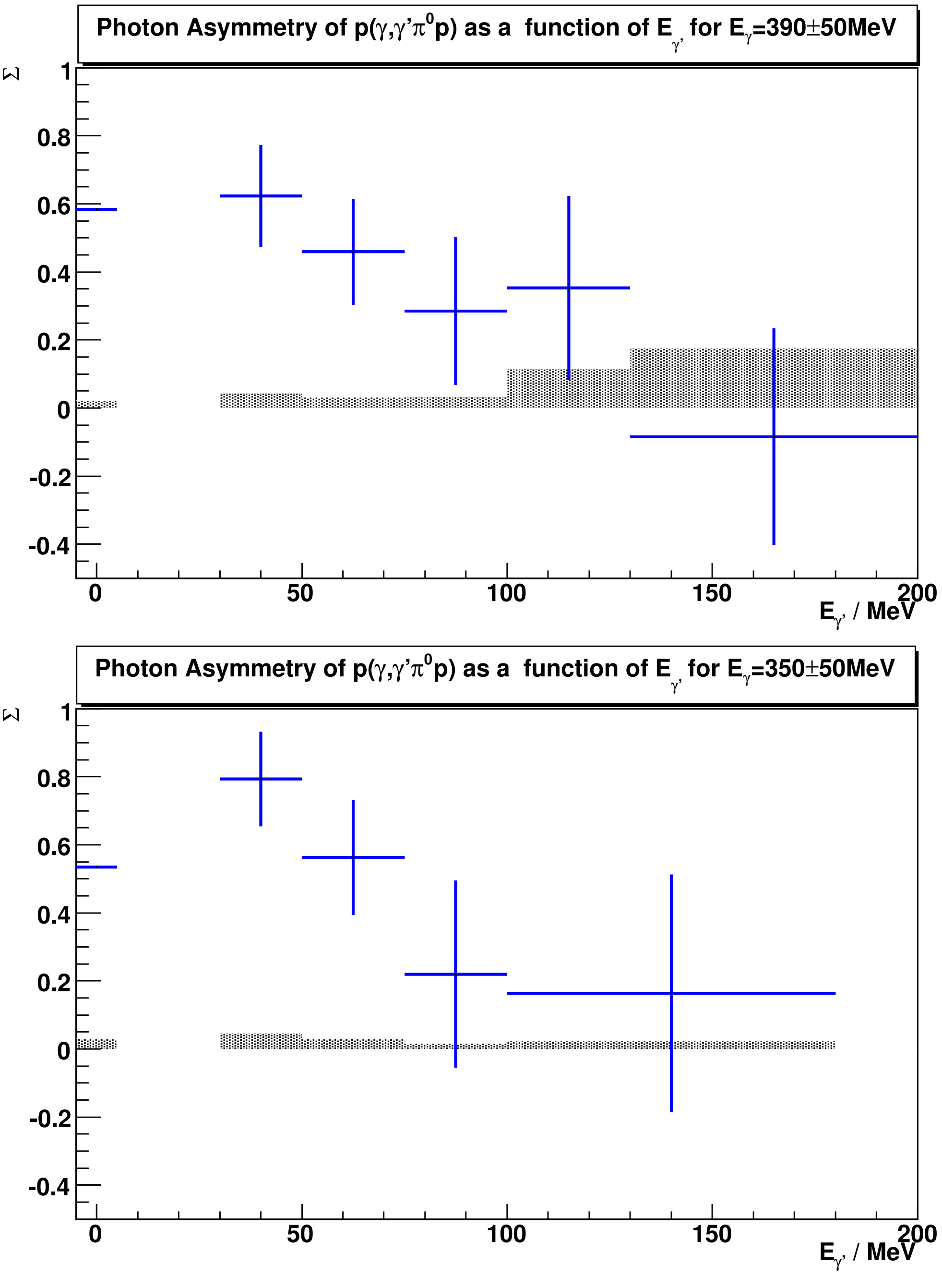

Figure 7.12: Variation of asymmetry with $E_{\gamma'}$ for $p(\gamma,\gamma'\pi^0p)$ for all θ_{π^0} and $E_{\gamma'}$ using: July data set with 340 MeV $< E_\gamma <$ 440 MeV (upper panel) and September data set with 300 MeV $< E_\gamma <$ 400 MeV (lower panel). The points at $E_{\gamma'} = 0$ MeV are derived from the analysis of $p(\gamma,\pi^0p)$ with the same cuts as $p(\gamma,\gamma'\pi^0p)$. Points show statistical error bars, grey-shaded bars show the magnitude of the absolute systematic error in each bin. The smaller systematic uncertainty for 300 MeV $< E_\gamma <$ 400 MeV is due to the factor of $\sim$10 lower $p(\gamma,\pi^0\pi^0p)$ contamination. The model predictions are shown in Figure 7.13 for comparison.

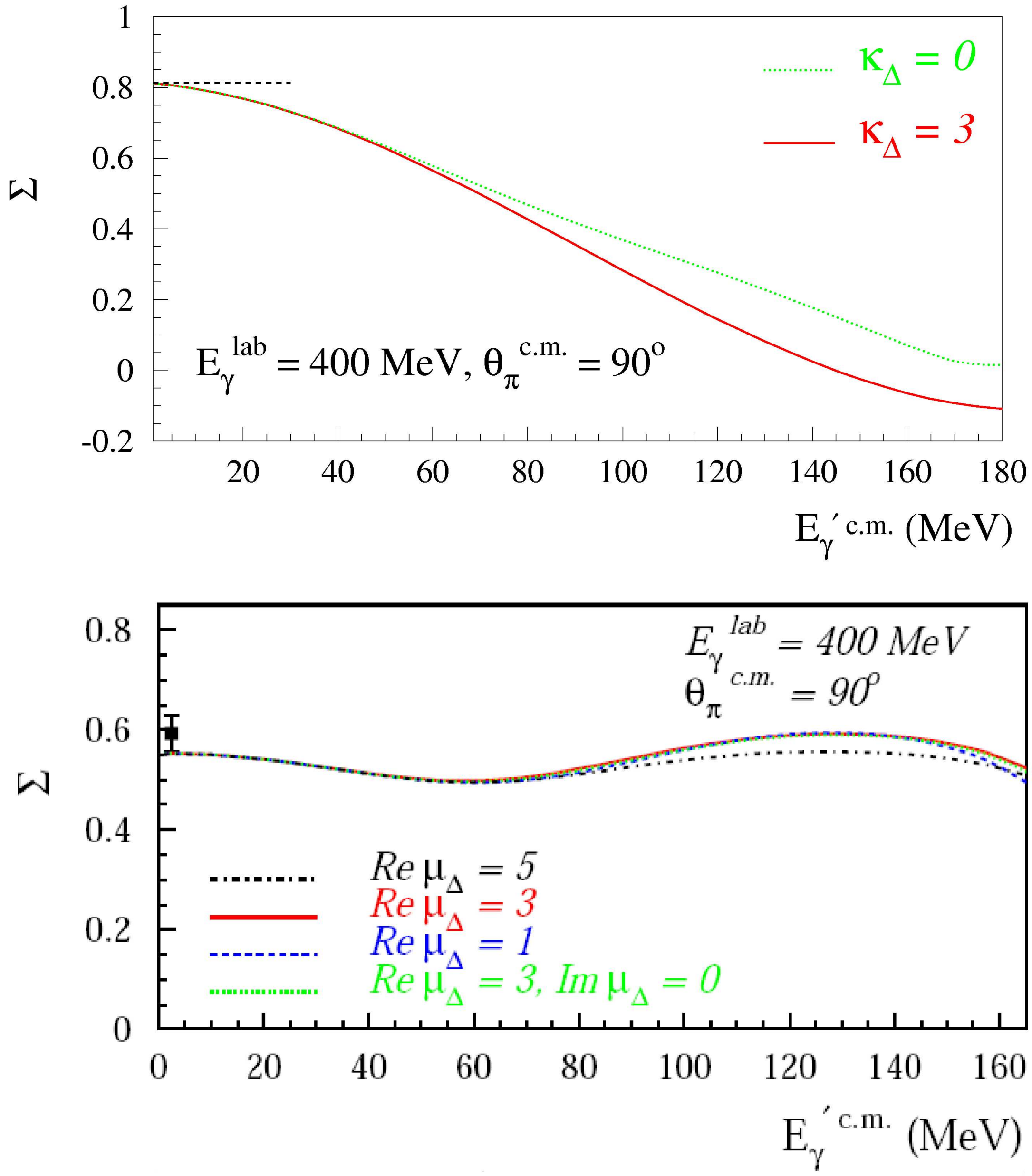

Figure 7.13: Variation of asymmetry with $E_{\gamma'}$ for $p(\gamma, \gamma'\pi^0 p)$ as predicted by the Unitary model (upper panel) and the χEFT model (lower panel). The Unitary model result appears to agree better with the data shown in Figure 7.12 than the χEFT model.

proportion of events in each $E_{\gamma'}$ bin that result from the $p(\gamma,\pi^0\pi^0 p)$ background. We estimated the total level of $p(\gamma,\pi^0\pi^0 p)$ contamination in the 340 MeV $< E_\gamma <$ 440 MeV July sample and the 300 MeV $< E_\gamma <$ 400 MeV September sample using the π^0 invariant mass fit (Section 6.5), which gave 2.93 % and 0.199 % respectively (Figure 7.14). We then scaled the $E_{\gamma'}$ distribution obtained from the simulated $p(\gamma,\pi^0\pi^0 p)$ simulation results until it accounted for the appropriate proportion of the whole event sample. It was then possible to calculate on a $E_{\gamma'}$-bin-by-$E_{\gamma'}$-bin basis what fraction of the involved events came from $p(\gamma,\pi^0\pi^0 p)$ - see Figure 7.14. As the maximum possible change in Σ is twice the fraction of $p(\gamma,\pi^0\pi^0 p)$ contamination in each bin, and the minimum change would be zero (when the asymmetry in the background process is the same as that in the process of interest), we took the mean value - the fraction of $p(\gamma,\pi^0\pi^0 p)$ contamination in each bin - as our systematic error in the asymmetry measurement due to $p(\gamma,\pi^0\pi^0 p)$ contamination. For example, 5 % $p(\gamma,\pi^0\pi^0 p)$ contamination leads to an error of ±0.05 in the asymmetry measurement. It would be possible to better determine the effect of the $p(\gamma,\pi^0\pi^0 p)$ background on the final asymmetry by selecting on the $p(\gamma,\pi^0\pi^0 p)$ region of the π^0 invariant mass plot and evaluating the photon asymmetry of the background process, but this was not possible within the time scale of this work.

When evaluating the possible systematic effects in the calculation of degree of linear polarisation we focused on the effect of shifting polarisation edge position. As we assumed that *anb* (Section 5.7, [84]) is accurate to within ~1 %, and the effect of polarisation edge shifting causes changes of between 4 % and 20 % in the final asymmetry results, we considered only the dominant effect. During experimental running, the maximum deviation from the chosen coherent edge position ever allowed was 2 Tagger channels. This corresponds to a maximum edge position shift of < 5 MeV.

We constructed polarisation tables for edge positions shifted by approximately 5 MeV either side of that used in the main analysis (Figure 7.15). We then recalculated the photon asymmetries for both data sets with the shifted coherent edge polarisation tables. We calculated the absolute magnitude of the maximum shift in the asymmetry caused by using the alternative polarisation tables. We found that, in both cases, the maximum shift was caused by the polarisation tables corresponding to a coherent edge position 5 MeV higher than the mean, and took the magnitude of the shifts caused by this as the error in the final asymmetry due to the uncertainty in the degree of linear polarisation normalisation.

We could not properly evaluate the full effect of $p(\gamma,\pi^0 p)$ contamination as we did not have a sufficiently large simulated event set to perform an estimation as for the $p(\gamma,\pi^0\pi^0 p)$ contamination on an $E_{\gamma'}$-bin-by-bin basis. However, from the small simulated $p(\gamma,\pi^0 p)$ event sample that we do have, we see that the $p(\gamma,\pi^0 p)$ contamination is worst at lowest $E_{\gamma'}$, where the $p(\gamma,\gamma'\pi^0 p)$ event sample is largest. Thus the $p(\gamma,\pi^0 p)$ contamination will form a far smaller fraction of the relevant $E_{\gamma'}$ bin than the $p(\gamma,\pi^0\pi^0 p)$ contamination achieves by peaking at higher $E_{\gamma'}$. This requires further investigation which cannot be achieved within the scope of this work and so this effect is not yet included in the reported systematic error. We estimate that it may cause an additional systematic error of ±0.02, taking

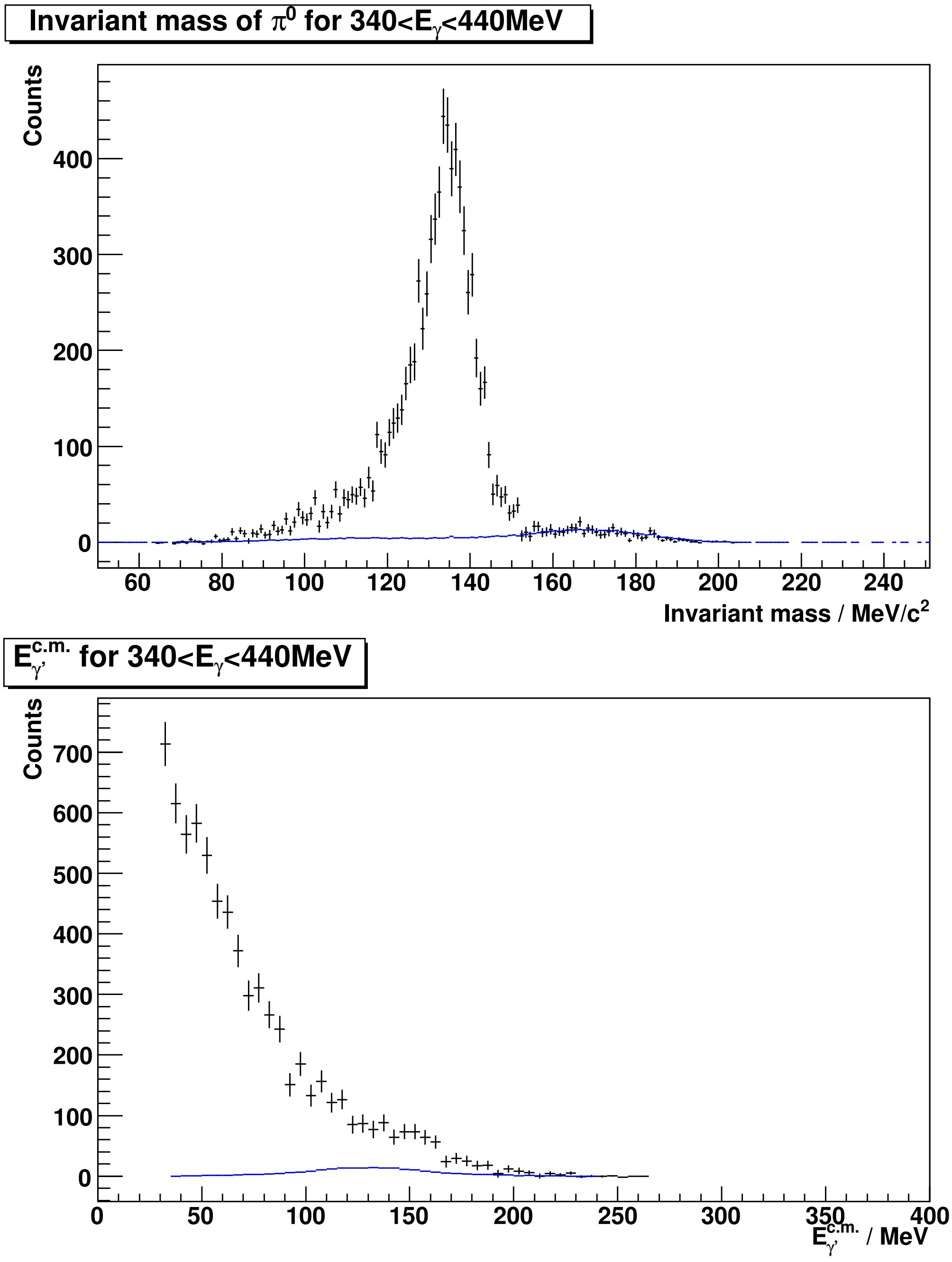

Figure 7.14: Evaluation of systematic error due to $p(\gamma,\pi^0\pi^0p)$ contamination for 340 MeV $< E_\gamma <$ 440 MeV (July data), black points show real event sample, blue points show simulated $p(\gamma,\pi^0\pi^0p)$ results. Upper panel shows π^0 invariant mass fit which gives the scaling factor for $p(\gamma,\pi^0\pi^0p)$ contamination. Lower panel shows resulting contribution of simulated $p(\gamma,\pi^0\pi^0p)$ to the $E_{\gamma'}$ distribution. The expected contamination in the September data set is a factor of ten smaller.

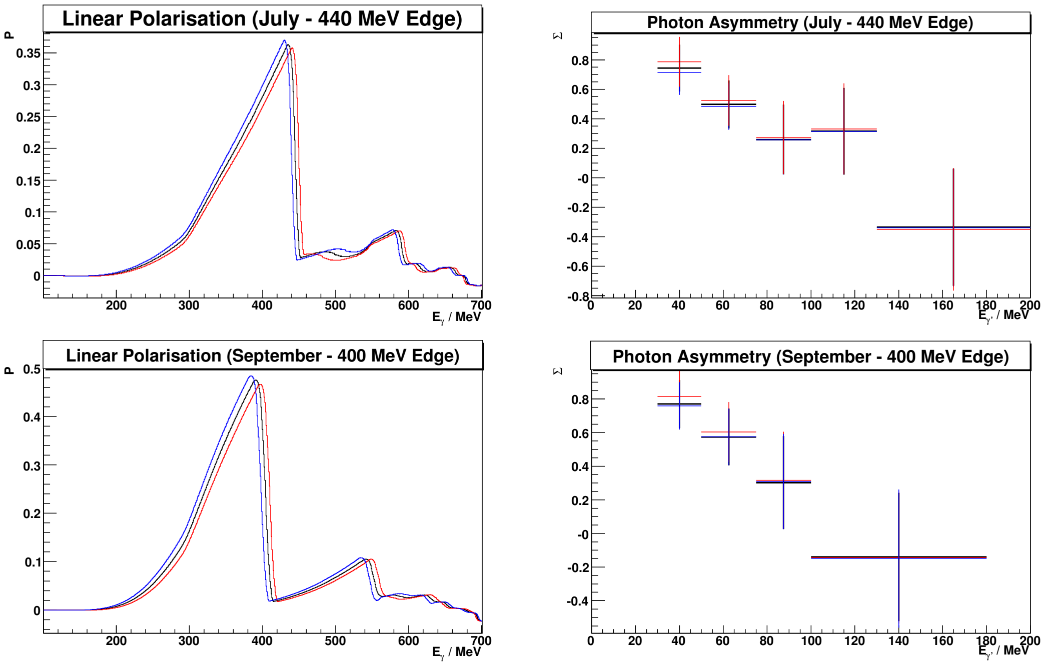

Figure 7.15: Evaluation of systematic error due to shifting coherent edge position. Upper panels show July results, lower show September. Left panels show the polarisation tables for three coherent edges: blue for a coherent edge position ∼5 MeV lower and red for one ∼5 MeV higher than the black mean edge position used in the final analysis. The right hand side shows the resulting asymmetries, colour coded according to their corresponding edge position.

in to account that the $p(\gamma,\pi^0 p)$ photon asymmetry is ~0.5, close to that of the reaction of interest in the low $E_{\gamma'}$ bins, and so the photon asymmetry will change little due to the $p(\gamma,\pi^0 p)$ contamination.

The total systematic error in our asymmetry measurements was calculated as the algebraic sum of that due to the degree of linear polarisation and that due to $p(\gamma,\pi^0\pi^0 p)$ contamination. As can be seen in Figure 7.16, systematic errors are much smaller for the September data set and result mainly from the linear polarisation normalisation, whereas the July data set suffers from the $p(\gamma,\pi^0\pi^0 p)$ contamination to a much greater degree due to the higher E_γ range. The total systematic error in the asymmetry measurements ranges from ±0.02 to ±0.18, where the statistical error ranges from ±0.14 to ±0.35 (save for the $E_{\gamma'} = 0$ MeV point which results from a much greater event sample). Full results are listed in Appendix D.

7.3 Discussion of $\gamma p \to p\pi^0\gamma'$ Photon Asymmetry

From the results shown in Figure 7.12 and discussed above, it appears that photon asymmetry drops both with increasing E_γ and $E_{\gamma'}$. This trend at first appears to agree well with the predictions of the unitary model, but not with those of the chiral model (both detailed in Chapter 2 and shown in Figure 7.13). However, some additional factors should be taken into account. Firstly, due to the combined statistical and systematic error in the measurement, either model could currently describe the data. Secondly, the unitary model has been in development for longer than the chiral model and consequently includes more detail, such as the Born terms, which the chiral model currently lacks. It is anticipated that once the Born terms are added to the chiral model, the predicted photon asymmetry will begin to show a downward trend with increasing E_γ and $E_{\gamma'}$ [112]. However this addition will take some time, as other terms of the same order also must be calculated and added to the chiral Lagrangian in order to maintain the systematic power counting of the chiral model.

The reduction of $p(\gamma,\pi^0\pi^0 p)$ contamination for the 340 MeV $< E_\gamma <$ 440 MeV bin is desirable, but not essential as the 300 MeV $< E_\gamma <$ 400 MeV bin is of more interest for the μ_{Δ^+} determination, being nearer the peak of the $\Delta(1232)$. The method of $p(\gamma,\pi^0\pi^0 p)$ contamination evaluation could be improved by the construction of a full model-based $p(\gamma,\pi^0\pi^0 p)$ generated event set in order to ensure the resulting simulated background "$E_{\gamma'}$" distribution matches that of the experiment and the measurement of the photon asymmetry of the background process.

7.4 Conclusions

A sample of ~20,000 $p(\gamma,\gamma'\pi^0 p)$ events has been extracted from the first phase of the CB@MAMI experimental series. Due to improvements in the angular coverage of the new detector system this represents a factor ~ 40 increase in counts over the only other measurement [1]. Both total cross sections and photon

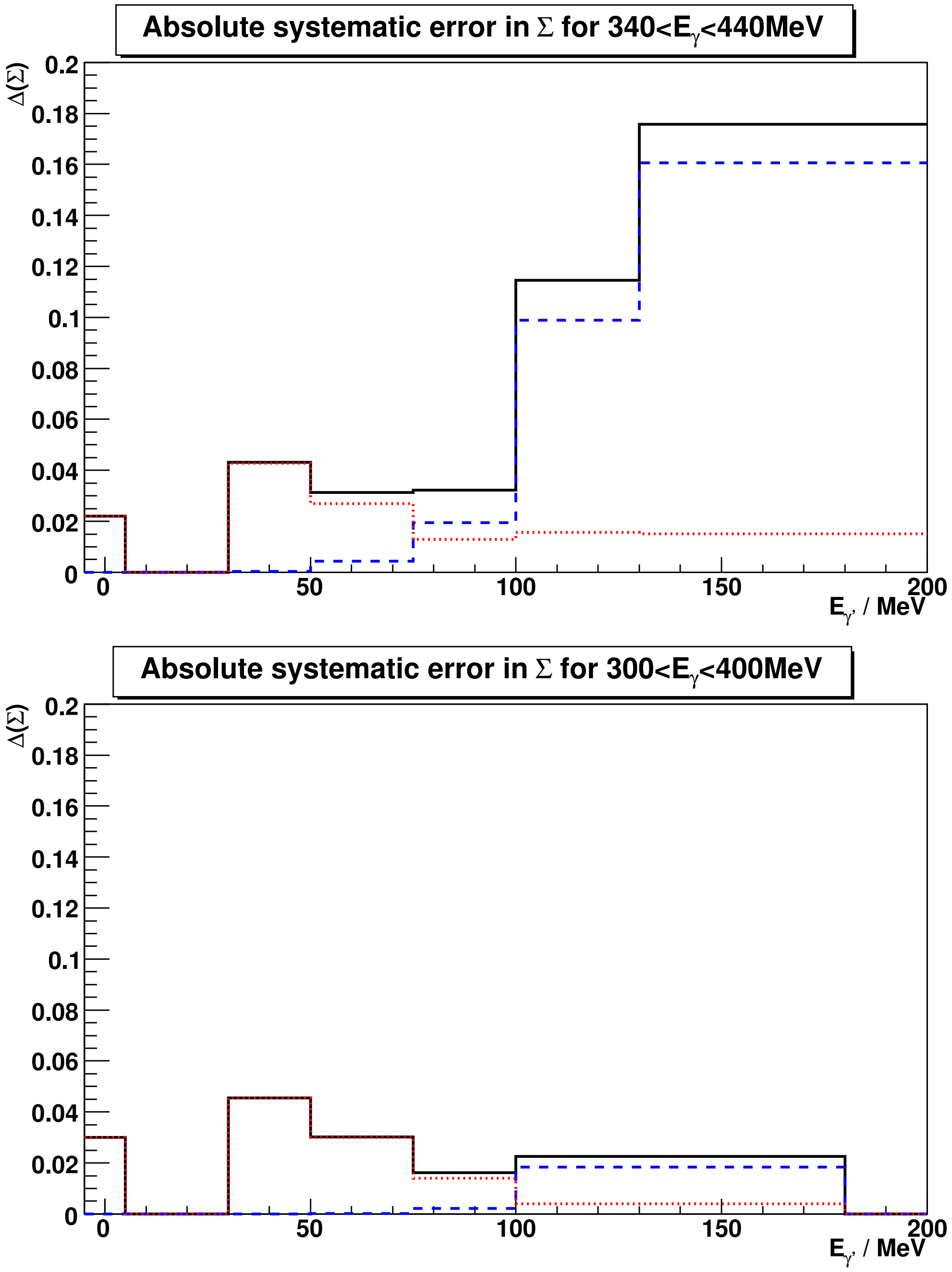

Figure 7.16: Evaluation of magnitude of total systematic error (solid line) showing error contribution due to shifting coherent edge position (dotted line) and error contribution due to $p(\gamma, \pi^0\pi^0 p)$ contamination (dashed line). The upper panel shows error composition for 340 MeV$< E_\gamma <$ 440 MeV (July data) and the lower panel shows error composition for 300 MeV $< E_\gamma <$ 400 MeV (September data).

asymmetries have been extracted from this data and are presented herein. The cross sections require further analysis, however the photon asymmetries are well established and reliable. Differential cross sections and the circularly polarised photon asymmetries are under study by other members of the A2 Collaboration [21,105].

The greatest cause of systematic error in the photon asymmetries is $p(\gamma,\pi^0\pi^0p)$ contamination. We have confidence that this contamination is well under control as both of the devised background subtraction methods result in cross sections which are in agreement within the E_γ range of interest. Due to the low statistics and limitations of our simulation, bin-by-bin subtraction was not practicable for the photon asymmetry measurements, so instead we provided what we believe to be an accurate estimation of the deviation in the asymmetry measurement likely to result from this contamination.

The main systematic limitation of the current $p(\gamma,\gamma'\pi^0p)$ total cross section and $p(\gamma,\pi^0p)$ normalised yield is the detector acceptance, ϵ_{CBTAPS}. This has great potential for improvement, and should ultimately reach a level of accuracy far better than that achieved in the earlier lone-TAPS experiments, which were hindered by edge-effects in the TAPS block configurations. After detector response, geometry and trigger effects are modelled more accurately, the simulation should be able to describe the highly uniform CBTAPS detector arrangement very well. Furthermore, improvements of the physics models incorporated in the event generator will provide more realistic input of kinematic distributions. This work will take some time, but once implemented the author anticipates that high quality cross sections with far smaller error bars than those seen in the previous measurements [1,24] will result.

Some further improvements can be made to the existing analysis methodology to improve the statistical errors and reduce the influence of $p(\gamma,\pi^0\pi^0p)$ contamination:-

1. Random subtraction can be done on the basis of a PID-Tagger timing sum rather than the Photon Tagger alone. This improves the prompt:random ratio, and thereby reduces the statistical error that results from the random subtraction.

2. A better cluster reconstruction algorithm can be developed for the photon calorimeters, especially the Crystal Ball. This would reduce the incidence of both reconstruction "split-off" and artificial cluster merging, improving our recognition of real events and reducing the confusion that introduces both $p(\gamma,\pi^0\pi^0p)$ and $p(\gamma,\pi^0p)$ contamination into our data set.

3. The use of constrained fit analyses [113] (kinematic fitting), rather than the traditional method of applying data cuts, would both increase the size of our event sample and give us a better understanding of our background processes and the resulting levels of event sample contamination. Kinematic fitting applies the measured detector resolutions and basic principles such as energy and momentum conservation to establish the probability that a given event was of a particular type. Testing the probability that each event was

$p(\gamma, \gamma'\pi^0p)$, $p(\gamma, \pi^0\pi^0p)$ and $p(\gamma, \pi^0p)$, would allow us to extract $p(\gamma, \gamma'\pi^0p)$ events above a certain probability threshold, while rejecting those which have a known $p(\gamma, \pi^0\pi^0p)$ or $p(\gamma, \pi^0p)$ probability in excess of our predetermined background probability thresholds. This statistical method of event selection accepts / rejects a known fraction of events determined by the probability thresholds and so would be a useful tool in the interpretation and understanding of the data.

4. The application of event-by-event calculation of normalisation constants will reduce the systematic errors in both photon asymmetry (due to the degree of linear polarisation) and cross section (due to the tagging efficiency) slightly. This will become more important as the statistical error is improved by the methods described above and the $p(\gamma, \pi^0\pi^0p)$ and $p(\gamma, \pi^0p)$ contamination is reduced.

Although a massive improvement on the previous measurement, the statistics of this measurement still produce error bars more than twice the size of those resulting from the systematic error. Even with the improvements listed above, we feel that the statistics of the measurement will ultimately limit the accuracy of any μ_{Δ^+} extraction far more than the systematic error, and that further experimental study of $p(\gamma, \gamma'\pi^0p)$ is indicated.

In conclusion, accessing the magnetic dipole moment of the $\Delta^+(1232)$ with greater accuracy than the previous measurement would provide important detail in the study of hadronic physics. Although not yet at the stage of μ_{Δ^+} extraction, the preliminary cross sections and the photon asymmetries herein represent both an improvement in the statistical accuracy of the previously available experimental observables and, more importantly, a new set of constraints to test the extraction model. Further experimental measurement may be necessary to achieve the desired precision. However, this recent measurement, coupled with the recent contributions by Chiang, Pascalutsa and Vanderhaeghen *et al.* to the reaction model development [2,9], moves us closer to the first definitive extraction of the magnetic moment of a strongly-decaying resonance.

Appendix A

Design & Construction of The Particle Identification Detector

The Particle Identification Detector (PID) (see Figure A.1) was designed to complete the CB/TAPS setup specifically for this experimental run. It is a scintillator-based ΔE detector used for particle identification and trigger purposes.

A.1 Detector Design

The main problems faced in the detector design were tight physical constraints on the size and positioning of the detector. Ideally, the detector would have been situated between the MWPC and the Crystal Ball in order to optimise the vertex location by the MWPC which is degraded by multiple scattering in the PID. However, there was less than a 1 mm difference between the external radius of the outer wire chamber and the inner radius of the Crystal Ball beam pipe - effectively ruling out this option. Thus we chose to construct the detector as a segmented barrel of 24 plastic scintillators (each running parallel to the beam axis and covering 15° in ϕ) located between the inner wire chamber and the outer wall of the target (see Figure A.1). We chose EJ204 plastic scintillator due to its low density (giving a lighter detector) and most importantly for its short time constant, which is important for trigger timing purposes.

This then presented an additional consideration in the choice of scintillator thickness due to the effect on the MWPC resolution of increasing scintillator thickness. Thicker scintillators absorb more energy as a given particle passes through and therefore produce more light and hence better our $\frac{\Delta E}{E}$ resolution. However increasing scintillator thickness also increases multiple scattering and thereby worsens the MWPC position resolution. The author constructed a Geant 4 simulation featuring a simple particle gun firing protons of selected energies at a block of scintillator of varying thickness. This was used to ascertain the effects of multiple scattering and the energy deposit in various scintillator thicknesses with varying angles of incidence (see Section A.4 for sample results). The final decision was to use scintillators that were 2 mm thick, measuring 314.9 mm by 13 mm (see Figure A.6). It was also decided to make the scintillator profile asymmetric. This means that we should not lose all information at the scintillator

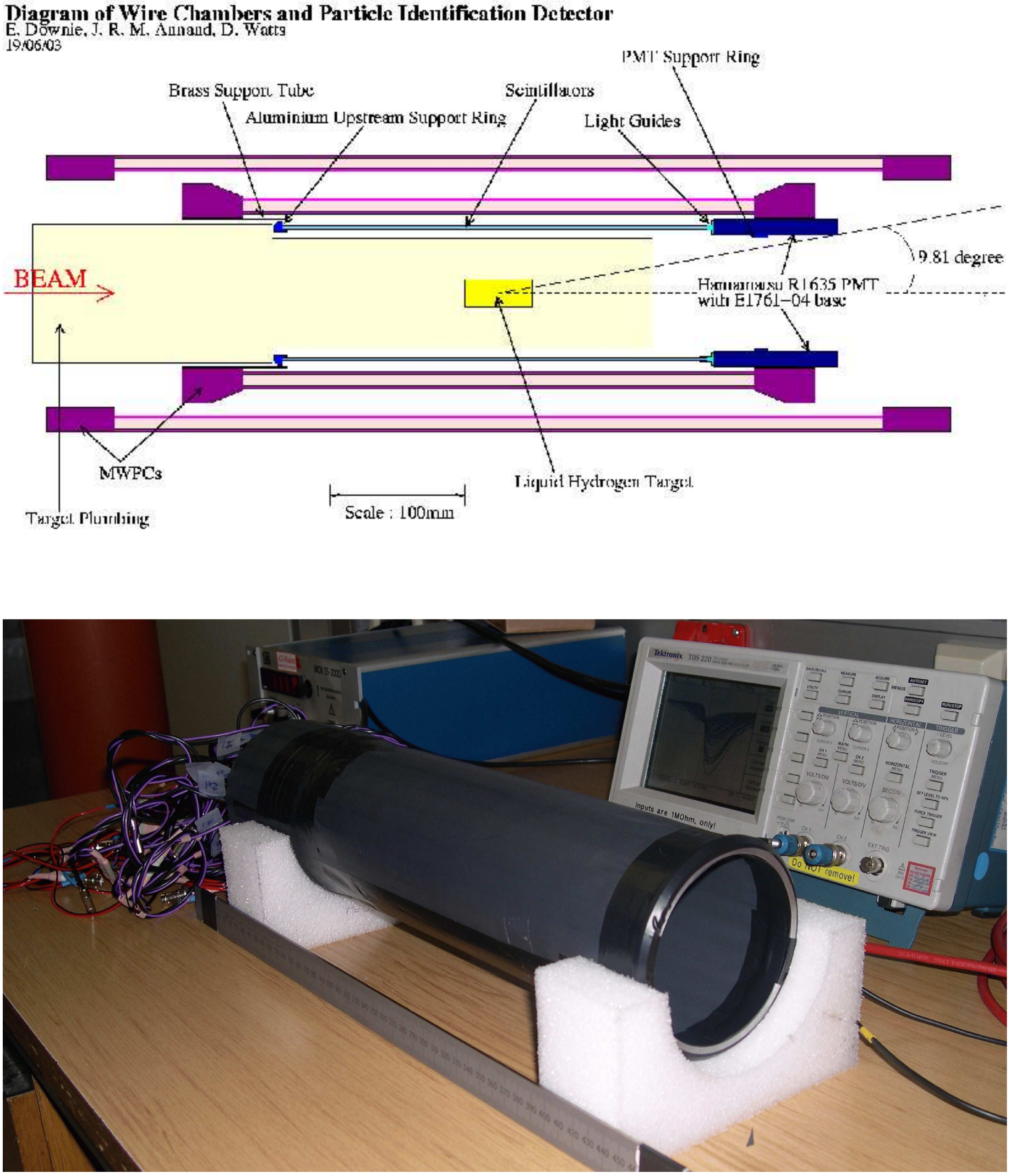
Diagram of Wire Chambers and Particle Identification Detector
E. Downie, J. R. M. Annand, D. Watts
19/06/03
PMT Support Ring
Brass Support Tube
Scintillators
Aluminium Upstream Support Ring
Light Guides
BEAM
9.81 degree
Hamamatsu R1635 PMT with E1761–04 base
MWPCs
Liquid Hydrogen Target
Scale : 100mm
Target Plumbing
Tektronix TDS 220
Inputs are 1MOhm only!
Do NOT remove!

Figure A.1: The Particle Identification Detector. The upper diagram shows the positioning of the PID between the target enclosure and wire chambers. The lower photograph shows the assembled PID connected to an oscilloscope for testing prior to installation.

joints for particles travelling radially out from the target. The joint lies off-axis so particles deposit some energy in both neighbouring scintillators rather than just in the mylar at the joint. This energy deposit may not be sufficiently resolved to identify the type of particle accurately, but it should ensure we have an effective veto of charged particles through the whole azimuthal range that the PID covers. This asymmetry also improved the ease of scintillator cutting, having one right-angled side and one angled at 105° rather than two 97.5° angled sides which had to be accurate to within $\sim 0.1°$ in order for the scintillator barrel to be properly formed and structurally self-supporting (see Figure A.6).

The next issue concerned the positioning of the photomultiplier tubes (PMTs). Most of the experimental data we are interested is in the forward (downstream) region and thus we wanted to avoid blocking the forward angle with PMTs and readout electronics. However, the reduction in scintillation light collection from the scintillators would worsen the quality of our forward-angle data if we positioned the PMTs upstream of the scintillators. There would also be a positioning problem due to the diameter of the target enclosure at this point (see Figure A.1), leading to complex-geometry light guides which might again worsen our light collection and energy resolution. On balance it was decided to place the PMTs downstream of the scintillators, to use the most compact PMTs and bases available (Hamamatsu R1635 PMTs and E1761-04 bases) and to minimise the length of our light guides (see Figure A.7). This reduced the clear forward half angle from 12° to 9.81°(see Figure A.1(a)).

We then had to work out how to physically support our PMTs and scintillators in order to avoid damage to the quite delicate plastic scintillators and to maintain rigidity in the structure. To allow heat dissipation from the PMTs, we used metal supports but also aimed to minimise: the structural weight to avoid damage to the supporting wire chambers; the density to minimise material in the region of interest; and the physical volume to reduce the forward angle loss. This led to the design of an aluminium ring to hold the PMTs (see Figure A.10) and the choice of a Tedlar (P.V.F.) jacket to provide light-proofing, structural support and protection for the scintillators. The scintillators were also individually wrapped in alumnised Mylar film to provide light isolation. At the upstream end we again chose an aluminium support ring (see Figure A.8), which locates on a thin brass cylinder (see Figure A.9) attached to the wire chamber mount to avoid interfering with the target enclosure. To avoid the trajectories of particles from any point in the active target volume that would otherwise reach the active area of the wire chambers the brass tube is just long enough to reach the Aluminium support ring.

Placing the PID inside the wire chambers has the benefit of clearing up a potential ambiguity of deposited energies. For non-relativistic particles there would be an ambiguity as to whether the deposited energy resulted from a higher energy particle passing through the detector, or a lower energy particle being stopped by the detector. As the wire chamber is immediately beyond our detector, a signal from the wire chamber in coincidence with the PID confirms transmission thereby helping to pin down the original particle energy. If the PID were outside of the wire chambers, the Crystal Ball could have performed this function but it

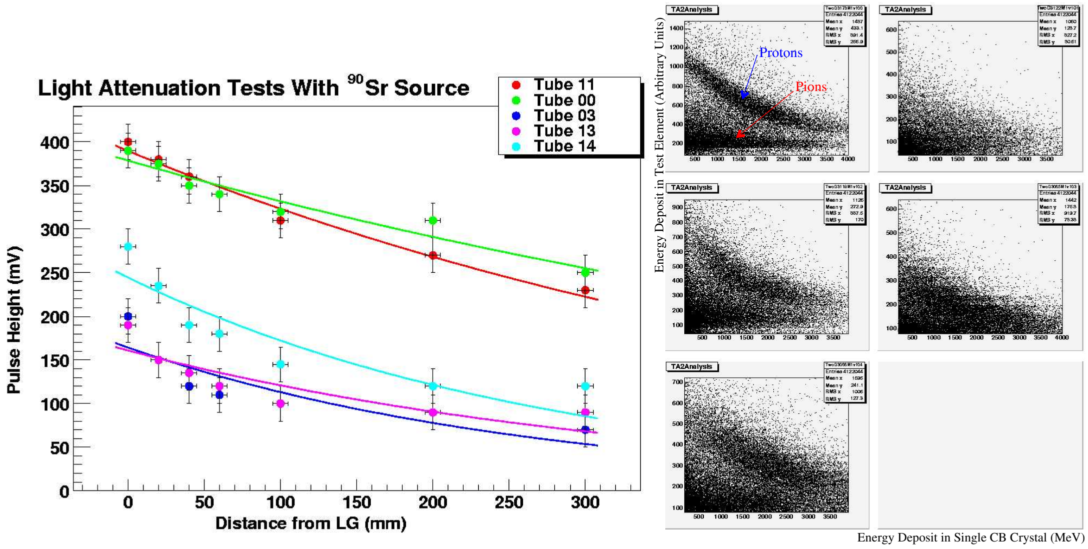

(a) Light attenuation tests with a Sr-90 source.

(b) Prototype DE/E plots with MAMI B photon beam.

Figure A.2: Tests of Five Prototype Elements

takes a minimum of 40 MeV for protons to reach the NaI and create a discernible signal. The MWPCs have a much lower detection threshold and so we can assume that if a proton goes undetected by the MWPC, it was not in transmission.

A.2 Construction

In mid-2003, all of the final designs for the PID were complete and the various parts were on order. By the last quarter of 2003, the pieces began to arrive and final preparations for assembly began. We tested over 60 PMT tubes in January 2004 at three different supply voltages with a standard light source in order to select the best twenty-four for pulse size and shape. We polished around thirty light guides and glued them to scintillators, then wrapped each of these assemblies in foil to provide light isolation of individual detector elements. We tested various silicon cement mixes for light transmission and physical strength in order to establish the optimum fixing solution for the light guide-PMT join. We also took the PMT support ring to Mainz to check for a “sliding fit” inside the wire chambers and that there was sufficient clearance inside the PID for the target housing.

In order to gain early indication of the detector performance, we connected the first five of these scintillator assemblies to PMT tubes and appropriate electronics and wrapped them in black PVC for testing. Firstly, we used a collimated β source in order to test the light attenuation properties of the detector elements. The results were very favourable (see Figure A.2(a)) as the pulse height only drops by a factor of two along the length of the scintillator. We then took those same elements to Mainz for tests in beam. The test elements were placed in a plastic

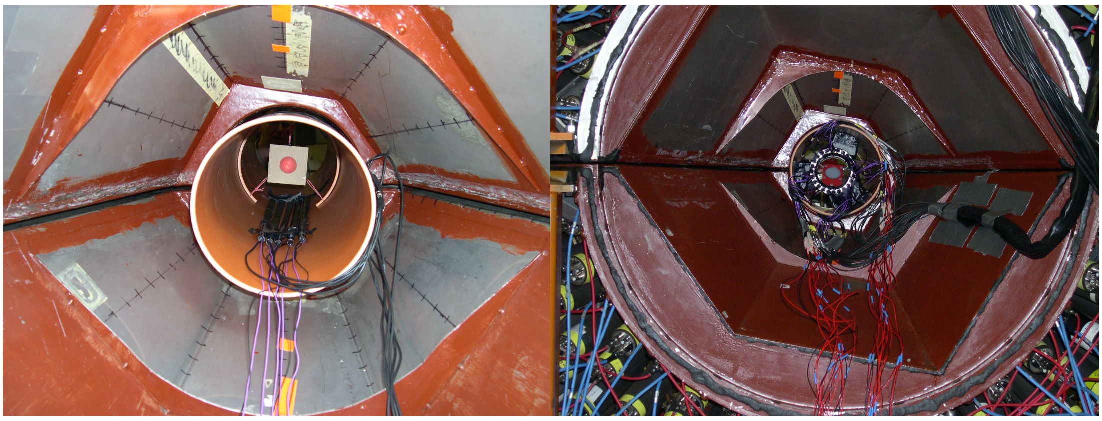

Figure A.3: PID positioning in the Crystal Ball. The left panel shows the positioning of the prototype elements in a plastic tube inside the CB for testing. The right panel shows the final assembled detector positioned in the plastic tube inside the CB before the MWPCs were ready.

pipe inside the Crystal Ball (see Figure A.3(a)) and the tagged photon beam was incident on a CH_2 target. These results were also promising, clearly showing the anticipated "banana-shaped" structures attributable to charged pion and proton passage through the scintillators (see Figure A.2(b)).

To assemble the detector, we first connected the PMTs and bases, re-wrapped them, covered them with mu metal shields (to protect the PMTs and bases from any stray magnetic fields) and inserted them into the PMT support ring, tightening the screws (Figure A.10) until the PMT entrance windows formed a firm and flat surface for connection to the scintillators. A brass tube was constructed to provide support for the PMT ring throughout the assembly process (see Figure A.4(a)). The light guides were attached to each scintillator using silicon cement. We then formed the scintillator barrel by rolling the twenty-four scintillators onto a second brass former with the same external diameter as the inscribed diameter of the final scintillator barrel. We manipulated the scintillators gently into place until the barrel was self-supporting. The brass cylinder was not structurally required, but provided added protection and remained in place until the detector was safely in Mainz (see Figure A.4(b)). We then cleaned the light guide and PMT faces, applied glue to the PMT windows and brought the scintillator barrel down on top of the PMT ring (see Figure A.4(c)). The detector was left in this configuration for several days until the glue was set firmly.

We transported the detector to Mainz, where we removed the brass former and finalised the light-proofing – the whole detector was wrapped in black Tedlar (PVF) and sealed with black PVC tape (see Figure A.1(b)). We aligned the gains of the various elements as far as possible by β source testing and altering each supply voltage individually, this took several iterations. We then set up the readout and control electronics (Figure A.5) and placed the detector inside the Crystal Ball in the same plastic tube as before, this time with polystyrene supports to centre it (see Figure A.3(b)). After beam tests with carbon, CH_2 and CD_2 targets, we found all of the detector elements to be working as designed, or

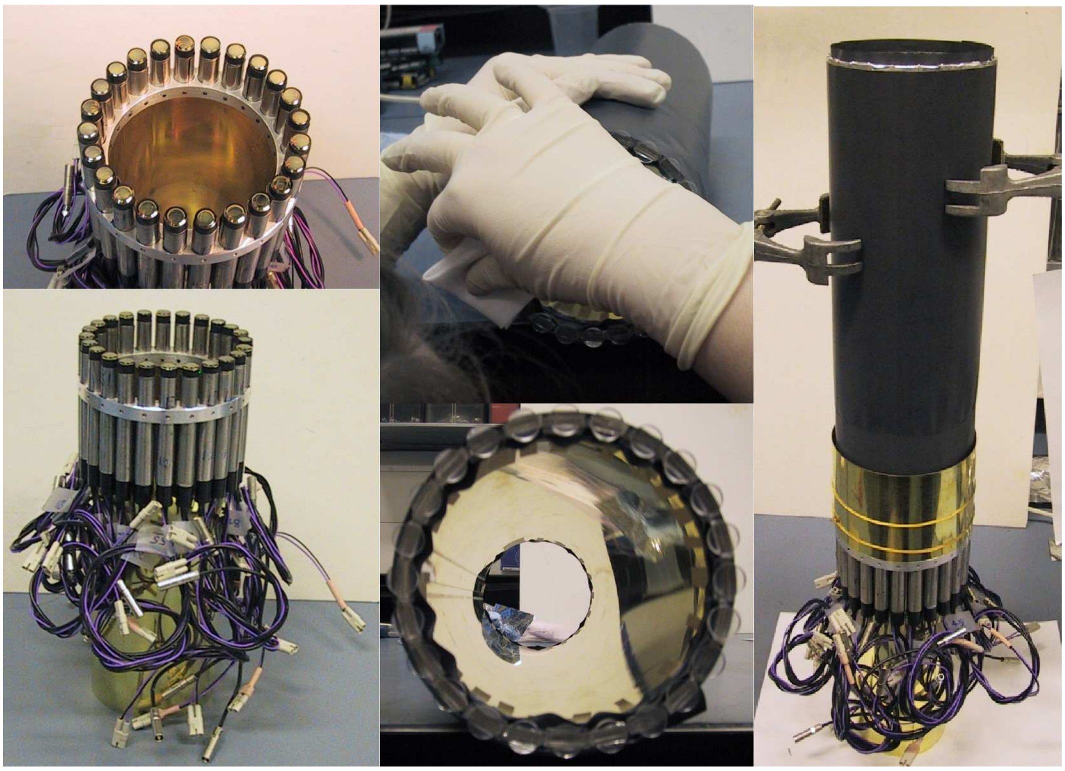

Figure A.4: Construction of the PID. The left panel shows the barrel of PMTs assembled on the brass support tube ready for gluing. The middle panel shows the assembly of the self-supporting scintillator barrel. The right panel shows the final gluing when the PMT and scintillator barrels were connected.

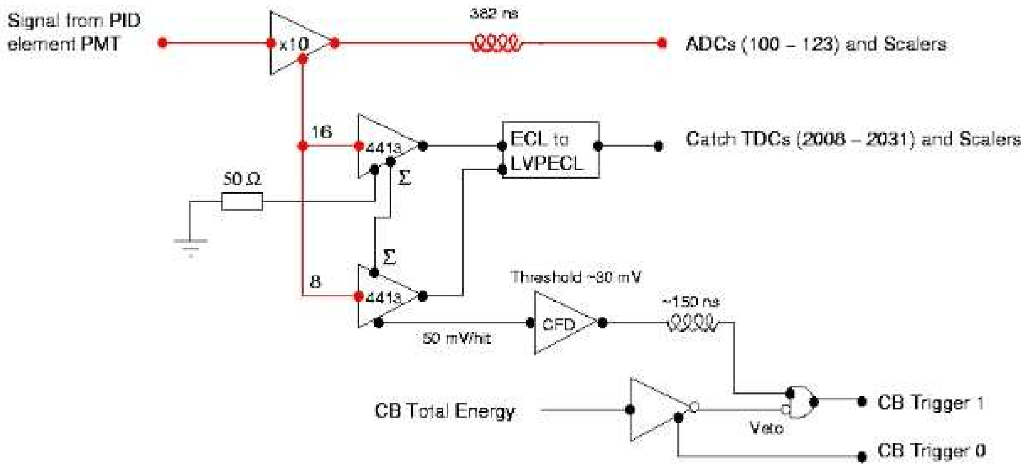
Signal from PID element PMT
x10
382 ns
ADCs (100 – 123) and Scalers
16
4413
ECL to LVPECL
Catch TDCs (2008 – 2031) and Scalers
50 Ω
Σ
Σ
8
4413
Threshold ~30 mV
~150 ns
CFD
50 mV/hit
CB Total Energy
Veto
CB Trigger 1
CB Trigger 0

Figure A.5: PID electronics.

to have minor, remediable faults, which were fixed before the final installation.

In April 2004 the detector was moved to its final position inside the MWPCs and the MWPCs were inserted into the Crystal Ball. All the final wiring was completed, the Hydrogen target was moved into position and, as of June 2004, all PID elements were working as planned.

A.3 Detector Designs

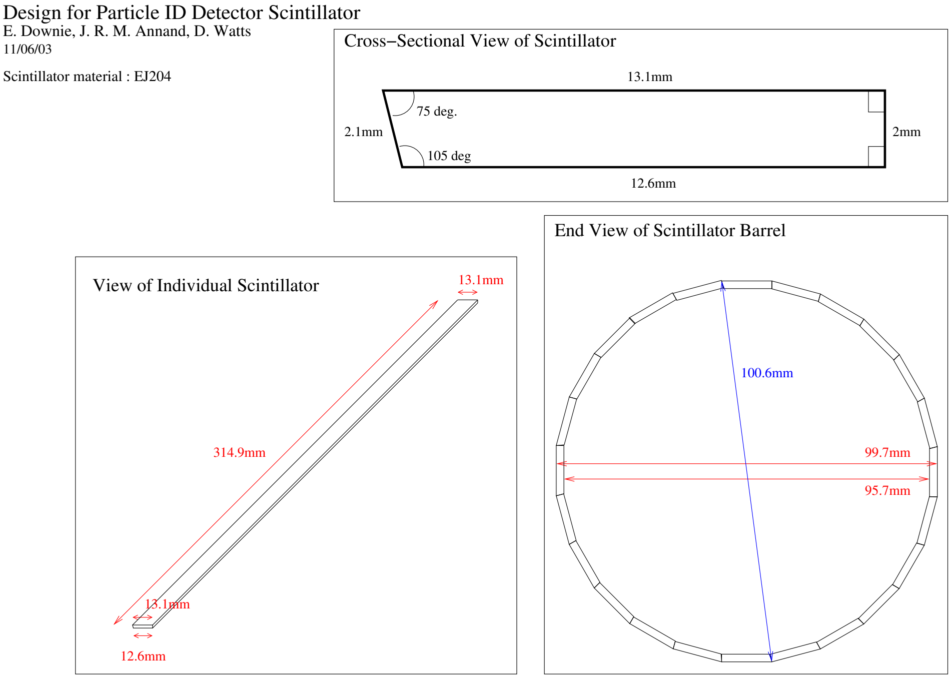
Design for Particle ID Detector Scintillator
E. Downie, J. R. M. Annand, D. Watts
11/06/03
Scintillator material : EJ204
Cross–Sectional View of Scintillator
13.1mm
75 deg.
2.1mm
105 deg
2mm
12.6mm
End View of Scintillator Barrel
100.6mm
99.7mm
95.7mm
View of Individual Scintillator
13.1mm
314.9mm
13.1mm
12.6mm

Figure A.6: Scintillator element design.

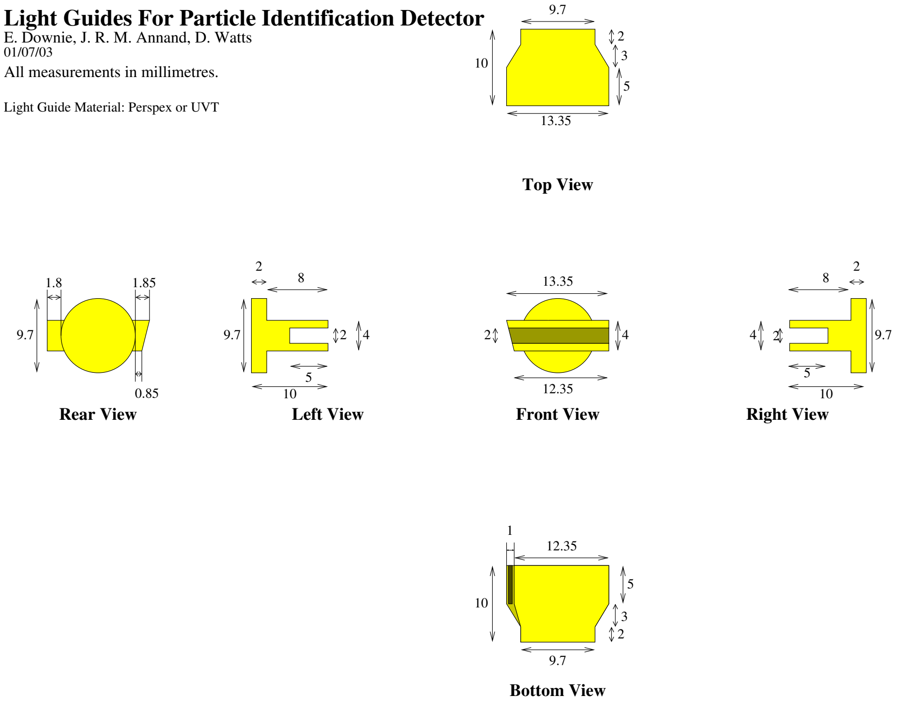
Light Guides For Particle Identification Detector
E. Downie, J. R. M. Annand, D. Watts
01/07/03
All measurements in millimetres.
Light Guide Material: Perspex or UVT
9.7
2
3
5
10
13.35
Top View
1.8
1.85
9.7
0.85
Rear View
2
8
9.7
2
4
5
10
Left View
13.35
2
4
12.35
Front View
8
2
4
2
9.7
5
10
Right View
1
12.35
10
5
3
2
9.7
Bottom View

Figure A.7: Light guide design.

Upstream End Support for Particle ID Detector (1/2)

E. Downie, J. R. M. Annand, D. Watts

27/06/03

All measurements are in millimetres unless otherwise stated.

Support Ring Material: Aluminium

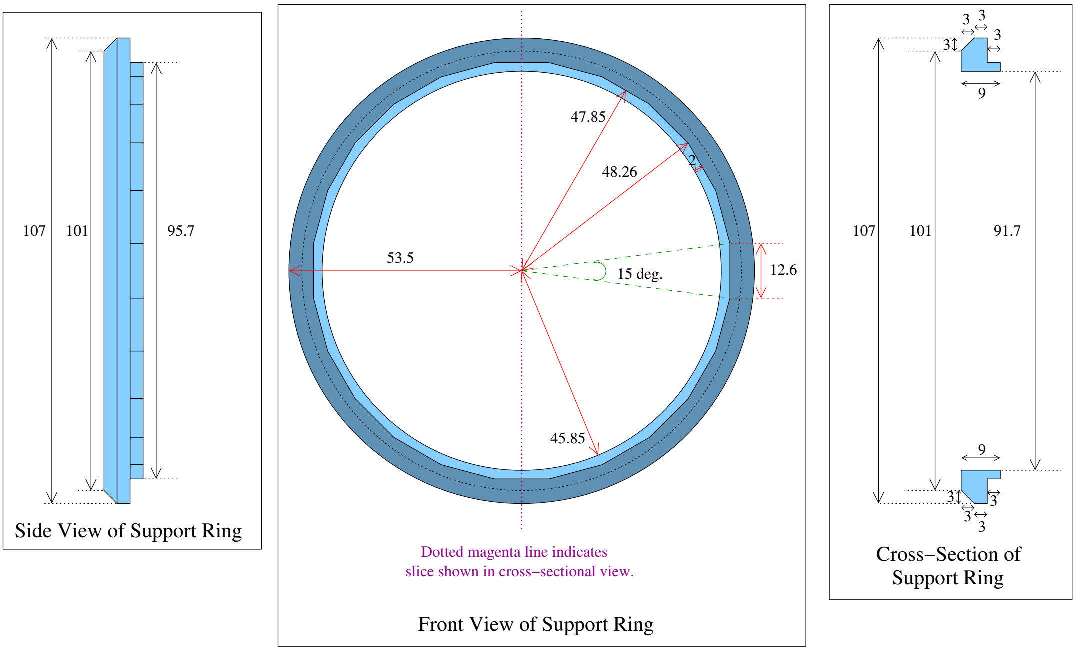
107
101
95.7
47.85
48.26
2
53.5
15 deg.
12.6
45.85
3
3
3
3
9
91.7
9
3
3
3
3
Dotted magenta line indicates slice shown in cross–sectional view.

Side View of Support Ring

Front View of Support Ring

Cross–Section of Support Ring

Upstream End Support for Particle ID Detector (2/2)

E. Downie, J. R. M. Annand, D. Watts

27/06/03

All measurements are in millimetres unless otherwise stated.

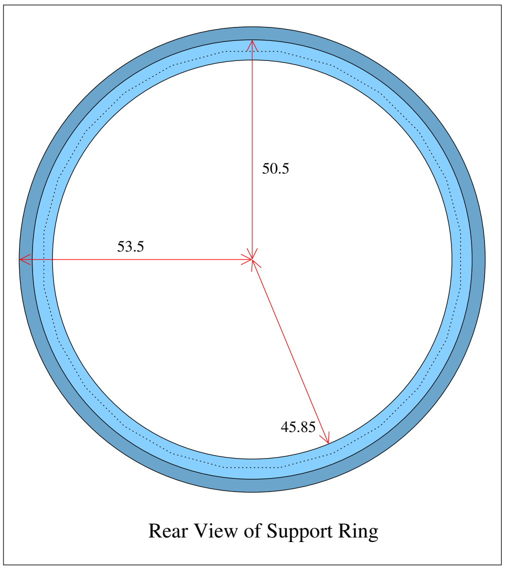
50.5
53.5
45.85

Rear View of Support Ring

Figure A.8: Aluminium upstream support ring.

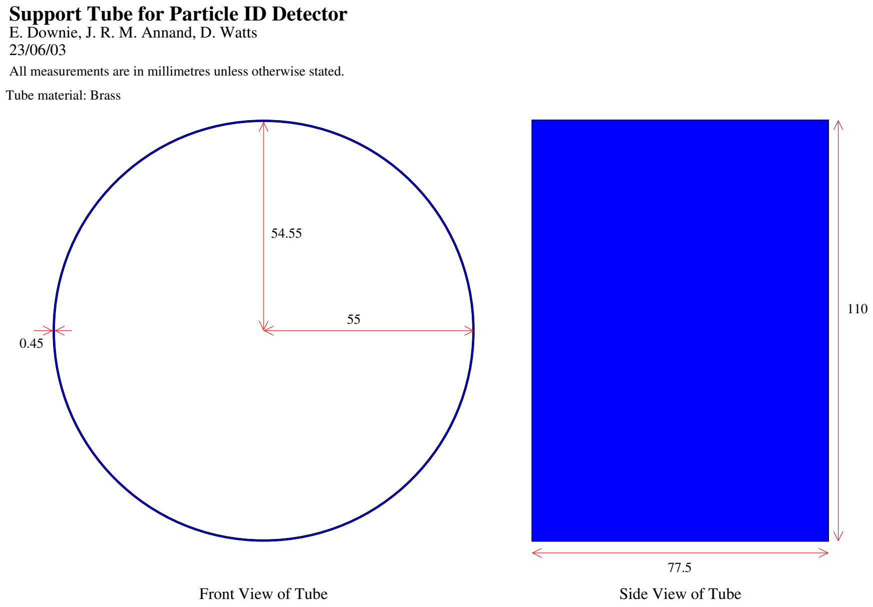
Support Tube for Particle ID Detector
E. Downie, J. R. M. Annand, D. Watts
23/06/03
All measurements are in millimetres unless otherwise stated.
Tube material: Brass
54.55
55
0.45
110
77.5
Front View of Tube
Side View of Tube

Figure A.9: Brass tube for upstream support ring location.

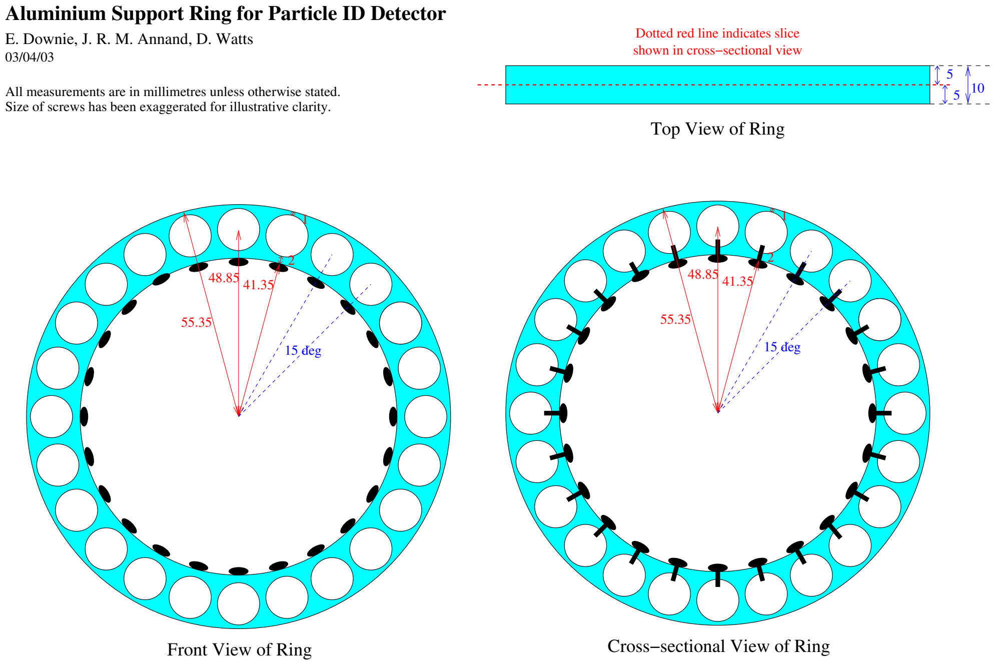
Aluminium Support Ring for Particle ID Detector
E. Downie, J. R. M. Annand, D. Watts
03/04/03
All measurements are in millimetres unless otherwise stated.
Size of screws has been exaggerated for illustrative clarity.
Dotted red line indicates slice
shown in cross−sectional view
5
5
10
Top View of Ring
1
2
48.85
41.35
55.35
15 deg
Front View of Ring
1
2
48.85
41.35
55.35
15 deg
Cross−sectional View of Ring

Figure A.10: PMT support ring.

A.4 Simulation Results

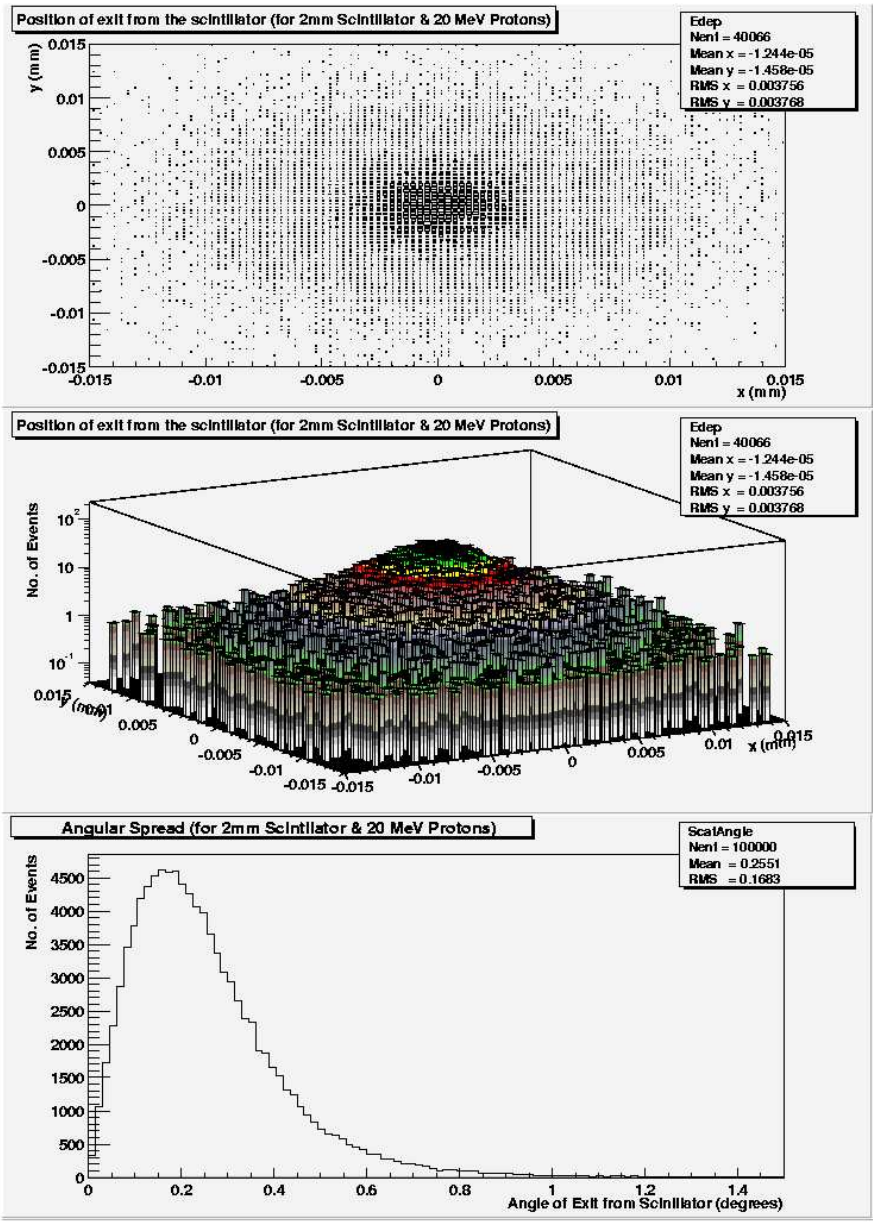

Figure A.11: Sample results for simulation showing exit position and angular spread for 20 MeV protons passing through 2 mm of scintillator.

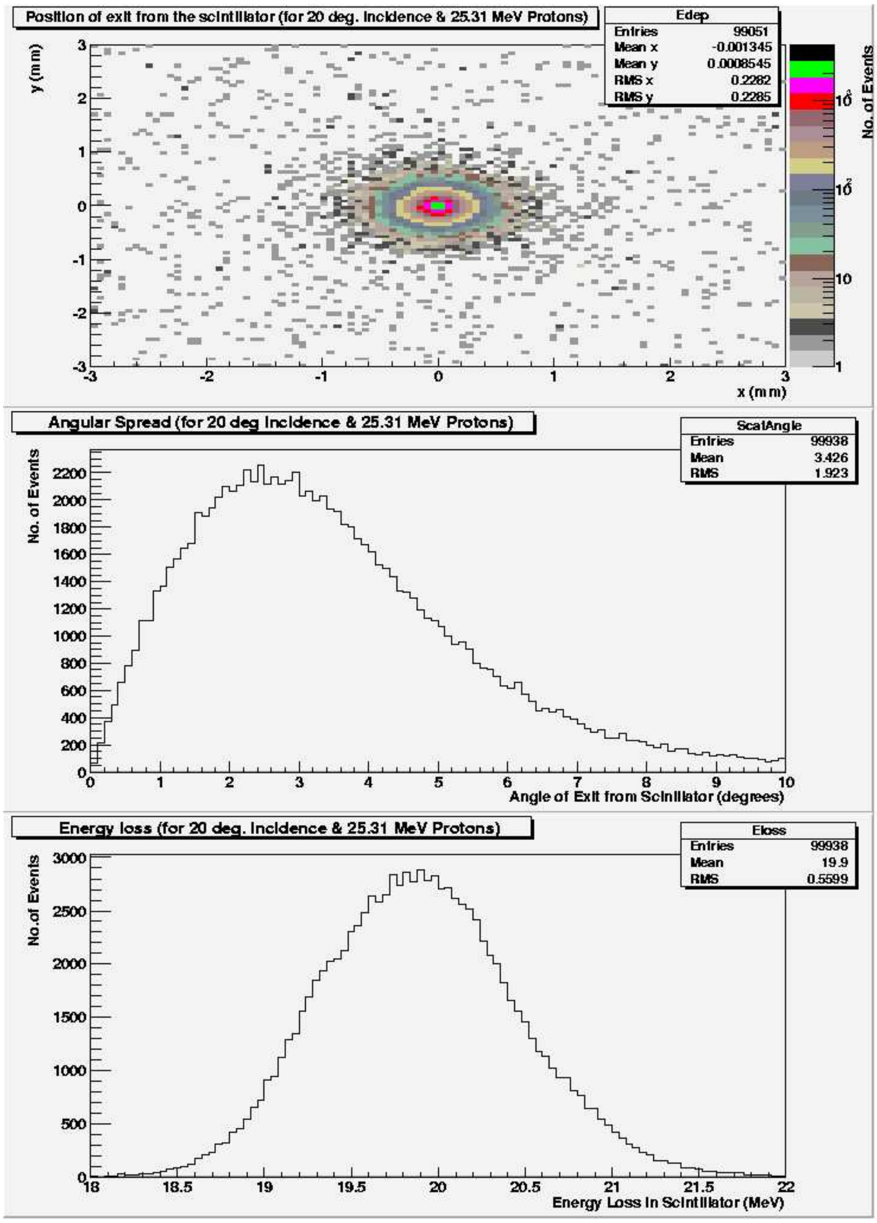

Figure A.12: Sample results for simulation showing the energy loss, exit position and angular spread for 25.31 MeV protons passing through a 2 mm scintillator at a 20° angle.

N.B. Only a single sample of each result type is given as there were ten runs of the type shown in Figure A.11 (with varying scintillator thickness) and over thirty runs of the type shown in Figure A.12 (with different particles and entrance angles). These simulation results allowed us to investigate the effects of varying scintillator thickness and angle of incidence for various particles of different energies.

Appendix B

Polarised Photon Production

The term bremsstrahlung ("braking radiation") describes the process whereby a charged particle is slowed by an electric field with the emission of a real photon and some small momentum transfer to a third body. For the purposes of our discussion, we will look at the bremsstrahlung resulting from the deceleration of a relativistic electron in the field of an atomic nucleus which is described by the equation $e + N \rightarrow N' + e' + \gamma$. From this process we can derive the following relations (in natural units $\hbar = c = 1$):-

$$\mathbf{p_0} = \mathbf{q} + \mathbf{p} + \mathbf{k} \tag{B.1}$$

$$E_0 = E + k \tag{B.2}$$

where the momenta are represented by $\mathbf{p_0}$ and $\mathbf{p}$ for the initial and final electron respectively, $\mathbf{q}$ for the nucleus (or nucleii), and $\mathbf{k}$ for the photon. The energies are represented similarly, E_0 and E for the initial and final electron energy respectively and k for the outgoing photon. Note that the energy transfer to the nucleus is not included in Equation B.2 as $\mathbf{q}$ is negligible compared to E and k owing to the large nuclear mass.

As the bremsstrahlung process is azimuthally symmetric around the direction of $\mathbf{p_0}$, the momentum transfer to the nucleus is conventionally split into its longitudinal (q_l) and transverse (q_t) components with respect to $\mathbf{p_0}$. From Equations B.1 and B.2, it is possible to calculate the limits on the recoil momentum imparted to the nucleus. This gives us an allowed region in momentum space [80,84] defined by the relationships:-

$$\frac{\delta}{x} \geq q_l \geq q_l^{min} = \delta + \frac{q_t^2}{2E_0}, \tag{B.3}$$

$$2x \gtrsim q_t \geq 0, \tag{B.4}$$

where:

$$\delta = \frac{x}{2E_0(1-x)}, \tag{B.5}$$

and

$$x = \frac{k}{E_0}. \tag{B.6}$$

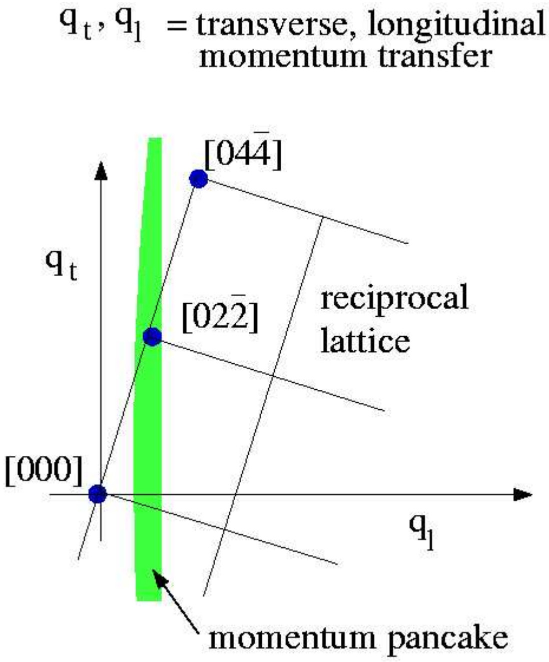

Figure B.1: Representation of the reciprocal lattice and the allowed momentum pancake in momentum space. By orientation of the crystalline radiator, it is possible to position only the reciprocal lattice vector of choice within the allowed momentum pancake.

The upper limits to this region are not strongly defined as they result from the rapidly decreasing cross section with increasing q, while the lower boundaries are hard limits set by kinematic considerations. The allowed region, often referred to as the momentum "pancake" due to its small longitudinal compared to its large transverse extent (combined with the cylindrical symmetry), sweeps through momentum space as x increases.

The differential cross section for bremsstrahlung for a photon energy k is proportional to $(1/k)\cos^2\xi$, where ξ is the azimuthal angle of the polarisation vector around $\mathbf{p_0}$ with respect to the plane $(\mathbf{p_0}, \mathbf{q})$, so the cross section peaks when the photon polarisation vector lies in the plane of the incoming electron and the momentum transfer [84]. In an amorphous radiator the momentum transfer to the nucleus can lie anywhere within the momentum pancake, which is azimuthally symmetric, and so the outgoing photon energy distribution exhibits a smooth $1/k$ drop-off and the resulting photon beam is, on average, unpolarised (Figure B.2).

With a crystalline radiator, the momentum transfer is to the lattice rather than an individual nucleus and, as such, is constrained to be equal to one of the reciprocal lattice vectors described by

$$\mathbf{g} = \sum_{k=1}^{3} h_k \mathbf{b}_k,\ k = integer, \tag{B.7}$$

where $\mathbf{g}$ is a reciprocal lattice vector, $\mathbf{b}_k$ is a reciprocal lattice basis vector and h_k corresponds to the set of Miller induces $[h_1, h_2, h_3]$.

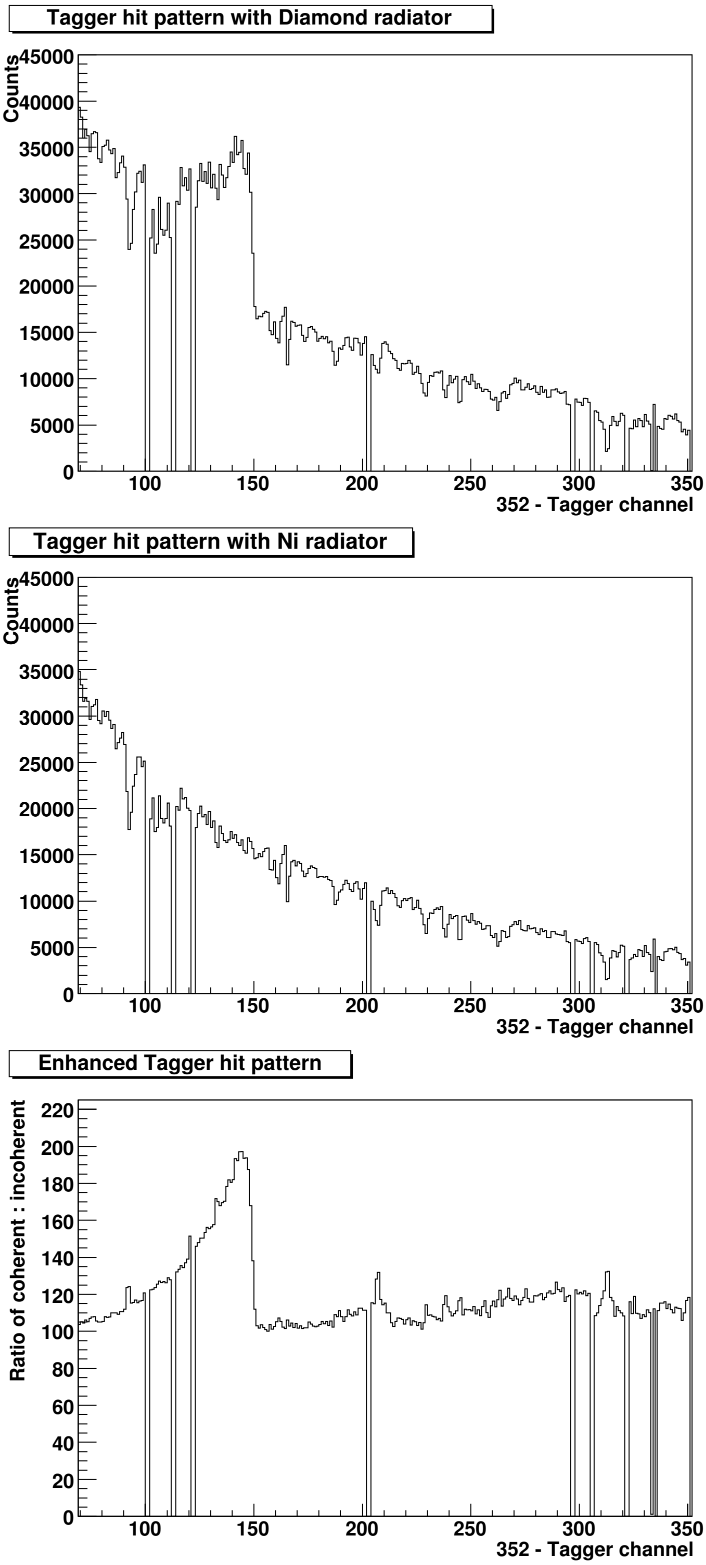

Figure B.2: The effect of radiator type on Tagger hit pattern (Tagger channels are shown in reverse order to highlight $1/E_\gamma$ dependence). The spectrum for a crystalline diamond radiator (upper panel) is divided by that due to an amorphous Ni radiator (middle panel) to produce the enhanced plot (lower panel) which clearly shows the position of the coherent edge.

If we orient the crystal correctly, we can ensure that only our reciprocal lattice vector ($\mathbf{g}$) of choice lies within the allowed momentum pancake as illustrated in Figure B.1. As the recoil momentum is constrained to be equal to $\mathbf{g}$, the azimuthal bremsstrahlung distribution is no longer symmetrical around $\mathbf{p_0}$ and the most probable photon polarisation lies in the plane $(\mathbf{p_0}, \mathbf{g})$, producing a photon beam which is polarised on average. As x increases, so does q_l^{min}, and eventually we see a discontinuity in the coherent bremsstrahlung spectrum as $\mathbf{g}$, our reciprocal lattice vector, drops out of the allowed momentum pancake. This discontinuity is known as the "coherent edge", see Figure B.2.

The spectrum produced by a crystalline radiator also has an incoherent contribution due to thermal effects. The resulting spectrum has a similar structure to that of an amorphous radiator, with some enhancement which increases as k gets closer to the coherent edge and then has a sudden discontinuity as the increase in k causes $\mathbf{g}$ to leave the allowed momentum pancake. To study the effect of the coherent part of the spectrum, it is conventional to make an incoherent reference spectrum using some amorphous radiator (in our case Ni) and divide the electron energy spectrum produced by the crystalline radiator by the incoherent reference to give an "enhanced" plot, see Figure B.2.

In our experiment, diamond was chosen as the crystalline radiator due to its small lattice spacing and low mass which favour the coherent processes. We used a **100** diamond[1] and aligned it so that the $[02\bar{2}]$ reciprocal lattice vector was just inside the momentum pancake to produce a coherent edge of $k = 440$ MeV for the first (July) experimental run and $k = 400$ MeV for the subsequent data taking periods. In practise, as k increases beyond the coherent edge of interest, other reciprocal lattice vectors can enter the momentum pancake producing smaller coherent enhancements with corresponding edges at higher photon energies. We only utilise the beam polarisation in the region of the main coherent peak in this work.

To increase the degree of linear polarisation of our photon beam, it is possible to use collimation of the photon beam [83]. Bremsstrahlung from an amorphous radiator has a characteristic angle described by $\Theta_\gamma = mc^2/E_0$. Half of all of the emitted photons lie within Θ_γ and $\sim 80\%$ lie within $2\Theta_\gamma$. Coherent bremsstrahlung is more strongly forward peaked, so if we collimate the photon beam resulting from a diamond radiator, we remove a considerable fraction of the incoherent bremsstrahlung, while leaving the coherent bremsstrahlung only slightly reduced, thereby increasing the relative coherent contribution and the degree of effective linear polarisation. This is important for the measurement of photon asymmetries where the "quality factor" in data taking is proportional to the square of the degree of polarisation.

Further details of the calculation of the degree of linear polarisation can be found in Section 5.7.

---

[1] A **100** diamond has both faces perpendicular to the $\mathbf{b_1}$ lattice basis vector.

Appendix C

Measuring a Photon Asymmetry

C.1 Experimental Definition of Photon Asymmetry

The differential cross section of a photon induced reaction depends on the incomming photon polarisation. The polarised photon cross section (σ_{pol}) is related to the unpolarised cross section (σ_0) by

$$\sigma_{pol}(\phi) = \sigma_0(1 + PA\cos(2\phi - \phi_0)), \tag{C.1}$$

where P is the degree of linear polarisation of the photon beam and A is the amplitude of the photon asymmetry, and ϕ refers to the azimuthal angle of the reaction plane; in our case, the azimuthal angle of the π^0. We can determine PA (the amplitude of the $\cos(2\phi - \phi_0)$) by fitting $\sigma_0(1 + PA\cos(2\phi - \phi_0))$ to the polarised photon azimuthal cross section distribution, or we can take the ratio of the polarised to unpolarised cross section, σ_{pol}/σ_0 to reduce the complexity of the fit [114].

Rather than measuring the cross section with both polarised and unpolarised photon beams, we can measure the cross section using photons polarised in two different orientations that are rotated by 90°. The orientations used in our experiment were known as “para” (where the photon polarisation was perpendicular to the photon beam axis and parallel to the floor of the experimental hall) and “perp” (where the photon polarisation was perpendicular to the beam axis and perpendicular to the floor of the experimental hall).

If we rotate the orientation of polarisation by 90°, we shift the phase of the $\cos(2\phi)$ component by 180°. Thus, assuming ϕ_0 is constant, we can express the polarised cross sections ($\sigma_\perp$ and $\sigma_\|$ for perp and para respectively) as:

$$\sigma_\perp(\phi) = \sigma_0(1 + P_\perp A\cos(2\phi - \phi_0)), \tag{C.2}$$

$$\sigma_\|(\phi) = \sigma_0(1 - P_\| A\cos(2\phi - \phi_0)). \tag{C.3}$$

We can then reconstruct the unpolarised cross section by summing $\sigma_\perp$ and $\sigma_\|$ or double the amplitude of the $\cos(2\phi - \phi_0)$ by taking the difference. This approach makes maximum use of the available statistics.

In the situation where the degree of linear photon polarisation is the same for both parallel and perpendicular data sets, we get the simple, standard asymmetry relationship:

$$\frac{\sigma_{\perp}(\phi) - \sigma_{\parallel}(\phi)}{\sigma_{\perp}(\phi) + \sigma_{\parallel}(\phi)} = PA\cos(2\phi - \phi_0). \tag{C.4}$$

Equation C.4 illustrates that a major advantage of measuring a photon asymmetry is that many of the absolute normalisations required for a cross section measurement cancel out in the calculation of the asymmetry. However, in practise we need to allow for the possibility that $P_{\parallel} \neq P_{\perp}$. If we look at Equations C.2 and C.3, in terms of actual experimental quantities we find:-

$$\frac{n_{\perp}(\phi)}{N_{\gamma}^{\perp} N_p^{\perp} \epsilon_{\perp}(\phi)\omega_{\perp}} = \frac{n_0(\phi)}{N_{\gamma}^0 N_p^0 \epsilon_o(\phi)\omega_0}(1 + P_{\perp}A\cos(2\phi - \phi_0)), \tag{C.5}$$

$$\frac{n_{\parallel}(\phi)}{N_{\gamma}^{\parallel} N_p^{\parallel} \epsilon_{\parallel}(\phi)\omega_{\parallel}} = \frac{n_0(\phi)}{N_{\gamma}^0 N_p^0 \epsilon_o(\phi)\omega_0}(1 - P_{\parallel}A\cos(2\phi - \phi_0)), \tag{C.6}$$

where N_{γ}^0, $N_{\gamma}^{\perp}$ and $N_{\gamma}^{\parallel}$ are the total number of photons incident on the target, N_p^0, $N_p^{\perp}$ and $N_p^{\parallel}$ are the total number of protons in the active area of the target, $\epsilon_0(\phi)$, $\epsilon_{\perp}(\phi)$ and $\epsilon_{\parallel}(\phi)$ are the detector system acceptance, ω_0, $\omega_{\perp}$and $\omega_{\parallel}$ are the ϕ bin widths, and $n_0(\phi)$, $n_{\perp}(\phi)$ and $n_{\parallel}(\phi)$ are the number of π^0 mesons in the given ϕ bin, all for unpolarised, perpendicularly polarised and parallel polarised data sets, respectively. There is no difference in the θ distributions of σ_0, $\sigma_{\perp}$ and $\sigma_{\parallel}$, and so the acceptance at a given ϕ (or over sufficiently small ϕ bins) should not vary with photon polarisation, making $\epsilon_0(\phi) = \epsilon_{\perp}(\phi) = \epsilon_{\parallel}(\phi)$. As we changed polarisation orientation from parallel to perpendicular approximately every fifteen minutes throughout the experiment and we intend to reconstruct σ_0 using a combination of the parallel and perpendicular data sets, we can assume that $N_p^0 = N_p^{\perp} = N_p^{\parallel}$. We evaluate the above equations over the same ϕ bin widths for each data set so $\omega_0 = \omega_{\perp} = \omega_{\parallel}$. This leaves us with:-

$$\left(\frac{n_{\perp}(\phi)}{N_{\gamma}^{\perp}}\right) = \left(\frac{n_0(\phi)}{N_{\gamma}^0}\right)\left(1 + P_{\perp}A\cos(2\phi - \phi_0)\right), \tag{C.7}$$

$$\left(\frac{n_{\parallel}(\phi)}{N_{\gamma}^{\parallel}}\right) = \left(\frac{n_0(\phi)}{N_{\gamma}^0}\right)\left(1 - P_{\parallel}A\cos(2\phi - \phi_0)\right). \tag{C.8}$$

We cannot be sure that the experiment ran with parallel and perpendicular polarisations for exactly equal lengths of time with a perfectly constant photon flux, and as the unpolarised data will be reconstructed from a combination of the parallel and perpendicular data sets, we have to take account of possible differences in the number of photons (N_{γ}) impinging on the proton target to produce each data set. As mentioned above, we also have to be aware of possible differences in the degree of linear polarisation of the photon beam between parallel and perpendicular data sets.

To remove the direct dependence upon N_{γ}, we can look to the fact that the incoming photon polarisation does not alter the magnitude of the total cross section, only the distribution of it's strength in ϕ, as can be shown by integrating

Equations C.2 and C.3 over the full 2π of ϕ. Let $N_\perp$, $N_\parallel$ and N_0 be the azimuthally integrated total number of detected events for perpendicular, parallel and unpolarised data sets, respectively. We know that the total cross section is calculated as the total number of detected events ($N_\perp$, $N_\parallel$ or N_0), normalised by the product of the total number of photons incident on the target ($N_\gamma^\perp$, $N_\gamma^\parallel$ or N_γ^0), the number of protons in the target ($N_p^\perp$, $N_p^\parallel$ or N_p^0) and the overall detector acceptance ($\epsilon_\perp$, $\epsilon_\parallel$ or ϵ_0). This gives:

$$\left(\frac{N_\perp}{N_p^\perp N_\gamma^\perp \epsilon_\perp}\right) = \left(\frac{N_\parallel}{N_p^\parallel N_\gamma^\parallel \epsilon_\parallel}\right) = \left(\frac{N_0}{N_p^0 N_\gamma^0 \epsilon_0}\right). \tag{C.9}$$

We can eliminate N_p on the grounds given earlier. In the case of the CB@MAMI experimental setup, the detector acceptance is almost identical and can be made absolutely identical for both parallel and perpendicular data sets by applying suitable cuts to the data (see Section 5.8). In the case where the construction of identical acceptances is not possible, the dependence upon the exact value of the acceptances can be removed by replacing $\epsilon_\parallel$ with $(\epsilon_\perp \epsilon_\parallel)/\epsilon_\perp$ and similarly for ϵ_0. Then the exact $\epsilon_\perp$ value cancels, leaving only the ratios $\epsilon_\perp/\epsilon_\parallel$ and $\epsilon_\perp/\epsilon_0$ to modify the $N_\parallel$ and N_0 numerators, respectively. In the CB@MAMI case of equal acceptance we then have:-

$$\left(\frac{N_\perp}{N_\gamma^\perp}\right) = \left(\frac{N_\parallel}{N_\gamma^\parallel}\right) = \left(\frac{N_0}{N_\gamma^0}\right). \tag{C.10}$$

This can be used to eliminate N_γ from Equations C.7 and C.8. Leaving:

$$\left(\frac{n_\perp(\phi)}{N_\perp}\right) = \left(\frac{n_0(\phi)}{N_0}\right)(1 + P_\perp A\cos(2\phi - \phi_0)), \tag{C.11}$$

$$\left(\frac{n_\parallel(\phi)}{N_\parallel}\right) = \left(\frac{n_0(\phi)}{N_0}\right)(1 - P_\parallel A\cos(2\phi - \phi_0)). \tag{C.12}$$

To construct the unpolarised data set, we have to take care of the possible differences between $P_\perp$ and $P_\parallel$. To do this, we multiply both sides of Equation C.12 by $P_\perp/P_\parallel$ giving:

$$\left(\frac{n_\parallel(\phi)P_\perp}{N_\parallel P_\parallel}\right) = \left(\frac{n_0(\phi)}{N_0}\right)\left(\left(\frac{P_\perp}{P_\parallel}\right) - P_\perp A\cos(2\phi - \phi_0)\right). \tag{C.13}$$

If we then take the sum of Equations C.11 and C.13, we find that the $\cos(2\phi - \phi_0)$ terms exactly cancel:

$$\left(\frac{n_\perp(\phi)}{N_\perp}\right) + \left(\frac{n_\parallel(\phi)P_\perp}{N_\parallel P_\parallel}\right) = \left(\frac{n_0(\phi)}{N_0}\right)\left(1 + \frac{P_\perp}{P_\parallel}\right). \tag{C.14}$$

We can then take the difference between Equations C.11 and C.12 to eliminate the baseline:

$$\left(\frac{n_\perp(\phi)}{N_\perp}\right) - \left(\frac{n_\parallel(\phi)}{N_\parallel}\right) = \left(\frac{n_0(\phi)}{N_0}\right)\left(\left(P_\perp + P_\parallel\right)A\cos(2\phi - \phi_0)\right). \tag{C.15}$$

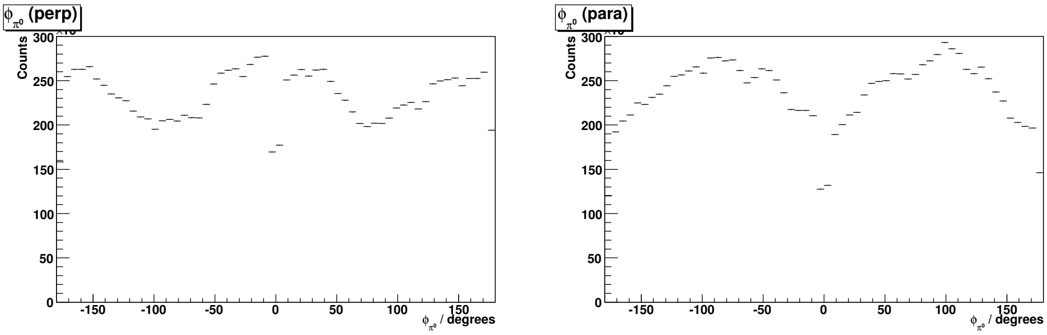

Figure C.1: Raw histograms of ϕ_{π^0} in the reaction $\mathrm{p}(\gamma, \pi^0\mathrm{p})$, with no limits on θ_p and 340 MeV $< E_\gamma <$ 440 MeV for perpendicular polarisation orientation (left) and parallel polarisation orientation (right). The effect of the metal plate between the CB hemispheres can be seen at 0° and ±180°.

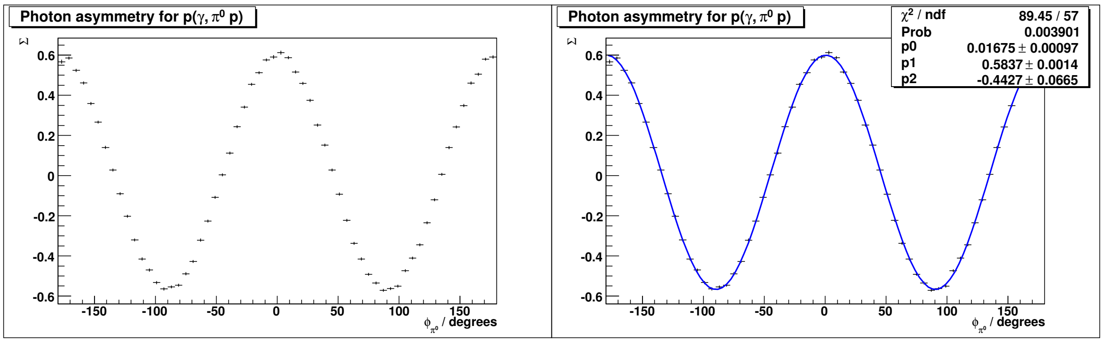

Figure C.2: Illustration of photon asymmetry for $\mathrm{p}(\gamma, \pi^0\mathrm{p})$ with no limits on θ_p and 340 MeV $< E_\gamma <$ 440 MeV. Applying Equation C.16 to the distributions illustrated in Figure C.1 gives a properly normalised $\cos(2\phi - \phi_0)$ distribution (left). To this distribution, we apply a fitting function to determine the amplitude A of the photon asymmetry and ϕ_0 and to check for any vertical offset (right).

If we divide Equation C.15 by C.14, we find Equation C.16:

$$\frac{\left(1 + \frac{P_\perp}{P_\parallel}\right)}{(P_\perp + P_\parallel)} \left(\frac{\left(\frac{n\perp(\phi)}{N_\perp}\right) - \left(\frac{n_\parallel(\phi)}{N_\parallel}\right)}{\left(\frac{n_\perp(\phi)}{N_\perp}\right) + \left(\frac{P_\perp}{P_\parallel}\right)\left(\frac{n_\parallel(\phi)}{N_\parallel}\right)} \right) = A\cos(2\phi - \phi_0). \tag{C.16}$$

This formulation of the asymmetry calculation was used to produce the final $p(\gamma, \gamma'\pi^0 p)$ photon asymmetries reported in Chapter 7 and Appendix D. Assuming that $P_\perp \simeq P_\parallel \equiv P$ (a good assumption to within less than 0.1% for MAMI data), this reduces to

$$\frac{1}{P} \left(\frac{\left(\frac{n_\perp(\phi)}{N_\perp}\right) - \left(\frac{n_\parallel(\phi)}{N_\parallel}\right)}{\left(\frac{n_\perp(\phi)}{N_\perp}\right) + \left(\frac{n_\parallel(\phi)}{N_\parallel}\right)} \right) = A\cos(2\phi - \phi_0). \tag{C.17}$$

This reduction was used to make first calculations of $\mathrm{p}(\gamma, \pi^0\mathrm{p})$ reaction asymmetries before the polarisation tables were properly established (Section 5.8).

We construct the $\cos(2\phi)$ distributions by computing Equation C.16 for each of the points in the raw ϕ_{π^0} distributions shown in Figure C.1. We then fit a function of the form

$$\Sigma(\phi) = A\cos(2\phi - \phi_0) + c \tag{C.18}$$

to the resulting histograms (Figure C.2). If our detector systems are well aligned, ϕ_0 should be near zero, c should be consistent with zero and A should give the amplitude of the photon asymmetry. In every fit we have performed on various subsets of the data for both $\mathrm{p}(\gamma,\pi^0\mathrm{p})$ and $\mathrm{p}(\gamma,\gamma'\pi^0\mathrm{p})$ photon asymmetries, we have found c to be consistent with zero. As ϕ_0 is a constant related to the physical alignment of the Goniometer and the detector system, it is advisable to use the $\mathrm{p}(\gamma,\pi^0\mathrm{p})$ reaction asymmetry measurements (which have several orders of magnitude higher statistics than the $\mathrm{p}(\gamma,\gamma'\pi^0\mathrm{p})$ reaction) to fix ϕ_0 in the fits to the lower statistics data. An uncertainty-weighted mean from the separate $\mathrm{p}(\gamma,\pi^0\mathrm{p})$ measurements recorded in Table 5.2 gave $\phi_0 = 0.5625°$. Thus only a two-parameter fit, with ϕ_0 fixed at the predetermined value, was applied to the $\mathrm{p}(\gamma,\gamma'\pi^0\mathrm{p})$ distributions.

The final quoted asymmetry measurements are simply the A values obtained from fitting Equation C.18 to the $cos(2\phi)$ distribution using Minuit [97].

C.2 Calculation of Statistical Errors in a Photon Asymmetry Measurement

To calculate the statistical error in our asymmetry measurement for $p(\gamma,\gamma'\pi^0p)$, we used the expression of asymmetry given in Equation C.16. The systematic error due to the determination of the degree of linear polarisation is discussed in Chapter 7 and for the purposes of statistical error determination we will regard the polarisation related terms as constants:

$$\gamma = \frac{P_\perp}{P_\|}, \tag{C.19}$$

$$c = \frac{\left(1 + \frac{P_\perp}{P_\|}\right)}{\left(P_\perp + P_\|\right)}. \tag{C.20}$$

We then regard the experimentally observed quantities as E and H defined in Equations C.21 and C.22:

$$E = \frac{n_\perp(\phi)}{N_\perp}, \tag{C.21}$$

$$H = \frac{n_\|(\phi)}{N_\|}. \tag{C.22}$$

We take the uncertainty in these observed quantities to be:

$$\Delta\left(\frac{n(\phi)}{N}\right) = \left(\left(\frac{\Delta(n(\phi))}{n(\phi)}\right)^2 + \left(\frac{\Delta(N)}{N}\right)^2\right)^{\frac{1}{2}} \frac{n(\phi)}{N}, \tag{C.23}$$

$$\Delta(n(\phi)) = \left(\left(\sqrt{n(\phi)_{prompt}}\right)^2 + \left(\beta\sqrt{n(\phi)_{random}}\right)^2\right)^{\frac{1}{2}}, \tag{C.24}$$

$$\Delta(N) = \left(\left(\sqrt{N_{prompt}}\right)^2 + \left(\beta\sqrt{N_{random}}\right)^2\right)^{\frac{1}{2}}, \tag{C.25}$$

where (as explained above) $n(\phi)$ refers to the number of counts in a particular ϕ_{π^0} bin, N refers to the total number of counts in the raw ϕ_{π^0} histograms (as illustrated in Figure C.1), β is the ratio of the prompt and random window widths (used to scale the random sample - see Section 5.2.1) and the *prompt* and *rand* subscripts refer to the prompt and random window samples respectively, as explained in Section 5.2.1. This uncertainty calculation is not strictly accurate as we combine the errors in $n(\phi)$ and N as if they were completely uncorrelated, when in truth, there will be some slight correlation between the two values. However, as every histogram we deal with has at least fifteen ϕ_{π^0} bins we consider the correlation between the contents of an individual bin and the integral of the whole to be extremely weak and, in this analysis, it is neglected.

Using E, H, γ and c as defined above, and setting $A\cos(\phi - \phi_0) = y$ for ease of expression, Equation C.16 becomes:

$$y = \frac{(cE - cH)}{(E + \gamma H)}, \tag{C.26}$$

and from basic error propagation we find Equation C.27:

$$\Delta(y)^2 = \frac{(H + \gamma H)^2(\Delta(E))^2c^2 + (E + \gamma E)^2(\Delta(H))^2c^2}{(E + \gamma H)^4}. \tag{C.27}$$

The y-error for each point in the ϕ_{π^0} asymmetry distribution is calculated using Equation C.27. These errors are then taken into account by Minuit when it is used to fit the distribution described in Equation C.18 to the results. The final error given in each of our asymmetry measurement is simply the error on the amplitude parameter of the fit as reported by Minuit [97].

Appendix D

Tables of Results

D.1 Cross Section of $p(\gamma, \gamma'\pi^0 p)$

E_γ / MeV	$\sigma(E_\gamma)$ / nb	$\Delta(\sigma)$ statistical / nb
312.5 ± 12.5	39.4	2.9
337.5 ± 12.5	43.6	2.6
362.5 ± 12.5	48.5	2.4
387.5 ± 12.5	54.0	2.0
412.5 ± 12.5	59.8	2.1
437.5 ± 12.5	66.0	2.3
462.5 ± 12.5	65.0	2.8
487.5 ± 12.5	65.8	3.4

Table D.1: Total cross section of $p(\gamma, \gamma'\pi^0 p)$ for $E_{\gamma'}^{c.m.} > 30$ MeV, based on the entire data set, systematic error is estimated to be $\pm 14.5\%$.

D.2 Photon Asymmetry of $p(\gamma, \gamma'\pi^0 p)$

E_γ/MeV	$\Sigma(E_\gamma)$	$\Delta(\Sigma)$ statistical	$\Delta(\Sigma)$ systematic
350 ± 50	0.571	0.097	0.030
390 ± 50	0.404	0.087	0.022

Table D.2: The photon asymmetry of $p(\gamma, \gamma'\pi^0 p)$ for $E_{\gamma}^{c.m.} > 30$ MeV.

$E_{\gamma'}$/MeV	$\Sigma(E_{\gamma'})$	$\Delta(\Sigma)$ statistical	$\Delta(\Sigma)$ systematic
0	0.584	0.001	0.022
40 ± 10	0.622	0.150	0.043
62.5 ± 12.5	0.459	0.156	0.031
87.5 ± 12.5	0.285	0.216	0.032
115 ± 15	0.353	0.270	0.115
165 ± 35	-0.084	0.319	0.176

Table D.3: The photon asymmetry of $p(\gamma, \gamma'\pi^0 p)$ for 340 MeV $< E_\gamma <$ 440 MeV, based on the July data set. The result for $E_{\gamma'} = 0$ MeV is derived from the analysis of $p(\gamma, \pi^0 p)$ with the same E_γ range as $p(\gamma, \gamma'\pi^0 p)$.

$E_{\gamma'}$/MeV	$\Sigma(E_{\gamma'})$	$\Delta(\Sigma)$ statistical	$\Delta(\Sigma)$ systematic
0	0.534	0.001	0.030
40 ± 10	0.793	0.139	0.045
62.5 ± 12.5	0.563	0.168	0.030
87.5 ± 12.5	0.220	0.274	0.016
140 ± 40	0.164	0.348	0.023

Table D.4: The photon asymmetry of $p(\gamma, \gamma'\pi^0 p)$ for 300 MeV $< E_\gamma <$ 400 MeV, based on the September data set. The result for $E_{\gamma'} = 0$ MeV is derived from the analysis of $p(\gamma, \pi^0 p)$ with the same E_γ range as $p(\gamma, \gamma'\pi^0 p)$.

Bibliography

[1] M Kotulla, J. Ahrens, J. R. M. Annand, R. Beck, G. Casselotti, L. S. Fogg, D. Hornidge, S. Janssen, B. Krusche, J. C. McGeorge, I. J. D. MacGregor, K. Mengel, J. G. Messchendorp, V. Metag, R. Novotny, M. Pfeiffer, M. Rost, S. Sack, R. Sanderson, S. Schadmand, and D. P. Watts. The reaction $\gamma p \rightarrow \pi^0 \gamma' p$ and the magnetic moment of the Δ^+ resonance. *Physical Review Letters*, 89, 2002.

[2] W. Chiang, M. Vanderhaeghen, S. Yang, and D. Drechsel. Unitary model for the $\gamma p \rightarrow \gamma \pi^0 p$ reaction and the magnetic dipole moment of the $\Delta^+(1232)$. *Physical Review C*, 71:015204, 2005.

[3] M. MacCormick, G. Audit, N. d'Hose, L. Ghedira, V. Isbert, S. Kerhoas, L. Y. Murphy, G. Tamas, P. A. Wallace, S. Altieri, A. Braghieri, P. Pedroni, T. Pinelli, J. Ahrens, R. Beck, J. R. Annand, R. A. Crawford, J. D. Kellie, I. J. MacGregor, B. Dolbilkin, and A. Zabrodin. Total photoabsorption cross sections for ^{1}H, ^{2}H, and ^{3}He from 200 to 800 MeV. *Physical Review C*, 53:41–49, 1996.

[4] J. Ahrens, S. Altieri, J. R. Annand, G. Anton, H.-J. Arends, K. Aulenbacher, R. Beck, C. Bradtke, A. Braghieri, N. Degrande, N. d'Hose, H. Dutz, S. Goertz, P. Grabmayr, K. Hansen, J. Harmsen, D. von Harrach, S. Hasegawa, T. Hasegawa, E. Heid, K. Helbing, H. Holvoet, L. van Hoorebeke, N. Horikawa, T. Iwata, P. Jennewein, T. Kageya, B. Kiel, F. Klein, R. Kondratiev, K. Kossert, J. Krimmer, M. Lang, B. Lannoy, R. Leukel, V. Lisin, T. Matsuda, J. C. McGeorge, A. Meier, D. Menze, W. Meyer, T. Michel, J. Naumann, R. O. Owens, A. Panzeri, P. Pedroni, T. Pinelli, I. Preobrajenski, E. Radtke, E. Reichert, G. Reicherz, C. Rohlof, D. Ryckbosch, F. Sadiq, M. Sauer, B. Schoch, M. Schumacher, B. Seitz, T. Speckner, M. Steigerwald, N. Takabayashi, G. Tamas, A. Thomas, R. van de Vyver, A. Wakai, W. Weihofen, F. Wissmann, F. Zapadtka, and G. Zeitler. Helicity Dependence of $\gamma p \rightarrow N\pi$ below 450 MeV and Contribution to the Gerasimov-Drell-Hearn Sum Rule. *Physical Review Letters*, 84:5950–5954, 2000.

[5] D. A. McPherson, D. C. Gates, R. W. Kenney, and W. P. Swanson. Positive Photopion Production from Hydrogen Near Threshold. *Physical Review*, 136:1465–1471, 1964.

[6] K. G. Fissum, H. S. Caplan, E. L. Hallin, D. M. Skopik, J. M. Vogt, M. Frodyma, D. P. Rosenzweig, D. W. Storm, G. V. O'Rielly, and K. R. Garrow. Inclusive positive pion photoproduction. *Physical Review C*, 53:1278–1289, 1996.

[7] R. Beck, H. P. Krahn, J. Ahrens, J. R. Annand, H. J. Arends, G. Audit, A. Braghieri, N. d'Hose, D. Drechsel, O. Hanstein, J. C. McGeorge, R. O. Owens, P. Pedroni, T. Pinelli, G. Tamas, L. Tiator, and T. Walcher. Determination of the E2/M1 ratio in the γN$\rightarrow\Delta$(1232) transition from a simultaneous measurement of p(γ,p)π^0 and p(γ,π^+)n. *Physical Review C*, 61(3):035204, 2000.

[8] H. Genzel et al. Photoproduction of neutral pions on Hydrogen below 500 MeV. *Zeitschrift für Physik*, 268:43, 1974.

[9] V. Pascalutsa and M. Vanderhaeghen. Magnetic Moment of the Δ(1232) Resonance in Chiral Effective-Field Theory. *Physical Review Letters*, 94(10):102003, 2005.

[10] R. Beck, H. P. Krahn, J. Ahrens, H. J. Arends, G. Audit, A. Braghieri, N. d'Hose, S. J. Hall, V. Isbert, J. D. Keellie, I. J. D. MacGregor, P. Pedroni, T. Pinelli, G. Tamas, T. Walcher, and S. Wartenberg. Measurement of the E2/M1 ratio in the N$\rightarrow$ Δ transition using the reaction $p(\gamma,p)\pi^0$. *Physical Review Letters*, 78:606–609, 1997.

[11] B. M. K. Nefkens, M. Arman, H. C. Ballagh, P. F. Glodis, R. P. Haddock, K. C. Leung, D. E. A. Smith, and D. I. Sober. Differential cross sections for pion-proton bremsstrahlung at 269, 298 and 324 MeV. *Physical Review D*, 18:3911–3932, 1978.

[12] M. K. Liou and W. T. Nutt. Soft-photon analysis of pion-proton bremsstrahlung. *Physical Review D*, 16:2176–2180, 1977.

[13] P. Pascual and R. Tarrach. Radiative π^+p scattering and the magnetic moment of the Δ^{++}. *Nuclear Physics B*, 134:133–140, 1978.

[14] A. Bosshard, C. Amsler, M. Döbeli, M. Doser, M. Schaad, J. Riedlberger, P. Truöl, J. A. Bistirlich, K. M. Crowe, S. Ljungfelt, C. A. Meyer, B. van den Brandt, J. A. Konter, S. Mango, D. Renker, J. F. Loude, J. P. Perroud, R. P. Haddock, and D. I. Sober. Analyzing power in pion-proton bremsstrahlung, and the Δ^{++}(1232) magnetic moment. *Physical Review D*, 44:1962–1974, 1991.

[15] C. A. Meyer, C. Amsler, A. Bosshard, K. M. Crowe, M. Döbeli, M. Doser, L. van Elmbt, R. P. Haddock, Q. Ingram, S. Ljungfelt, J. F. Loude, J. P. Perroud, J. Riedlberger, D. Renker, M. Schaad, D. I. Sober, and P. Truöl. Measurement of pion-proton bremsstrahlung for pions at 299 MeV. *Physical Review D*, 38:754–767, 1988.

[16] M. Kotulla. Magnetic moment of the $\Delta^+(1232)$ resonance. *Progress in Particle and Nuclear Physics*, 50:295–303, 2003.

[17] D. Drechsel and M. Vanderhaeghen. Magnetic dipole moment of the $\Delta^+(1232)$ from the $\gamma p \rightarrow \gamma \pi^0 p$ reaction. *Physical Review C*, 64(6):065202, 2001.

[18] B. Seitz. *Helizitätsabhängigkeit der Photoproduktion neutraler Mesonen im Energiebereich 150 MeV bis 780 MeV*. PhD thesis, University of Göttingen, 1999.

[19] A. Thomas. *Crystal Ball Hydrogen (Deuterium) Target Manual.* A2 Collaboration, Institut für Kernphysik,University of Mainz, 2004.

[20] J. R. M. Annand. *Data analysis within an AcquRoot Framework.* University of Glasgow, 2005.

[21] B. Boillat. *In preparation.* PhD thesis, University of Basel, 2007.

[22] S. Lugert. Pulse shape analysis MDM1. Report at CB@MAMI analysis meeting, 2005.

[23] M. Kotulla. *Experiment zur Bestimmung der magnetischen Moments der* $\Delta^+(1232)$ *Resonanz.* PhD thesis, II. Physikalisches Institut, Justus-Liebig-Universitat Giessen, 2001.

[24] R. Leukel. *Photoproduktion neutraler Pionen am Proton mit linear polarisierten Photonen im Bereich der* $\Delta(1232)$ *Resonanz.* PhD thesis, Johannes Gutenberg University, Mainz, Germany, 2001.

[25] Carolyn Mocket et al. The particle adventure. Website of the Particle Data Group at LBNL, 2006. http://particleadventure.org/particleadventure/index.html.

[26] E. Rutherford. The scattering of α- and β- particles by matter and the structure of the atom. *Phil. Mag.*, 21:669, 1911.

[27] Brian Cathcart. *The Fly in the Cathedral.* Farrar, Straus and Giroux, 2004.

[28] E. Rutherford. Collision of α particles with light atoms IV. an anomalous effect in Nitrogen. *Phil. Mag.*, 37:581, 1919.

[29] J. Chadwick. The existence of a neutron. *Proc. Roy. Soc. A*, 136:692, 1932.

[30] J. D. Cockcroft and E. T. S. Walton. Disintegration of Lithium by swift protons. *Nature*, 129:649, 1932.

[31] E. O. Lawrence and M. S. Livingston. A method for producing high speed Hydrogen ions without the use of high voltages. *Phys. Rev.*, 37:1707, 1931.

[32] W.M. Brobeck, E.O. Lawrence, K.R. MacKenzie, E.M. McMillan, R. Serber, D.C. Sewell, K.M. Simpson, and R.L. Thornton. Initial performance of the, 184-inch cyclotron of the University of California. *Phys. Rev.*, 71:449, 1947.

[33] M. Planck. Über eine Verbesserung der Wienschen Spektralgleichung / On an improvement of the Wien's law of radiation. *Verhandl. Dtsch. Phys. Ges.*, 2:202, 1900.

[34] M. Planck. Zur Theorie das Gesetzes der Energieverteilung im Normalspektrum / On the theory of energy distribution law of the normal spectrum radiation. *Verhandl. Dtsch. Phys. Ges.*, 2:237, 1900.

[35] M. Planck. Über das Gesetz der Energieverteilung im Normalspektrum / On the energy distribution law in the normal spectrum radiation. *Annalen der Physik*, 4:553, 1901.

[36] N. Bohr. On the constitution of atoms and molecules. I. *Phil. Mag.*, 26:1, 1913.

[37] A. Einstein. Über einen die Erzeugung und Verwandlung des Lichtes betreffenden heuristischen Gesichtspunkt / On a heuristic point of view about the creation and conversion of light. *Annalen der Physik*, 17:132, 1905.

[38] W. Heisenberg. Quantum-theoretical reinterpretation of kinematic and mechanical connections. *Zeitschrift für Physik*, 33:879, 1925.

[39] L. de Broglie. *Recherches sur la théorie des quanta.* PhD thesis, University of Paris, 1924.

[40] L. de Broglie. Ondes et quanta / Waves and quanta. *Compt. Ren.*, 177:507, 1923.

[41] L. de Broglie. Quanta de lumiere, diffraction et interferences / Light quanta, diffraction, and interference. *Compt. Ren.*, 177:548, 1923.

[42] E. Schrödinger. Quantisierung als Eigenwertproblem (Erste Mitteilung) / Quantization as a problem of proper values. Part I. *Annalen der Physik*, 79:361, 1926.

[43] W. Heisenberg. Über den anschaulichen Inhalt der quantentheoretischen Kinematik und Mechanik / The actual content of quantum theoretical kinematics and mechanics. *Z. Phys.*, 43:172, 1927.

[44] W. Pauli. Über den Zusammenhang des Abschlusses der Elektronengruppen im Atom mit der Komplexstruktur der Spektren / On the connection between the completion of electron groups in an atom with the complex structure of spectra. *Z. Phys.*, 31:765, 1925.

[45] NIST. The NIST reference on constants, units and uncertainty. Website of NIST, 2006. http://www.physics.nist.gov/cgi-bin/cuu/Value?mp.

[46] M. Gell-Mann. A schematic model of baryons and mesons. *Phys. Lett.*, 8:214–215, 1964.

[47] M. Breidenbach, J. I. Friedman, J. I. Kendal, E. D. Bloom, D. H. Coward, H. C. de Staebler, J. Drees, L. W. Mo, and R. E. Taylor. Observed behavior of highly inelastic electron-proton scattering. *Phys. Rev. Lett.*, 23:935, 1969.

[48] B. McKinnon et al. Search for the Θ^+ pentaquark in the reaction $\gamma d \rightarrow pK^-K{+}n$. *Phys. Rev. Lett.*, 96(212001), 2006.

[49] A. Einstein. Ist die Trägheit eines Körpers von seinem Energieinhalt abhängig? / Does the inertia of a body depend upon its energy content? *Annalen der Physik.*, 18:639, 1905.

[50] G. Breit and E. P. Wigner. Capture of slow neutrons. *Phys. Rev.*, 49:519, 1936.

[51] A. Kondratyuk and L. A. Ponomarev. Possibility of measuring the magnetic moment of the isobar $\Delta^{++}(1236)$ in radiative π^+p scattering. *Soviet Journal of Physics*, 7:82, 1968.

[52] S. Eidelman et al. Review of Particle Physics. *Physics Letters B*, 592:1, 2004.

[53] F. Schlumph. Magnetic moments of the baryon decuplet in a relativistic quark model. *Physical Review D*, 48(9):4478–4480, 1993.

[54] D. B. Leinweber, T. Draper, and R. M. Woloshyn. Decuplet baryon structure from lattice QCD. *Physical Review D*, 46(7):3067–3085, 1992.

[55] M. N. Butler, M. J. Savage, and R. P. Springer. Electromagnetic moments of the baryon decuplet. *Physical Review D*, 49(7):3459–3465, 1994.

[56] H. C. Kim, M. Praszalowicz, and K. Goeke. Magnetic moments of the SU(3) decuplet in the chiral quark-soliton model. *Physical Review D*, 57(5):2859–2870, 1998.

[57] T. M. Aliev, A. Ozpineci, and M. Savci. Magnetic moments of Δ baryons in light cone QCD sum rules. *Nuclear Physics A*, 678:443–454, 2000.

[58] A. I. Machavariani, A. Faessler, and A. J. Buchmann. Field theoretical description of electromagmetic Δ resonance production and determination of the magnetic moment of the $\Delta^+(1232)$ resonance by the $ep \rightarrow e'N'\pi'\gamma'$ and $\gamma p \rightarrow N'\pi'\gamma'$reactions. *Nuclear Physics A*, 646:231–257, 1999.

[59] D. Drechsel, M. Vanderhaeghen, M. Giannini, and E. Santopinto. Inelastic photon scattering and the magnetic moment of the $\Delta(1232)$ resonance. *Physics Letters B*, 484:236–242, 2000.

[60] R. D. Mattuck. *A Guide to Feynman Diagrams in the Many-Body Problem.* Dover Publications, New York, second edition, 1992.

[61] S. Scherer. Introduction to chiral perturbation theory. *Advances in Nuclear Physics*, 27, 2003.

[62] V. Pascalutsa and D. R. Phillips. Effective theory of the $\Delta(1232)$ resonance in Compton scattering off the nucleon. *Physical Review C*, 67(5):055202, 2003.

[63] V. Pascalutsa and D. R. Phillips. Model-independent effects of Δ excitation in nucleon polarizabilities. *Physical Review C*, 68(5):055205, 2003.

[64] C. Picciotto. Fits to $\pi^- p$ bremsstrahlung. *Journal of Physics G Nuclear Physics*, 13:L23–L25, 1987.

[65] S. M. Playfer, W. van Doesburg, A. G. Zephat, T. Bressani, E. Chiavassa, S. Costa, J. D. Davies, G. Dellacassa, C. W. E. van Eijk, M. Gallio, R. W. Hollander, J. V. Jovanovich, G. Kernel, W. Lourens, J. Lowe, E. G. Michaelis, A. Musso, F. Sever, F. Siohan, A. Stanovnik, and N. W. Tanner. $\Pi^- p$ bremsstrahlung at 300 MeV/c. *Journal of Physics G Nuclear Physics*, 13:297–310, 1987.

[66] F. E. Low. Bremsstrahlung of Very Low-Energy Quanta in Elementary Particle Collisions. *Physical Review*, 110:974–977, 1958.

[67] B. M. K. Nefkens and D. I. Sober. External-emission dominance in pion-proton bremsstrahlung. *Physical Review D*, 14:2434–2436, 1976.

[68] D. I. Sober, M. Arman, D. J. Blasberg, R. P. Haddock, K. C. Leung, B. M. K. Nefkens, B. L. Schrock, and J. M. Sperinde. Measurement of radiative pion-proton scattering at backward photon angles. *Physical Review D*, 11:1017–1035, 1975.

[69] M. Arman, D. J. Blasberg, R. P. Haddock, K. C. Leung, B. M. Nefkens, B. L. Schrock, D. I. Sober, and J. M. Sperinde. Measurement of Radiative Pion-Proton Scattering near the $\Delta(1236)$ Resonance. *Physical Review Letters*, 29:962–965, 1972.

[70] M. A. Bég, B. W. Lee, and A. Pais. SU(6) and Electromagnetic Interactions. *Physical Review Letters*, 13:514–517, 1964.

[71] L. Heller, S. Kumano, J. C. Martinez, and E. J. Moniz. Pion-nucleon bremsstrahlung and Δ electromagnetic moments. *Physical Review C*, 35:718–736, 1987.

[72] CERN. *Geant Detector Description and Simulation Tool*, 1994. Application and Software Group, Computing and Network Division, CERN.

[73] A. Jankowiak. The Mainz Microtron MAMI - past and future. Technical Report 1, KPH, 2005.

[74] H. Herminghaus. First operation of the 850 MeV c.w. electron accelerator MAMI. In *Proc. of the 1990 Linear Acc. Conf., Albuquerque, N.M, 10.9. - 14.9.90*, page 362, 1990.

[75] S. P. Kapitsa. The microtron and its fields of application. *Journal of Nuclear Energy*, 8:183–190, 1966.

[76] K. Aulenbacher, C. Nachtigall, H. G. Andresen, J. Bermuth, T. Dombo, P. Drescher, H. Euteneuer, H. Fischer, D. V. Harrach, P. Hartmann, J. Hoffmann, P. Jennewein, K. H. Kaiser, S. Köbis, H. J. Kreidel, J. Langbein, M. Petri, S. Plützer, E. Reichert, M. Schemies, H.-J. Schöpe, K.-H. Steffens, M. Steigerwald, H. Trautner, and T. Weis. The MAMI source of polarized electrons. *Nuclear Instruments and Methods in Physics Research A*, 391:498–506, 1997.

[77] I. Anthony, J. D. Kellie, S. J. Hall, G. J. Miller, and J. Ahrens. Design of a tagged photon spectrometer for use with the Mainz 840 MeV microtron. *Nuclear Instruments and Methods in Physics Research A*, 301:230–240, 1991.

[78] S. J. Hall, G. J. Miller, R. Beck, and P. Jennewein. A focal plain system for the 855MeV tagged photon spectrometer at MAMI-B. *Nuclear Instruments and Methods in Physics Research A*, 368:698–708, 1996.

[79] A. Reiter et al. A microscope for the Glasgow photon tagging spectrometer in Mainz. *European Physical Journal A*, 30, 2006.

[80] U. Timm. Coherent bremsstrahlung of electrons in crystals. *Fortschritte der Physik*, 17:765–808, 1969.

[81] D. Lohmann, J. Peise, J. Ahrens, I. Anthony, H. J. Arends, R. Beck, R. Crawford, A. Hünger, K. H. Kaiser, J. D. Kellie, C. Klumper, P. Krahn, A. Kraus, U. Ludwig, M. Schumacher, O. Selke, M. Schmitz, M. Schneider, F. Wissmann, and S. Wolf. Linearly polarised photons at MAMI, (Mainz). *Nuclear Instruments and Methods in Physics Research A*, 343:494–507, 1994.

[82] K. Livingston. The Stonehenge technique: a new method of crystal alignment for coherent bremsstrahlung experiments. In *International Conference on Charged and Neutral Particles Channeling Phenomena, Proceedings of the SPIE, Volume 5974*, pages 170–176, 2005.

[83] F. Rambo, J. Ahrens, H. J. Arends, R. Beck, G. Galler, J. D. Kellie, H. P. Krahn, A. Kraus, U. Ludwig, J. Peise, A. Schmidt, M. Schumacher, F. Smend, F. Wissmann, and S. Wolf. Enhancement of the linear polarisation of coherent bremsstrahlung by collimation of the photon beam. *Physical Review C*, 58(1):489–501, 1998.

[84] F. A. Natter, P. Grabmayr, T. Hehl, R. O. Owens, and S. Wunderlich. Monte Carlo simulation and the analytical calculation of coherent

bremsstrahlung and its polarisation. *Nuclear Instruments and Methods in Physics Research B*, 211:465–486, 2003.

[85] B. M. K. Nefkens. The Crystal Ball. Technical Report 1, UCLA, 1995.

[86] G. Audit, A. Bloch, N. d'Hose, V. Isbert, J. Martin, R. Powers, D. Sunnerman, G. Tamas, P. A. Wallace, S. Alteri, A. Bragheri, F. Fossati, P. Pedroni, T. Pinelli, J. Bechade, P. H. Carton, S. Conat, D. Foucaud, and M. Goldsticker. DAPHNE: a large-acceptance tracking detector for the study of photoreactions at intermediate energies. *Nuclear Instruments and Methods in Physics Research A*, 301:473–481, 1991.

[87] E. Bosze, J. Simon-Gillo, J. Boissevain, J. Chang, and R. Seto. Rohacell foam as a silicon support structure material for the PHENIX multiplicity vertex detector. *Nuclear Instruments and Methods in Physics Research A*, 400:224–232, 1997.

[88] R. Novotny. The BaF_2 photon spectrometer TAPS. *IEEE Transactions on Nuclear Science*, 38:379–385, 1991.

[89] Konrad Kleinknecht. *Detectors for Particle Radiation.* Cambridge University Press, 1986.

[90] R. Novotny, R. Beck, W. Doering, V. Hejny, A. Hofstaetter, V. Metag, and K. Roemer. Scintillators for photon detection at medium energies - a comparative study of BaF_2, CeF_3 and $PbWO_4$. *Nuclear Instruments and Methods in Physics Research A*, 486:131–135, 2002.

[91] i-tr0nics GmbH. *Multi-Channel Sampling Analogue to Digital Convertor Module i-SADC108032 for the Mainz Crystal Ball Detector.* i-tr0nics GmbH, i-tr0nics GmbH Erikastrasse 18b, D-185521 Hohenbrunn, Germany, 2003. wwww.i-tronics.net.

[92] P. Marciniewski. *Fast Digital Trigger Systems for Experiments in High Energy Physics.* PhD thesis, Uppsala Dissertations from the Faculty of Science Technology, Uppsala, (Sweden), 2001. http://www.tsl.uu.se/~pavel/ 10. Feb. 2006.

[93] J. R. M. Annand and D. Krambrich. DAQ for Crystal Ball @ MAMI. Technical report, CB@MAMI, 2002.

[94] R. Beck, D. Hornidge, M. Lang, and D. Krambrich. Upgrade of the Crystal Ball electronics. Technical report, University of Mainz, 2002.

[95] P. Drexler et al. The new readout electronics for the BaF_2 calorimeter TAPS. *IEEE Transactions on Nuclear Science*, 50:969, 2003.

[96] J. R. M. Annand, I. Anthony, A. H. Sibbald, K. Livingston. *ACQU Data acquisition system for nuclear physics, 3rd Edition.* University of Glasgow, 1997.

[97] Rene Brun and Fons Rademakers et al. *ROOT User's Guide 4.04*. CERN, 2005. CERN.

[98] R. Brun and Fons Rademakers. ROOT - an object oriented data analysis framework. *Nuclear Instruments and Methods in Physics Research A*, 389:81–86, 1997.

[99] A. Nikolaev. *In preparation.* PhD thesis, University of Mainz, 2007.

[100] R. Codling. *In preparation.* PhD thesis, University of Glasgow, 2007.

[101] I. Anthony. Private communication. 2006.

[102] M. Unverzagt. *In preparation.* PhD thesis, University of Mainz, 2007.

[103] J.Brudvik. *In preparation.* PhD thesis, UCLA, 2007.

[104] D. Krambrich. *In preparation.* PhD thesis, University of Mainz, 2007.

[105] S. Schuman. *In preparation.* PhD thesis, University of Mainz, 2007.

[106] F. Zehr. *In preparation.* PhD thesis, University of Basel, 2007.

[107] S. Lugert. *In preparation.* PhD thesis, University of Giessen, 2007.

[108] R. Gregor. *In preparation.* PhD thesis, University of Giessen, 2007.

[109] C. Allgower. Getting started with the Crystal Ball Monte Carlo Package - a step by step guide. Technical report, UCLA, 1999.

[110] W. B. Tippens. Crystal Ball Monte Carlo Analyser in PAW. Technical Report 2, UCLA, 1996.

[111] D. Glazier. Private communication.

[112] M. Vanderhaeghen. Private communication.

[113] P. Avery. Applied fitting theory I-VII. http://www.phys.ufl.edu/˜avery/fitting.html, December 2006.

[114] K. Livingston. Linearly polaried photons at CLAS. Technical report, University of Glasgow, 2006.